S
665.772
M26mhdg
V.2
October
1977
Montana Energy and
MHD Research and
Development
Institute
MHD power
generation

MHD POWER GENERATION

RESEARCH, DEVELOPMENT,
AND ENGINEERING

Volume II

Annual Report
October 1977

STATE DOCUMENTS COLLECTION

JUL 03 1996

MONTANA STATE LIBRARY
1515 E. 6th AVE.
HELENA, MONTANA 59620

The Montana Energy and MHD Research and Development Institute, Inc.

Post Office Box 3809
Butte, Montana 59701

PLEASE RETURN

Montana State Library
3 0864 1006 8657 8

EF-77-C-01-2524-16

MHD POWER GENERATION

RESEARCH, DEVELOPMENT, AND ENGINEERING

Volume II

Annual Report
October 1977

prepared by

THE MONTANA ENERGY AND MHD
RESEARCH AND DEVELOPMENT INSTITUTE, INC.
P. O. Box 3809
Butte, Montana 59701

prepared for

THE U.S. DEPARTMENT OF ENERGY

Under Contract No. EF-77-C-01-2524

TABLE OF CONTENTS

Title and Principal Investigator		Page
VOLUME II		
TASK G1	Slag Physical Properties: Properties of Current Carriers, V.H. Schmidt, S.M. Sharma, and S. Snyder.	321
TASK G2	Physical Properties of Coal Slag: Thermionic Emission, J. Anderson and G.J. Lapeyre.	332
TASK H1	MHD Systems Instrumentation and Data Acquisition, R. Johnson and T. Robles.	376
TASK H3	Cycle Analysis and Control, D. Pierre, D. Rudberg, C. Dudding, and N. Du.	441
TASK M	Preliminary ETF Environmental Analysis and Site Study, S. Brown.	498
TASK N	Materials Evaluation and Management of University and MERDI Supporting Science and Technology, J.J. Rasmussen.	532
TASK Q	CDIF Environmental Monitoring and Evaluation, E. Kukay.	590
TASK S1	MHD CDIF Pre-Operational Biological Baseline Surveillance Program, R. Portch, J. Cornish, S. Bentsen, M. Griffin, T. Pelletier, and D. Dolenc.	623

Digitized by the Internet Archive
in 2017 with funding from
Montana State Library

https://archive.org/details/mhdpowergenerat1979mont_0

TASK G1

Slag Physical Properties: Properties of Current Carriers

V. H. Schmidt, S. N. Sharma, and S. Snyder

ABSTRACT

Work on Hall mobility and nuclear magnetic resonance (NMR) studies of electronic and ionic conductivity in coal slag and related materials was continued. Improvements were made in the heater for these experiments, which has been operated up to 1500°C in fields up to 12,000 gauss. The Hall effect was observed to 900°C in Fe_2O_3, a constituent of slag. An upper limit of 0.01 cm^2/volt-sec was established for the Hall mobility in Rosebud slag at 925°C, indicating that the conductivity is primarily ionic in this slag at this temperature. The Al^{27} NMR signal was studied in Rosebud slag to 700°C. Narrowing of the NMR line was observed between 430 and 500°C, but the electrical conductivity at these temperatures is so low that even if the conductivity is entirely ionic, the rate of ionic motion is not sufficient to cause the observed narrowing in this sample. Compositions of synthetic slags intended for future Hall and NMR studies are presented.

I. OBJECTIVE AND SCOPE OF WORK

The concentrations and mobilities of current carriers in coal slag and seed-slag mixtures are to be determined using Hall mobility and NMR (nuclear magnetic resonance) measurements. Initial measurements will be made at temperatures up to 1600°C, with an eventual goal of 2200°C. The Hall mobility work will begin with a continuation of apparatus check-out, followed by measurements on slag and seed-slag samples. Some design and construction of the NMR apparatus must precede apparatus check-out and sample measurements.

Hall mobility and NMR methods also will be used to examine the nature of conduction processes in certain ceramic materials used or planned for use in MHD channels.

The slags to be examined will be mostly from Western and especially Montana coals. The seed compounds will be potassium carbonate and potassium sulfate. Provision will be made for control of partial pressure of oxygen to maintain reasonable constancy of seed-slag composition during a given run. The ceramics to be tested will be mainly those in which the conduction mechanism at high temperature is in doubt.

II. SUMMARY OF PROGRESS TO DATE

A. Hall Effect

The apparatus suitable for the study of the Hall mobility has been assembled. The electronics and experimental procedures have been checked

out using a commercial Hall generator chip. Hall measurements on the sample of Fe_2O_3 have been carried out below and above the Neel temperature (960 K). Measurements on Rosebud slag and seeded slag samples have been attempted. From an experiment at 925°C, an upper limit of 0.01/cm^2/volt-sec for the Hall mobility of unseeded slag was established. A new technique has been developed to avoid the use of contact cement.

B. Nuclear Magnetic Resonance

The NMR spectrometer is working well, and measurements on Rosebud slag have been made up to 700°C. The signal-to-noise ratio is reasonable. Narrowing of the Al^{27} NMR line occurred above 400°C. The signal-to-noise ratio is satisfactory up to 600°C. The slag sample becomes increasingly conductive with rising temperature, and at about 700°C, it loads the spectrometer circuit to the extent that the signal becomes difficult to observe.

III. DETAILED DESCRIPTION OF TECHNICAL PROGRESS

A. Hall Effect

A detailed description of the design of the Hall effect apparatus appears in last year's annual report. The design is based on the premise that a large volume sample is desirable, both to increase the volume-to-surface ratio of the sample to reduce the rate of composition change from evaporation and to increase the resistance of the crucible and electrodes to corrosion by the slag. The large volume requirement made the use of an a-c magnetic field impractical from the standpoints of cost and power consumption. Therefore, a large d-c electromagnet with 15-inch diameter pole pieces, which was available, was fitted with new pole caps giving a 5-inch gap, and a Hall cell was designed with sufficient thermal insulation with about 100 cm^3 useful sample volume (3 cm diameter by 10 cm high). The magnet with these pole caps gives a field of up to 13,500 gauss and can operate continuously at 12,000 gauss.

For ionic carriers, the Hall mobility is too small to give an observable Hall voltage, so any observed Hall signal can be taken as an indication of electronic conductivity. If ionic and electronic conductivity coexist, the observed Hall mobility is smaller than the electronic Hall mobility by the ratio (electronic conductivity/total conductivity).

In the apparatus, the d-c magnetic field is horizontal, and a vertical a-c current is applied to the slag by means of platinum electrodes. The Hall effect then causes an electric field at the same a-c frequency which is perpendicular to both the applied magnetic and electric fields. The Hall signal is picked up by a second pair of electrodes and extracted from the noise by means of a lock-in amplifier.

This year's work began with an attempt to check out the electrical circuits for determining the Hall mobility. Since one ultimate aim of these experiments is to get information on slag properties in the molten state, it seemed wise to choose a liquid as the specimen. Liquid mercury for which the Hall mobility has been measured was chosen. Since mercury is a very good conductor, it was necessary to feed more than one ampere of a-

c current to have any chance of observing a signal. A power amplifier was added to the current to obtain such large currents, but the spurious signals caused by these currents in the sample even in the absence of a magnetic field necessitated discontinuation of the mercury test. A solid sample of known Hall mobility which would give a very small Hall voltage for sufficiently small applied electric and magnetic fields was chosen next. A commercial integrated circuit chip with a Hall generator was used. The Hall voltage generated by the chip was proportional to the d-c output of the lock-in amplifier, which was displayed on a chart recorder. When the magnetic field was reversed, the d-c output was shifted above or below a base or reference line, depending on the direction of the field. By varying the magnitude of the magnetic or applied electric field, a proportional change in the magnitude of the Hall voltage was recorded. A Hall voltage as small as 3 nV was measured with a signal-to-noise ratio of 2. This checked out the electronics and the experimental technique.

Next, an attempt was made to measure the Hall coefficient of a solid sample of unseeded Rosebud slag at 925°C. The sample had the dimensions of 0.85 cm x 0.27 cm x 0.13 cm and was attached to nickel wire electrodes with silver paint. The assembly was suspended in an alumina crucible inside the furnace. Because of the high resistance of slag[1] (for this sample, R≈1.18 MΩ at 925°C) and the low impedance of the balance circuit, only a small fraction of any Hall voltage would have appeared at the preamplifier of the lock-in. Hence, the signal-to-noise ratio was not very good, and no Hall voltage was observed. It was concluded, however, that the maximum mobility at 925°C was μ_{max} = 0.01 cm^2/volt-sec if electronic conductivity primarily by one carrier (electrons or holes) is assumed. This maximum mobility is lower than almost all mobilities reported[2] in oxides such as Fe_2O_3, so it seems likely that conduction in this slag is primarily ionic at 925°C.

A new balance circuit was designed and built to improve the signal-to-noise ratio. In the new circuit, one of the Hall terminals is connected directly to the "A" terminal of the high impedance preamplifier, thus eliminating electrical loading of the sample. The phase shift caused by the capacitive impedance to ground of the coaxial cable from the Hall contact to the "A" terminal is nulled out by a variable capacitor between the signal generator and the Hall contact. The preamplifier "B" terminal is connected to the slider of a potentiometer connected between the a-c supply and ground. For the "A minus B" mode of operation, adjustments of these phase and amplitude controls allow any misalignment voltage to be nulled out so that the d-c output of the lock-in is then zero in the absence of a Hall signal.

Difficulty was encountered in doing the experiment with this balance circuit because the balance point of the circuit constantly drifted. This made it impossible to establish a stable base line on the chart recorder, especially in the sensitivity range required by the experiment. The cause of this drift is not known. Possibly, the silver paint connecting the electrodes to the slag sample evaporates slowly and consequently changes the contact resistance. It also may be that temperature fluctuations in the furnace caused the resistance of the sample to vary continuously. Based on Pollina's[1] work, a temperature change of 1 K will produce a 1.44 percent change in the sample resistance.

During these experiments, the heater contacts became loose, so the furnace was rewound using only a single heater element. It also was improved by adding clamps to hold the lid down tightly. This maintained the argon atmosphere better and prevented the Grafoil insulation from burning.

Because of the difficulty of observing the Hall effect in natural unseeded slag, it was decided first to try certain slag constituents and work by steps toward mixtures corresponding to natural slags. The work began with n-type Fe_2O_3 (hematite) because its Hall mobility had been measured previously.[2] Below its antiferromagnetic transition (Neel) temperature of 960 K, a magnetic-field-dependent Hall mobility in agreement with results of Morin[2] was observed as shown in Figures 1 to 3. Above the Neel point, the observed value of 0.02 ± 0.02 cm^2/volt-sec was consistent with the value of 0.025 ± 0.005 cm^2/volt-sec found by van Daal and Bosman,[3] who attempted to explain the unusual occurrence of positive mobility in an n-type electronic semiconductor. Measurements could be made only to 1160 K. Above this temperature, the noise level became very high, perhaps because the silver used to cement the contact wires to the sample was approaching its melting point and becoming soft, thereby making the contacts noisy. Similar difficulties occurred at high temperature in those slag measurements in which silver cement was used on the contacts. Several companies were contacted in order to obtain some cements which could withstand higher temperatures. Surprisingly, it seems that no such cement is available. After considerable effort, a technique has been developed where no cement is needed to mount the electrodes. The procedure is rather difficult but the electrodes, made of platinum wire, are embedded in the sample itself. It is very important that the sample prepared in this manner should be raised well above the melting point and annealed while cooling. It is planned to try tests on the samples prepared in this way.

B. Nuclear Magnetic Resonance

NMR experiments were begun by checking out the electronics and the spectrometer using saturated aqueous solutions of lithium and aluminum inorganic compounds. Being limited to 12,000 gauss magnetic field, the spectrometer was optimized at about 12 MHz in order to study the Al^{27} resonance. Observation of the aluminum resonance line with high signal-to-noise ratio was very important because the Al^{27} nuclear isotope was chosen as the NMR probe for the initial study of coal slag. This is because Al_2O_3 constitutes about 20 percent of the slag, and Al^{27} is a good NMR nucleus. Next, some experiments were done on pure Al_2O_3 powder. This system has been studied well.[4] After the NMR signal of Al^{27} in alumina powder was optimized, a sample of Rosebud slag was tried. The signal-to-noise ratio on an unannealed sample was very low so the sample was annealed. Using the Robinson spectrometer, the Varian magnet, and a Northern Scientific NS-575 Signal Averager, the aluminum resonance in slag at room temperature was obtained. The line is very broad at room temperature. The presence of the paramagnetic iron ions or interaction of electric field gradients with the Al^{27} nuclear quadrupole moment may be responsible for this.

The spectrometer was improved further and now the Al^{27} resonance can be observed at room temperature with reasonable signal-to-noise ratio using a signal averager. The temperature dependence of the aluminum resonance

was measured in steps of 100°C up to 700°C. A narrowing of the NMR line with increase in temperature was observed from 43 gauss at 430°C to 32 gauss at 500°C. Such narrowing indicates that the magnetic fields or electric field gradients responsible for the linewidth fluctuate with a correlation time τ of the order of a microsecond in the 430 to 500°C temperature range. Such fluctuations could be caused by diffusion of aluminum ions or neighboring ions or neutral groups or by hindered rotations of ionic or neutral groups. To test the hypothesis that diffusion of aluminum or aluminum-containing ions is responsible both for the linewidth and the electrical conductivity, it was noted first that ionic jumps of the typical interatomic distance a of about 3 A° with the above correlation yield a diffusion constant $D = a^2/\tau \simeq 10^{-9}$ cm^2/sec. By using the Einstein relation $qD = \mu kT$ between D and mobility μ, where q is carrier charge and k is Boltzmann's constant, the conductivity $\sigma = nq\mu$ is predicted to be of order 10^{-3} (ohm-cm)$^{-1}$ if the aluminum ion concentration $n \simeq 10^{22}$/cm^3 and charge $q = 3e$ are used. A slight extrapolation of Pollina's conductivity data[1] for unseeded Rosebud bottom ash slag yields $\sigma \simeq 2 \times 10^{-7}$ (ohm-cm)$^{-1}$ in this temperature range. Accordingly, it was concluded that for this slag in this temperature range, the line narrowing is caused either by hindered rotation or by diffusion of neutral groups.

In these NMR experiments, the copper NMR coil was held in place on the slag sample with a Sauereisen cement. This arrangement proved satisfactory to 700°C at which temperature the slag conductivity had increased to the extent that the spectrometer circuit was loaded excessively and the signal became difficult to observe.

IV. CONCLUSIONS

A. Hall Effect

The tests with a silicon Hall chip showed that the circuit has very good sensitivity under favorable conditions, being able to measure a Hall voltage of a few nanovolts. The tests with Fe_2O_3 up to 1160 K showed some need for improvement because the standard deviation was four times as great as that of van Daal and Bosman.[3] An upper limit of 0.01 cm^2/volt-sec for the Hall mobility in unseeded Rosebud bottom ash slag at 925°C has been established. Because most known electronic semiconductors have mobilities above this value, it seems likely that conduction in this slag is primarily ionic at this temperature. The present apparatus should be capable of detecting primarily electronic conductivity in slag up to at least 925°C. Measurements will be made next on slags containing more iron oxide, which are more likely to be electronic conductors, and will develop the apparatus and sample preparation techniques further so that measurements can be made on both liquid and solid samples at higher temperatures.

B. Nuclear Magnetic Resonance

The NMR spectrometer is working well, and the Al^{27} resonance has been observed from room temperature to 700°C in Rosebud bottom ash coal slag. A narrowing of the NMR line was observed between 430 and 500°C. The rate of ionic motion necessary to produce such narrowing would produce an electrical conductivity much greater than the observed[1] value, so the line narrowing is attributed to hindered rotation or diffusion of neutral groups.

Because ionic diffusion does provide the principal NMR line narrowing or spin-lattice relaxation mechanism in many substances, it is expected that NMR measurements will provide information on ionic motion in solid slag samples of other compositions and particularly in liquid slags because ionic diffusion is not impeded in liquids.

Measurements on the above sample could not be made beyond 700°C because of increasing sample conductivity with rising temperature. To go to higher temperatures, it may be necessary to powder the sample and mix it with an insulating powder, as is standard practice in NMR of metals. This method will not work for liquid samples so an attempt will be made to adapt techniques used in NMR studies of liquid metals at high temperatures.

C. Selection of Slag Compositions for Further Studies

For this discussion, slags will be divided into categories of seeded and unseeded, and iron-containing and iron-free. It is planned to make NMR measurements on iron-free samples to determine whether the iron ions have important effects on NMR linewidth and relaxation in the iron-containing slags. Slags with higher iron content than normally found in Montana coal ash will be used for Hall effect studies because they are expected to exhibit primarily electronic conductivity. Slags seeded with both K_2CO_3 and Na_2CO_3 will be used in NMR studies. The phase diagrams for the sodium-containing compositions are reasonably similar to those for the potassium-containing mixtures, and the availability of Na^{23} as a second NMR nucleus will help identify the nature of any ionic diffusion present.

Specific possibilities in the iron-free, unseeded category are anorthite ($CaO \cdot Al_2O_3 \cdot 2SiO_2$) which melts at 1553°C and the ternary eutectic of anorthite, pseudowollastonite ($CaO \cdot SiO_2$), and tridymite (SiO_2) which occurs at 1170°C. The projection of the Rosebud bottom ash composition onto the CaO-Al_2O_3-SiO_2 ternary plane[5] falls almost midway between the above two compositions. Use of single-composition or eutectic samples such as these would avoid problems in interpreting results presented by samples of arbitrary composition for which the sample is part liquid and part solid in a certain temperature range and consists of large crystals of one substance imbedded in a solid mixture of other substances at lower temperatures.

Phase diagrams[6] for the Na_2O-Al_2O_3-FeO-SiO_2 system yield several possibilities for a seeded iron-rich synthetic slag. One of these is the ternary eutectic at 990°C of nephelite ($NaAlSiO_4$), albite ($Na_2O \cdot Al_2O_3 \cdot 6SiO_2$), and fayalite ($2FeO \cdot SiO_2$) of composition 13.4 percent Na_2O, 9.0 percent FeO, 21.9 percent Al_2O_3, and 55 percent SiO_2. A quaternary eutectic[7] near the composition 17.3 percent Na_2O, 10.8 percent Al_2O_3, 17.3 percent Fe_2O_3, and 54.6 percent SiO_2 has higher iron content. Both lack the calcia and magnesia found in Rosebud coal but otherwise do not approximate too badly a slag which could result from adding seed and iron oxide (to enhance electronic conductivity) to Rosebud coal. The electronic conductivity is expected to depend on the FeO-Fe_2O_3 ratio which, in turn, will depend on oxygen partial pressure, so measurements on such samples would be made with various oxygen partial pressures.

MILESTONE CHART

STATUS DATE _____

TASK G1

PROGRESS

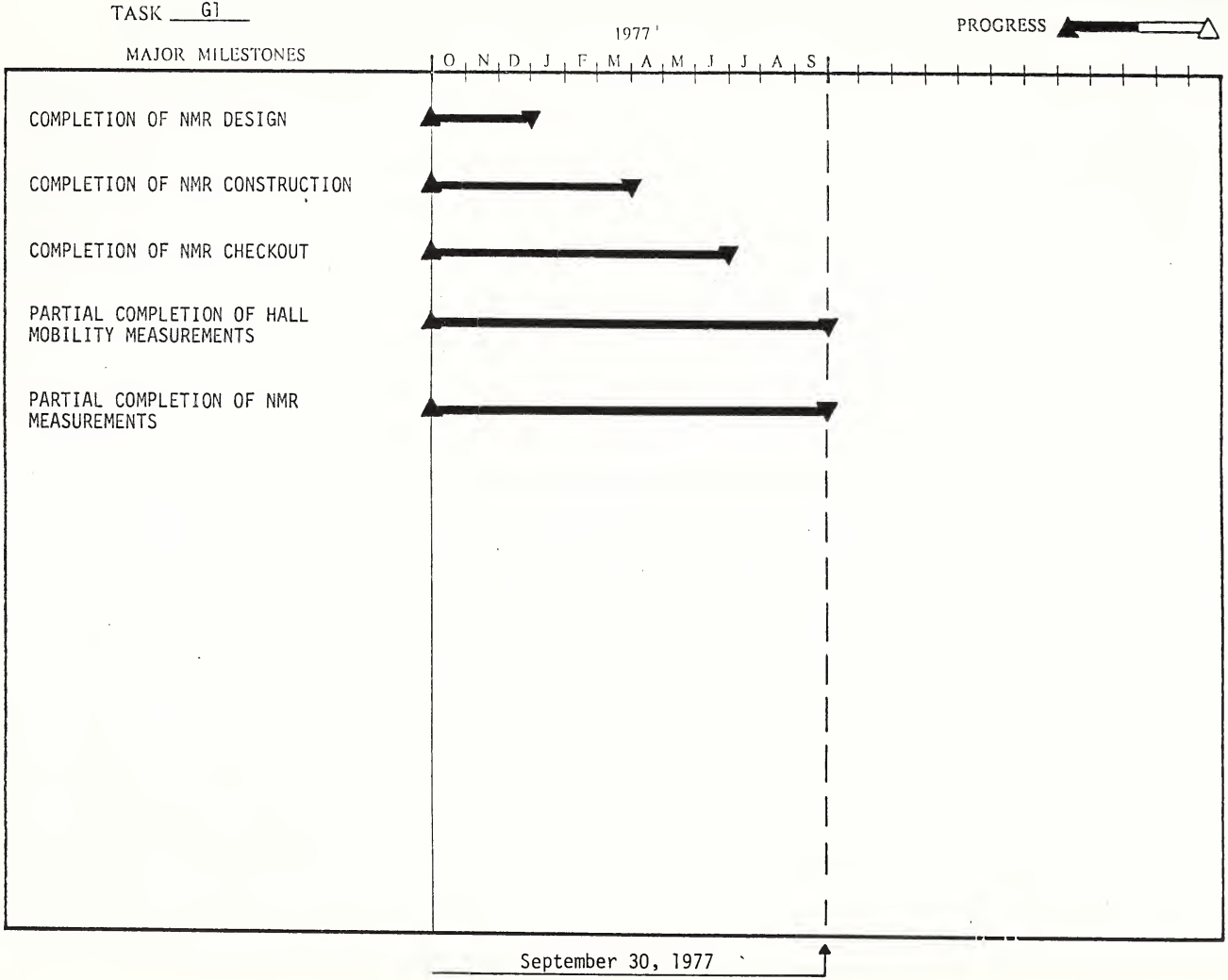
MAJOR MILESTONES
1977
O N D J F M A M J J A S
COMPLETION OF NMR DESIGN
COMPLETION OF NMR CONSTRUCTION
COMPLETION OF NMR CHECKOUT
PARTIAL COMPLETION OF HALL MOBILITY MEASUREMENTS
PARTIAL COMPLETION OF NMR MEASUREMENTS
September 30, 1977

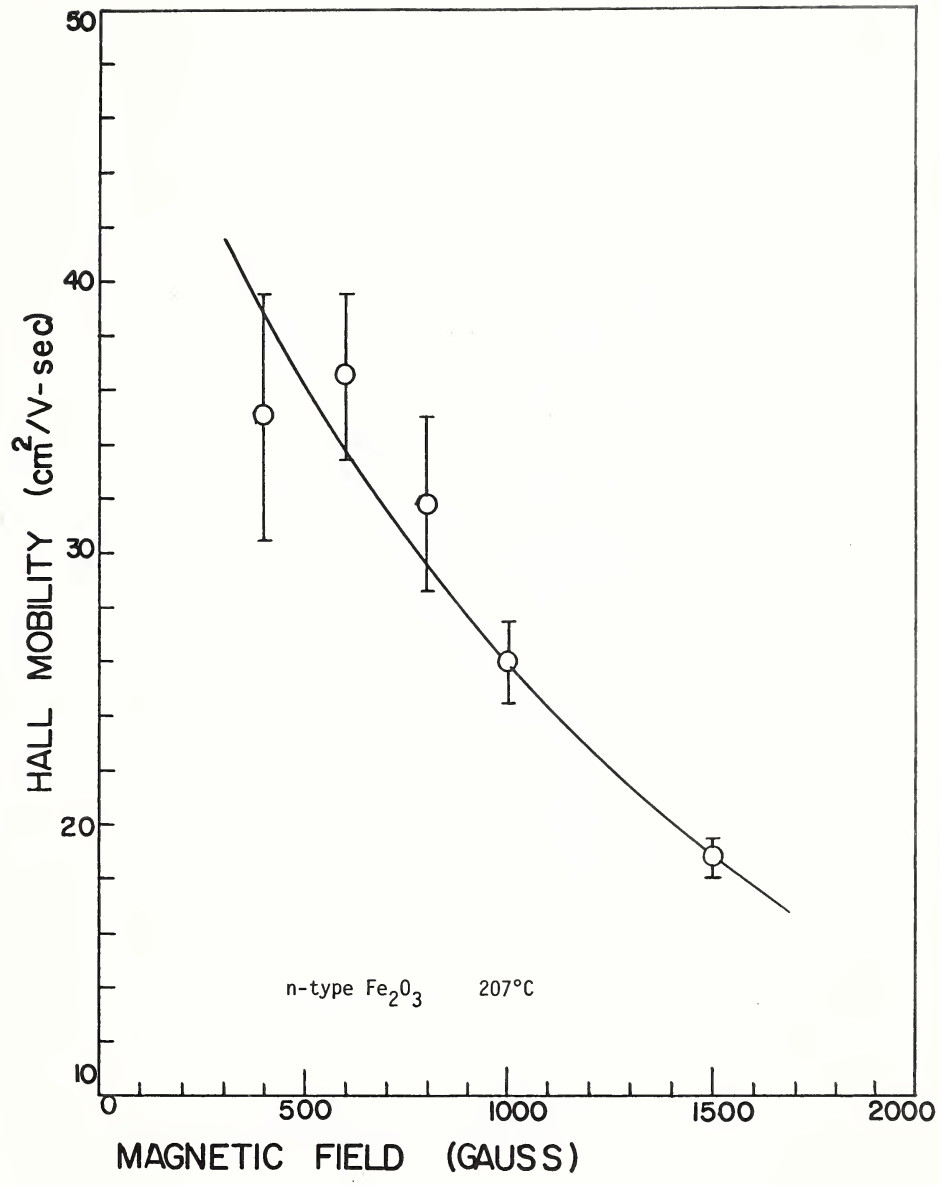

Figure 1.--Magnitude of Hall mobility vs. applied magnetic field at 207°C

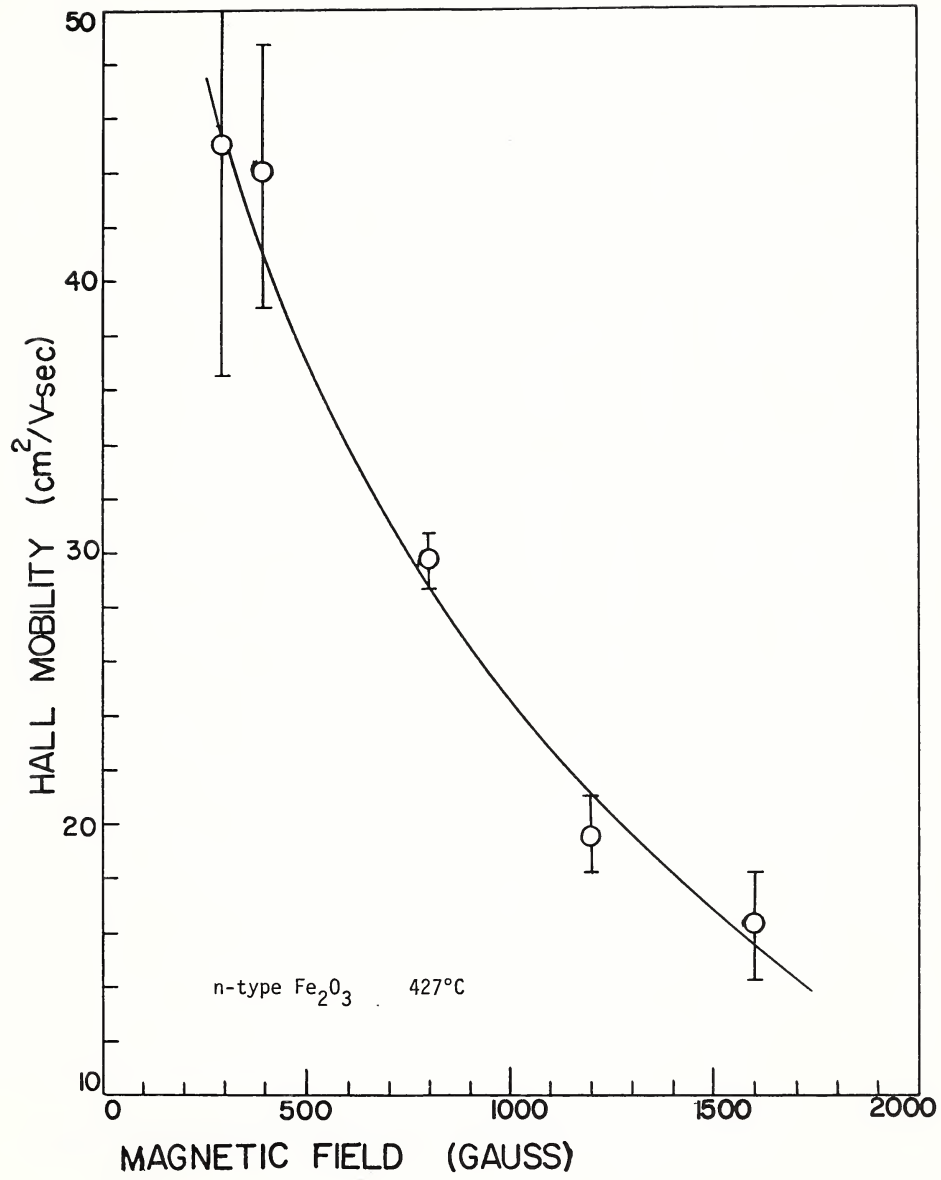

Figure 2.--Magnitude of Hall mobility vs. applied magnetic field at 427°C

60
40
30
20
10
0
500
1000
HALL MOBILITY (cm²/V-sec)
MAGNETIC FIELD (GAUSS)

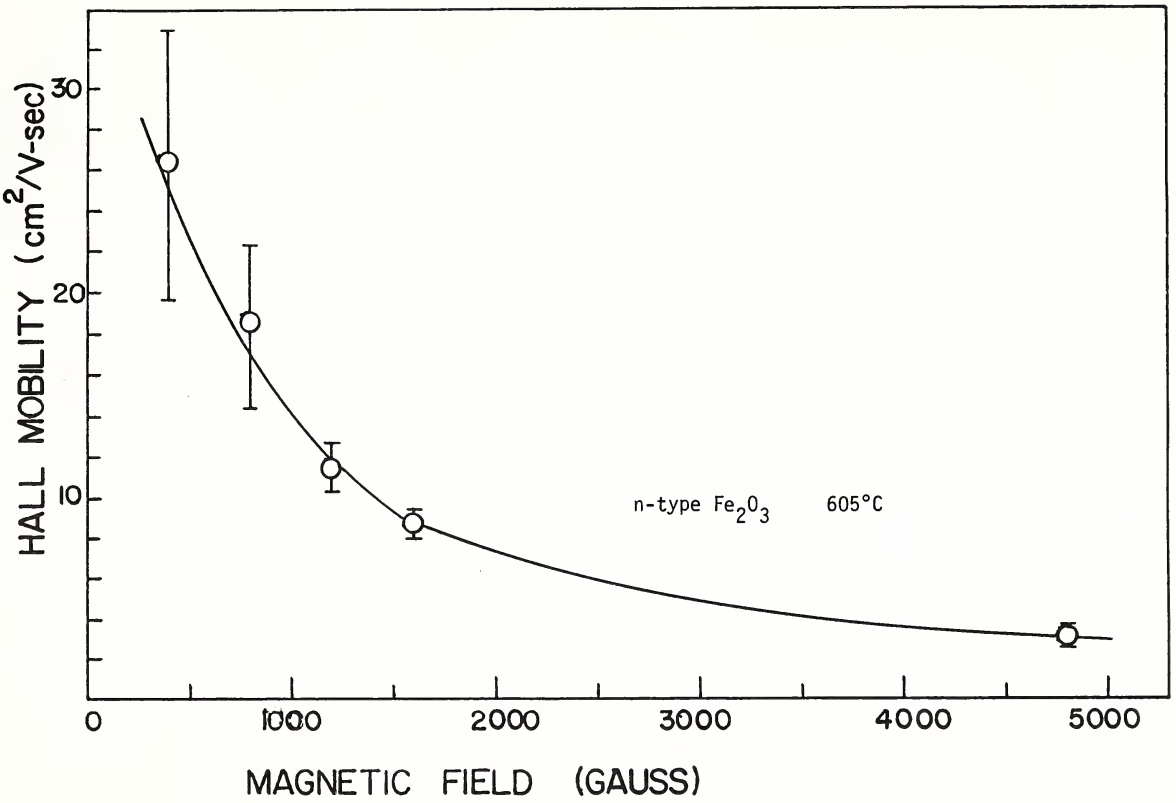

Figure 3.--Magnitude of Hall mobility vs. applied magnetic field at 605°C

REFERENCES

1. R. J. Pollina, MHD Power Generation--Research, Development and Engineering, Montana Energy & MHD Research & Development Institute, Quarterly Report, October-December 1976.

2. R. J. Morin, Phys. Rev. 83, 1005 (1951).

3. H. J. Van Daal and A. J. Bosman, Phys. Rev. 158, 736 (1976).

4. R. V. Pound, Phys. Rev. 79, 685 (1950).

5. E. M. Levin, C. R. Robbins, and H. F. McMurdie, Phase Diagrams for Ceramicists, American Ceramics Society, Inc., Columbus, Ohio, p. 219, 1964.

6. Ref. 5, p. 284.

7. Ref. 5, p. 180, 1969 Supplement.

TASK G2

Physical Properties of Coal Slag: Thermionic Emission

J. Anderson and G. J. Lapeyre

ABSTRACT

During the contract year the thermionic emission apparatus was completed in its final form, including the Auger electron spectroscopy section. Thermionic emission measurements were made on samples of natural and synthetic slag without potassium and measurements were begun on samples of synthetic slag containing potassium. The Auger system was set up and adjustments were made to obtain the best performance. The Auger spectra on slag clearly showed the presence of all the principal constituent elements in the slag even at temperatures up to 1300°C, demonstrating that: 1) Auger spectroscopy is applicable to materials of this sort, and 2) the surface can be analyzed under the same conditions under which the emission measurements are made.

The current density from slag not containing potassium was found to be very low, typically a few microamperes per sq. cm. in the temperature range around 1300°C. The first measurements on slag containing potassium have yielded a similar result, even though the Auger measurements indicate a substantial quantity of potassium at the surface.

The slag samples studied were found to emit current densities of positive ions which were much larger than the electron emission currents. Maximum ion currents for slag not containing potassium were about one milliampere per sq. cm. at 1400°C, increasing exponentially with inverse temperature. Preliminary measurements on slag with potassium indicate an ion current up to ten times larger.

I. OBJECTIVE AND SCOPE OF WORK

The objective of this project is to determine the thermionic emission properties (e.g., thermionic work function) of coal slag, including slag-seed mixtures.

Initial measurements will be performed on synthetic slags of various compositions at temperatures both below and above the temperature at which the slag is liquid.

Since the actual surface composition is of paramount importance in determining the work function and the thermionic emission, in situ surface analysis will be carried out by Auger electron spectroscopy. Materials desorbing and evaporating from the surface will be determined by mass spectrometry.

II. SUMMARY OF PROGRESS TO DATE

The progress during this contract year has been in two areas:

1. Measuring the thermionic emission of electrons and of positive ions from some slag samples with and without adding potassium; and

2. Modification and improvement of the equipment, including setting up the Auger electron spectroscopy system and testing it on hot slag.

For the first item, Auger measurements were used to detect the presence of potassium on the slag surface under the same conditions at which the emission measurements were taken.

A. Thermionic Emission Measurements

A comparison of the thermionic emission from slag without potassium to preliminary measurements on slag with 10 percent K_2O yielded the unanticipated result that the potassium in the slag had little or no effect on the work function. Measurements were made on slags K214 and K524, the former containing no potassium and the latter containing 10 percent K_2O by weight.[1] The relative proportions of the other constituents were somewhat different, but that fact is not expected to account for our observations. The emission from both slags was found to be very small at temperatures up to 1630 K, amounting to only a few microamperes per sq. cm. at 1630 K. This corresponds to an effective work function of about 4.4 eV. This is in spite of the fact that the Auger measurements showed the presence of a large amount of potassium on the surface of K524 at the temperature of the emission measurements. If the potassium had lowered the work function only to 4.0 eV, the emission would have been 130 microamperes per sq. cm. If this behavior persists to higher temperatures and with other slags, it may be necessary to re-examine the role of potassium in inducing large emission currents from the slag-covered cathode.

All the slag samples studied emitted large quantities of positively charged ions. The ion current density depended on the immediate history of the sample. Under steady-state conditions, the current probably was controlled by the diffusion of the ion species to the slag surface. For K214 at T=1630 K, the ion current density was 33 microamperes per sq. cm. in the steady state. Under transient or non-steady-state conditions (to be explained in a later section), the maximum ion emission was about 500 microamperes per sq. cm. at the same temperature. Preliminary results with K524 slag (containing potassium) indicate an ion current density at least ten times larger than for K214. If this ion emission persists and increases exponentially at higher temperatures as with previous slag measurements, then it could constitute a significant charge injection mechanism in an MHD channel.

B. Improvement and Modification of Experimental Equipment

Certain modifications in the thermionic emission apparatus were made, some a matter of convenience and others a matter of necessity. Included in the latter was a re-design of the anode-guard ring structure to electrostatically shield the anode wire and prevent the collection and measurement of stray current. The anode and guard-ring also were mounted on a moveable support to allow them to be pivoted out from over the slag specimen in order to make the Auger measurements. An isolation amplifier was built to protect the emission current recording device from the high potentials applied to the anode.

The Auger electron spectroscopy (AES) system arrived in May 1977; the necessary associated electronics and other apparatus were constructed, and it was tested for proper operation. Thereafter, considerable effort was spent on determining the operating procedure for obtaining the best Auger spectra with optimum signal/noise ratio. The unit was tested successfully on synthetic slag samples at temperatures to 1300°C. As anticipated, the elevated slag temperatures were no impediment to obtaining the spectra and, with some qualifications discussed in the next section, all the constituent elements of the slag were detected with a satisfactory signal/noise ratio. In particular, the potassium spectral line showed up quite well, showing that the potassium is retained in the slag and on the surface at these temperatures.

III. DETAILED DESCRIPTION OF TECHNICAL PROGRESS

A. Work Accomplished

The work accomplished during this contract year can be divided into two categories: 1) development and improvement of the experimental apparatus, including installation and testing of the Auger electron spectroscopy (AES) system and 2) measurement of the thermionic emission of electrons and ions from slag specimens.

1. Experimental Apparatus

The basic configuration of the thermionic emission measuring apparatus has been described in previous reports and is illustrated in Figure 1. Briefly, the slag sample to be studied is in the form of a thin disc resting on a holder of platinum sheet. The holder and the slag are heated from underneath by electron bombardment. The current emitted by the slag is collected by the anode and passes through a load resistor, R_L, and the voltage drop across R_L, which is proportional to the anode current, is plotted on the Y-axis of an X-Y recorder. The anode voltage, V_A, is applied to the X-axis, and as V_A is swept, curves of anode current versus anode voltage (I-V curves) are plotted out. The guard ring surrounds the anode and ensures that only current from the middle portion of the slag, not its edges or the adjacent platinum sheet, is measured.

Our measurements of the thermionic emission so far have shown a very small electron current, about a microampere or so. As a result,

equally small stray currents, originating from the bombardment heater or other sources, could be collected by the lead-out wire from the anode and interfere with the measurements. Thus, we redesigned the anode-guard ring structure to permit nearly complete shielding of the lead-out wire. To perform the Auger measurements, an unimpeded path from the slag to the Auger optics is required, so the new design also included provisions for rotating the anode and guard ring out from over the slag.

As can be seen from Figure 1, a measurement of the emission current rather inconveniently requires that the Y-input of the recorder be floated at the anode potential. This condition was corrected by putting a unity-gain isolation amplifier between the load resistor and the recorder.

The AES system was assembled, the associated retarding potential ramp power supply was built, and the unit was tested first on samples of stainless steel and nickel. These test materials were selected for ease of preparation and because of prior understanding of what their Auger spectra should look like. After checking for proper operation, the unit was tested on samples of slag, and a very large number of spectra were run to determine the operating conditions giving the largest signals with optimum signal/noise ratio. Eventually, quite satisfactory spectra were obtained. Figure 2 is an example of an Auger spectrum from slag K214 at an estimated temperature of 700°C.[2] With the exception of calcium, all the elements present are detected by the presence of their characteristic spectral lines. The iron, silicon, and aluminum lines are small relative to oxygen but with care can be discerned easily on a more sensitive scale. The calcium line at 291 volts is actually present but is masked by the very large carbon line at 272 volts. The carbon probably is due to the interaction of the primary electron beam with adsorbed CO or hydrocarbon gases leaving a residue of carbon on the surface. The absolute quantity of carbon cannot be large because if the carbon were more than a few atomic layers thick, it would not be possible to detect (for instance, the iron lines from the bulk of the slag because of the short mean free path of the Auger electrons). However, due to the extreme surface sensitivity of the Auger technique, the carbon line appears disproportionately large. At higher temperatures, the carbon is not a problem either because the carbon-containing gases do not deposit on the surface or because the carbon diffuses into the bulk of the slag as fast as it is formed. Spectra from K214 slag show only a very small carbon line, and the calcium line is easily detected because it is about 10 to 15 percent of the height of the oxygen line.

Although the theory and practice of AES has been dealt with in previous reports, a brief summary is appropriate. When the surface of a solid is bombarded with a primary beam of high energy electrons (3000 volts in the present case), it will emit a quantity of secondary electrons at all kinetic energies up to that of the primary beam. In addition, it will emit electrons at certain discrete kinetic energies (Auger electrons) due to the decay of atoms put into excited states by the impact of the primary beam. The Auger electrons can be detected

separately by electronic means, and the energies at which they appear (the Auger lines) uniquely identify the element from which they were emitted since those energies are related to the electron energy levels of the atoms. What actually is displayed in the spectra is the second derivative, with respect to kinetic energy, of the total electron yield (secondaries plus Auger) plotted against kinetic energy. The second derivative varies rapidly at the Auger energies and gives rise to the observed peaks.

The principal reason for the Auger system is to monitor the quantity of potassium on the slag surface. Figure 3 shows a spectrum taken from slag K524, which contains 10 percent by weight K_2O. The slag temperature was 1200°C, and the spectrum was taken up to 600 volts to display both the potassium line at 252 volts and the oxygen line at 510 volts. Also evident is a small calcium line at about 292 volts. The large potassium line shows that that element may be detected readily on the slag and at elevated temperatures. The actual concentration of potassium at present cannot be accurately inferred, but we believe it to be quite large, possibly as much as half a monolayer.

2. Thermionic Emission of Electrons and Ions

The slag samples studied so far have shown quite low levels of thermionic emission of electrons. Figure 4 shows a series of I-V curves for K214 slag at various temperatures. The saturated current densities range from 0.65 to 3.3 microamperes per sq. cm. over the range of temperatures indicated. The calculated effective work functions average to be 4.41 eV with rms deviation of 0.14 eV. A work function of this magnitude might be expected for a material which does not have potassium or some other substance on the surface which specifically lowers the work function. However, in experiments so far with K524 slag, approximately the same results have been obtained even though the Auger spectra (Figure 3) indicate the presence of considerable quantities of potassium.

The I-V curves shown in Figure 4 are what one may term "well-behaved." That is, their shape approximates that which is theoretically expected from this experimental geometry. There is a steeply-rising portion (space charge limited region) followed by a nearly level plateau (saturated emission) with the transition region, or knee, occuring at low anode voltage. Frequently, the I-V curves are not so well-behaved, as exemplified in Figure 5. The cause of such behavior is not yet understood and is still under investigation. In such cases, the exact value of the saturated emission is more difficult to determine. The current level at the somewhat distorted knee may be a reasonable approximation and certainly sets an upper limit.

All the slag samples studied so far were found to emit positively charged ions. The ion emission was manifest as a measured current, flowing in the opposite sense to electron emission when the anode was biased negatively. This current was proved by experimentally and theoretically to be due to the emission of positive ions. This point was discussed at some length in earlier reports and in a published paper[3] and is discussed briefly below.

The detailed behavior of the ion emission is somewhat complex; nevertheless, we have an explanation which appears to fit the facts. With the anode biased positively, no ion current flows. When the anode is switched negative, an ion current begins to flow, and it decays with time to a constant or steady-state value. Figure 6 shows this behavior where we have adopted the convention that the ion current is negative. Sweeping the anode voltage toward zero results in I-V curves such as those shown in Figure 7 (lower left section). The detailed shape of those curves matches well, both qualitatively and quantitatively, to that expected for thermionic emission of ions. The space-charge region is concave downwards and obeys a power law as a function of applied voltage

$$I \propto V^n \qquad (1)$$

where, experimentally n = 1.35 as compared to a theoretical value of 1.5. From the Child-Langmuir law, relating the space-charge current to the various parameters of the system, it is possible to calculate the mass of the emitted particle. A precise mass determination is difficult, and we find it to be on the order of 25 atomic mass units within a possible factor of two. Since an atom must have a low ionization potential to be desorbed as an ion, we tentatively identify the ion as calcium although this identification has not yet been verified. The effect we are observing appears to be the following: Under steady-state conditions, calcium atoms diffuse to the surface and are desorbed rapidly as positive ions. The rate-controlling step is the diffusion to the surface. Applying a positive bias to the anode prevents the ions from leaving the surface and they accumulate there. Then, applying a negative bias, a large instantaneous current flows, which decreases with time as the accumulation layer is depleted and the current returns to its steady-state value.

The instantaneous ion current mentioned above was found to vary exponentially with inverse temperature,

$$F \propto \exp\{-E/kT\} \qquad (2)$$

as the Arrhenius plot in Figure 8 shows where E can be identified with an activation energy for description. Extrapolation to 2000 K gives a current density of 70 milliamperes per sq. cm., which may be significant in terms of channel operation.

Experiments with K524 slag also have shown ion currents but much larger in magnitude than for K214. At 1350 K, the steady-state current density was 37 microamperes per sq. cm.; at 1550 K, the current was at least several milliamperes per sq. cm., large enough to blow out the isolation amplifier so that an exact measure of the current was not obtained. We believe it probable, but have not demonstrated yet, that these are potassium ions. Future mass spectrometer experiments, as well as measurements on slag K517 which has about the same composition as K524 but without potassium, should shed some light on this matter.

B. Discussion

The rather high work function and consequent low thermionic electron emission found for slags without potassium might be expected. Somewhat unexpected, however, are the initial results for slag with potassium which indicate an equally high work function, even though the Auger measurements indicate that there is potassium at the surface. That is, the potassium seemed to have no effect on the work function at all. This would seem to be contradictory to the work of Koester, et al.[4] who found stable diffuse emission up to one ampere per sq. cm. at only slightly higher temperature in a slag-coated channel. That high emission possibly might be attributed to the presence of a plasma, the higher temperature, or the higher potassium content (about 20 percent K_2O) in the slag. Further measurements will be required to determine if the behavior we have observed is peculiar to the temperature range studied or persists to higher temperatures. In any case, the question arises as to how we are to explain this situation. The work function reducing property normally associated with potassium arises when the atom rests atop a surface and shares its valence electron with the surface. The resulting dipole moment then reduces the potential barrier for electron emission. It may be that under the conditions of our measurements, this does not occur at the surface of heated slag. As an example of possible circumstances that could lead to no lowering of the work function, we might consider the following model: the potassium is bound chemically to the slag surface, for instance to an oxygen atom, forming a KO entity. Such an entity would be highly polar, but because of thermal motion, it is oriented randomly on the surface. As a result, no net dipole moment would be established. Whether such a picture is tenable must await further experiments and analysis of the results. Whatever the outcome, we expect that those results will yield a better understanding of the physical processes that control the emission of electrons in a channel.

A surprising aspect of our measurements is the large ion currents. Our measurements indicate that ion currents on the order of 0.1 may not be unreasonable at ambient channel temperatures. Whether this estimate needs to be modified for the case of emission into the plasma is not clear yet. Although such ion flow may not constitute a conduction mechanism across the width of the channel because of the low ion mobility, it could be a significant charge injection mechanism at the anode, forming near the anode surface a part of the total current loop.

Another possible implication of the observed ion current has to do with mass transport. Tests on operating channels have shown a marked difference in behavior between the anode and the cathode, and at least part of this is no doubt due to differences in the chemistry between the two elements of the channel. An ion current of 0.1 amperes per sq. cm. corresponds to a significant amount of mass movement; a millimeter-thick layer of slag could be depleted of potassium in 2 to 3 minutes. At the cathode, the electric field would serve to inhibit the desorption of potassium. It seems clear that in ion emission, as modified by electric fields, there is a possible mechanism for influencing seeded slag chemistry at the anode and cathode.

IV. CONCLUSIONS

Experiments have shown that Auger electron spectroscopy is a workable method of monitoring the elemental composition of slag surfaces even at high temperatures and in conjunction with thermionic emission measurements. Thermionic emission measurements on slag without potassium and slag with potassium showed electron emission currents measured in microamperes per sq. cm. at temperatures around 1300°C, corresponding to an effective work function in the neighborhood of 4.4 eV. For the slag with potassium, Auger tests showed the presence of potassium at the surface. The amount of potassium was not determined but may be as high as half a monolayer. Nevertheless, the potassium seemed ineffective in reducing the work function of the surface. It is not possible yet to draw general conclusions about the action of potassium on electron emission. Further experiments will be necessary to determine if this behavior persists in other slags and at higher temperatures. A possible explanation is that thermal motion orients, in a random way, the dipole moment associated with the potassium atom, resulting in no net potassium-induced dipole layer at the surface.

The slags studied so far have been found to emit currents of positive ions. The identity of these ions is not known yet, but they tentatively are presumed to be calcium and/or potassium. The ion current densities were much larger than for electrons; current densities up to several milliamperes per sq. cm. were found in the temperature region around 1300°C. The variation of the ion current with temperature indicates that much larger ion currents may be expected at channel temperatures, perhaps as much as 0.1 amperes per sq. cm. If this is the case, then ion emission could be a significant mechanism for current injection into the channel and for mass transport as it affects the seeded slag chemistry at the anode and cathode.

MILESTONE CHART

STATUS DATE _____

TASK G2

PROGRESS

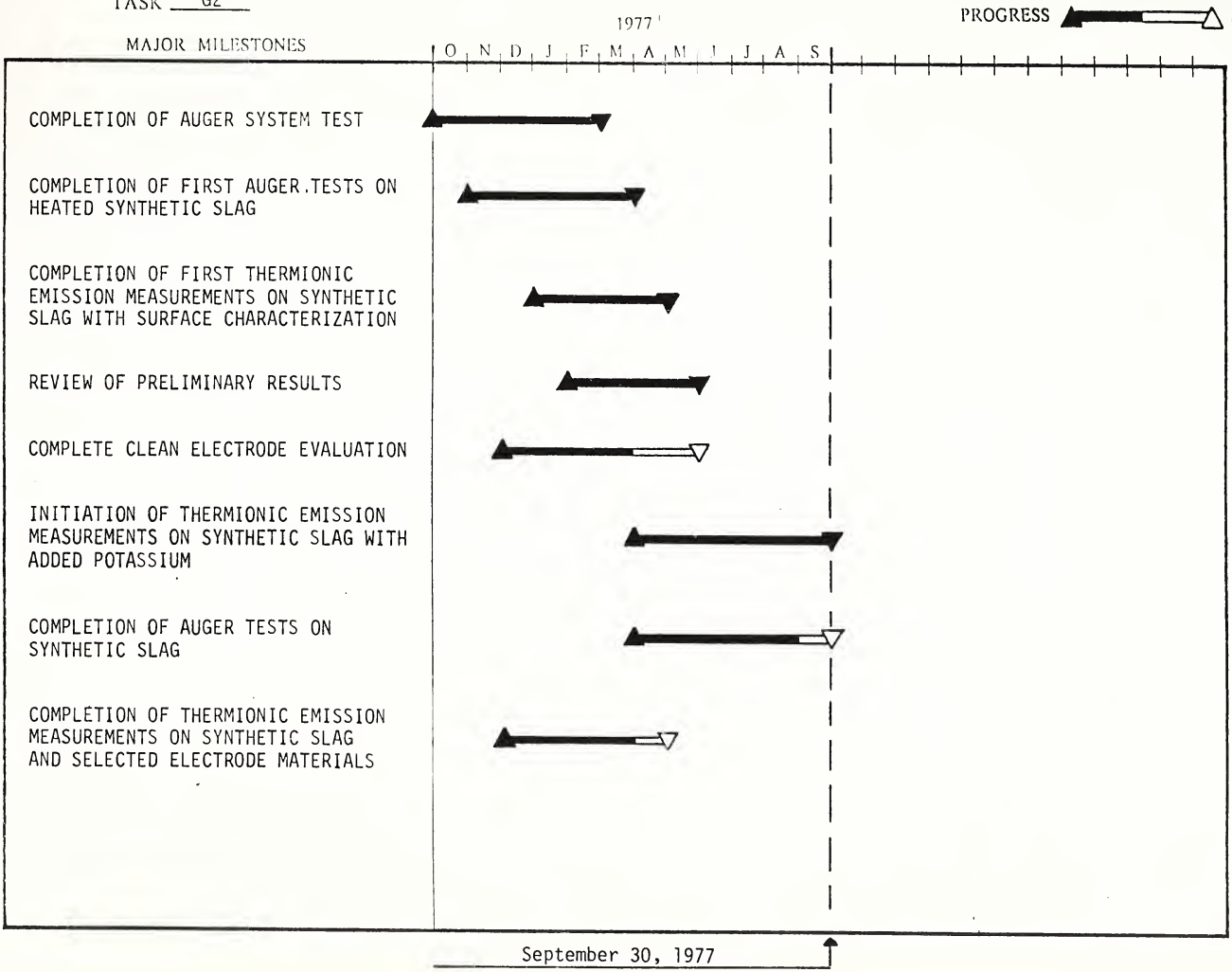
MAJOR MILESTONES
1977
O N D J F M A M J J A S
COMPLETION OF AUGER SYSTEM TEST
COMPLETION OF FIRST AUGER TESTS ON HEATED SYNTHETIC SLAG
COMPLETION OF FIRST THERMIONIC EMISSION MEASUREMENTS ON SYNTHETIC SLAG WITH SURFACE CHARACTERIZATION
REVIEW OF PRELIMINARY RESULTS
COMPLETE CLEAN ELECTRODE EVALUATION
INITIATION OF THERMIONIC EMISSION MEASUREMENTS ON SYNTHETIC SLAG WITH ADDED POTASSIUM
COMPLETION OF AUGER TESTS ON SYNTHETIC SLAG
COMPLETION OF THERMIONIC EMISSION MEASUREMENTS ON SYNTHETIC SLAG AND SELECTED ELECTRODE MATERIALS
September 30, 1977

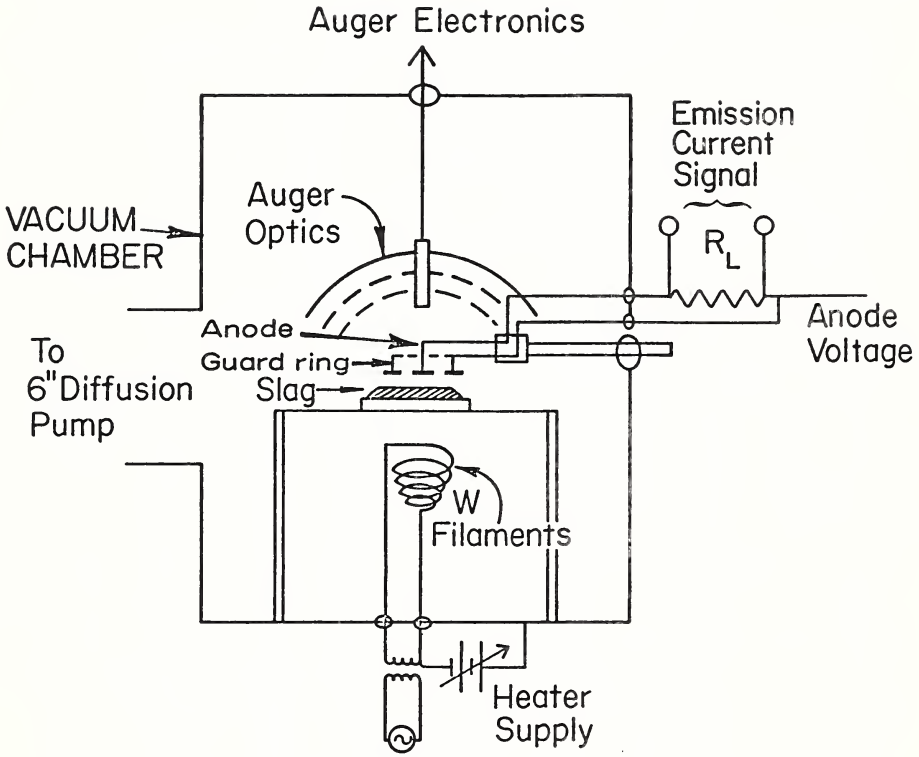

MEASUREMENT GEOMETRY

Figure 1.--A diagram of the experimental layout. Note that the guard-ring/anode structure can be moved, so Auger and quadrupole studies can be performed.

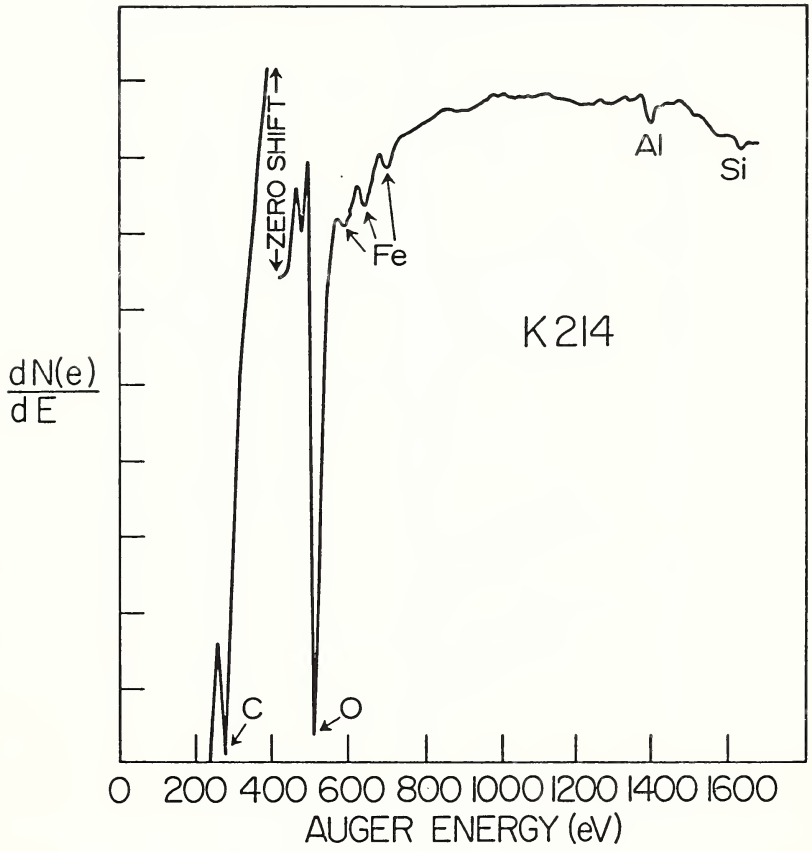

Figure 2.--Typical Auger spectrum of K214 slag at a temperature ~800°C. All elements of this slag are visible. The carbon peak is due to carbon deposited upon the surface from background gases.

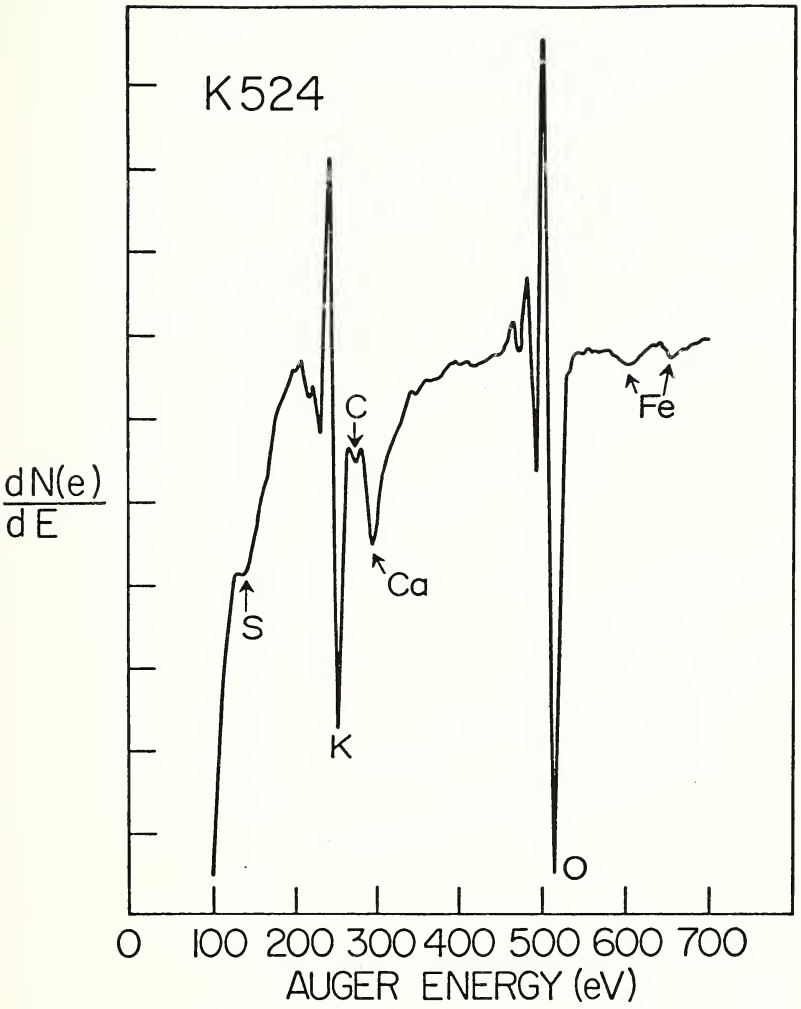

Figure 3.--Typical Auger spectrum of K524 slag. Note the large amount of potassium on the surface. The temperature is ∿800°C.

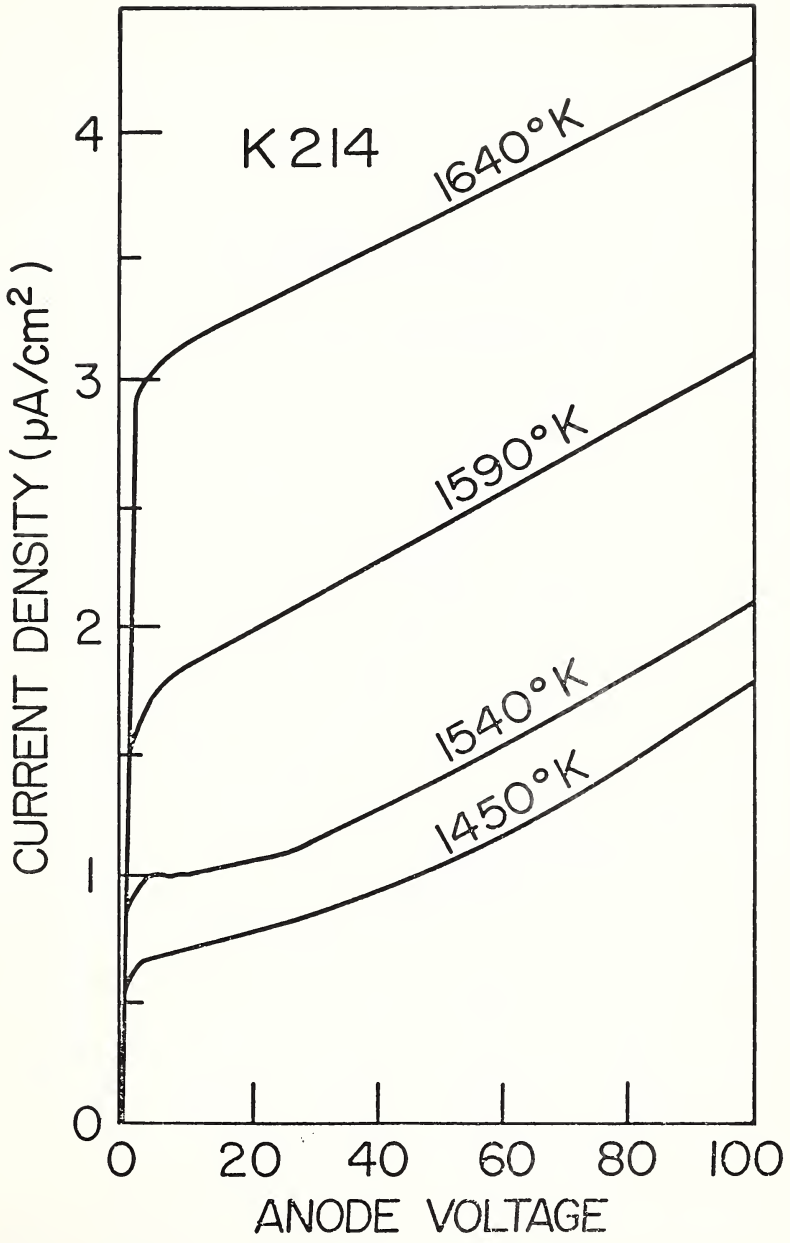

Figure 4.--Thermionic emission curves for K214 slag at various temperatures.

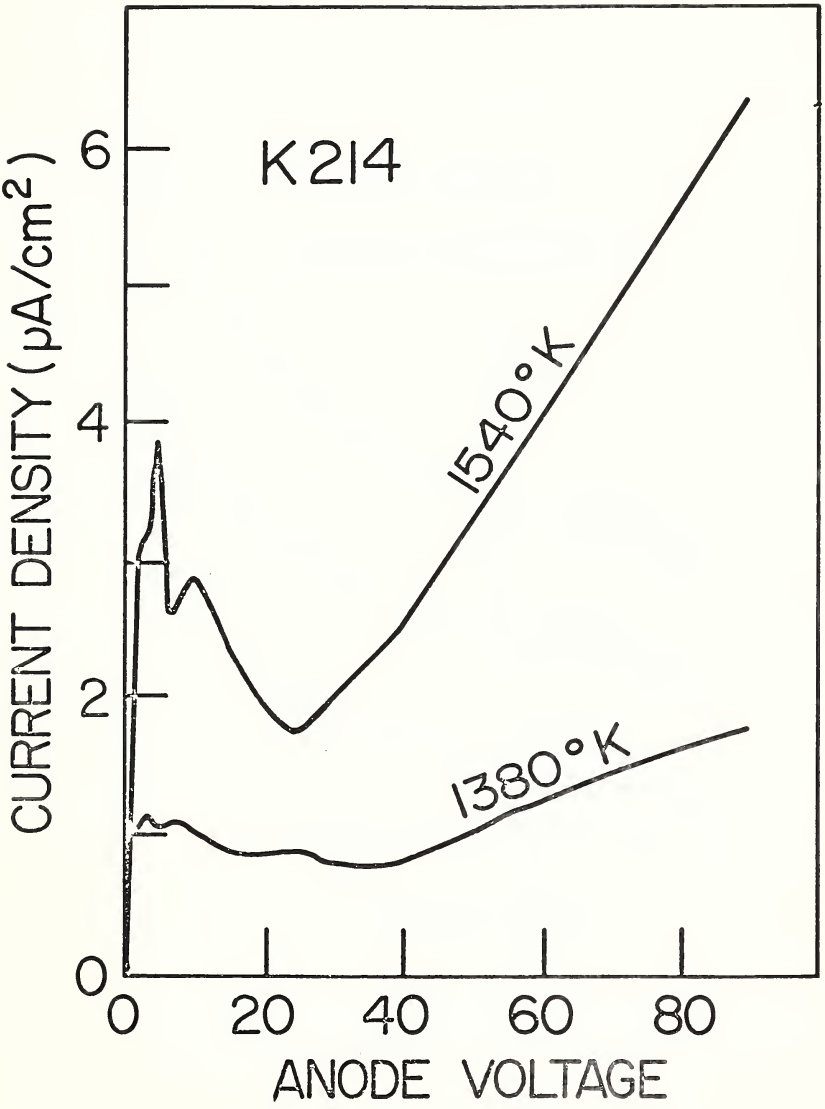

Figure 5.--Appearance of "badly behaved" thermionic emission curves.

CURRENT DENSITY (μA/cm²)
0
4
8
0
20
40

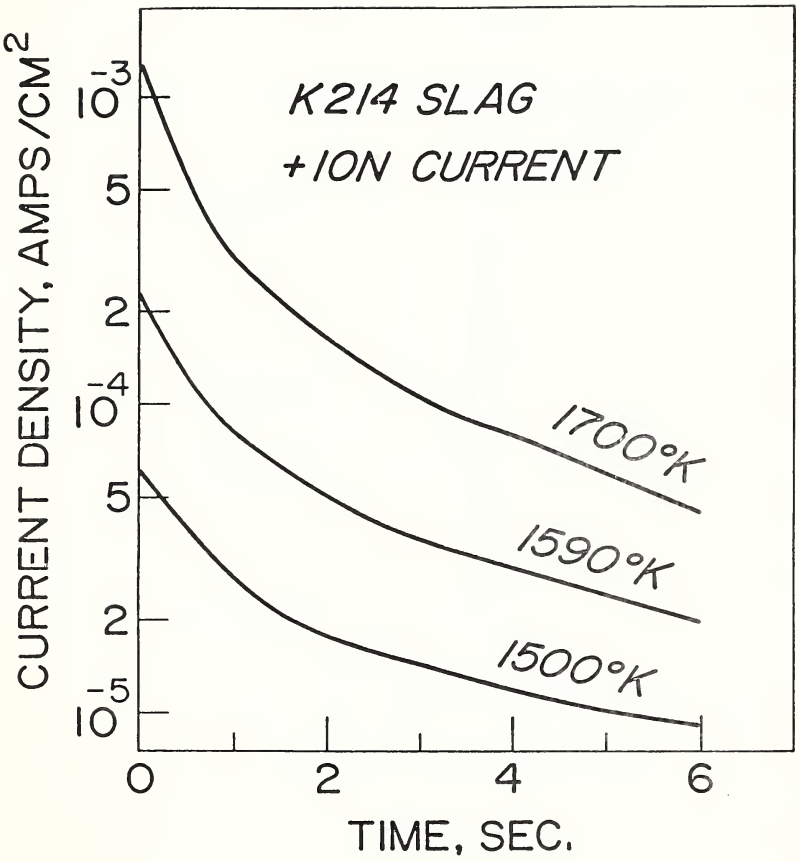

Figure 6.--Illustrates the decay of ion current as a function of time, and temperature. After a long time, the ion current comes to a constant level.

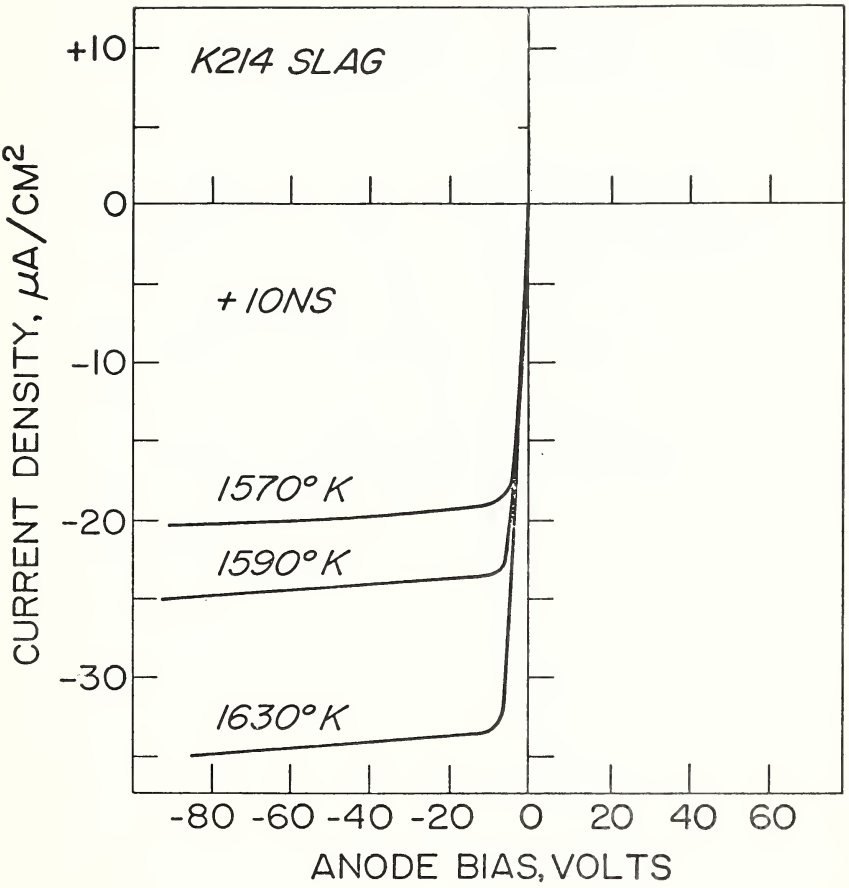

Figure 7.--Some typical ion emission curves at various temperatures for K214 slag. Note the current density is an order of magnitude larger than electron emission, shown in Figure 4.

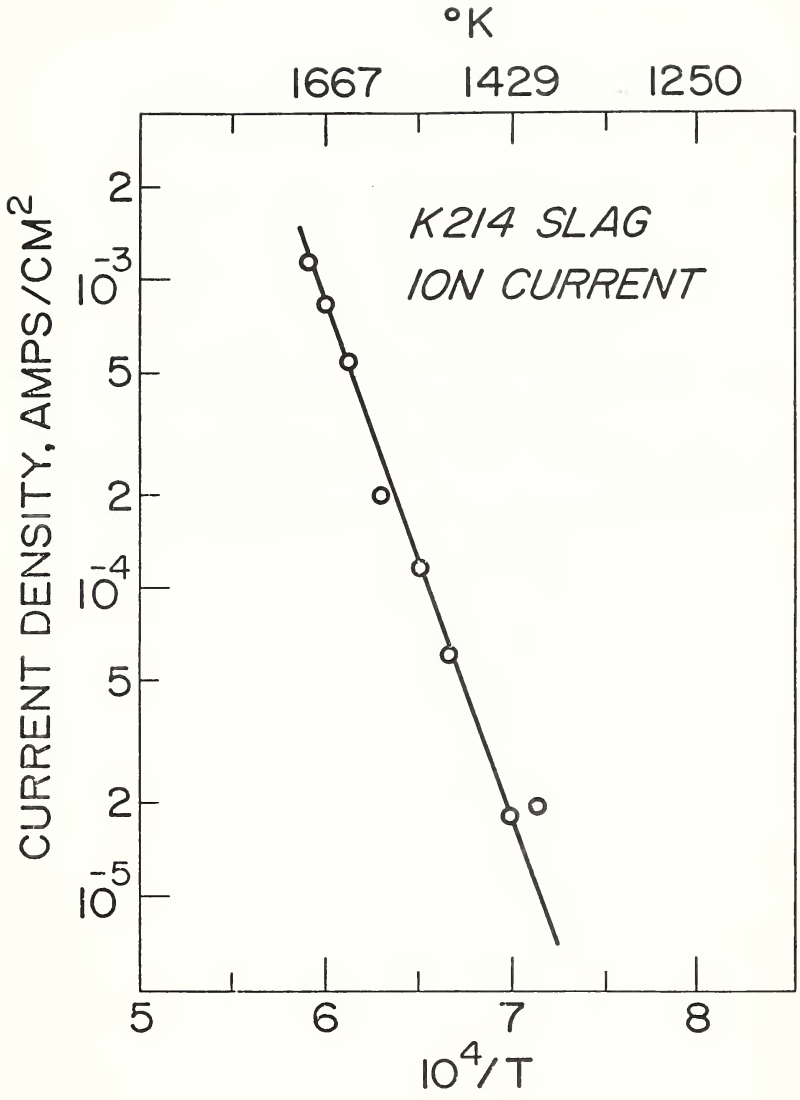

Figure 8.--The temperature dependence of the ion current, in an Arrhenius plot.

FOOTNOTES AND REFERENCES

1. The natural slag is a fly ash from the Corette Plant in Butte, Montana. Slag K214 and K524 were obtained from the National Bureau of Standards MHD Materials Group. The major components of these slags by weight percent are tabulated below.

	SiO_2	Al_2O_3	Fe_3O_4	MgO	CaO	K_2O
Fly Ash	40	24.5	4.4	5.8	18.9	---
K214	37.6	31.9	19.98	---	10.53	---
K524	54	22.5	9	1.8	2.7	10

2. It is necessary to warm the slag somewhat to make it conductive. Cold slag tends to become charged during the Auger measurements, modifying the electric fields and distorting the spectra.

3. J. Anderson, G. J. Lapeyre, R. J. Smith, and M. Wilson, "Some Thermionic Emission Properties of Synthetic Coal Slag," Proceedings of the Conference on High Temperature Sciences Related to Open-Cycle, Coal-Fired MHD Systems, Argonne, Illinois, p. 208, April 1977.

TASK G3
Slag Physical Properties:
Electrical and Thermal Conductivity
R. Pollina

ABSTRACT

We have been able to show that, over a limited temperature range, the slag electrical conductivity of Rosebud coal can be described by a closed-form mathematical expression to an accuracy of about ten percent as a function of temperature and iron content. This kind of result has long been awaited by planners and design engineers. Although we have not included seed as a variable, we hope in the short term to extend this work to wider temperature ranges and to include oxygen partial pressure as an additional parameter in this equation. Complications are posed by the occurrence of phase transitions within the material which are accompanied by anomalous variations in the conductivity. These are difficult to include in any mathematical expression of the data. Preliminary results are given for seeded slag data which indicate that similar curve fitting may be possible for this case also--at least over a limited temperature range. X-ray analysis confirms the nature of the high temperature phase transition at 1650 K as the development of an anorthite crystalline phase. Rosebud ash has been simulated from basic oxide ingredients and its conductivity is quite close to the real ash. Thus we are now in a position to reduce the CaO content of Rosebud ash to determine the role of the electrical conductivity. Ash samples with additions of alumina do not have a significantly reduced electrical conductivity at high temperature. This result may prove to be important for electrode replenishment if a more favorable chemical environment at the electrode-slag interface is necessary.

The conductivity of natural Rosebud ash was found to be only weakly dependent upon oxygen partial pressure. Graded samples of bottom ash with additions of K_2CO_3 were studied to determine the effect of potassium seed addition on the conductivity of Montana coal ash. Large additions (up to 30 percent) of K_2CO_3 produce only small changes in the electrical conductivity at high temperatures (above 1550 K) but important and substantial changes occurred at temperatures below this.

I. OBJECTIVE AND SCOPE OF WORK

The objectives of this task are to determine the electrical and thermal conductivities of unseeded and seeded coal slags under isothermal conditions. The electrical conductivity measurements will be determined by the NBS four-lead technique up to 1450°C and by a two-lead technique at higher temperatures. The thermal conductivity measurements will be made below the slag softening point using a cut bar conduction system, and up to 1250 K in refractory materials.

II. SUMMARY OF PROGRESS TO DATE

The most important result of the research during the past year is the generation of sufficient data to fit the electrical conductivity, σ, of Rosebud coal ash over a limited range of temperature and iron content to a mathematical form such as

$$\ln \sigma = a + \frac{b}{T} + \left[c + \frac{d}{T}\right]X + \left[e + \frac{f}{T}\right]\ln X$$

where X is the mole fraction of iron present and a to f are constants. Coal slag conductivity is extremely sensitive to the iron content of the slag. A large body of iron-containing slag conductivity data has been obtained this past quarter and attempts are being made to unify it. Complications are posed by the occurrence of phase transitions within the material which are accompanied by anomalous variations in the conductivity. These are difficult to include in any mathematical expression of the data. Preliminary results are given for seeded slag data which indicate that similar curve fitting may be possible for this case also--at least over a limited temperature range. X-ray analysis confirms the nature of the high temperature phase transition at 1650 K as the development of an anorthite crystalline phase. Rosebud ash has been simulated from basic oxide ingredients and its conductivity is quite close to the real ash. Thus we are now in a position to reduce the CaO content of Rosebud ash to determine the role of the electrical conductivity. Ash samples with additions of alumina do not have a significantly reduced electrical conductivity at high temperature. This result may prove to be important for electrode replenishment if a more favorable chemical environment at the electrode-slag interface is necessary.

The conductivity of natural Rosebud ash was found to be only weakly dependent upon oxygen partial pressure. Graded samples of bottom ash with additions of K_2CO_3 were studied to determine the effect of potassium seed addition on the conductivity of Montana coal ash. Large additions (up to 30 percent) of K_2CO_3 produce only small changes in the electrical conductivity at high temperatures (above 1550 K) but important and substantial changes occurred at temperatures below this.

III. DETAILED DESCRIPTION OF TECHNICAL PROGRESS

In an MHD generator channel the conductivity of the slag layer adhering to the walls of the generator must be in a range appropriate for the slag to act as a good conductor for the generator output current and yet must be low enough to prevent shorting of the axially directed Hall current. The mathematical analysis of the current flow indicates opposing demands upon the slag conductivity.[1] However, the criterion by which we judge the suitability of a given slag with respect to the magnitude and character (ionic or electronic) of its electrical conductivity is yet to be determined. The ultimate goal of this project is to satisfy demands of the designers for data necessary in modeling the output of the channel and to predict empirically the behavior of slag under any constraints which might occur when larger scale projects such as the CDIF become operational.

The coal ash used in these experiments is from the Rosebud seam and was obtained from a local power company.[2] The combustor temperature was approximately 1900 K[3] and bottom and fly ash were supplied from the combustor and the base of the stack respectively. The samples were received in the form of powder, and each was homogenized and melted in alumina or platinum crucibles in air at 1700-1750 K for 1 to 36 hours and then air quenched. Corrosion of alumina crucibles was generally not observable until the seed content was increased. Above 10 percent K_2CO_3 a changeover to platinum crucibles was necessary.

The bottom and fly ash compositions were essentially the same except for slightly higher concentrations of sulphur, potassium, and calcium in the bottom ash as seen in an intensity analysis[4] of the proton induced x-ray spectrum (PIX) of each sample.

In the conductivity tests below 1800 K, samples were contained in alumina boats of 99.8 percent purity[5] (interior dimensions 2 x 4 x 4 mm.). The a-c conductivity was measured using the conventional 4-lead technique because of its sensitivity, reproducibility, and ability to separate polarization effects[6,7] from the true conductivity. A-C conductivity is measured using a two-lead technique and an a-c resistance bridge. Pulverized samples were placed in a crucible into which four leads had been suspended. A type B thermocouple (platinum-6 percent rhodium vs platinum-30 percent rhodium), which was checked periodically at the gold point, monitored the temperature.

The procedure was that samples were raised to the maximum temperature and data was taken starting at the highest temperature and moving downwards. During a run the ceramic boats developed a web of cracks[8] indicating that the slag had a lower thermal expansion than alumina.

In an effort to determine whether or not there were any time-dependent effects in the d-c conductivity measurements, a sample was held under a d-c current for 24 hours and both the conductance of the sample and the charge build-up at the current electrode were monitored. This charge build-up is measured by the compliance voltage necessary to maintain constant current through the sample. The data is shown in Figure 1 for a Rosebud ash sample with 20 percent K_2CO_3 equivalent of added potassium seed. This sample was chosen because of its strong ionic effects and should have a strong time-dependent conductivity because of charge build-up on the electrodes. The compliance voltage varies from 2.5 to 135 volts while the conductance drifts slowly and not by an amount sufficient to affect the data. Typically the conductivity follows the Arrhenius' law and even an error as large as 50 percent is not enough to affect the temperature dependence of the electrical conductivity in coal slag. Because the voltage and current leads were separated, the ionic charge build-up resulting from current flow does not affect the accuracy of the measurements.

Figure 2 shows a preliminary run of electrical conductivity of a Rosebud ash sample with 20 percent Fe_2O_3 equivalent iron added. The high temperature data was taken in the new two-lead sample holder designed to fit in the graphite tube furnace with alumina muffle tube. The high temperature data has been normalized to fit the "low" temperature run. Above

the last crystallization temperature, that of anorthite, the conductivity follows an Arrhenius's law with a higher activation energy than below the anorthite transition. These experiments are in progress and will be reported on in a future publication.

C. Synthetic Slag

Any effort to study empirically the behavior of individual slag components must not only include additive variations but subtractive ones as well. In other words, it is not good enough merely to add components to the slag and check its behavior. One must also subtract components, especially when, as in the case of CaO in Rosebud ash, they occur in such high percentages. The first attempts toward this end were to produce a synthetic version of Rosebud ash which exhibited conductivity behavior similar to the natural ash. In addition to the usual precautions of avoiding phase separation and insuring homogeneity, one must be especially concerned with the need for complete reaction of the constituents in the liquid state. One cannot merely mix oxides and assume that one has coal slag. Nor, on the other hand, does one have to raise the temperature of the mix beyond that of the highest melting point constituent. If one major component melts first it can act as a flux and dissolve the other components. At this point, all remaining crystalline phases will have disappeared and any chemical interactions will proceed to equilibrium, provided no significant separation of liquid phases occurs. Figure 3 shows a comparison between the electrical conductivities of Rosebud ash and a synthetic ash of comparable elemental composition produced in our laboratory. The desirability of producing a synthetic coal ash has often been expressed but to the author's knowledge this is the first attempt to reproduce the conductivity behavior of a natural slag. Although the anomalies that generally occur in Rosebud ash at about 1615 K and 1390 K (presumably due to the mode of devitrification taking place) were not evident in the synthetic sample, the behavior of the synthetic closely follows the natural to within experimental error. Having been able to prepare a synthetic slag, it will now be possible to vary chemical components. One of the first things to be done is to reduce the CaO content of the slag to determine to what extent it contributes to the electrical conductivity. Also, a heavier ion such as Ba^{2+} or Sr^{2+} will be substituted for the calcium.

Figure 4 displays the electrical conductivity data for Rosebud coal ash (Ash 1) with graded additions (10, 20, and 30 percent) of K_2CO_3 as seed. The corresponding potassium content of these samples is 7, 14, and 21 percent K_2O. Below approximately 1540 K there is a strong dependence of the conductivity on potassium content. This dependence increases with decreasing temperature. The potassium concentration dependence of conductivity above 1540 K is weak and somewhat erratic in that different runs will shift the curves. This is exemplified by the behavior of the 10 percent sample above 1650 K which has a slightly lower conductivity than Ash 1 in this run, but higher in another run. Much practical importance is placed on the strong low-temperature dependence of conductivity on potassium content since channel wall temperatures may be in this temperature region. All four of the samples displayed here were prepared simultaneously in platinum crucibles, so their thermal history is similar.

In Figure 5, we show lines of constant conductivity as a function of added K_2CO_3 from 1000 K to 1667 K. The temperature dependence of the electrical conductivity of seeded Rosebud ash has been presented previously,[9] but Figure 5 illustrates in a better way its seed concentration dependence. All isotherms exhibit approximately a linear behavior in conductivity as a function of K_2CO_3 seed additions up to 20 percent K_2CO_3. Above this seed concentration, the behavior changes drastically, indicating a possible change in the system's chemistry. We shall investigate this effect in further detail in the future.

In Figure 5, a continual flattening of the isotherms can be seen as higher temperatures are approached. This gradual loss of sensitivity of electrical conductivity to seed content at higher temperature may indicate a gradual decrease of the electronic contribution to the conductivity. If so, then at 1667 K ($10^4/T = 6$), where the electrical conductivity is independent of seed content up to 20 percent K_2CO_3, the conductivity may be predominantly ionic. This is one possible explanation of the effect, but speculation is best left until more is known about the charge carrier, diffusion rates, and activation energies.

There is little change in the slopes of isotherms at $10^4/T = 8$, 9, and 10 below 20 percent K_2CO_3. Above these temperatures the slopes gradually flatten, coinciding with the softening of the crystal. In Figure 6, the X-ray pattern obtained from four samples of Rosebud bottom ash is shown. All have the same composition but different heat treatments. This sequence shows the onset of the crystallization of anorthite from Rosebud ash. Near 1378°C (1651 K) the growth of an anorthite peak is first noticed. It becomes more pronounced at 1265°C. The sample, slow-cooled from 1450°C (1773 K), exhibits a strong anorthite spectrum since it had more time to anneal. It also shows unidentified peaks marked with checkmarks above them. If one considers this Rosebud ash sample as comprised only of CaO, Al_2O_3, and SiO_2, then the composition falls in the anorthite region of the phase diagram at these temperatures.[10]

This past quarter, a paper was presented at the MHD conference[11] held at Argonne Laboratory which summarized our work to that time.

Figure 7 illustrates the results of a study of Rosebud coal ash conductivity at three different oxygen pressures as indicated in the figure. The solid line is drawn through the 10^{-3} atm. data points. Here, as in all conductivity figures, the log of the conductivity in $(ohm\text{-}cm)^{-1}$ is plotted as a function of $10^4/T(K)$. The top scale shows the corresponding Kelvin temperatures. Two regions of instability are noticeable. They are characterized by a sharp change in the electrical conductivity accompanied by long relaxation times. The first instability occurs at a reduced temperature of 6.1 K^{-1} and the second at 7.15 K^{-1}. These instabilities regularly appear in the Rosebud ash and generally occur at 6.2 ± 0.2 K^{-1} (1615 K) and 7.2 ± 0.2 K^{-1} (1390 K). They are due to the mode of devitrification taking place within the sample. The dashed line in this figure is taken from data on Montana coal ash published by Bates.[12] A comparison of the chemical compositions of our own Rosebud bottom ash and the Battelle sample designated SMF-0 is contained in Table 1. SMF-0 appears to be substantially more silica rich and alumina poor than our Rosebud ash.

Figure 8 shows some interesting results obtained by measuring the conductivity of Rosebud bottom ash with 20 percent alumina enrichment and with both 20 percent alumina and 20 percent K_2CO_3 enrichment. On removing the latter two samples from the sample holder after the experiments had terminated, no noticeable corrosion of the alumina boats was observed. This is in sharp contrast to earlier runs with seeded slag in which substantial corrosion was observed for the high seed concentration (20-30 percent K_2CO_3) slags. This corrosion inhibition effect gives added weight to the arguments of those who favor electrode replenishment. Several items are to be considered in Figure 8. The sample of 80 percent ash and 20 percent alumina (----) illustrates the mild sensitivity of slag conductivity and alumina content. This is to be expected since alumina is an insulator and would not contribute charge carriers. Fe_2O_3 and CaO would appear to supply the major contribution to the slag conductivity, though we have not looked at CaO yet. It is interesting to note that below 1400 K alumina actually enhances the conductivity. Of equal interest is the fact that above 1667 K slag conductivity is virtually independent of the additives. The 80 percent ash and 20 percent K_2CO_3 line (-·-·) is taken from the data of Figure 4 and is merely repeated here for comparison. Again, note that the enhancement of conductivity contributed by the addition of 20 percent K_2CO_3 (12 percent K_2O equivalent) appears to be significant only below 1667 K and would matter little in a hot wall channel. Finally, we looked at the sample 60 percent ash and 20 percent each of Al_2O_3 and K_2CO_3. This sample was prepared because we observed a substantial decrease in corrosiveness on adding alumina. It was then decided to find out if this decreased corrosiveness was maintained in the presence of seeded slag, and indeed it was. The alumina addition decreases the conductivity of a seeded slag but the decrease is only significant below 1250 K, where replenishment is unnecessary. This led to the conclusion that electrode replenishment cannot be ruled out on the grounds that replenishment lowers the slag conductivity.

The principal research effort this past quarter was a study of the conductivity of Rosebud ash as a function of temperature, oxygen partial pressure, P_{O_2}, and iron oxide content expressed as mole-percent iron, X_{Fe}. Although the study has not been completed yet, there is sufficient preliminary data to justify presentation of the results obtained so far. These results justify a cautious optimism towards being able to describe the conductivity of a basic Rosebud ash composition in a single equation for each oxygen partial pressure with T and X_{Fe} as independent variables.

Because the presence of phase transitions can produce anomalies in the conductivity at certain temperatures, the range of temperature over which such a fit of the conductivity to a single equation may be possible is sometimes limited to a small temperature region. However, at certain slag compositions these anomalies may be small and a useful fit will be possible over a comparatively large temperature range.

Because of the high sensitivity of coal slag conductivity to iron content, such an equation would be of enormous use to systems designers in predicting slag conductivity. In future work, emphasis will be turned towards obtaining similar results for seed content, X_K. It is not clear

that a single equation can describe the conductivity as a function of all the vital parameters, T, P_{O_2}, X_{Fe}, X_K, etc.

Although large amounts of data are presented here, it will be condensed into easily manageable equations in future reports. Final analysis must wait until completion of several more sample runs to obtain data in iron contents both lower and higher than are presented here. It is hoped then to fit the conductivity of Rosebud ash over a wide range of iron content from 0 to 30 percent Fe_2O_3 equivalent.

It is well known that iron plays a key role as a charge carrier in slag. It is presumably charge transfer between double and triple valence states that makes the iron contribute substantially to the conduction in slag. The ratio of Fe^{2+} to Fe^{3+} depends upon slag composition, temperature, and oxygen partial pressure above the slag. Because of the role of iron as a major contributor to the conductivity, it is important that the nature and empirical behavior of its contribution be studied. There has been some recent work on this subject[12] and the matter will be pursued further. The natural Rosebud ash studied until now contains 4.4 percent Fe_2O_3.

Since chemical analysis results rarely add up to 100.0 percent, with no other detectable elements present, all compositions will be referred to as 100 percent. Thus, if Rosebud ash contains 4.4 percent Fe_2O_3 (see Table 1) and the analysis totals to 95.3 percent, then referred to 100 percent the Fe_2O_3 content is 4.6 percent.

The electrical conductivity of coal ash is considered to be a function of the following parameters: T, P_{O_2}, X_{Fe}, X_K, X_G where X_K is the mole fraction of alkali metals and X_G is the remaining glass matrix composition of the slag. In a typical coal seam X_G plays a lesser role in the conductivity since the mole fraction of the components which make up the matrix G--SiO_2, Al_2O_3, CaO, MgO--do not vary sufficiently to make as significant a difference in the conductivity as do the normal variation of X_{Fe}, X_K, and of P_{O_2} in the channel itself. Thus, these studies are limited at present to the first four independent variables above.

$$\sigma = \sigma(T, P_{O_2}, X_{Fe}, X_K)$$

Figure 9 shows oxygen pressure isobars of the temperature dependence of the d-c conductivity of a coal ash with 9.4 percent Fe_2O_3(X_{Fe} = 2.66 percent). The conductivity exhibits a distinct maximum near the oxygen partial pressure of 10^{-5} atm. Figure 10 illustrates five isotherms (1450, 1350, 1250, 1150, and 1050°C) of the d-c conductivity vs P_{O_2} on a log-log scale. This data is taken from Figure 9. Note the magnitude of the maxima in conductivity between 10^{-4} and 10^{-6} atm. This effect will be important for generators with lower wall temperatures and it may possibly be related to $X_{Fe^{3+}}/X_{Fe^{2+}} = R$. This is difficult to determine experimen-

tally and so the study of this oxygen atmosphere effect must be done indirectly, that is, without a knowledge of the value of R. We must have iron activity data to understand this effect. The mole fraction of iron is not sufficient to analyze the data. The ionic activities are sufficient.

The log of conductivity as a function of $X_{Fe_2O_3}$ for both a-c and d-c measurements behaves much more smoothly than for P_{O_2}. Because of this, T and X_{Fe}, as the independent variables in a preliminary computer, fit of the data and samples, were chosen with constant P_{O_2} and X_K. Thus, the form to be analyzed is

$$\sigma = \sigma(T, X_{Fe})\Big|_{\substack{P_{O_2} \\ X_K \\ X_G}}$$

X_{Fe} instead of $X_{Fe_2O_3}$ is arbitrarily used because the oxidation state probabilities for iron in these samples is not known.

The data for the electrical conductivity of Rosebud ash at an oxygen partial pressure of 10^{-3} atm is fit over a temperature range of 1223-1523 K for iron content between 2.6 percent and 6.9 percent Fe or 9.6-23.7 percent Fe_2O_3. The equation of the fit Kelvin temperatures is

$$\ln \sigma = a + \frac{10^4 b}{T} + \left[c + \frac{10^4 d}{T}\right] X_{Fe} + \left[e + \frac{10^4 f}{T}\right] \ln X_{Fe}$$

where
$a = -6.778$
$b = 2.902$
$c = 55.74$
$d = -11.10$
$e = -1.390$
$f = 0.9794$

The excellence of the fit is shown in Figure 11 when the constants are used in the above equation. For a direct, graphical reading of b from $\log \sigma$ vs $\frac{10^4}{T}$ plot $b = \frac{\text{slope}}{\log e}$. Figure 11 shows the excellent fit of this equation (solid lines) to the data points plotted. Above 1523 K, the conductivity increases anomalously because of the onset of the anorthite phase transition and cannot be accounted for in a simple manner. Below 1223 K, the available data is limited and not sufficient for fitting purposes. The mole fraction range of Fe will be extended during the coming quarter.

Several approaches to the analysis of our iron conductivity data and the results will be presented in a future report. This expression represents conductivity terms linear in charge carrier density with a quadratic

contribution to allow for curvature and a cross term with temperature dependence. The linear terms for σ appear, of course, as log terms in our expansion of log σ. These terms are $[e + \frac{10^4 f}{T}] \ln X_{Fe}$. The remaining terms, linear in log σ and exponential for σ, are an attempt to expand the activation energy in terms of mole fraction and temperature analogously to the prefactor term before the exponential. These are the terms $[c + \frac{10^4 d}{T}] X_{Fe}$.

The second type of analysis to be undertaken is to fit the data to expressions with more physical meaning to their parameters. These fits may be less accurate but might offer more theoretical knowledge.

The third type of analytical fit is less accurate yet. It will be an attempt to fit all of the data to a single equation less accurately. Hopefully, it will be to within one half an order of magnitude so that designers will be able to maximize the usefulness of this data in modeling programs. Until now, models have used only crude approximations to the ash conductivity. It is hoped that this work will change that.

D. Thermal Conductivity

This past quarter, a decision was reached on the type of thermal conductivity system which would be most suitable for our purposes. Because of a cooperative effort with MERDI, which has undertaken to design and construct an oxygen atmosphere laser flash thermal diffusivity system, the emphasis at MSU is on low temperature accuracy and wide range of measurement capability. For this reason, a comparative method was chosen over an absolute method such as the guarded hot plate technique. The advantages of the comparative method over absolute methods are that the data is obtained more quickly, a small sample may be used and easily installed, and the range of measurement both in temperature and conductivity is larger than for most absolute methods.[13-15] Conceptually, the experiment is quite simple. A stack is made consisting from top to bottom of an upper heater, a standard material, the unknown slag or ceramic, another layer of standard reference material and a lower heater followed by an insulator and a heat sink. Between each element of the sandwich is a thermocouple which enables accurate profiling of the stack thermal gradient. By comparing the thermal gradient across the standard reference material to that of the unknown, the thermal conductivity of the unknown may be determined. The two most important criteria for accuracy are good thermal contact between stack elements and uniform heat flow. Good thermal contact is obtained by using a thermal heat sink compound between stack elements and uniform heat flow is obtained by using guard heaters at either end of the stack to insure a planar temperature gradient across the stack. The details of the design and the selection of standards have been carefully worked out at the National Bureau of Standards.[16-17] The system chosen will enable the determination of thermal conductivity to state-of-the-art accuracy at maximum temperatures of 1200-1300 K. Here the data can be combined with thermal diffusivity data to help eliminate the various unknowns associated with such a difficult experimental technique as pulsed diffusivity. In addition, high temperature (1100-1300 K) thermal conductivity measurements can be combined with thermal diffusivity results to give the specific heat of high tempera-

ture materials as a side benefit. The system was used to study a piece of Corhart RFG firebrick, the thermal conductivity of which was needed by Task E of the MSU/MHD project. The data is shown in Figure 12. The behavior is quite smooth over the temperature region studied with a possible dip in the vicinity of 650 K. For comparison purposes the thermal conductivity shown for Corhart RFG brick is about half that of 99.8 percent alumina at 1100 K.

IV. CONCLUSIONS

We have been able to show that, over a limited temperature range, the slag electrical conductivity of Rosebud coal can be described by a closed-form mathematical expression to an accuracy of about ten percent as a function of temperature and iron content. This kind of result has long been awaited by planners and design engineers. Although we have not included seed as a variable, we hope in the short term to extend this work to wider temperature ranges and to include oxygen partial pressure as an additional parameter in this equation.

Over the past two years there have been persistent recommendations for the use of iron[18] or iron-containing spinel electrodes such as hercynite.[19,20] Iron enhances considerably the electrical conductivity of slag with some percentage, perhaps only ten percent, of this contribution being electronic.[21,22] In spite of this low percentage of electronic contribution, these electrode materials may be compatible with ionic transfer through the slag. It still remains a problem, however, that there is a large amount of bulk transport of iron from the cathode[23] which puts a limit on the total accumulated charge transfer from these materials to the slag. Special designs might serve to bypass this problem. The work shows that current flow in slags will produce a loss of iron at the anode and a deposition of SiO_2 on the anode from current neutralization of SiO_{2+n}^{-2n} anion complexes where n=1,2. It has recently been observed in preliminary measurements by Roger Perkins[24] that silica did indeed coat a platinum anode in d-c conductivity experiments. This reduced the effective conductivity of the electrode-slag system and severely inhibited conductivity in the reverse direction (i.e., reverse polarity) after the SiO_2 had been coated electrolytically on the anode. This has not been observed heretofore since bulk conductivity measurements are normally either a-c or low current density d-c measurements. Although the bulk conductivity is not a function of current density, electrode slag interactions require a sufficient build-up of reaction products to be observable and this naturally requires high current densities or long time measurements.

In addition, the Lockheed group[24] also observed a substantial amount of intermittent arcing at the anode surface presumably caused by current punching its way through the silica barrier being deposited.

These observations have substantial and important implications for the operation of an MHD electrode assembly both in the choice of electrode and in generator operating conditions. Since precious metal electrodes cannot contribute iron to the slag, as iron is removed from the slag at the anode surface a silica layer is formed producing the effects described above. If iron electrodes are used, iron is continually transferred to the slag at the anode and this maintains the high conductivity of the slag near the

slag-anode interface. At the interface itself, there would appear to be a low concentration of iron which will be discussed in a forthcoming report by Kent Koester.[25] It remains to be seen what other metal electrodes will encounter the same problems with silica deposition. In the choice of operating conditions, the occurrence of crystallization-induced anomalies in the conductivity behavior of Rosebud ash will be very important and will affect the stability of electrode operation. Fluctuations in bulk conductivity over a narrow temperature range can lead to disruption of the character of the current transfer mode at the electrode surface. This is true in the arc mode and large variations in diffuse mode performance have been correlated well with a function of slag layer resistance.[25] Stable operation of an electrode will be dependent upon maintenance of the current transfer mode for which it was designed. Diffuse mode electrodes would not withstand the severe deterioration which would occur from the thermal hot spotting characteristic of the arcing mode.

Because alumina addition has only a small effect on the seeded coal slag conductivity but greatly improves the resistance of alumina materials to slag corrosion, the possibility of slag beneficiation--depending on the materials involved--should not be ruled out of future research.

MILESTONE CHART

STATUS DATE _____

TASK G3

PROGRESS

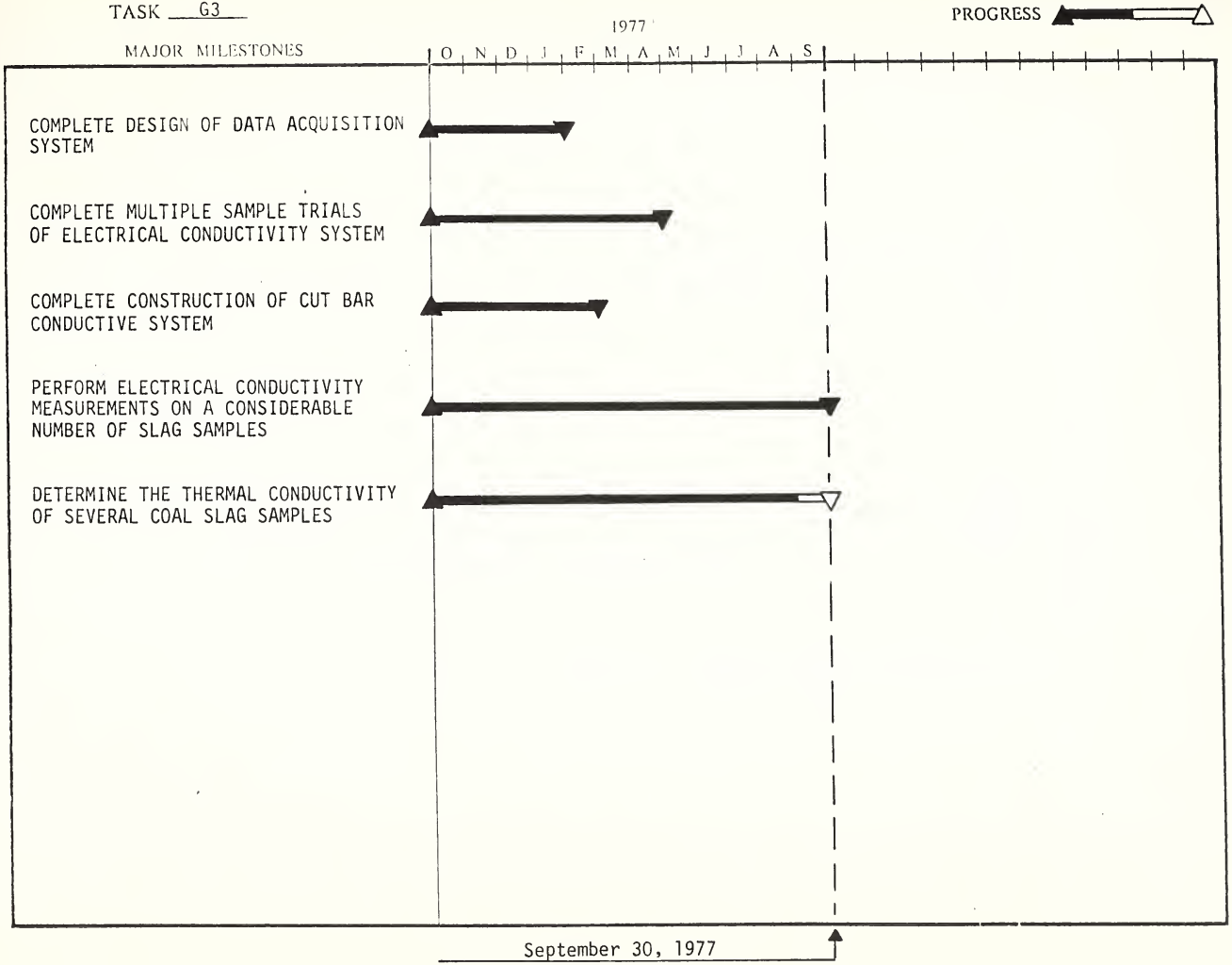
1977
MAJOR MILESTONES
O N D J F M A M J J A S
COMPLETE DESIGN OF DATA ACQUISITION SYSTEM
COMPLETE MULTIPLE SAMPLE TRIALS OF ELECTRICAL CONDUCTIVITY SYSTEM
COMPLETE CONSTRUCTION OF CUT BAR CONDUCTIVE SYSTEM
PERFORM ELECTRICAL CONDUCTIVITY MEASUREMENTS ON A CONSIDERABLE NUMBER OF SLAG SAMPLES
DETERMINE THE THERMAL CONDUCTIVITY OF SEVERAL COAL SLAG SAMPLES
September 30, 1977

TABLE 1.--The Compositions of MHD-12 and Two Montana Coal Ashes

	Rosebud Ash	MHD-12	SMF-0
SiO_2	40.34%	50%	47%
Al_2O_3	24.6	21	20.7
CaO	18.9	1	21.9
MgO	5.8	5	6.6
Fe_2O_3	4.4	14	5.0
K_2O	0.53	1	0.43
Na_2O	0.46	--	0.40
SO_3	0.28	2	--
TiO_2	--	--	1.0
P_2O_5	--	--	0.39

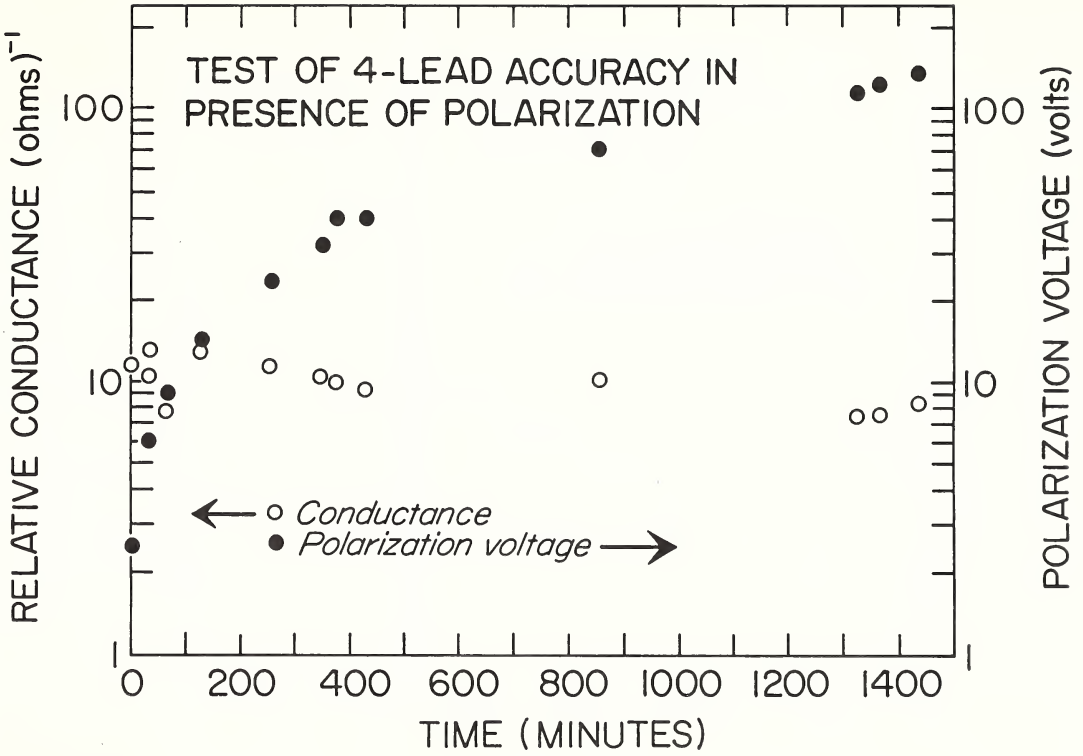

Figure 1.--Test of four-lead accuracy in presence of polarization

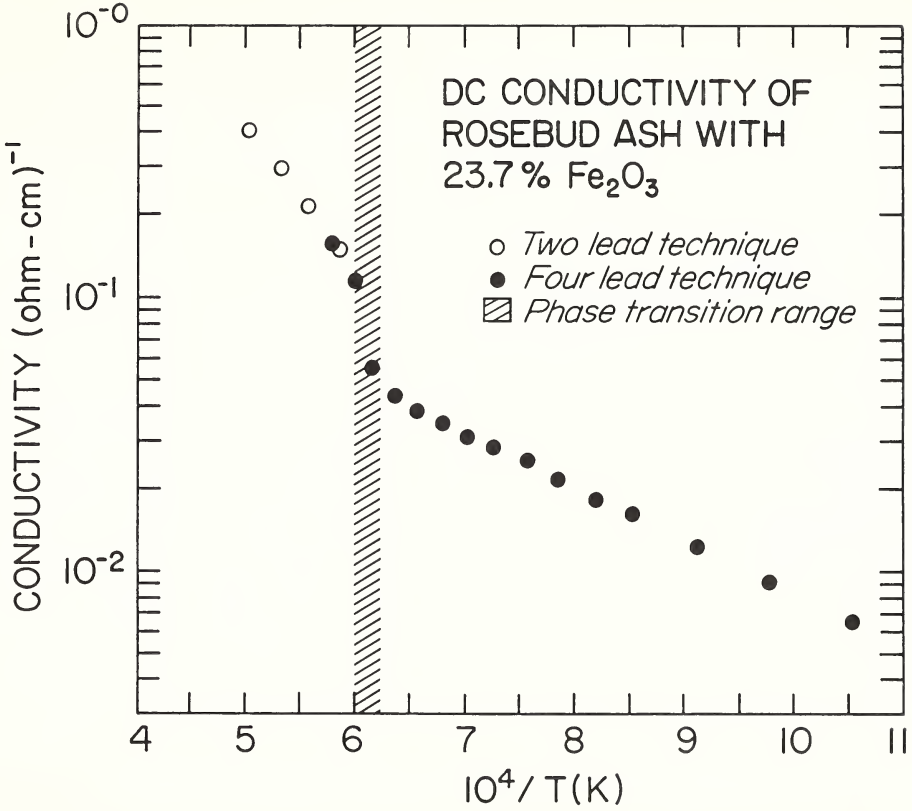

Figure 2.--D-C conductivity of Rosebud ash with 23.7 percent Fe_2O_3; two-lead data normalized to four-lead data

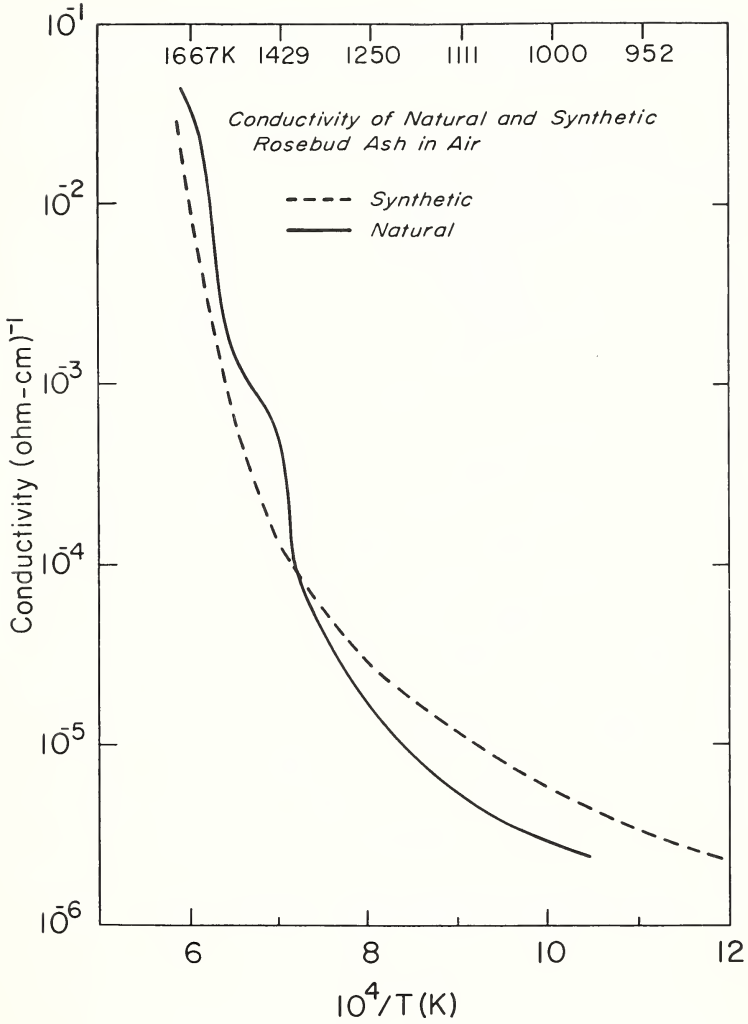

Figure 3.--Comparison of electrical conductivity of natural and simulated Rosebud ash

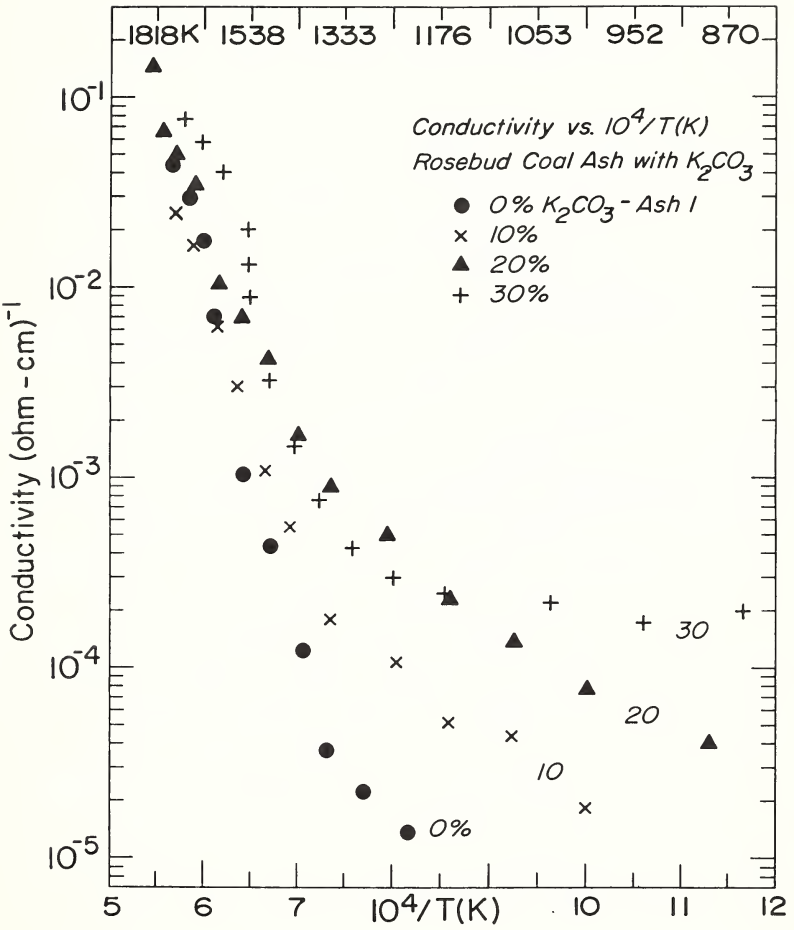

Figure 4.--Conductivity of natural Rosebud ash with varying amounts of K_2CO_3 seed

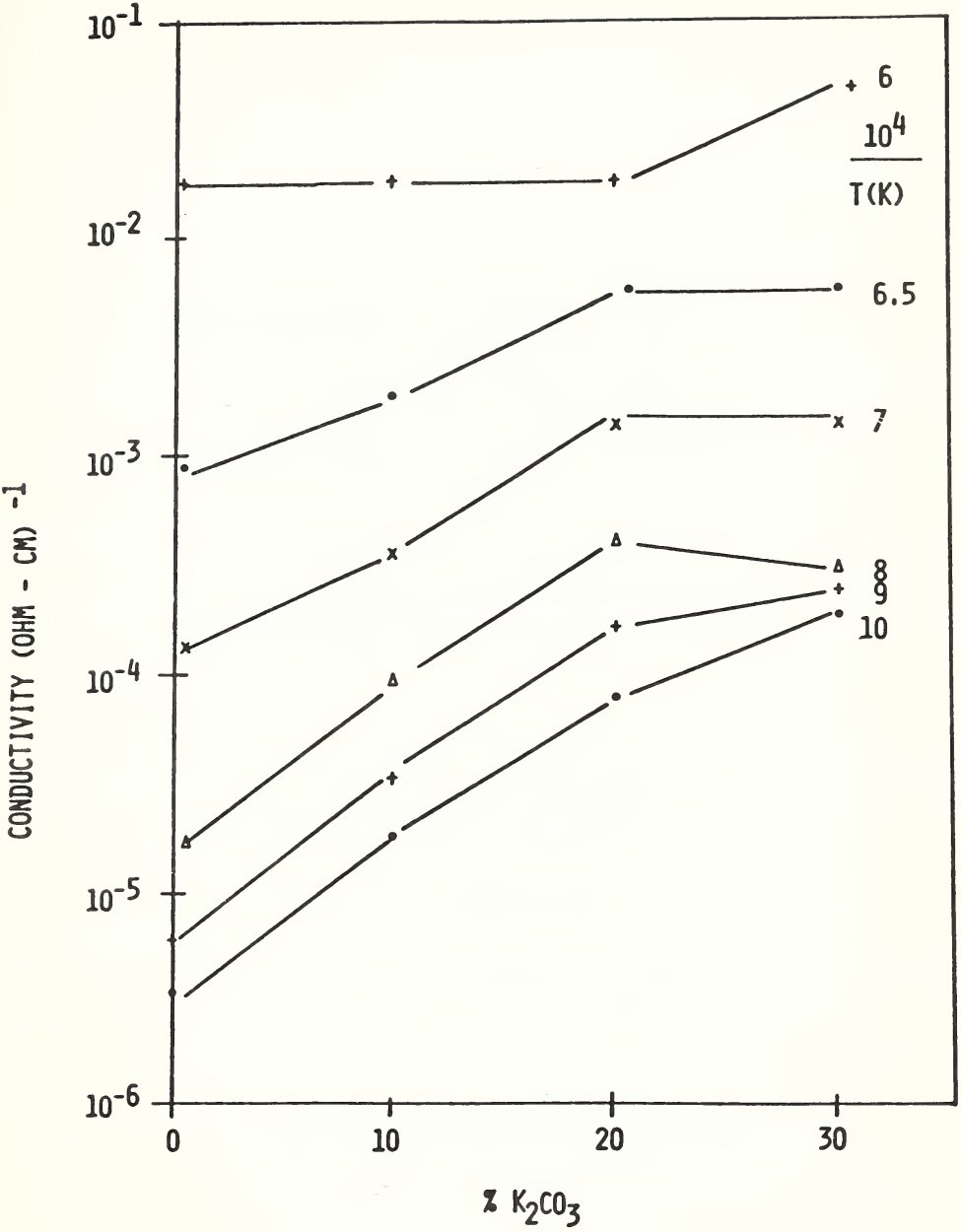

Figure 5.--Isotherms of electrical conductivity of Rosebud ash as function of K_2CO_3 content

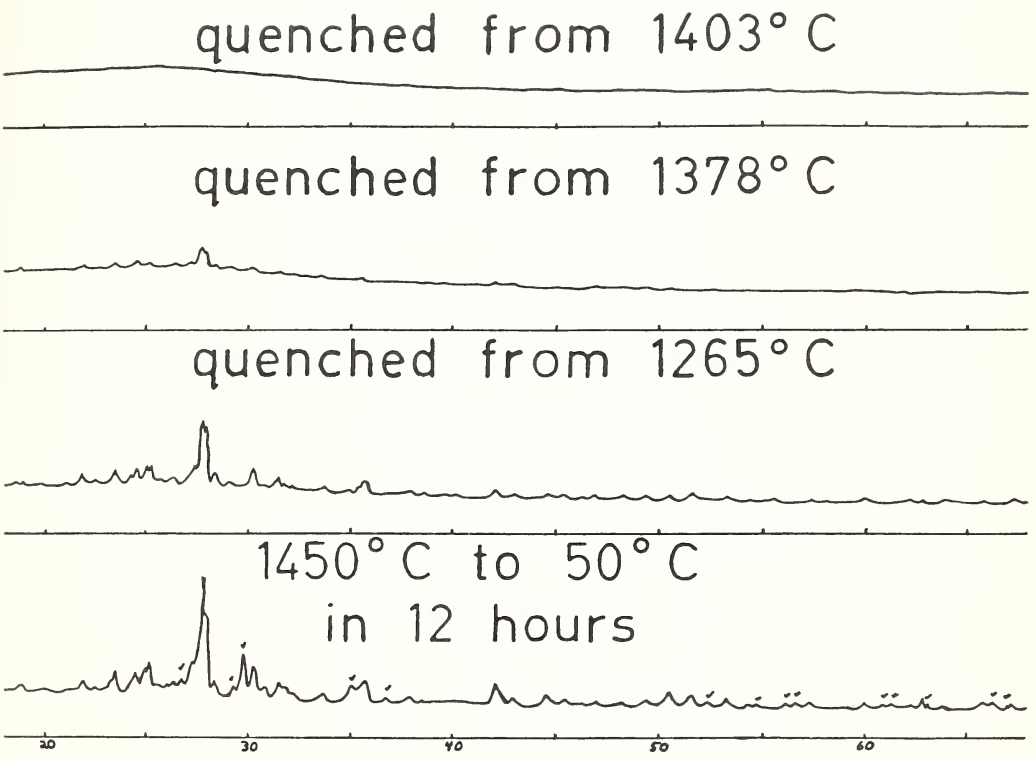

Figure 6.--X-ray spectra showing crystallization behavior of Rosebud natural ash as affected by thermal history of sample. Checked peaks have not been identified. Unchecked peaks are characteristic of anorthite.

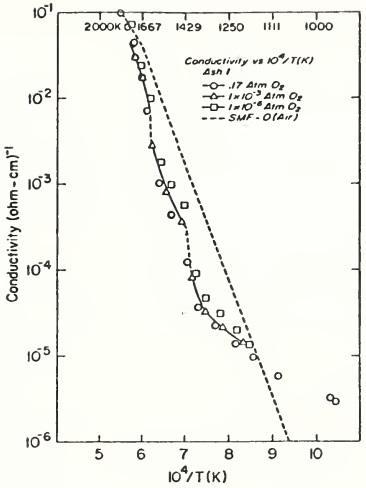

Figure 7.--Rosebud ash conductivity at varying oxygen pressure

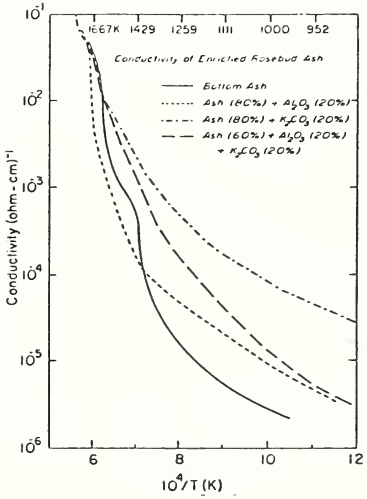

Figure 8.--Effect of alumina enrichment on seed and unseeded Rosebud ash

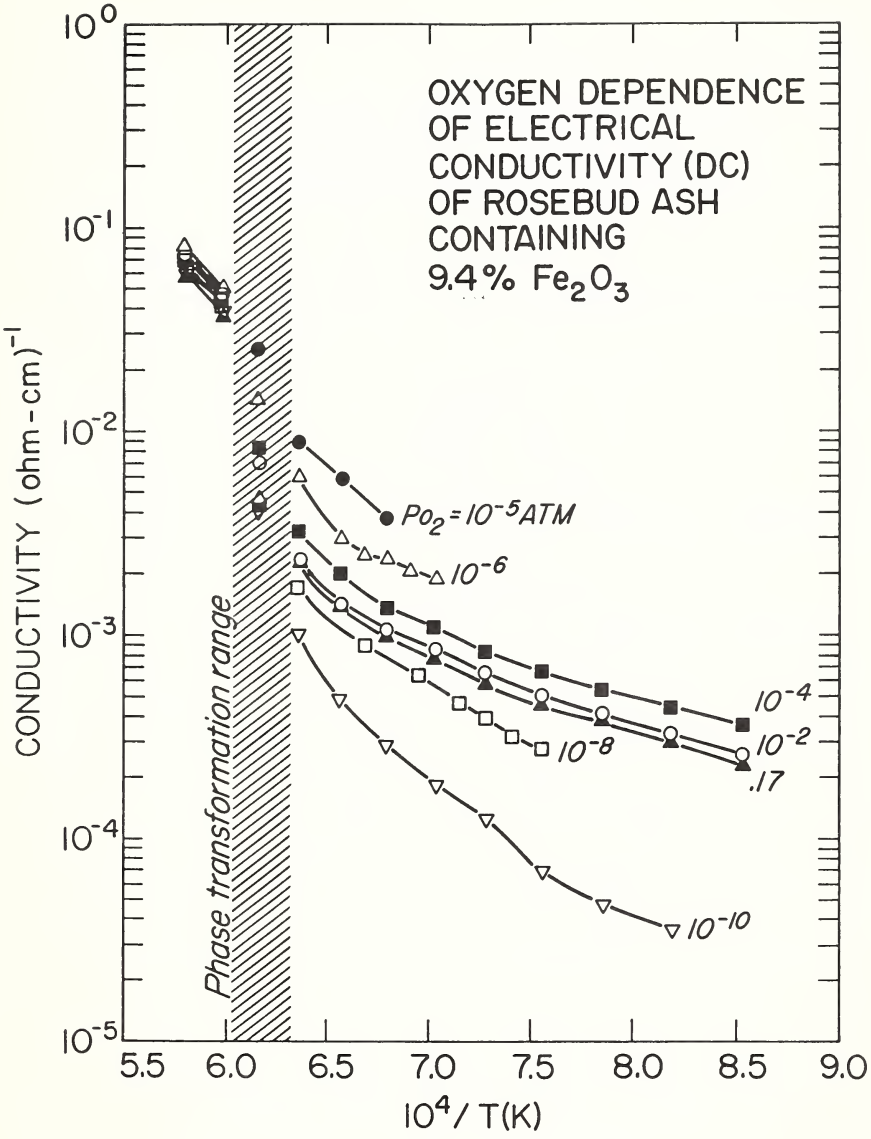

Figure 9.--Oxygen dependence of electrical conductivity (d-c) of Rosebud ash containing 9.4 percent Fe_2O_3

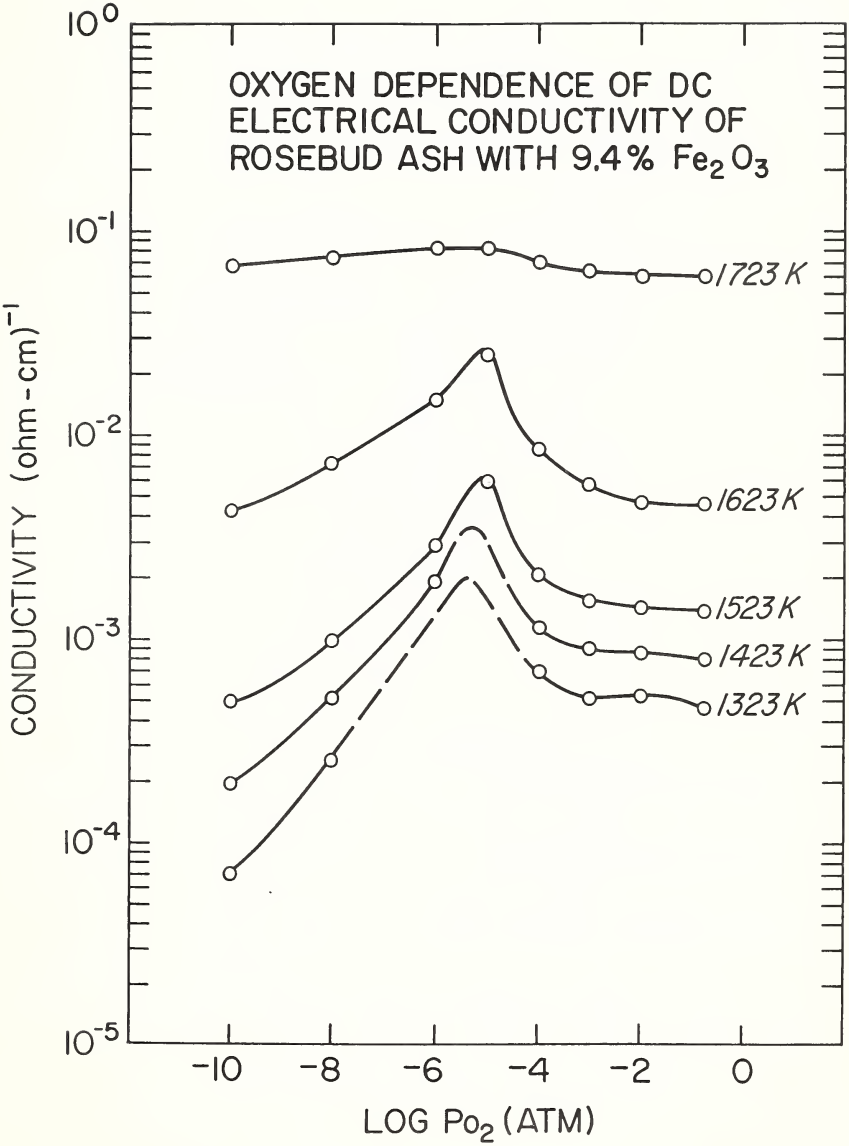

Figure 10.--Oxygen dependence of d-c electrical conductivity of Rosebud ash with 9.4 percent Fe_2O_3

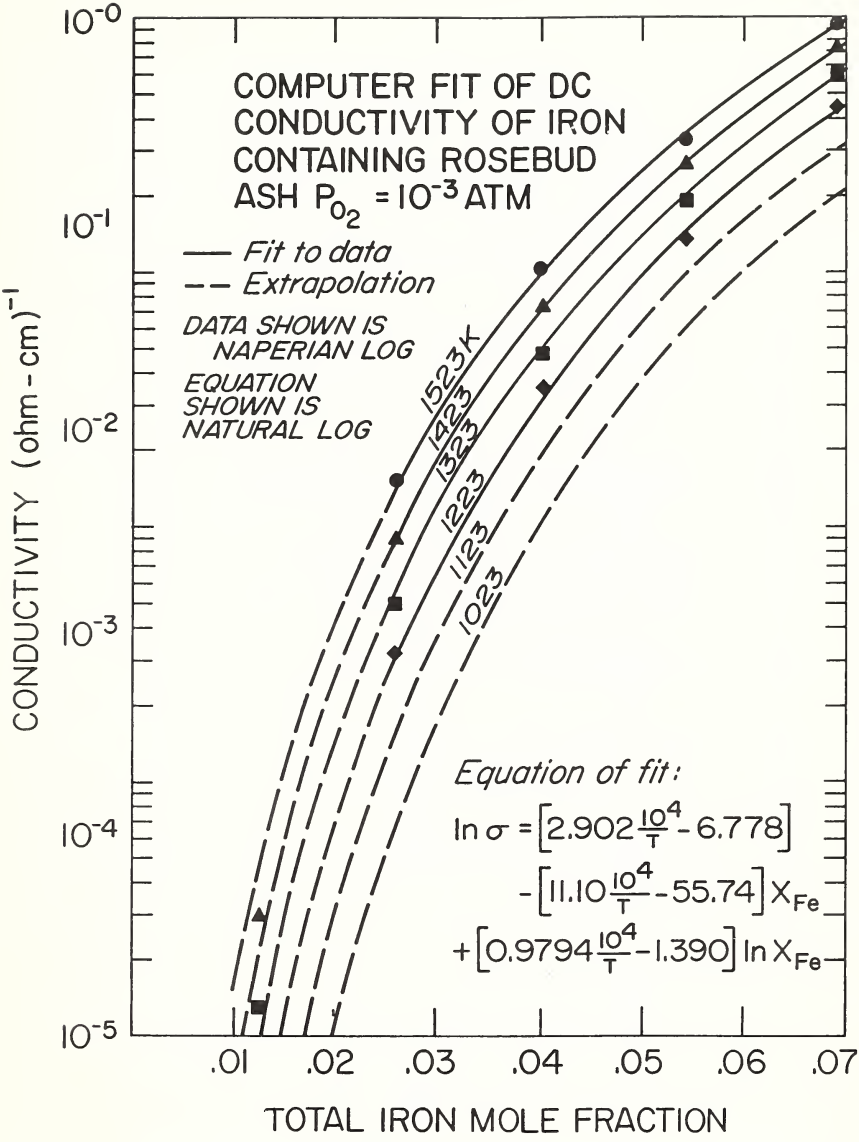

Figure 11.--Computer fit of d-c conductivity of iron containing Rosebud ash $P_{O_2} = 10^{-3}$ atm.

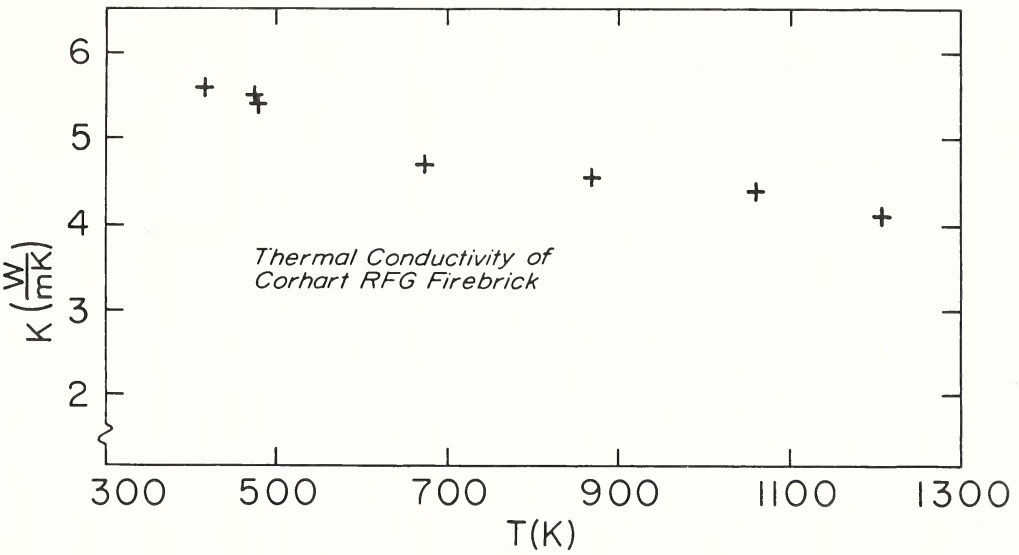

Figure 12.--Thermal conductivity of Corhart RFG firebrick

REFERENCES

1. R. J. Rosa, "Design Considerations for Coal-Fired MHD Generator Ducts," Fifth International Conference on MHD Electrical Power Generation, Munich, 1971.

2. Montana Power Company, Corette Plant, Billings, Montana.

3. Montana Power Company, Private Communication.

4. This work was done by W. Beezhold and R. Burghard using the MSU ion beam facility.

5. McDanel Refractors, Beaver Falls, Pennsylvania.

6. V. Gottardi and G. Bonetti, Verres Refract., 24, 41, 1970.

7. B. Lotto and S. Lazzari, Vetro Silic., 9, 5, 1965.

8. Montana Energy and MHD Research and Development Institute, MHD Power Generation: Research, Development, and Engineering, Task G1, Quarterly Report Prepared for ERDA, March 1976.

9. Montana Energy and MHD Research and Development Institute, MHD Power Generation: Research, Development, and Engineering, Task G1, Quarterly Report Prepared for ERDA, September 1976.

10. E. M. Levin, C. R. Robbins, and H. F. McMurdie, Figure 630, Phase Diagrams for Ceramists, Third Edition, American Ceramic Society, Columbus, Ohio, 1974.

11. Argonne National Laboratory, Conference on High Temperature Sciences Related to Open-Cycle, Coal-Fired MHD Systems, Report No. ANL-77-21, 1977.

12. Batelle Pacific Northwest Laboratories, Final Progress Report on Properties of Molten Coal Slags Relating to Open Cycle MHD, Richland, Washington, BNWL-B-466, December 1975.

13. R. K. Francis and J. R. Tinkelpaugh, Journal of the American Ceramic Society, 43, 560, 1960.

14. J. Francl and W. D. Kingery, Journal of the American Ceramic Society, 37, 80, 1954.

15. V. V. Mirkovich, Journal of the American Ceramic Society, 48, 387, 1965.

16. D. R. Flynn, "Thermal Guarding of Cut-Bar Apparatus," unpublished Proceedings of the Conference on Thermal Conductivity Methods, Battelle Memorial Institute, Columbus, Ohio, October 1961.

17. D. R. Flynn and H. E. Robinson, "The National Bureau of Standards High Temperature Absolute Cut-Bar Apparatus," unpublished Proceedings of the Third Conference on Thermal Conductivity, Gatlinberg, Tennessee, 1963.

18. Stanford University, Quarterly Report FE-2341-1, Palo Alto, California, January 1977.

19. J. B. Wachtman, Jr., J. Schneider, and Alan D. Franklin, "Role of Ceramics in Energy Systems," ERDA-NSF Workshop Proceedings on Ceramic for Energy Applications, Publ. No. CONF-751194, Columbus, Ohio, November 24-25, 1977.

20. H. K. Bowen, "Transport Properties in the Spinel Electrode Module," Conference on High Temperature Sciences Related to Open-Cycle, Coal-Fired MHD Systems, Pub. #ANL-77-21, Argonne National Laboratory, April 4-6, 1977.

21. J. Chipman and L. C. Chang, "The Ionic Nature of Metallurgical Slags," Simple Oxide Systems, Journal of Metals, pp. 191ff, 185, February 1949.

22. M. T. Simnad, G. Derge, and I. George, "Ionic Nature of Liquid Iron-Silicate Slags," Journal of Metals, 1386, 200, December 1954.

23. Kent Koester, Stanford University High Temperature Gasdynamics Laboratory, Private Communication, EPRI Contract #468-1.

24. Roger Perkins, Lockheed Palo Alto Research Laboratory, Private Communication, EPRI Contract #468_2.

25. Kent Koester et al in Proceedings of a Conference on Ash Deposits and Corrosion Due to Impurities in Combustion Gases (to be published), Henniker, New Hampshire, June 1977.

TASK H1

MHD Systems Instrumentation and Data Acquisition

R. Johnson and T. Robles

ABSTRACT

A time-dependent one dimensional nozzle-channel-diffuser computer code has been completed which is suitable for conducting sensitivity studies on MHD/steam power plants. Since a time-dependent combustor model is still in the process of development, the present program is most applicable to supersonic flow situations in which the combustor-channel interaction is minimized.

A general time-dependent model for a steam bottoming plant has also been completed. This code is suitable for studying the interaction effects on all bottoming cycle components including the variable cycling effects of transients on the phased regenerative high temperature air preheater system.

The data flow simulation model is being modularized to include distributed control by microprocessors rather than by centralized control as was originally intended.

I. OBJECTIVE AND SCOPE OF WORK

The work to be performed is in the general area of MHD systems, instrumentation, and controls and consists of two general parts:

A. The systems analysis and computer simulation of a time-dependent, one-dimensional model of a complete MHD/steam power plant to include combustor, nozzle, channel, diffuser, high-temperature air preheater, heat-exchanger array, inverters and steam plant. The simulation program should provide the capability to evaluate the sensitivity of a combined-cycle MHD/steam power plant to changes in operating conditions which may be induced both internally and externally. In particular, the effects of load variations due to fault conditions, changes in fuel and seed-flow rate, internally-simulated arcing conditions, and variable air-preheat heat-exchanger configurations should be eventually treatable by the program.

B. The continued development of a data flow and control simulation program for the study of the data processing requirements of a MHD/steam power plant. The program should allow for the introduction of various instrumentation configurations and complements, choice of control algorithms, and variation of operational loading scenario.

II. SUMMARY OF PROGRESS TO DATE

During the preceding quarter (April-June), time-dependent and steady state computer models for MHD channel simulations were completed. Simulation codes for both steady-state and time-dependent CDIF models were delivered to MERDI.

Two extremely long computer simulation runs of the time-dependent model were completed showing the complete generator transient response to a 5 percent change in d-c inverter voltage such as could be achieved by programmed ignition angle change. The detailed results of these runs still are being analyzed.

Work also has been completed on a dynamic model for the steam-bottoming plant and the air preheater system.

Work originally scheduled before the contract modification (to provide MERDI with CDIF codes) which remains undone includes a time-dependent code for a pressurized coal combustor including coupling to the time-dependent model completed above and the data flow and control simulation program.

III. DETAILED DESCRIPTION OF TECHNICAL PROGRESS

A. Time-Dependent MHD System Computer Runs

The development of detailed time-dependent and steady-state computer simulation models for the topping plant portion of a 250 MWt ETF plant have been covered extensively in the previous quarterly reports. At the end of the past quarter several seven- to twenty-one-hour runs of the time-dependent model were completed. The detailed results of these runs still are being analyzed and will be reported in the subsequent quarterly report along with several other transient studies to be undertaken. However, several preliminary conclusions concerning such studies can be given; these are detailed in the conclusion section.

B. Dynamic Steam Plant Model

The major progress to be reported is concerned with the dynamic model of the steam-bottoming plant and the air preheater system. Since the objective of these studies is to gain knowledge appropriate to the specification of instrumentation and data acquisition systems for the control of ETF and subsequent base load plants, the program first is being applied to ETF-type plants.

The ETF plant design previously completed is based upon direct combustion of coal with an air preheat temperature of 1920 K. Since it is expected that western sub-bituminous coals will play an important role in ETF development, a Montana sub-bituminous coal was assumed as input fuel. Analysis of this coal is summarized in Table 1.[1]

After it has been crushed and dried with waste heat from the flue gas exhaust, the coal is assumed to have 5 percent moisture content before combustion.

The MHD/steam power cycle analysis utilizes the numerical calculation method described in reference 2. This method only permits the calculation of the power produced by a postulated system, it does not provide a solution to the more practical problem of designing an optimum system. However, it is expected that the instrumentation or data response characteristics will not change appreciably because the dynamics of the system will be relatively unchanged for minor variations in the design.

1. Engineering Test Facility Configuration

An MHD plant size of 250 MWt was chosen for evaluation after consultation with MHD/ERDA. The design conditions and the performance of a base load plant could be simulated reasonably and extrapolated from this size plant. A block diagram of the system is shown in Figure 1.

The combustor is operated with 100 percent stoichiometric air at a pressure of 5 atmospheres with a wall temperature of 1600 K. Two-stage combustion is assumed with 90 percent ash and slag removal in the first stage. Seed is added in the second stage which is electrically isolated from the first stage. The seed is in the form of K_2CO_3 and K_2SO_4. The amount of each constituent is based on the sulfur content of the fuel. Proper balance between the sulfur and potassium is assumed to be maintained so that all the sulfur in the fuel is captured in the seed condenser in the form of K_2SO_4.

The flow through the MHD channel (acceleration nozzle, generator, and diffuser) was represented by quasi one-dimensional MHD equations. The MHD generator is a square cross-section that operates at subsonic conditions with a wall temperature of 1600 K. A segmented Faraday generator configuration is considered and the electrode pitch selected so that the Hall voltage between adjacent electrodes does not exceed 40 volts. The voltage drop in the anode and the cathode and the voltage drop near the electrodes (across the boundary layer) are regarded as an effective voltage drop of 100 volts. The effects of finite electrode segmentation have been taken into account. The superconducting magnet is assumed to have a tapered magnetic field and a maximum field of 6 Tesla.

The square cross-section ceramic-lined diffuser, with expansion angle of 5° and wall temperature of 1600 K, decelerates the gas exiting from the generator.

A two-stage air preheater supplies air to the combustor at 1920 K. The first stage, a recuperative, counterflow, shell-and-tube type, preheats the air to 1100 K. The second stage is a cored brick regenerative type preheater. The regenerator system consists of 11 units, of which at any time 4 are on gas, 4 on air, and 2 on pressurization and depressurization during switchover. One unit is provided as a heat buffer (heat capacitor) to reduce the air temperature ripple due to cycling.

A seed condenser is provided between the high-temperature air heater and the superheater for seed collection. The combustion gas entering the seed condenser is cooled down by recycling combustion gas from the electrostate precipitator exit. This causes the formation of liquid and solid K_2SO_4 at 1340-1350 K. The seed collected flows to the seed recovery system for sulfur removal.

The steam-bottoming plant is a once-through (universal pressure boiler) single reheat operating on supercritical pressure. The working fluid is pumped through all the pressure-part heating tubes sequentially where it is converted to steam as it absorbs heat. There is no recirculation of water within the plant.

2. ETF Steam Cycle

The block diagram of the steam cycle is shown in Figure 2. The steam plant is partitioned into the following sections:

a. Feedwater heater,
b. Feedwater pumps,
c. Wall-cooling tubes -- combustor, MHD channel,
d. Economizer,
e. Radiant boiler,
f. Superheater,
g. Reheater,
h. Condenser, and
i. Steam turbines.

As a first step towards the simulation of a complete ETF steam-bottoming plant, a simple open-loop model of the steam plant is considered. The components included in the model are the economizer, radiant boiler, superheater, reheater, and wall-cooling tubes. The effect of the feedwater heater, and the feedwater pump dynamics were omitted because the added complexity would not result in any significant contribution to the model performance. The design parameters of the steam plant also are shown in Appendix E.

3. The Air Cycle

The block diagram of the air cycle is shown in Figures 3 and 4. The air is compressed to the desired pressure using air compressors with blades of low relative roughness and relative clearance. An efficiency of 90 percent was assumed for this advanced air compressor. The first stage is a recuperative, counterflow, shell-and-tube type preheater designed to heat the air up to 1100 K. Special alloys are used in the high-temperature section. The second stage is a cored brick regenerative type preheater. This stage consists of 10 phased array heat exchangers of which at any time 4 are on gas (reheat), 4 on air (blowdown), and 2 on pressurization and depressurization during switchover (or soaking). During the reheat phase, the hot gas passes through the heat exchanger (cored bricks) for a fixed reheat time.

During the blowdown phase, the energy stored in the brick matrix is transferred to the cooler counterflow air stream. Due to cycling of the heat exchangers, the air exit temperature varies, from a maximum at the start of the blowdown cycle to a minimum at the end of the cycle. A heat capacitor or buffer is provided between the heat exchangers and the combustor to reduce the temperature ripple.

4. The Gas Cycle

From the MHD channel, the gas flows through the radiant boiler where the heat transfer mode is primarily by radiation. The next section is the regenerative high-temperature air heater. The variation of the gas temperature leaving the high-temperature air heater is similar to a sawtooth waveform (due to cycling of the heat exchanger). The gas then flows to a seed condenser where it is cooled to approximately 1350 K by the addition of recycled flue gas from the electrostatic precipitator. This process results in the formation and removal of liquid K_2SO_4. From the seed condenser, the gas flows sequentially through the superheater, low temperature air heater, reheater, and economizer. These components are recuperative, shell-and-tube type heat exchangers. Removal of K_2SO_4 from the gas in the seed condenser assures clean tube surfaces in these heat exchangers. An electrostatic precipitator is provided after the economizer to collect 99 percent of the remaining solid particles. A gas cleaner is provided before the stack to remove NO and SO_2 from the flue gas ensuring clean effluents from the MHD system.[2] The block diagram is shown in Figure 4.

5. Formulation of the Dynamic Model of the Steam Plant

a. The dynamic behavior of the steam plant and the low temperature air heater may be represented by non-linear, partial differential equations related to fluid flow and heat transfer. The solution of a set of these equations is time-consuming and difficult, thus, simplified assumptions have to be made. The steam plant is divided into a number of sections; and for each lumped-parameter section, the property of steam and gas is assumed to vary only in the axial direction and linearly with space. These assumptions reduce the set of partial differential equations into a set of ordinary differential equations. The assumptions made in the formulation of the dynamic model can be summarized as follows:

1. Fluid flow is a one-dimensional, fully developed turbulent flow.

2. Heat transfer from the tube wall to the internal fluid may be expressed by the Nusselt equation.[3]

3. All gravitational and kinetic energy terms are neglected.

4. The heat transfer along the length of the tube or along the length of the fluid flow is negligible.

5. Heat storage in the tube is concentrated at the center of the tube wall.

6. Fluid properties are defined by average values over the cross-sectional area.

7. The dynamics of the combustion gas are negligible.

Every section of the steam plant consists of hundreds of parallel tubes. Uniform distribution among the parallel flow is assumed; thus, a single fluid flow may be used to represent the multiple flow path of each unit.

The film conductance of the steam is assumed to vary with the 0.8 power of the fluid flow inside the tube, and the film conductance on the gas side is assumed to vary as the 0.6 power of the gas flow.[4] The variation of the heat transfer and friction coefficients with temperature is neglected. The gas-side radiant heat transfer is represented by the Stefan-Boltzmann law.[4] The volumes and weights of the connecting pipes are considered to be lumped with their adjacent section.

Each steam plant component is divided into four sections in order to obtain a more accurate representation of the fluid and tube properties.

Since the dynamic response of the turbine-generator combination is much faster than that of the boiler, only the steady-state equation of the turbine is included in the model. Likewise, the wall-cooling tubes are represented by steady-state parameters.

The mathematical model of each section is based on the governing laws of fluid dynamics (conservation of mass, conservation of momentum, and conservation of energy), empirical heat transfer relationships, and the equation of state described in standard textbooks.[4,5,6]

Conservation of Mass

$$A \frac{\partial \rho}{\partial t} + \frac{\partial w}{\partial x} = 0$$

Conservation of Momentum

$$\frac{\partial p}{\partial x} + \rho \left(\frac{\partial u}{\partial t} + u \frac{\partial u}{\partial x} \right) + 2C_f \frac{\rho u^2}{D} = 0$$

Conservation of Energy

$$\frac{\partial}{\partial x} (wh) + A \frac{\partial}{\partial t} (u\rho) = q_w$$

Equation of State

$$\rho = (p,h)$$

$$T = T(p,h)$$

Heat Storage in the Tube Wall

$$q_g - q_s = A_w \rho_w C_w \frac{\partial T_w}{\partial t}$$

Heat Transfer from the Tube Wall to the Fluid

$$q_s = C_g \pi D \, (W_s/W_{so})^{.8} \, (T_w - T_s)$$

Convective Heat Transfer from the Gas Side to the Tube Wall

$$q_g = C_g \pi D_o (w_g/w_{go})^{.6} \, (T_g - T_w)$$

Radiative Heat Transfer from the Gas Side to the Tube Wall

$$q_g = \pi D_o S (T_g^4 - T_w^4)$$

The partial differential equations representing the fluid dynamics may be reduced to ordinary differential equations valid only for small disturbances about the operating point.

The fluid dynamic equations then may be reduced to:

Conservation of Mass

$$V \frac{d\rho}{dt} = w_i - w_o$$

Conservation of Momentum

$$P_i - P_o \rho = f \, w_i^2 / \rho_i$$

Conservation of Energy

$$w_i h_i + Q_s - W_o H_o \rho = V \frac{d}{dt} (\rho h)$$

The heat transfer equations may be rewritten:

Heat Storage in the Tube Wall

$$Q_g - Q_s = W_w C_w \frac{dT_w}{dt}$$

Heat Transfer from the Tube Wall to the Fluid

$$Q_s = \text{constant} \times w_s^{.8} (T_w - T_s)$$

Convective Heat Transfer from Gas Side to the Tube Wall

$$Q_g = \text{constant} \times s_g^{.6} (T_g - T_w)$$

Radiative Heat Transfer from the Gas Side to the Tube Wall

$$Q_g = \text{constant} \times (T_g^4 - T_w^4)$$

The properties of steam and air ($T(p,h)$, $\rho(p,h)$) are represented accurately by polynomial equations derived from the steam tables[7] using the non-linear programming least-squares method developed by Pierre and Lowe.[8] This reduces the number of calculations required by approximately 80 percent, and the large storage requirements encountered in table-look-up procedures are avoided.

6. High-Temperature Air Preheater with Heat Capacitor

A cored brick regenerator is proposed to heat the air from 1100 K to 1920 K. The regenerator was designed using the computer codes developed in reference 10 (Appendix F). The heat capacitor was provided between the high-temperature air preheater and the combustor to reduce the air preheat temperature ripple (Appendix F).

The dynamic response of the regenerator may be determined accurately from the simulation of the thermal equations describing the regenerator behavior.

Using the simplified assumptions described in section A and the lumped-mass generator model described in Appendix F, the dynamic response of the high-temperature air heater may be characterized by these equations:

Conservation of Mass

$$\frac{d\rho_o}{dt} = (W_i - w_o)/V$$

Conservation of Momentum

$$p_i - p_o = f\, w_i^2/\rho_i$$

Conservation of Energy

$$w_i h_i + Q_a - w_o h_o = V \frac{d}{dt}(\rho h)$$

Heat Storage in the Ceramic Wall

$$Q_g - Q_a = w_c C_c \frac{dT_c}{dt}$$

Equivalent Heat Transfer from Ceramic Wall to the Air

$$Q_a = h_a (T_c - T_a)$$

Equivalent Heat Transfer from the Gas Side to the Ceramic Wall

$$Q_g = h_g (T_g - T_c)$$

7. The Gas Path

The combustion gas leaving the diffuser flows through the steam plant and air heaters in the following order: the radiant boiler, the high-temperature air heater, the seed condenser, the superheater, the low-temperature air heater, the reheater, and the economizer. As the hot gases flow through these sections, heat is absorbed and the gas temperature drops progressively. In the following equations for the gas path, the inertia and the heat capacitance of the gases are neglected. The air/fuel ratio and heat transmission coefficients are assumed to remain constant for each section and the gas specific heat varies with temperature (Appendix D).

The heat transfer equations are:

$$Q_g = \text{constant} \times (T_g^4 - T_m^4) + \text{constant} \times W_g^{.6} (T_g - T_m)$$

$$T_g = T_{gi} - Q_g/(C_g w_g)$$

8. Computer Implementation of the Dynamic Model

The behavior of the steam plant and the air heaters are characterized by a set of ordinary differential equations of the form

$$\frac{dU}{dt} + F(U) = 0$$

and a set of algebraic equations. There are several numerical methods that can be used in solving a system of first order differential equations. The choice of the method to be used is based on many factors such as the following:

a. the accuracy required--the error in the solution depends on the error incurred at each step of the integration and the propagation of the error in later steps;

b. the speed at which the computation will be performed;

c. the ease with which the estimation of the errors at each step may be made; and

d. the ease with which a method can be programmed for a computer solution and the availability of the computer program.

The various numerical procedures are roughly classified into two groups, the one-step methods and the multi-step methods,[11] employing either the direct or indirect use of Taylor's expansion series of the solution function. The single step methods use only the results obtained for (t_i) in the approximation of the value at (i+1). In the multi-step methods the results obtained for (t_i, t_{i-1}, t_{i-2}, . . ., t_{k-p}) are required, the number p being dependent on the formula utilized. There are many methods in both categories,[11-12] but the most

commonly used methods are the Runge-Kutta (single step) and the predictor-corrector (multi-step) methods.[12]

The following are characteristics of these two methods:

a. Runge-Kutta method

1) They are self-starting, 2) they require several evaluations of the function and are, therefore, time-consuming (a fourth order requires four evaluations of the function), 3) being self-starting, they permit an easy change in the step size, and 4) they provide no easily obtainable information about the truncation error.

b. predictor-corrector method

1) They are not self-starting; hence, they require a method such as the Runge-Kutta method for starting, 2) since they require information about prior points for repeated evaluation of the function, they are more efficient, 3) a change in the step size requires a temporary reversion to a Runge-Kutta method, and 4) a good estimate of the truncation error is available out of the computational algorithm.

A more complete and useful method would be a combination of the Runge-Kutta (to start the computation) and the predictor-corrector method (to evaluate succeeding values of the function). However, the complexity of the program involving both methods makes it imperative to use the single-step method. Furthermore, the Runge-Kutta method is comparable in accuracy (often more accurate) than the corresponding order predictor-corrector method although it requires twice as much calculation time. Because of the difficulty of estimating the per step error, the step size may be chosen conservatively (smaller than is actually necessary) to achieve the desired accuracy.

A fourth order Runge-Kutta algorithm was used with the step size varied according to the accuracy required. A derivation of this algorithm may be found in reference 11.

The set of ordinary first-order differential equations is expressed in explicit form

$$\frac{dy}{dt} = f(y,t)$$

The fourth order Runge-Kutta calculation procedure is

$$y_{i+1} = y_i + \frac{h}{6}(k_1 + 2k_2 + 2k_3 + k_4)$$

where $k_1 = f(t_i, y_i)$,

$k_2 = f(t_i + \frac{h}{2}, y_i + \frac{h}{2} k_1)$,

$$k_3 = f(t_i + \frac{h}{2}, y_i + \frac{h}{2} k_2),$$

$$k_4 = f(t_i + h, u_i + hk_3), \text{ and}$$

where h is the step size.

Since the error will not be calculated in the Runge-Kutta method, the differential equations are solved using different step sizes and the behavior of the solution is observed with regard to stability and convergence. To reduce the round-off errors, double precision arithmetic is employed.

IV. CONCLUSIONS

A. Time-Dependent Model Simulations

The preliminary conclusions after performing several extensive computer runs of the time-dependent MHD nozzle-channel-diffuser model are as follows:

1. The onset of chocking sometimes is extremely difficult to predict from running steady-state generator models alone; time-dependent models also must be run.

2. The prediction of the final steady-state to be reached after a transient has occurred is much more difficult for a Faraday-connected generator than for a diagonally connected two-terminal generator.

The first conclusion appears to arise from the difficulty of designing a highly efficient, short diffuser section (especially for the supersonic flow case) for an MHD generator. If a low loss design is incorporated in which flow separation is avoided marginally,the chances of choking are greatly increased. From a practical standpoint this is of no great concern provided unstable flow is confined to the diffuser section. However, this is not always possible. It is hoped that a two-dimensional diffuser analysis code to be obtained shortly from Argonne National Laboratory will ameliorate this problem.

The second conclusion stems from the lack of contraints in the general Faraday generator connection scheme. The two-terminal diagonal connection has the very strong constraint that all electrode current must be equal, whereas this is not true in the Faraday system unless some external control is applied. The general time-dependent code requires detailed knowledge of the gas flow and electrical solutions at some steady-state condition as initial conditions. These conditions are obtained for the problems in question by running a steady-state program iteratively until a steady-state is reached at the desired operating condition. However, in the Faraday design, a power extraction ratio or voltage-current profile with channel length must be assumed to establish a given load factor. In general, this is not unique. Thus, at the end of a transient, the voltage-current vs. length profile may end up different than desired; another run of the steady-state program verifies that the surprising distribution is consistent.

In summary, it can be concluded that extensive transient simulations for a given channel generator design are necessary before a "feel" for the non-steady-state performance is obtained. These will be time-consuming and expensive using presently existing codes.

B. Open-Loop Steam Plant and Air Preheater Performance

Several computer runs were made to determine the response of the steam plant and air preheater to variations in the input parameters, such as combustion gas and air mass flow rates and combustion gas temperature. The state of the gas (pressure and temperature) entering the radiant boiler is a function of the operating conditions of the MHD channel. The variations in the power output of the MHD generator will cause a corresponding variation in the dynamic and thermodynamic parameters of the gas. A reduction in the MHD generator output will cause an increase in the combustion gas temperature leaving the diffuser and vice versa.

1. Case I.

An open-loop transient response was obtained for a +100 K (+ 8.15 percent change in the thermal input to the steam plant and air preheaters) step change in the combustion gas temperature entering the steam plant while the gas, steam, and air flow rates were fixed.

The results are shown in Figures 7 through 10. The variation of the exit steam temperature at the superheater is shown in Figure 7. The cyclic dips (60 sec. cycle) of the superheater steam temperature curve caused by the cyclic variation in the mass flow rate of the gas entering the superheater are negligible. The response to a +100 K change in gas temperature can be approximated by the empirical equation

$$\Delta T_s = .3278\ \Delta T_g\ (1 - e^{-t/112.})$$

where ΔT_g = step change in gas temperature = 100 K, and
ΔT_s = overall change in the steam temperature at the superheater exit.

Thus, the time constant for the high-pressure section of the steam plant is approximately 112 seconds. As shown on Figure 7, the effects of the cycling of the high-temperature air preheater is negligible. The steam pressure drop is approximately 38 psia (Figure 8), due to the increase in steam temperature with the mass flow rate (hence, mass density) remaining constant.

The variation of the gas temperature leaving the economizer (Figure 9) is approximately 1.25 K which has a negligible effect on the downstream steam plant components.

The variation of the air temperature is shown in Figure 10. The average air temperature leaving the regenerative heat exchangers (high-

temperature air preheaters) can be approximated by the empirical equation

$$\Delta T_{air} = .75\ \Delta T_g\ (1 - e^{-t/260})$$

where ΔT_g = step change in gas temperature, and

ΔT_{air} = overall change in the average air temperature at the HTAH exit.

The time constant of the regenerative heat exchanger is approximately 260 seconds. The actual air temperature leaving the HTAH varies by as much as $\pm$ 13 K about the average air temperature. It is shown that with the use of the heat capacitor the air temperature ripple was reduced to less than 1 K and the rise in the air temperature was delayed. For example, at t=260 sec., the average air temperature leaving the HTAH is equal to 47 K while the air temperature leaving the heat capacitor is equal to 6.5 K. Without the heat capacitor the average air temperature reached 47 K after 260 sec and with the heat capacitor, it took 710 seconds to reach the same temperature.

Hence, the heat capacitor not only reduced the temperature ripple but also slowed down the air temperature changes due to variation in the gas temperature entering the preheater.

2. Case II.

An open-loop transient response was also obtained for a +8.15 percent step change in the air, fuel, and seed mass flow rates. This is equivalent to a +8.15 percent change in the thermal input to the MHD system. The MHD generator output was adjusted such that the combustion gas temperature leaving the diffuser remained constant (designed value). The steam mass flow rates were set at the designed values. The results are shown in Figures 11 through 14. After 120 sec, the steam temperature increased by +4.0 K (Figure 11) compared to +18.6 K in Case I. The cyclic dips of the superheater exit steam temperature are larger than in Case I (approximately .25 K). The overall steam pressure drop due to an increase in temperature with the mass density remaining constant is approximately 4.25 psia (see Figure 12). The variation of the air temperature is shown in Figure 13. The heat capacitor was effective in maintaining exit air temperature. After 260 seconds, the change in the average air temperature at the high-temperature air heater exit was 21 K. With the use of the heat capacitor, the change was only 2 K. As indicated in Appendix F, the heat capacitor reduces air temperature ripple from $\pm$13.5 K to less than $\pm$1 K. In addition to this function, the heat capacitor acts as a buffer to changes in combustion gas temperature and combustion gas mass flow rates. The overall time constant of the air preheater system increased from 260 sec without the heat capacitor to approximately 650 sec with the heat capacitor; thus, constant air preheat temperature can be easily maintained. The effect of the step change in gas mass flow rate on the gas temperature at the economizer exit is approximately the same as in Case I (Figure 14).

The results of these simulation studies are:

a. The effect of the temperature variation of the gas leaving the high temperature air preheater (due to heat exchanger cycling) on the steam temperature was negligible.

b. The time constant of the steam plant is approximately 112 seconds.

c. The time constant of the air preheaters is approximately 260 seconds without the heat capacitor and 650 seconds with the heat capacitor.

d. The heat capacitor was effective in reducing the temperature ripple of the air leaving the high temperature air preheater.

e. The effect of the changes in gas temperature, gas mass flow rate, and air flow rates on the air temperature leaving the air preheater can be compensated by the heat capacitor acting as a heat sink or reservoir.

C. The delivery of steady-state and time-dependent CDIF simulation codes to MERDI along with necessary documentation was accomplished as per the required milestones. The codes should provide needed sensitivity data for the determination of control factors for the proposed supersonic channel with conventional magnet scheduled for early 1979 testing. However, the follow-on test of a subsonic channel with a superconducting magnet will not be adequately modeled because of the strong coupling between the channel and the combustor. The combustor as yet has not been dynamically modeled. During the next contract period, the existing Task H3 plug flow combustor model will be used as the input to a first order (neglecting swirl and assuming nearest neighbor interactions only) dynamic model of a pressurized combustor. The sensitivity of the system flow conditions to load transients on the MHD generator then will be studied, particularly as it relates to control and control instrumentation.

The data flow and control simulation model has progressed nearly to completion using Task H3 model III control model[17] as the control algorithm and assuming centralized control of the entire plant. This work, however, is almost obsolete before completion as it is most likely that distributed control using parallel processing microprocessor systems will be used on the ETF system. This will drastically reduce the computer requirements for control of steady-state operation of the ETF system if properly designed. However, it is not clear that the CDIF will be adequately handled by such a system if fast diagnostic transients must be interpreted and controlled so as to minimize damage to experimental components.

MILESTONE CHART

STATUS DATE _____

TASK H1

PROGRESS

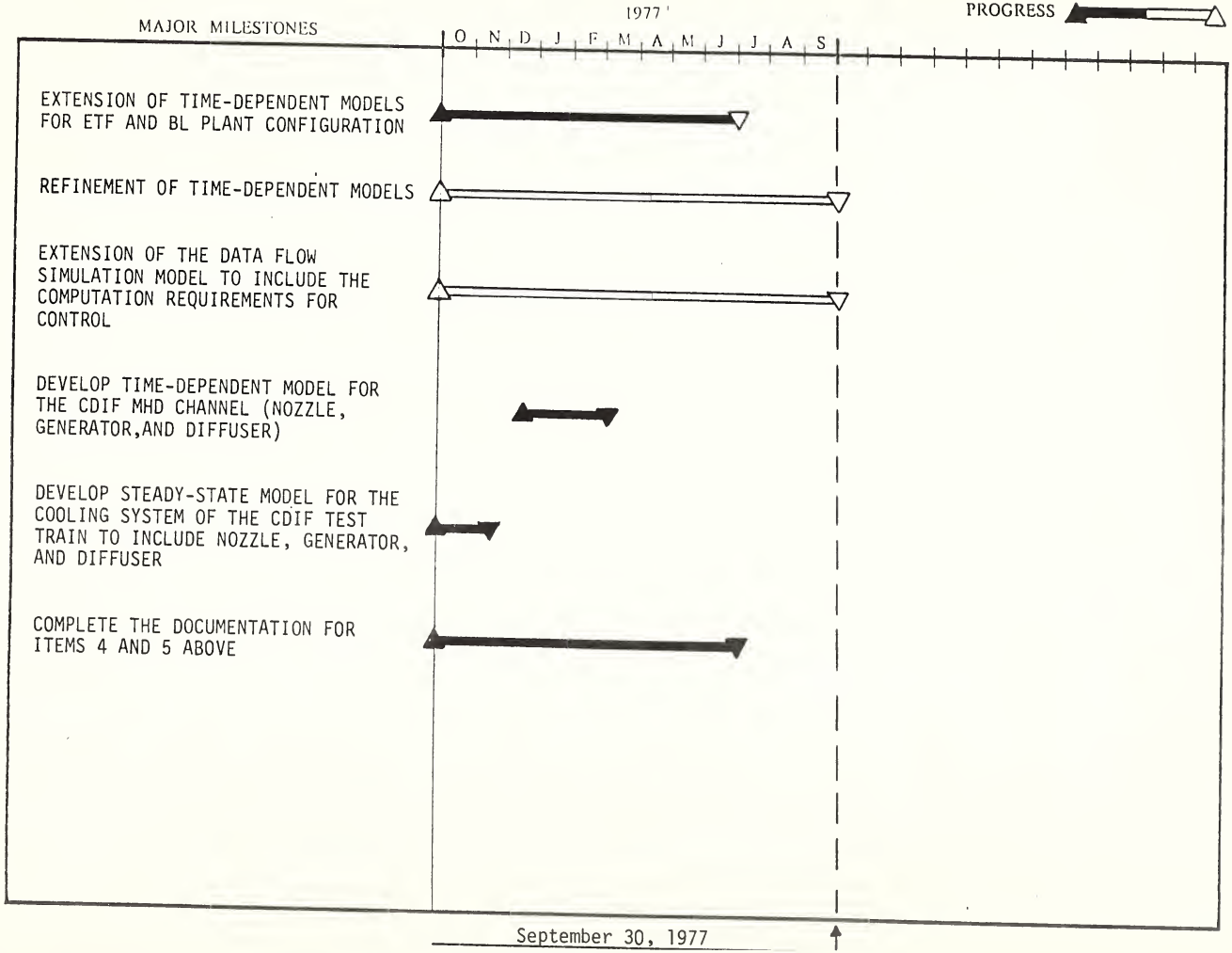
MAJOR MILESTONES
1977
O N D J F M A M J J A S
EXTENSION OF TIME-DEPENDENT MODELS FOR ETF AND BL PLANT CONFIGURATION
REFINEMENT OF TIME-DEPENDENT MODELS
EXTENSION OF THE DATA FLOW SIMULATION MODEL TO INCLUDE THE COMPUTATION REQUIREMENTS FOR CONTROL
DEVELOP TIME-DEPENDENT MODEL FOR THE CDIF MHD CHANNEL (NOZZLE, GENERATOR,AND DIFFUSER)
DEVELOP STEADY-STATE MODEL FOR THE COOLING SYSTEM OF THE CDIF TEST TRAIN TO INCLUDE NOZZLE, GENERATOR, AND DIFFUSER
COMPLETE THE DOCUMENTATION FOR ITEMS 4 AND 5 ABOVE
September 30, 1977

Table I.--Montana Subbituminous Coal Composition

Coal	Montana Subbituminous
Proximate Analysis	
(As Received)	
Moisture	24.3
Volatile	28.6
Fixed Carbon	39.6
Ash	7.5
	100.0
Ultimate Analysis	
(As Received)	
Ash	7.5
Sulfur	0.8
Hydrogen	6.1
Carbon	52.2
Nitrogen	0.8
Oxygen	32.6
Higher Heating Valve	
(As Received)	8944

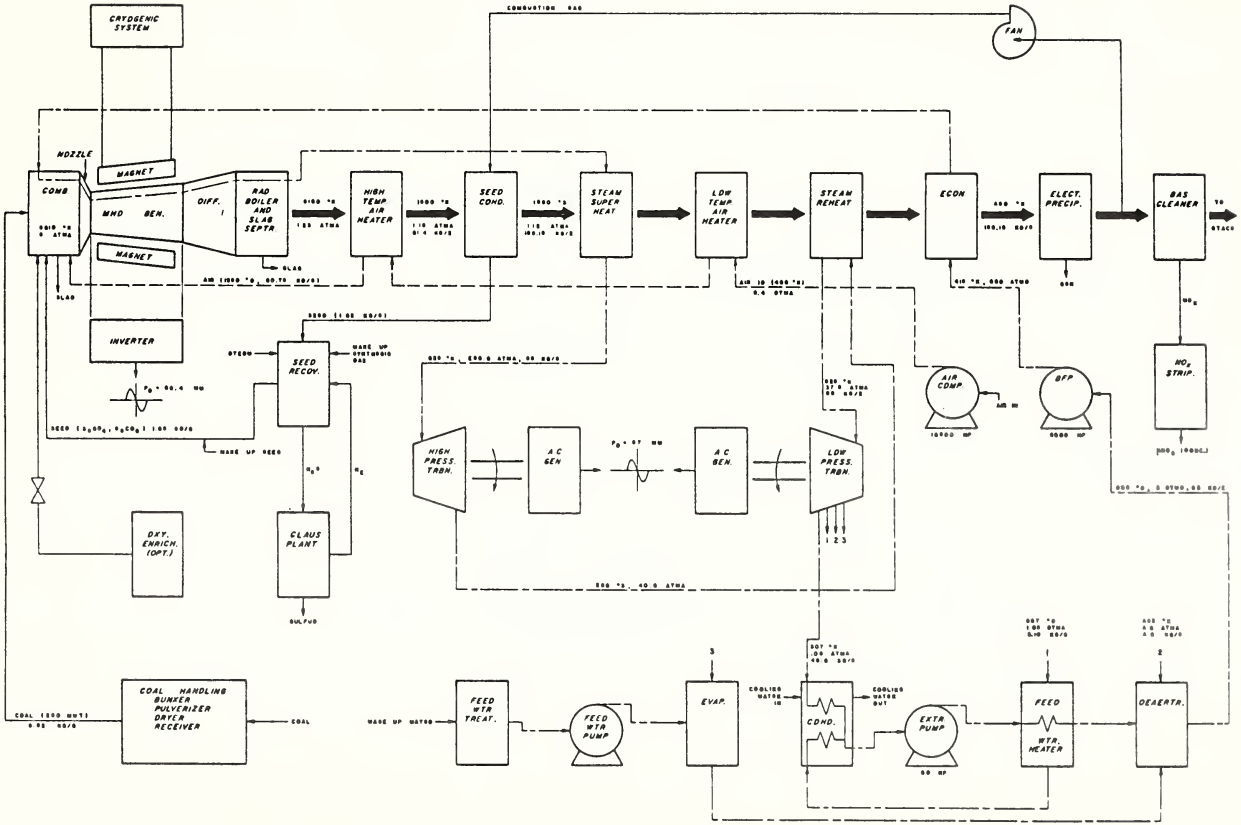

Figure 1.--250 MWT MHD ETF system configuration

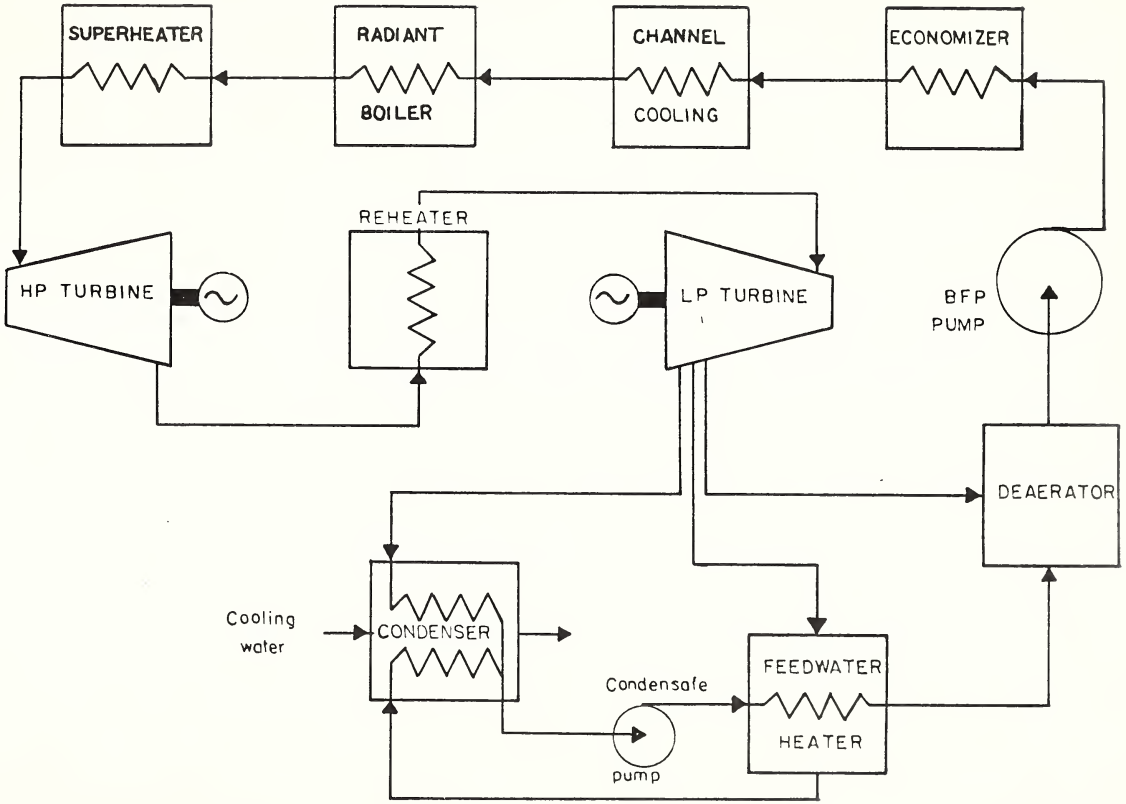

Figure 2.--Steam cycle--250 MWT ETF

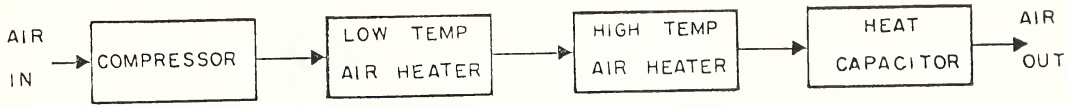

Figure 3.--Air cycle

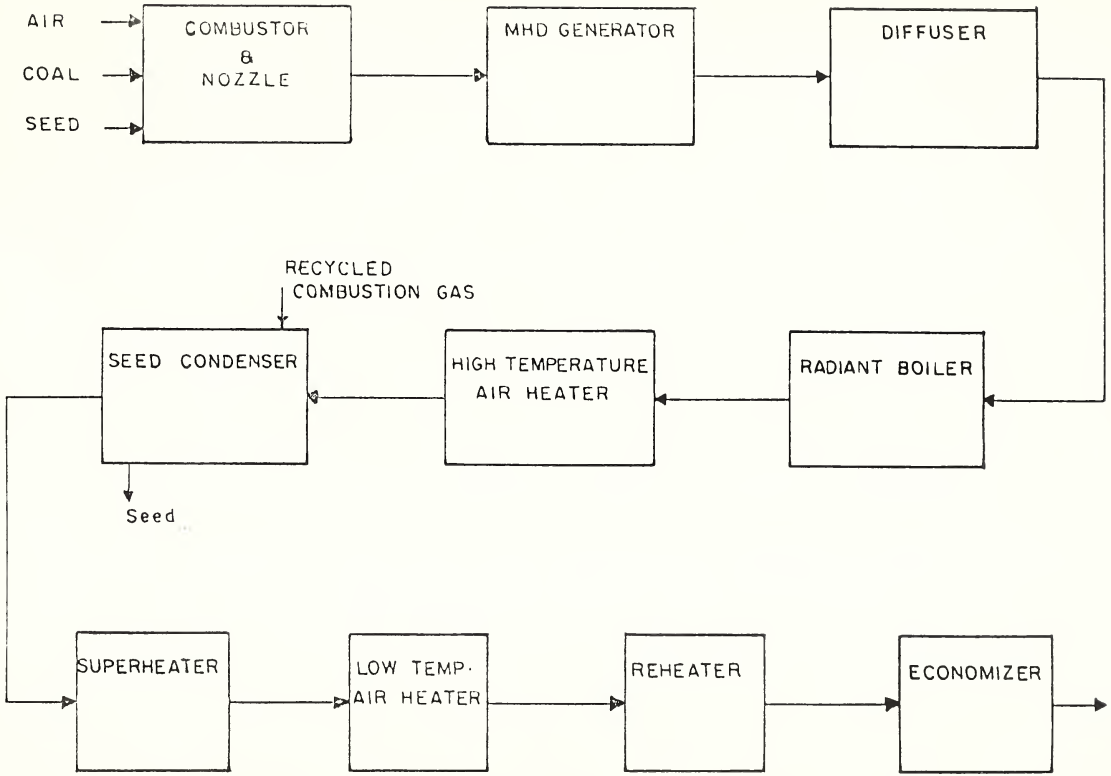

Figure 4.--Gas path--250 MWT ETF

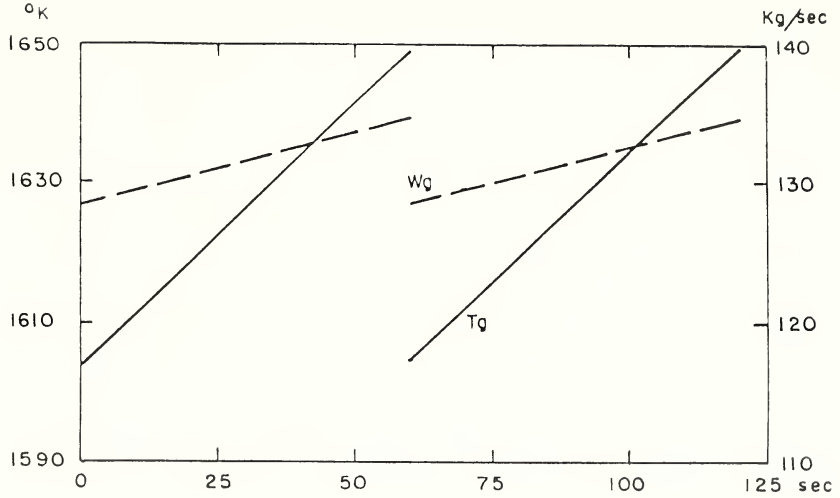

Figure 5. -- Variation of Gas Temperature (T_g) entering the Seed Condenser and Gas Mass Flow Rate (W_g) leaving the Seed Condenser.

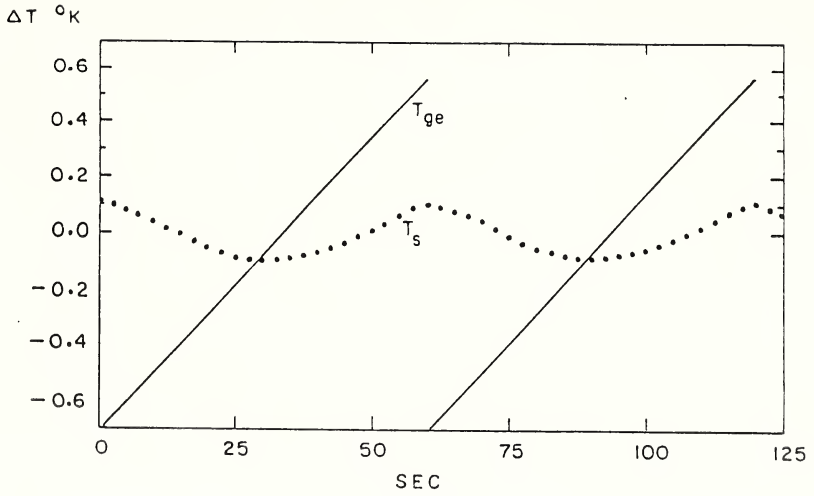

Figure 6. -- Effect of Heat Exchanger Cycling on the Steam Plant: Change in Steam Temperature (T_s) at the Superheater Exit and Gas Temperature (T_{ge}) leaving the economizer.

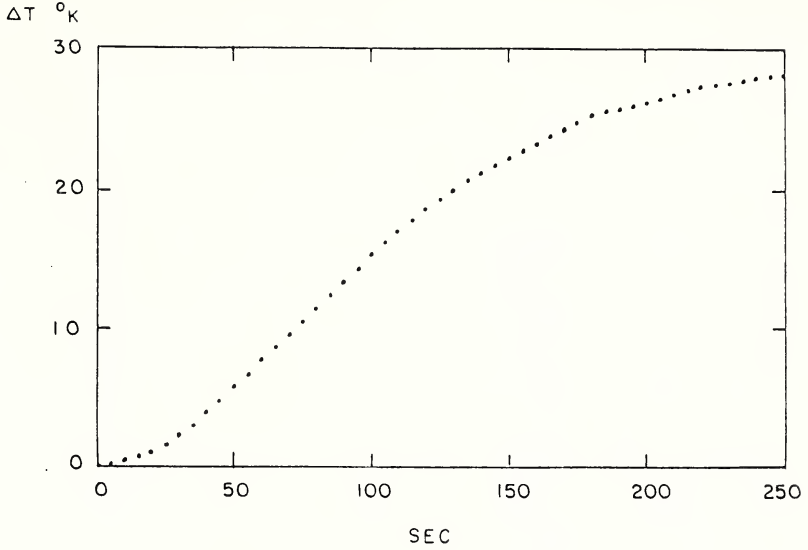

Figure 7.--Open-loop Response of the Steam Plant to a +100 K Step Change in Gas Temperature entering the Radiant Boiler : Change in Steam Temperature at the Superheater exit.

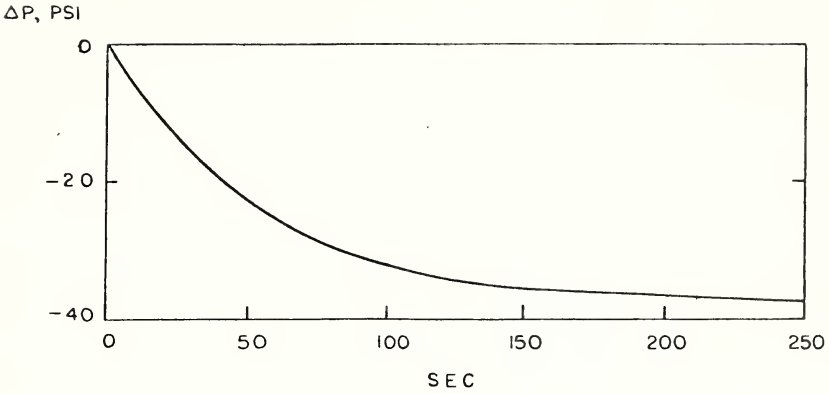

Figure 8. -- Open-loop Response of the Steam Plant to +100 K step change in Gas Temperature entering the Radiant Boiler: Change in Steam Pressure at the Superheater exit.

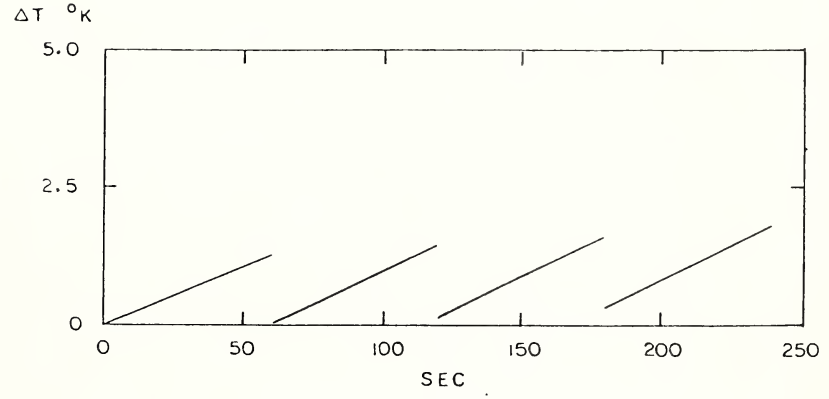

Figure 9. --Open-loop Response of the Steam Plant to a +100 K step change in Gas Temperature entering the Radiant Boiler : Change in Gas Temperature leaving the Economizer.

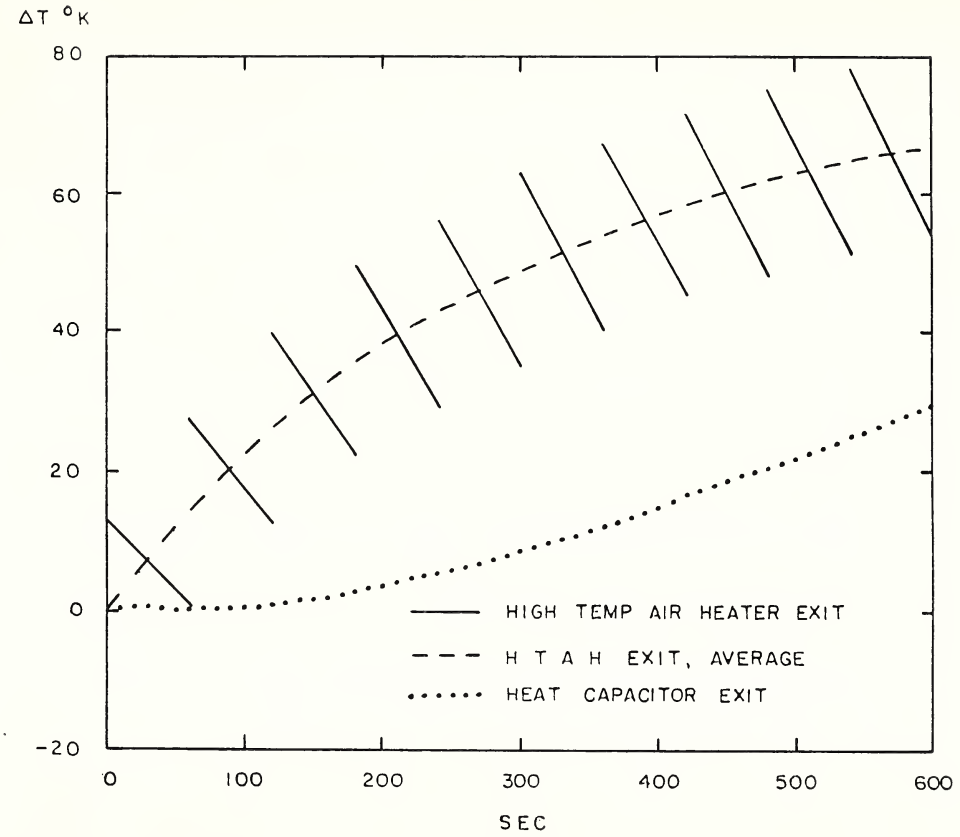

Figure 10. --Open-loop Response of the Air Preheaters to a +100 K step change in Gas Temperature entering the Radiant Boiler: Change in Air Temperature at the HTAH exit and the Heat Capacitor exit.

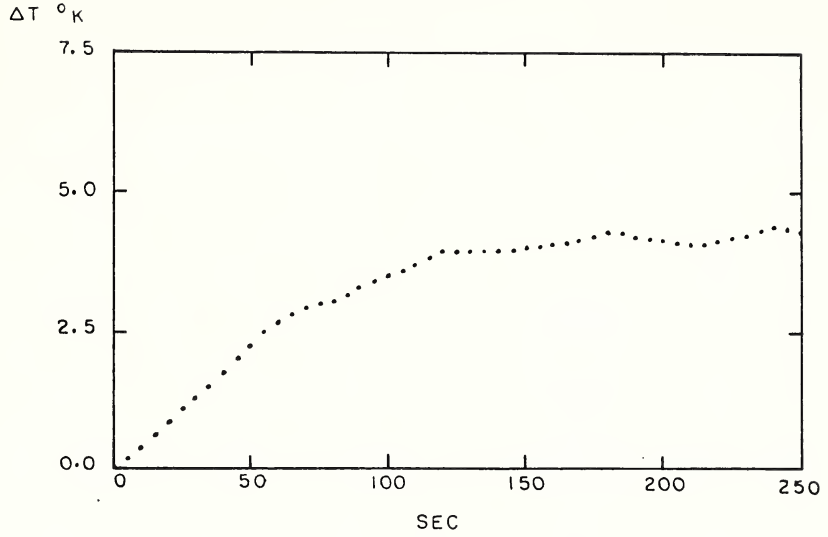

Figure 11. --Open-loop Response of the Steam Plant to a +8.15% step change in the Air, Fuel and Seed Mass Flow Rates: Change in the Steam Temperature at the Superheater exit.

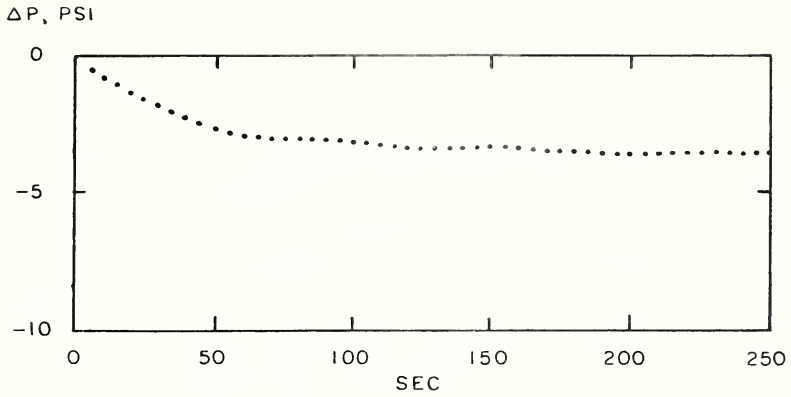

Figure 12.-- Open-loop Response of the Steam Plant to a +8.15% step change in the Air, Fuel and Seed Mass Flow Rates: Change in the Steam Pressure at the Superheater exit.

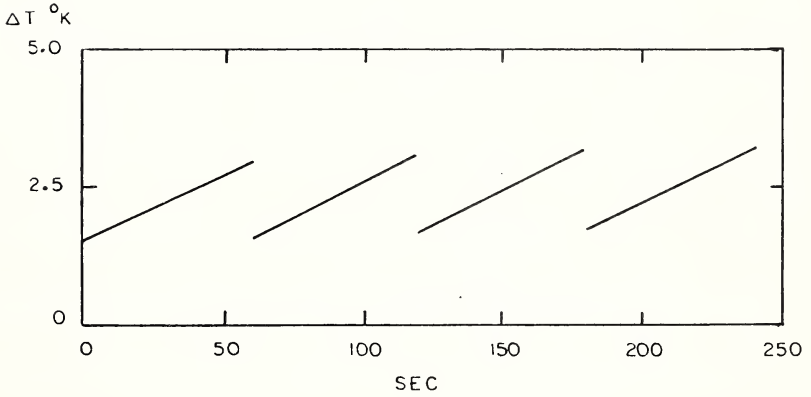

Figure 13. -- Open-loop Response of the Steam Plant to a +8.15% Step change in the Air, Fuel, and Seed Mass Flow Rates: Change in Gas Temperature leaving the Economizer.

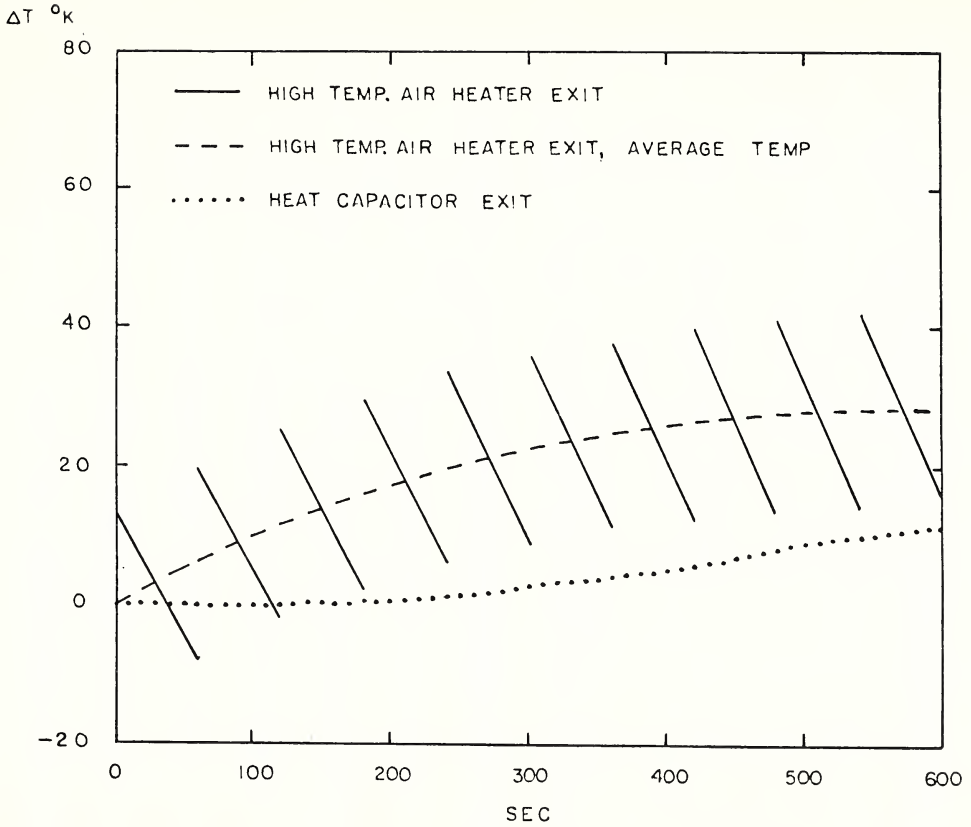

Figure 14. -- Open-loop Response of the Air Preheaters to a +8.15 % step change in the Air, Fuel and Seed Mass Flow Rates: Change in Air Temperature at the HTAH exit and at the Heat Capacitor exit.

REFERENCES

1. Northern Testing Laboratories, Analysis of Rosebud Area B Coal, prepared for Western Energy Company, Job 69-147, August 1974.

2. T. C. Robles, A Simulation Approach to a Magnetohydrodynamic/Steam Electrical Power Generation System, a Ph.D. Thesis, Montana State University, Bozeman, Montana, August 1975.

3. STEAM--Its Generation and Use, Babcock and Wilcox Company, 1972.

4. W. H. McAdams, Heat Transmission, McGraw-Hill Book Company, New York, 1954.

5. A. Shapiro, The Dynamics and Thermodynamics of Compressible Flow, Vol. I, Ronald Press Company, New York, 1953.

6. J. K. Salisbury, Steam Turbines and Their Cycles, John Wiley and Sons, New York, 1950.

7. J. H. Keenan, et al., Steam Tables--Thermodynamic Properties of Water Including Vapor, Liquid and Solid Mass, John Wiley and Sons, New York, 1969.

8. D. A. Pierre and M. J. Lowe, Mathematical Programming Via Augmented Langrangians: An Introduction with Computer Program, Addison-Wesley Publishing Company, 1975.

9. J. Hilsenrath, et al., Tables of Thermodynamics and Transport Properties of Gases, Pergamon Press, New York, 1960.

10. T. C. Reihman, et al., Thermal Analysis Techniques for Regenerative Heat Exchanger Simulation, ASME paper 76-WA/HT-7, July 26, 1976.

11. P. Henrici, Discrete Variable Methods in Ordinary Differential Equations, John Wiley and Sons, 1962.

12. A. Ralston, A First Course in Numerical Analyses, McGraw-Hill Book Company, New York, pp. 93-128, 1965.

13. J. Hilsenrath, et al., Tables of Thermodynamics and Transport Properties of Gases, Pergamon Press, New York, 1960.

14. J. A. Baylis, et al., "Duct Physics," Open Cycle MHD Power Generation, J. B. Heywood and G. J. Womack (eds), Pergamon Press, pp. 393-462, 1969.

15. T. C. Robles and R. M. Johnson, "A Heat Capacitor for MHD Power Generation System," 16th Symposium on Engineering Aspects of MHD, University of Pittsburgh, Pittsburgh, Pennsylvania, May 16-18, 1977.

16. T. C. Reihman, H. W. Townes, and C. J. Mozer, Thermal Analysis Techniques for Regenerative Heat Exchanger Simulation, ASME paper 76-WA/HT-7, July 26, 1976.

17. J. Aspnes and D. Pierre, "Dynamic Modeling and Control of MHD/Steam Electrical Power Generating Plants," 16th Symposium on Engineering Aspects of MHD, Pittsburg, PA, pp. I1.1-1.7, May 1977.

18. H. W. Kwan and J. H. Anderson, "A Mathematical Model of a 200 MW Boiler," International Journal of Control, Volume 12, pp. 977-998, June 1970.

APPENDIX A

THERMODYNAMIC AND ELECTRICAL PROPERTIES OF THE WORKING FLUID

The calculation of the thermodynamic and electrical properties of the working fluid (coal, air and alkali seed) was based on the chemical equilibrium equation for carbon, oxygen, nitrogen and hydrogen mixtures.[14] The units used are in International Units (SI).

The specific enthalpy of the combustion gas is given by:

$$h(T,p) = \left[\frac{4.187 \times 10^3}{(8\xi + 4)\phi + 32 + 28\psi}\right] \{T[2 + 2(7 - 4\xi)\phi + 7\psi + 5Y + 3U] + \left[\frac{2\,T_v}{e^{T_v/T} - 1}\right] [4 + (2 - 3\xi)\phi + \psi - 3Y - U] + (117 + 30\xi)\cdot(Y + \phi - 1) \times 10^3) + 135\cdot\xi\cdot U \times 10^3\} \quad ; \text{for } \phi \geq 1$$

$$h(T,p) = \left[\frac{4.187 \times 10^3}{(8\xi + 4)\phi + 32 + 28\psi}\right] \{T[7 + (9 - 8\xi)\phi + 7\psi + 5Y + 3U] + \left[\frac{2\,T_v}{e^{T_v/T} - 1}\right] [1 + (5 - 3\xi)\phi + \psi - 3Y - U] + (117 + 30\xi)\,(Y + \phi - 1) \times 10^3 + 135\cdot\xi\cdot U \times 10^3\} \; ; \text{for } \phi < 1$$

where

$\xi = 4\delta/(1 + 4\delta)$

$T_v = (3000 - 2000\xi + 300\psi)/(1 - .5\xi + .09\psi)$

δ = carbon to hydrogen ratio of the fuel

ψ = nitrogen to oxygen mole ratio of the combustion gas

ϕ = fuel mixture ratio (actual fuel to oxygen ratio/ stoichiometric fuel to oxygen ratio)

The extra number of molecules due to the dissociation of the triatomic molecules into diatomic molecules is

$$Y = \frac{X[1 + (1 - \phi)/X + .36([1 - \phi]/X)^2]}{[1 + .36(1 - \phi)/X]} \quad ; \text{ for } \phi < 1$$

$$= \frac{X}{[1 + .64(\phi - 1)/X + .3([\phi - 1]/X)^2} \quad ; \text{ for } \phi \geq 1$$

The extra number of molecules due to the dissociation of the diatomic molecules into monatomic molecules is

$$U = \frac{(1 - 2 \cdot \xi \cdot X)\ (2 - \xi + \psi)}{[4 \cdot X \cdot K_1 \cdot K_2 \cdot p\ (.985 \times 10^{-5})]}$$

where $X = Y$ for $\phi = 1$

$$X = \frac{A[3(2 - \xi + \psi + A\ \xi(5 - 2\xi + 2\psi)]}{3(1 + 2 \cdot A \cdot \xi)\ (2 - \xi + \psi) + 2 \cdot A^2 \cdot \xi^2 (5 - 2\xi + 2\psi)} \ ;$$

for $\phi \lesssim 1$

and $$A = \left[\frac{2 - \xi + \psi}{4 \cdot K_1^2 \cdot p(.987 \times 10^{-5})}\right]^{1/3}$$

$$K_1 = .39 \times 10^{-4} e^{(-.3\xi + 34000/T)}$$

$$K_2 = .14 \times 10^{-3} e^{(1.3\xi + 29000/T)}$$

The molecular weight of the combustion gas is

$$M = \frac{(8\xi + 4)\phi + 32 + 28\psi}{1 + (1 - \xi)\phi + \psi + Y + U} \quad ; \text{ for } \phi < 1$$

$$= \frac{(8\xi + 4)\phi + 32 + 28\psi}{(2 - \xi)\phi + \psi + Y + U} \quad ; \text{ for } \phi \geq 1$$

The equation of state is

$$p = \rho T/(M \times .120268 \times 10^{-3})$$

where p = pressure of the combustion gas, Newtons/sq m
T = temperature of the combustion gas, °Kelvin
ρ = mass density of the combustion gas, Kg/cu m

The electrical properties of the combustion gas are as follows:

Electron density --

$$n_e = \frac{4.22 \times 10^{23}[Q(p \times .987 \times 10^{-5})\, T^{.5}\, e^{-50400/T}]^{.5}}{1 + 2 \times 10^{-3}(e^{16800/50400})(Y/X)^{1/3}\, B^{2/3}}$$

where $B = (1 - \xi)(.987 \times 10^{-5} p)/(2 - \xi + \psi)$

Electron mobility --

$$\mu = T/\{[p \times .987 \times 10^{-5}][(4030 - 3110\xi)(2.72 - .457\psi) + (.15 + .3\xi)(.66\psi - 1.48)T + (1050 - 120\psi)Q + (.05\psi - .13)T \cdot Q + (1.1 + 3.7\psi)(n_e \times 10^{-19})]\}$$

Electrical conductivity --

$$\sigma = 1.6 \times 10^{-19} n_e \mu$$

APPENDIX B

THERMODYNAMIC PROPERTIES OF COMPRESSED STEAM AND WATER

The thermodynamic properties of compressed steam and water were obtained from reference 7. The mass density and the temperature are expressed as third order functions of the specific enthalpy and the pressure. The non-linear programming least squares method developed in reference 8 was used to obtain the desired polynomial expression for each region of interest with errors limited to less than .1%.

B.1. Economizer: $340\ K < T < 650\ K$

$3200\ psia < p < 4400\ psia$

$$T = 228.01 + .220252 \times 10^{-3}h + .238077 \times 10^{-10}h^2 - .299456 \times 10^{-16}h^3 + .538288 \times 10^{-5}p - .217592 \times 10^{-12}p^2 + .302715 \times 10^{-20}p^3 + .513092 \times 10^{-12}hp + .113679 \times 10^{-17}ph^2 - .391311 \times 10^{-19}p^2h$$

$$\rho = 1178.17 - .138382 \times 10^{-3}h - .884307 \times 10^{-10}h^2 - .415288 \times 10^{-16}h^3 - .161432 \times 10^{-4}p + .518101 \times 10^{-12}p^2 - .416639 \times 10^{-20}p^3 + .429589 \times 10^{-11}ph + .358964 \times 10^{-17}ph^2 - .184215 \times 10^{-18}p^2h$$

B.2. Radiant Boiler and Superheater: $600\ K < T < 850\ K$

$3200\ psia < p < 4400\ psia$

$$T = 1274.01 - .162680 \times 10^{-3}h - .180414 \times 10^{-9}h^2 + .523857 \times 10^{-16}h^3 - .467245 \times 10^{-4}p + .295327 \times 10^{-12}p^2 + .278532 \times 10^{-21}p^3 + .318630 \times 10^{-10}ph - .455448 \times 10^{-17}ph^2 - .122638 \times 10^{-18}p^2h$$

$$\rho = 1744.48 - .187847 \times 10^{-2}h + .569053 \times 10^{-9}h^2 - .464629 \times 10^{-16}h^3 + .653849 \times 10^{-4}p - .124399 \times 10^{-11}p^2 + .351978 \times 10^{-20}p^3 - .143181 \times 10^{-10}ph - .15339 \times 10^{-17}ph^2 + .33848 \times 10^{-18}p^2h$$

B.3. Reheater: $520\ K < T < 850\ K$

$400\ psia < p < 700\ psia$

$$T = -788.527 + .369822 \times 10^{-3}h + .375898 \times 10^{-10}h^2 - .447971 \times 10^{-17}h^3 + .112073 \times 10^{-3}p - .205449 \times 10^{-12}p^2 + .259426 \times 10^{-19}p^3 - .53489 \times 10^{-10}ph + .671504 \times 10^{-17}ph^2 - .737148 \times 10^{-19}p^2h$$

$$\rho = -10.578 + .125263 \times 10^{-5}h + .201967 \times 10^{-11}h^2 - .42656 \times 10^{-18}h^3 + .353412 \times 10^{-4}p + .583077 \times 10^{-13}p^2 - .395127 \times 10^{-20}p^3 - .179022 \times 10^{-10}ph + .220971 \times 10^{-17}ph^2 - .252869 \times 10^{-20}p^2h$$

where h - specific enthalpy, Joules/Kg

p - pressure, Newtons/m^2

T - temperature, °Kelvin

ρ - mass density, Kg/m^3

APPENDIX C

THERMODYNAMIC PROPERTIES OF AIR

The properties of air are represented by third order polynomial functions of pressure and enthalpy derived from reference 13 using the least square, non-linear program developed by Pierre and Lowe.[8]

C.1. Low Temperature Air Heater: $400\ K < T < 1250\ K$

$4\ atm < p < 10\ atm$

$$T = -17.3539 + .109126 \times 10^{-2}h - .134403 \times 10^{-9}h^2 + .202381 \times 10^{-16}h^3 + .16104 \times 10^{-5}p + .248907 \times 10^{-11}p^2 - .139433 \times 10^{-17}p^3 - .71253 \times 10^{-11}ph + .255809 \times 10^{-7}ph^2 + .799441 \times 10^{-18}p^2h$$

$$\rho = 2.72957 - .111822 \times 10^{-4}h + .136031 \times 10^{-10}h^2 - .517174 \times 10^{-17}h^3 + .45604 \times 10^{-4}p - .559536 \times 10^{-12}p^2 + .658533 \times 10^{-19}p^3 - .174845 \times 10^{-10}ph + .681821 \times 10^{-17}ph^2 + .136729 \times 10^{-18}p^2h$$

C.2. High Temperature Air Heater: $1000\ K < T < 1950\ K$

$4\ atm < p < 10\ atm$

$$T = 17.004 + .100581 \times 10^{-2}h - .699234 \times 10^{-10}h^2 + .437944 \times 10^{-17}h^3 + .126337 \times 10^{-4}p - .156503 \times 10^{-10}p^2 + .76645 \times 10^{-17}p^3 - .422634 \times 10^{-11}ph + .138612 \times 10^{-17}ph^2 - .139458 \times 10^{-22}p^2h$$

$$\rho = 1.87599 - .297046 \times 10^{-5}h + .187897 \times 10^{-11}h^2 - .384033 \times 10^{-18}h^3 + .516941 \times 10^{-5}p + .261263 \times 10^{-11}p^2 - .123399 \times 10^{-17}p^3 - .423679 \times 10^{-11}ph + .8743 \times 10^{-18}ph^2 + .285383 \times 10^{-20}p^2h$$

where h = air specific enthalpy, Joules/Kg

p = air pressure, Newton/sq. m.

T = air temperature, °Kelvin

ρ = air mass density, Kg/m^3

APPENDIX D

SPECIFIC HEAT OF THE COMBUSTION GAS

The average specific heat of the combustion gas in the steam plant and the air preheaters may be expressed as a polynomial function of the temperature at the inlet of the specified section. These equations were derived from the gas properties calculation shown in Appendix A. Since the gas pressure difference between the inlet and outlet of the steam plant is small, the effect of the pressure variation on the specific heat is negligible. The specific heat (constant pressure) equations are

D.1. Economizer and Reheater Sections: $400\ K < T < 1180\ K$

$$CGER = 912.15 + .1873794T + .37636759 \times 10^{-3}T^2 - .226393993 \times 10^{-6}T^3$$

D.2. Low Temperature Air Heater, Superheater, and Seed Condenser: $800\ K < T < 1780\ K$

$$CGLS = 277.41 + 2.10303376T - .153560266 \times 10^{-2}T^2 + .405417324 \times 10^{-6}T^3$$

D.3. High Temperature Air Heater: $1400\ K < T < 2300\ K$

$$CGAH = -2598.27 + 7.833455T - .5319947 \times 10^{-2}T^2 + .1233431 \times 10^{-5}T^3$$

D.4. Radiant Boiler: $2000\ K < T < 2480\ K$

$$CGRB = 16352.6 - 18.934569T + .72720216 \times 10^{-2}T^2 - .73902348 \times 10^{-6}T^3$$

where CGER = specific heat, Joules/Kg-°K

T = temperature, °Kelvin

APPENDIX E

250 MW_t ETF DESIGN PARAMETERS

A. Design Parameters

1. Combustor (2nd Stage)

Diameter	2.022 m I.D.
Length	1.5 m
Mass Flow Rates (Equivalence ratio = 1.0; n_2/O_2 ratio = 3.76)	
Coal (Montana subbituminous)	9.52 kg/sec
Air	80.76 kg/sec
Seed (K_2SO_4 + K_2CO_3)	1.92 kg/sec
H.H.V. of fuel (5% moisture)	26,248,900 Joules/kg
Total heat input	250 MW
Air preheat temperature	1920 °K
Combustion temperature	2810 °K
Combustion pressure	5.0 atma
Wall temperature	1600 °K
Heat loss	16.8 MW

2. Nozzle

Gas entry/exit	4.0861/.249 m^2
Length	.57 m
Gas temperature (in/out)	2810/2688 °K
Gas velocity (in/out)	35/768 m/sec
Gas mass flow rate	91.4 kg/sec
Average surface temperature	1800 °K
Heat flux	114./1056 Kw/m^2
Total heat loss	1.41 MW

3. MHD Generator

Gas entry/exit	.249/1.0446 m^2
Length	8. m
Electrode pitch	.01 m
No. of electrodes	800 pairs
Gas temperature (in/out)	2688/2287 °K
Gas velocity (in/out)	768/681 m/sec
Gas pressure (in/out)	3.62/.81 atma
Wall temperature	1600 °K
Heat flux	1056./202. KW/m^2
Total heat transfer	15.48 MW

Generator type - Faraday	
Inverter voltages	356/2478 volts
Current density	.26-1.06 amp/cm^2
Electric field, transverse	914-3617 volts/m
Electric field, axial	77-3220 volts/meter
Electrode current	14-55 amps
Magnetic field, maximum	6 Tesla
Electrical conductivity	11.9-4.9 mho/m
Hall parameter	.33-4.46
Voltage drop, electrodes and boundary layers	100 volts per electrode pair
Load factor	.79-.81
Enthalpy extraction	17.2 %
Power output	73.3 MW

4. Diffuser

Gas entry/exit	1.045/9.745 m^2
Length	12 m @ 5° wall angle
Gas temperature (in/out)	2287/2330. °K
Gas velocity (in/out)	681./52. m/sec
Gas pressure (in/out)	.81/1.16 atma
Surface temperature, average	1600 °K
Heat flux	202-26 Kw/m^2
Total heat loss	15.45 MW

5. Radiant Boiler

Tube enclosure	3.75x3.75
Tube size	3.8 cm o.d. x 6.35 mm thick
Tube pitch (touching but not welded)	3.8 cm
Total exposed tube surface	106 m^2
Thermal duty	30.2 MW
Gas temperature (in/out)	2330/2180 °K
Gas pressure (in/out)	1.16/1.16 atm
Gas velocity, average	35 m/sec
Gas mass flow rate	91.4 Kg/sec
Water temperature (in/out)	680/752 °K
Water pressure (in/out)	276/273 atma
Water velocity, average	1.25 m/sec
Water flow	55 Kg/sec
Average tube metal temperature	790 °K
Average heat flux to exposed surface	342 Kw/m^2
Heat loss	.15 Mw

6. High Temperature Air Heater
   Type - Regenerator with fixed bed of refractory cored bricks

Flow hole size	.019 m
Bed diameter	2.3 m
Bed length	3.8 m
No. of blowdown heat exchangers	4
No. of reheat heat exchangers	4
Soaking heat exchangers	2
Switching time	60 sec
Blowdown time	240 sec
Reheat time	240 sec

Reheat:

Temperature, in	2180 °K
Temperature, out	1616-1660 °K
Pressure (in/out)	1.16/1.13 atm
Velocity, average	60 m/sec
Flow rate	91.4 Kg/sec

Blowdown:

Temperature, in	1100 °K
Temperature, out	1933-1907 °K
Pressure (in/out)	5.12/5.10 atma
Velocity, average	6.3 m/sec
Flow rate	80.76 Kg/sec

7. Heat Capacitor
   Type - Regenerator with fixed bed of refractory cored bricks

Flow hole	.0127 m
Bed diameter	3.38 m
Bed length	3.049 m
No. of units	1
Air temperature, in	1933-1907 °K
Air temperature, out	1920.65-1919.95 °K
Air pressure (in/out)	5.10/5.08 atm
Air velocity, average	20 m/sec

8. Seed Condenser

Gas temperature, in	1616-1660 °K
Gas temperature, out	1350 °K
Gas pressure (in/out)	1.13/1.10 atma
Gas flow, in	91.4 Kg/sec
Recycled flue gas, in	39.2-44.9 Kg/sec
Seed flow, out	1.82 Kg/sec
Total gas flow out	128.8-134.5 Kg/sec

9. Superheater

Thermal duty	16.91 MW

Steam side (convection banks)

Tube size	3.8 cm o.d. x 6.35 mm wall
Tubes in parallel	36
Banks in series	14
Surface area	332 m^2
Flow rate	55 Kg/sec
Pressure (in/out)	273/238.6 atma
Tube wall temperature, average	810 °K
Temperature (in/out)	762/822 °K

Steam side (wall tubes)

Tube size	3.8 cm o.d. x 6.35 mm wall
Surface area	40 m^2
Temperature (in/out)	752/762 °K

Shellside (gas)

Temperature (in/out)	1350/1250 °K
Pressure (in/out)	1.10/1.09 atma
Heat flux, average	45.5 Kw/m^2
Heat loss	80 KW

10. Low Temperature Air Heater
Type - Shell and tube

Thermal duty	53.4 MW
Tube size	3.8 cm o.d. x 3.25 wall
Surface area	7200 m^2

Tube side (air)

Flow rate	80.76 Kg/sec
Temperature (in/out)	498/1100 °K
Pressure (in/out)	5.34/5.12 atma
Velocity, average	10 m/sec
Tube surface temperature, average	950 °K

Shell side (gas)

Temperature (in/out)	1250/932 °K
Pressure (in/out)	1.01/1.08 atma
Velocity (average	20 m/sec
Heat flux	7.4 Kw/m^2
Heat loss	.26 MW

11. Reheater

Type - shell and tube
Thermal duty - 36.9 MW

Tube size	5.08 cm o.d. 6.35 mm wall
Tubes in parallel	144
Banks in series	15
Surface area	4358 m^2

Tube side (steam)

Flow rate	55 Kg/sec
Temperature (in/out)	537/822 °K
Pressure (in/out)	40.9/37.5 atma
Velocity, average	20 m/sec
Tube surface temperature, average	700 °K

Shell side (gas)

Temperature (in/out)	932/698 °K
Pressure (in/out)	1.08/1.07 atma
Velocity, average	25 m/sec
Heat flux	8.5 Kw/m^2
Heat loss	.18 MW

12. Economizer

Thermal duty - 37.1 MW

Tube size	5.08 cm o.d. x 6.35 mm wall
Tubes in parallel	120
Banks in series	95
Surface area	16558 m^2

Tube side (water)

Temperature (in/out)	412/564 °K
Pressure (in/out)	286/283 atma
Velocity, average	.4 m/sec
Tube surface temperature	470 °K

Shell side (gas)

Temperature (in/out)	698/442 °K
Pressure (in/out)	1.07/1.06 atma
Velocity, average	10 m/sec
Heat flux	2.24 Kw/m^2
Heat loss	.18 MW

13. Deaerator

Thermal duty	9.4 MW
Water storage	13500 Kg

Water

Flow rate (in/out)	51/55 Kg/sec
Temperature (in/out)	366.8/409 °K
Pressure	3 atma

Steam

Flow rate	4 Kg/sec
Temperature	422 °K
Pressure	4.6 atma

Dimension

Shell diameter	2.64 m ID
Shell height	6.3 m

14. Feedwater Heater

Thermal duty	13 MW

Tube side (water)

Tube size	1.9 cm o.d. #16BWG
Tube pitch	2.38 cm triangular
Temperature	307.2/366.8 °K
Pressure	3.2/3 atma
Flow rate	51 Kg/sec

Shell side (steam)

Temperature	397/316 °K
Pressure	1.02/.087 atma
Flow rate	5.1 Kg/sec

15. Condenser - (Two-pass)

Shell side (cooling water)

Flow rate	2600 Kg/sec
Temperature rise	8.6 °K

Tube side (steam)

Tube type	admiralty metal tube
Tube size	7/8" o.d., #18BWG
Flow rate	51 Kg/sec
Temperature	307 °K
Pressure	.05 atma

16. Steam Turbine

High pressure

Pressure	238.6/40.9 atma
Temperature	822/550 °K
Flow rate	55 Kg/sec
Power out	20.9 MW

Low pressure

Pressure	37.5/.05 atma
Temperature	822/307 °K
Flow rate	55 Kg/sec
Power out	45.68 MW

17. Auxiliary Equipment

Condenser pump	50 hp
Boiler feed pump	3000 hp
Air compressor	19500 hp
Flue gas fan (to recycle flue gas)	825 hp

B. Steam Plant and Air Heater Design

The steam plant and air heaters were designed for a 250 MW thermal input to the MHD combustor. The thermal duty of each steam plant section was chosen such that each section is located at the temperature zone where the gas temperature is high enough to provide good heat transfer from the gas to the steam yet not so high as to result in excessive tube temperature.

The heat transfer equation for heat flow is [3].

$$q = US\Delta T \qquad (E.1)$$

where q = rate of heat flow, Joules/sec

U = overall combined conductance, Joules/sq m, sec, °K

S = heat transfer surface area, sq m.

ΔT = temperature difference causing heat flow, °K

The overall combined conductance (U) includes fluid convection conductance and intertube radiation conductance. The equation (E.1) may be expanded as follows, to show the quantitative relationship in the transfer of heat from a heating to a cooling fluid:

$$q = US\Delta T_m = wc(T_1 - T_2) = w'c'(T_2' - T_1') = w'(h_2' - h_1') \qquad (E.2)$$

where T_m = mean temperature difference between the heating and the cooling fluid (see chapter IV of reference [3]).

w = mass flow rate of hotter fluid, Kg/sec

c = mean specific heat of hotter fluid, Joules/Kg, °K (normally c_p)

c_p = specific heat of the fluid at constant pressure

T_1, T_2 = temperature of hotter fluid entering and leaving the heat transfer surface, °K

w' = mass flow rate of colder fluid, Kg/sec

c' = specific heat of colder fluid

T_1', T_2' = temperature of colder fluid entering and leaving the heat transfer surface

h_1', h_2' = specific enthalpy of the colder fluid entering and leaving the heat transfer surface, Joules/Kg

The inlet and exit temperature (of gas and steam) in each section were calculated using Equation E.2. The gas temperature leaving the last section of the steam plant (economizer) was assumed to be 420°K which is high enough to prevent condensation of sulfuric acid on the economizer tube wall [3].

APPENDIX F

HEAT CAPACITOR FOR MHD AIR PREHEATER SYSTEM[15]

I. INTRODUCTION

The cycling of the high temperature heat exchangers produces a variation in the air exit temperature similar to a sawtooth waveform. The temperature is maximum at the start of the cycle and minimum at the end of the cycle. This air temperature variation produces a corresponding temperature variation at the combustor. It is desirable (from the standpoint of operational stability) to have a small temperature variation in the combustion temperature to avoid large changes in the electrical conductivity of the combustion gas flowing through the MHD channel.

One method in obtaining lower temperature ripple is the use of a large number of phased array heat exchangers. Another method is to use a heat capacitor or heat reservoir to reduce the temperature ripple.

II. HEAT CAPACITOR LUMPED-MASS MODEL

The heat capacitor, a matrix made up of cored bricks, stores heat energy during the part of the cycle when the air temperature is greater than the brick temperature and discharges the heat energy to the air when the air temperature is lower than the brick temperature. To provide a better storage capability and have a more compact unit, bricks with smaller flow holes may be used. With the heat capacitor it is possible to limit the air temperature variation to less than 1 K by the proper choice of heat capacitor configuration (flow hole size, pitch to diameter ratio, bed diameter and bed length) while at the same time reducing the overall system cost.

The design and analysis of the heat capacitor was based on the computer simulation codes for a lumped-mass model of a regenerator presented in reference 16. The relationship between the convective surface temperature and the average ceramic temperature in the lumped-mass model was obtained from the steady-state radial temperature distribution in the ceramic (a first order approximation to the actual transverse temperature distribution in the ceramic). In particular, three assumptions are made. First, the transient energy storage in the fluid is negligible with respect to the change in the convection energy transport in the axial direction. Second, the axial conduction in the fluid is negligible with respect to the change in the convection transport. These assumptions are valid for turbulent flow conditions typical in MHD systems. The third assumption is made to reduce the computational complexity of the problem (converts the multi-dimensional problem into a series of one-dimensional problems). This assumption is justified if a small time increment is used.

The finite-difference equation for the ceramic temperature (TC) based on the above assumptions is

$$TC(J,2) = \frac{\alpha_1}{2(1A\alpha_4)}[TG(J) + TG(J+1)] + TC(J,1)$$

$$[1 - \frac{\alpha_1}{1+\alpha_4} - 2\alpha_3] + \alpha_3[TC(J-1,1) + TC(J+1,1)]$$

α_1 is associated with the heat transfer between the gas and the ceramic during the time interval; α_3 characterizes the axial conduction in the ceramic and α_4 is used to correct for the difference between the average ceramic temperature and the temperature at the convective surface. The finite difference equation for determining the gas temperature (TG) variation in the axial direction is

$$TG(J+1) = TG(J)\frac{[1 - \frac{\alpha_2}{2(1+\alpha_4)}]}{[1 + \frac{\alpha_2}{2(1+\alpha_4)}]} + TC(J,1)\frac{[\frac{\alpha_2}{1+\alpha_4}]}{[1 + \frac{\alpha_2}{2(1+\alpha_4)}]}$$

III. HIGH TEMPERATURE AIR PREHEATER FOR THE 250 MW_t ETF

The air preheater requirements for the 250 MW_t ETF are:

Reheat inlet temperature	2180 K
Reheat inlet pressure	124630 Pa
Reheat mass flow rate	91.4 Kg/sec
Blowdown inlet temperature	1100 K
Blowdown exit temperature	1920 K
Blowdown inlet pressure	526910 Pa
Blowdown mass flow rate	80.76 Kg/sec

The high temperature air preheater was designed using the lumped-mass computer simulation codes presented in reference 4. The block diagram of the high temperature air preheater is shown in Figure F-1. The design parameters of the system selected are shown in Table I. The operating characteristics of the heat exchangers are shown in Figures F-2 to F-4. It is shown that the air ripple temperature (Figure F-4) is approximately $\pm$ 13.25 K at the exit of the preheater.

IV. DISCUSSION

The operation of the heat capacitor was simulated using the lumped-mass model described in section II. The effectiveness of the heat capacitor in reducing temperature ripple is determined by the proper choice of design variables such as flow hole size, pitch to diameter ratio, bed diameter, and bed length. The flow hole size can be made as small as possible in order to have a compact unit. The pitch to diameter ratio is influenced by the allowable transverse temperature gradients, fabrication limitations and compressive load. The bed diameter should be chosen such that flow velocities are high enough to produce desirable convective heat fluxes with negligible erosion effects.

Several heat capacitor configurations were studied and the results showed that the design parameters suitable for the MHD air preheater system are:

flow hole size	.0127-.019 m
pitch to diameter ratio	1.34-1.45
flow velocity	20-30 m/sec

The bed length has a significant effect on the magnitude of the temperature ripple. The output ripple temperature can be empirically expressed, approximately as an exponential function of the bed length, i.e.,

$$\Delta T_{exit} = \Delta T_{inlet} \cdot e^{-aL}$$

where ΔT_{exit} = total exit ripple temperature

ΔT_{inlet} = total inlet ripple temperature

a = a numerical constant determined by the heat capacitor design parameters (heating surface area, air velocity, pitch to diameter ratio, hole diameter, etc.)

L = bed length

For the heat capacitor selected for the ETF (Table III), $a \simeq 1.22$. Figure 5 shows the variation of the air exit temperature with time for two different heat capacitor lengths.

As shown in Table III the air ripple temperature (Figure 6) was reduced from $\pm$ 13.24 to $\pm$ .35 K. The design parameters of the heat capacitor selected for the ETF are not the optimum design. Several items have to considered in designing an optimum heat capacitor such as allowable air ripple temperature, allowable material stress levels (affected by flow velocity) cost of materials and fabrication. However, the capacitor design parameters given here are a useable realistic design.

NOMENCLATURE

$\alpha_1 = 2ha(\Delta\theta)/\rho_c c_{pc}(b^2-a^2)$

$\alpha_2 = 2\pi ha\ (\Delta z)/(mC_{pg})$

$\alpha_3 = k_c(\Delta\theta)/(\Delta z^{-2}\rho_c C_{pc})$

$\alpha_4 = hab^2[.5a^2/b^2 + (b^2+a^2)/(4b^2) + b^2\ \ln(g/a)/(b^2+a^2) - .5]/k_c/(b^2-a^2)$

$\Delta\theta$ = time increment

ΔZ = length increment in the axial direction

θ = time

ρ_c = density of the ceramic

a = inside tube radius

b = equivalent outside tube radius

C_{pc} = specific heat of the ceramic

C_{pg} = specific heat of the gas

h = heat transfer coefficient between the gas and the ceramic

k_c = thermal conductivity of the ceramic

m = gas mass flow rate

TC(J,I) = ceramic temperature of axial location J and time I

TG(J) = gas temperature at axial location J, and time θ

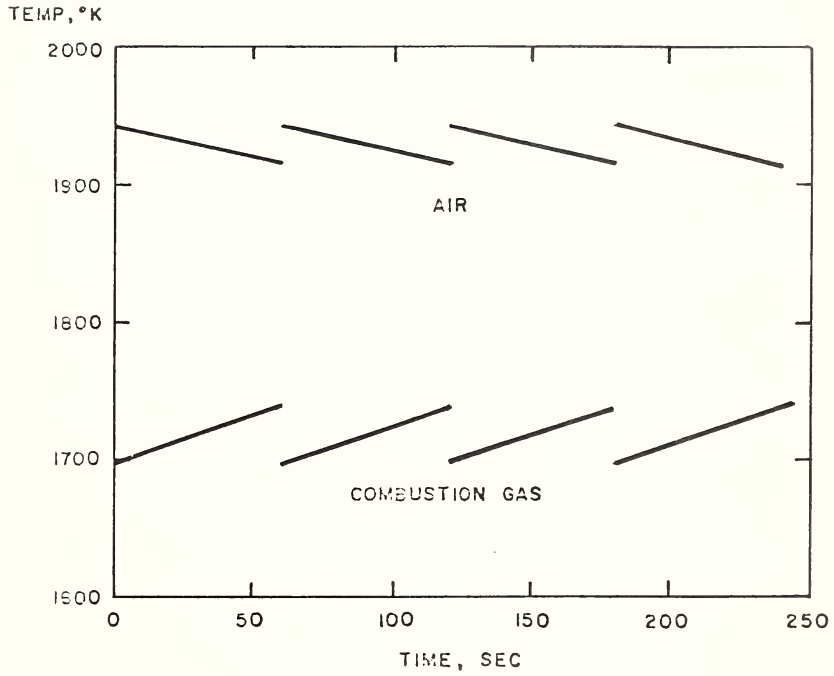

Figure 4.--Air preheater gas exit temperature

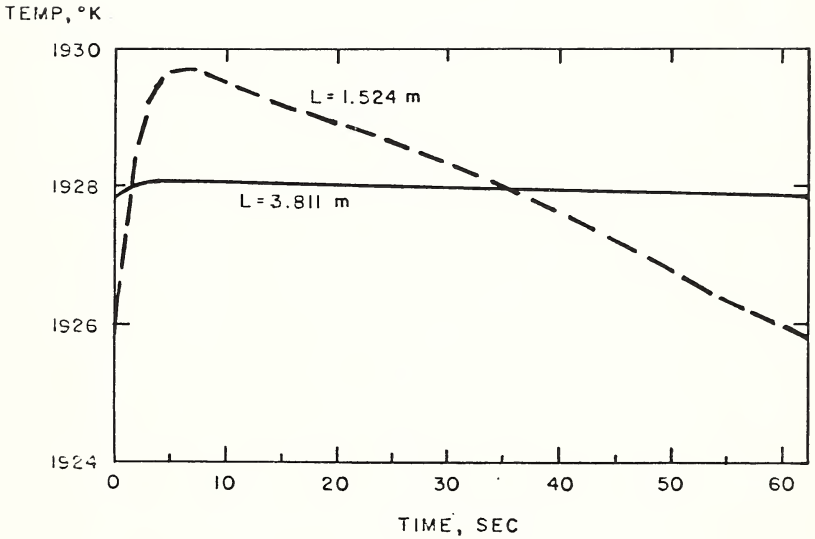

Figure 5.--Variation of heat capacitor air exit temperature (air inlet temperature=1942.5 to 1915.8 K)

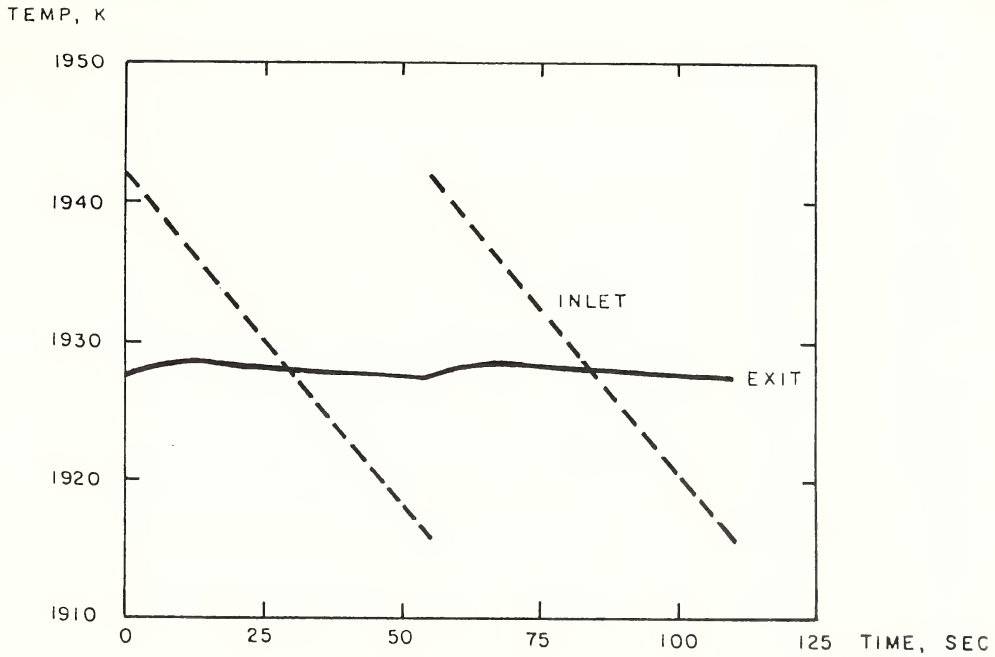

Figure 6.--Air temperature variation heat capacitor

APPENDIX G

COMPUTER PROGRAM
STEAM PLANT AND AIR PREHEATER SIMULATION

G.1. The computer program was written in Fortran IV language for processing in a SEL/55 computer. It consists of a main program, one function subprogram and four subroutine subprograms. The interconnection flow chart is shown in Figure G-1.

G.2. Main Program

The main program provides input/output functions and control of the solution. The flow diagram is shown in Figure G-2.

List of Variables

A11, A12, A13, A14 -- heat transfer constants, radiant boiler metal

A21, A22, A23, A24 -- heat transfer constants, HTAH bricks

A31, A32, A33, A34 -- heat transfer constant, superheater metal

A41, A42, A43, A44 -- heat transfer constant, LTAH metal

A51, A52, A53, A54 -- heat transfer constant, reheater metal

A61, A62, A63, A64 -- heat transfer constant, economizer metal

B11, B12, B13, B14 -- heat transfer constants, radiant boiler steam

B21, B22, B23, B24 -- heat transfer constants, HTAH air

B31, B32, B33, B34 -- heat transfer constants, superheater steam

B41, B42, B43, B44 -- heat transfer constants, LTAH air

B51, B52, B53, B54 -- heat transfer constants, reheater steam

B61, B62, B63, B64 -- heat transfer constants, economizer water

B7, B8 -- steam turbine constants

DT -- time step size

DX -- derivative of the state variables

E11, E12, E13, E14 -- radiant heat transfer constants, radiant boiler

F11, F12, F13, F14 -- tube design constants [friction coefficient x $_2$ tube length/tube diameter x (total flow area)^2], radiant boiler

F21, F22, F23, F24 -- tube design constants, HTAH and heat capacitor

F31, F32, F33, F34 -- tube design constants, superheater

F41, F42, F43, F44 -- tube design constants, LTAH

F51, F52, F53, F54 -- tube design constants, reheater

F61, F62, F63, F64 -- tube design constants, economizer

F7 -- cooling tubes design constant, MHD channel

HE -- enthalpy of water at economizer inlet

HL -- enthalpy of air at LTAH inlet

HT1, HT2, HT3, HT4 -- specific heat x brick mass of HTAH and heat capacitor

ICC, ICT -- counter

IPR -- variable identifier

IFREQ -- frequency of intermediate printout

NC -- counter

NO -- number of state variables

NOPEL -- total number of variables

TF -- time limit of integration

VB1, VB2, VB3, VB4 -- storage volume of radiant boiler

VE1, VE2, VE3, VE4 -- storage volume of economizer

VH1, VH2, VH3, VH4 -- storage volume of HTAH

VL1, VL2, VL3, VL4 -- storage volume of LTAH

VR1, VR2, VR3, VR4 -- storage volume of reheater

VS1, VS2, VS3, VS4 -- storage volume of superheater

WBM1, WBM2, SBM3, SBM4 -- specific heat x metal mass of radiant boiler

WEM1, WEM2, WEM3, WEM4 -- specific heat x metal mass of economizer

WE1 -- mass flow rate of steam at economizer inlet

WL1 -- mass flow rate of air at LTAH inlet

WLM1, WLM2, WLM3, WLM4 -- specific heat x metal mass of LTAH

WRM1, WRM2, WRM3, WRM4 -- specific heat x metal mass of reheater

WSM1, WSM2, WSM3, WSM4 -- specific heat x metal mass of superheater

X(1), X(4), X(7), X(10) -- mass density of water at economizer outlet, sections 1 - 4.

X(2), X(5), X(8), X(11) -- metal temperature of economizer, sections 1 - 4.

X(3), X(6), X(9), X(12) -- enthalpy of water at economizer outlet, sections 1 - 4.

X(13), X(16), X(19), X(22) -- mass density of steam at radiant boiler outlet

X(14), X(17), X(20), X(23) -- metal temperature of radiant boiler

X(15), X(18), X(21), X(24) -- enthalpy of steam at radiant boiler outlet

X(25), X(28), X(31), X(34) -- mass density of steam at superheater outlet

X(26), X(29), X(32), X(35) -- metal temperature of superheater

X(27), X(30), X(33), X(36) -- enthalpy of steam at superheater outlet

X(37), X(40), X(43), X(46) -- mass density of steam at reheater outlet

X(38), X(41), X(44), X(47) -- metal temperature of reheater

X(39), X(42), X(45), X(48) -- enthalpy of steam at reheater outlet

X(49), X(52), X(55), X(58) -- mass density of air at low temperature air heater (LTAH) outlet

X(50), X(53), X(56), X(59) -- metal temperature of LTAH

X(51), X(54), X(57), X(60) -- enthalpy of steam at LTAH outlet

X(61), X(64), X(67), X(70) -- mass density of air at high temperature air heater (HTAH) outlet

X(62), X(65), X(68), X(71) -- metal temperature of HTAH

X(63), X(66), X(69), X(72) -- enthalpy of air at HTAH outlet

X(87), X(89), X(165) -- mass density, pressure, temperature of water at economizer inlet

X(88) -- temperature of the combustion gas at the diffuser outlet

X(101), X(102), X(103), X(104) -- mass flow rate of water at economizer outlet

X(105), X(106), X(107), X(108) -- mass flow rate of steam at radiant boiler outlet

X(109), X(110), X(111), X(112) -- mass flow rate of steam at superheater outlet

X(113), X(114), X(115), X(116) -- mass flow rate of steam at reheater outlet

X(117), X(118), X(119), X(120) -- heat transfer rate to economizer metal

X(121), X(122), X(123), X(124) -- heat transfer rate to radiant boiler metal

X(125), X(126), X(127), X(128) -- heat transfer rate to superheater metal

X(129), X(130), X(131), X(132) -- heat transfer rate to reheater metal

X(133), X(134), X(135), X(136) -- heat transfer rate to the water at the economizer

X(137), X(138), X(139), X(140) -- heat transfer rate to the steam at the radiant boiler

X(141), X(142), X(143), X(144) -- heat transfer rate to the steam at the superheater

X(145), X(146), X(147), X(148) -- heat transfer rate to the steam at the reheater

X(149), X(150), X(151), X(152) -- temperature of the gas at economizer outlet

X(153), X(154), X(155), X(156) -- temperature of the gas at radiant boiler outlet

X(157), X(158), X(159), X(160) -- temperature of the gas at superheater outlet

X(161), X(162), X(163), X(164) -- temperature of the gas at the reheater outlet

X(166), X(167), X(168), X(169) -- temperature of the steam at economizer outlet

X(170), X(171), X(172), X(173) -- temperature of the steam at radiant boiler outlet

X(174), X(175), X(176), X(177) -- temperature of the steam at superheater outlet

X(178), X(179), X(180), X(181) -- temperature of the steam at reheater outlet

X(182), X(183), X(184), X(185) -- pressure of the steam at economizer outlet

X(186), X(187), X(188), X(189) -- pressure of the steam at radiant boiler outlet

X(190), X(191), X(192), X(193) -- pressure of the steam at the superheater outlet

X(194), X(195), X(196), X(197) -- pressure of the steam at the reheater outlet

X(198), X(199) -- electrical power output of the high pressure, and the low pressure steam turbines

X(201), X(202), X(203), X(204) -- heat transfer rate to the LTAH metal

X(205), X(206), X(207), X(208) -- heat transfer rate to the air at the LTAH

X(209), X(210), X(211), X(212) -- temperature of the gas at the LTAH outlet

X(213), X(214), X(215), X(216) -- mass flow rate of the air at the LTAH exit

X(217), X(226), X(243) -- temperature, pressure and mass density of the air at the LTAH inlet

X(218), X(219), X(220), X(221) -- temperature of the air at the LTAH outlet

X(222), X(223), X(224), X(225) -- pressure of the air at the LTAH outlet

X(230), X(231), X(232), X(233) -- mass density, temperature, enthalpy and pressure of the steam at the channel cooling tubes outlet

X(234), X(235), X(236), X(237) -- heat loss at the combustor, nozzle, generator and diffuser

X(238), X(239), X(240), X(241), X(242) -- enthalpy, mass density, temperature pressure and mass flow rate of the steam at the reheater inlet

X(246), X(247), X(248), X(249) -- pressure of the air at the HTAH outlet

X(250), X(251), X(252), X(253) -- heat transfer rate to the HTAH bricks

X(254), X(255), X(256), X(257) -- heat transfer rate to the air at the HTAH and heat capacitor

X(258), X(259), X(260), X(261) -- average temperature of the gas at HTAH outlet

X(262), X(263), X(264), X(265) -- mass flow rate of air at HTAH outlet

X(266), X(267), X(268), X(269) -- average temperature of air at heat capacitor outlet

X(270) -- actual temperature of the gas at HTAH outlet

X(273), X(274) -- seed condenser heat loss and heat recovered from the formation of K_2SO_4

X(275), X(277), X(278) -- mass flow rate, temperature and specific heat of the seed leaving the seed condenser

X(276), X(280), X(281) -- temperature of the gas at the outlet, temperature of the recycled gas and mass flow rate of the recycled gas, seed condenser

X(282) -- enthalpy of steam at the low pressure steam turbine outlet

X(299) -- mass flow rate of gas at the superheater, LTAH, reheater and economizer

X(300) -- mass flow rate of gas at radiant boiler and HTAH

G.3. Function INTEGD

This subprogram employs the fourth-order Runge-Kutta method with Kutta's coefficients to integrate a system of simultaneous first order ordinary differential equations, across one step of length DT in the independent variable T, subject to initial conditions.[18]

G.4. Subroutine STATE

This subprogram contains the state equations of the steam plant and air preheater. The parameter list must be (X, DX, T, DT, N) where

X -- vector of state variable values

DX -- vector of state variable derivatives

T -- independent variable, time

DT -- time step

G.5. Subroutine SIDE

This subprogram contains the algebraic equations for gas specific heat, steam properties, air properties, pressure drops, and heat transfer rates. These equations are required in the updating of the state of the system. The flow diagram is shown in Figure G-3.

G.6. Subroutine TEMP

This subprogram calculates the actual gas temperature at the HTAH outlet for a known average gas temperature.

G.7. Subroutine GAS

This subprogram calculates the convective heat transfer rates in the regenerative air heater. The parameter list must be (T, RHO, CP, H, W, ID) where

T - gas or air temperature

RHO - gas or air mass density

CP - gas specific heat

H - convective heat transfer rate from gas to brick or from brick to air

W - gas or air mass flow rate

ID - 1 gas
2 air

The additional variables used in this subprogram are:

A - flow area

CPG - specific heat

PR - Prandtl number

RE - Reynolds number

V - flow velocity

XKG - thermal conductivity

XMU - viscosity

XNUS - Nusselt number

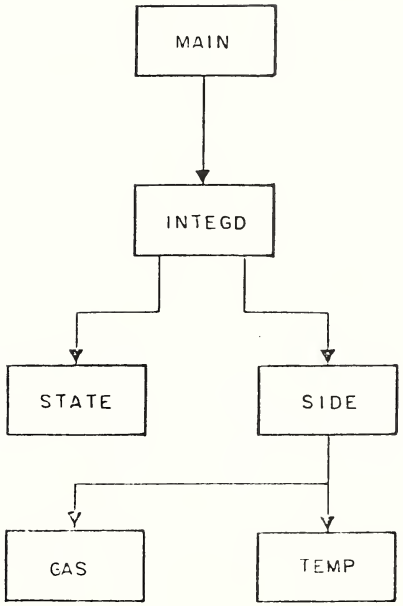

Figure G-1.--Interconnection flow chart

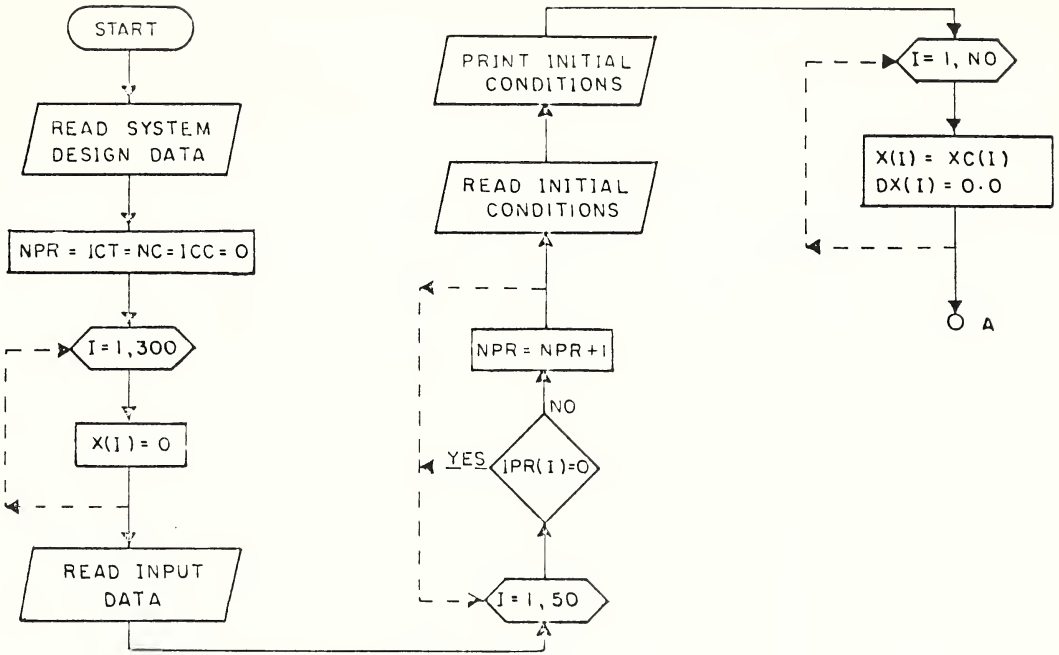

Figure G-2.--Flow diagram - main program

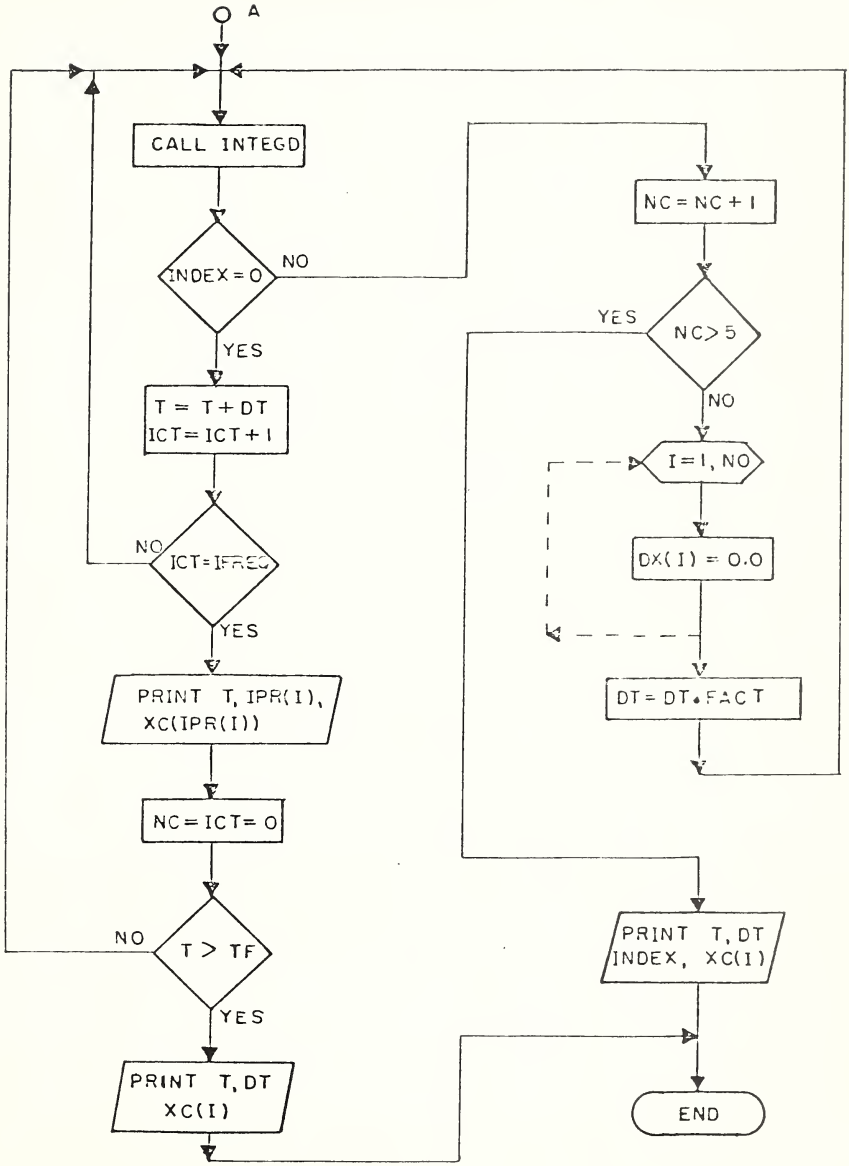

Figure G-2.--Continuation

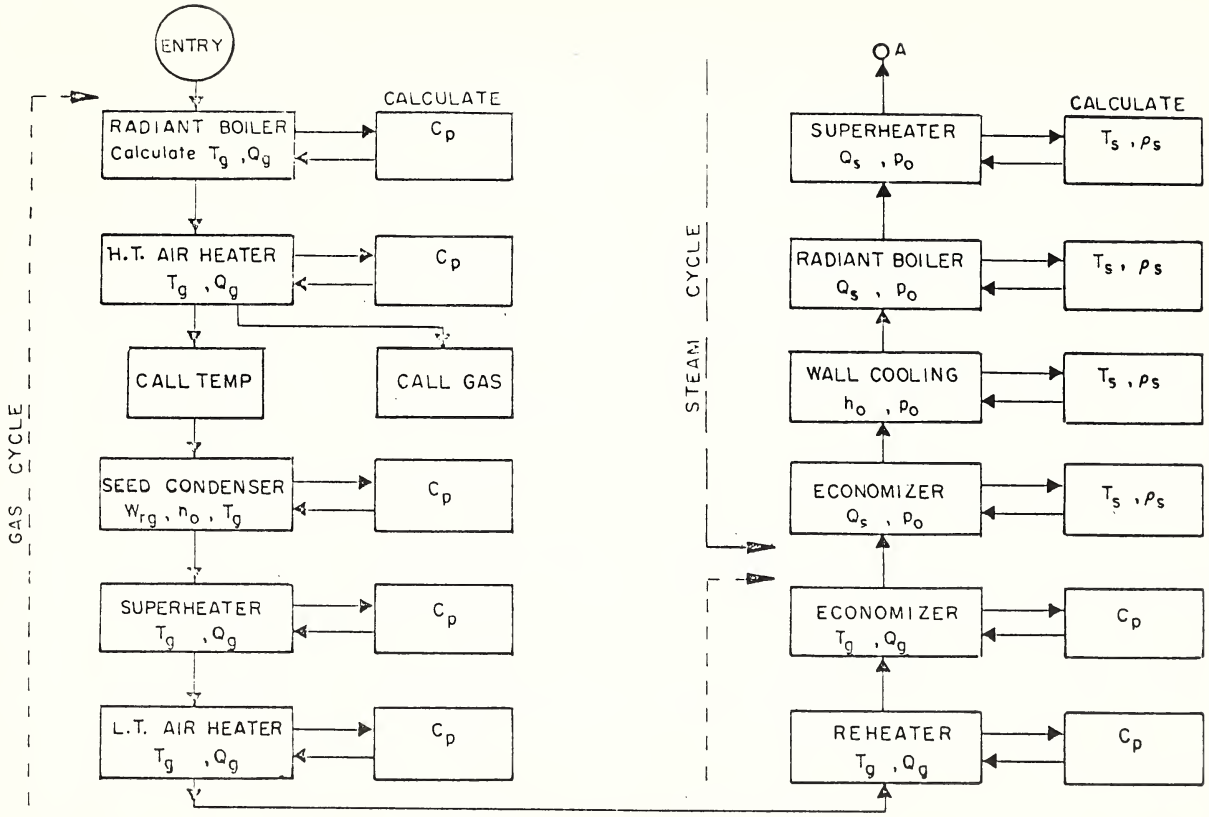

Figure G-3.--Flow diagram - subroutine SIDE

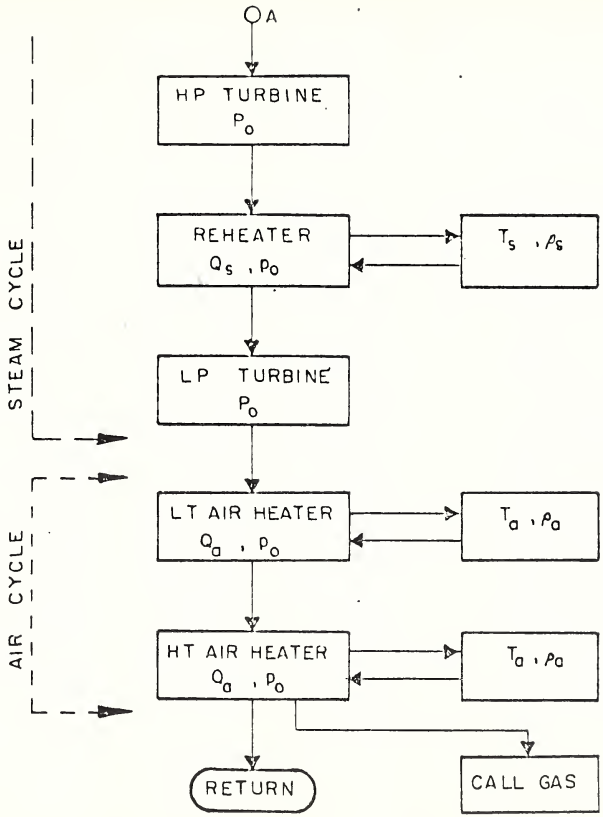

Figure G-3.--Continuation

TASK H3

Cycle Analysis and Control

D. Pierre, D. Rudberg, C. Dudding, and N. Du

ABSTRACT

Combined-cycle MHD/steam power systems are being modeled by digital computer simulation. Methods of providing efficient control of such systems are being investigated to insure stable modes of response and to obtain coordinated control of many interdependent subsystems. During the year, several papers[1,2,3] were presented at national meetings, and additional technical reports[4,5,17] were prepared. A subsystem of particular interest and importance is the coal combustor. A plug-flow combustor model having both one-stage and two-stage capability was completed; the code and documentation were delivered to MERDI. Efforts are directed at expanding the number of variables included in the control system models to determine the interaction effects of control strategies devised for particular subsystems of MHD/steam power systems.

I. OBJECTIVE AND SCOPE OF WORK

The objectives of the MHD systems cycle analysis and control project are twofold: 1) to provide accurate and reliable control system analysis of the behavior of MHD topping and steam-bottoming plant combinations, and 2) to establish desirable control configurations and parameters for a given MHD generator-bottoming plant configuration, taking into account the effects of measurement errors and input disturbances.

In open-cycle MHD systems, a bottoming plant is required to use the considerable quantity of heat rejected when the working plasma conductivity drops to a level unusable for MHD generation. Although many different cycles have been proposed, systems that have MHD topping and steam bottoming are currently the most plausible combination. Thus, research is directed at MHD/steam combined cycles.

To meet the first objective of understanding and evaluating the combined cycle mentioned above, it is necessary to computer model the MHD generator cycle and bottoming plant in a coupled form. This includes a high-order, state-variable characterization of the bottoming plant so that it can be included in a model of the overall system. This equation set contains nonlinear algebraic relations, coupled ordinary differential equations, and also differential-difference equations. Included in the characterization are appropriate control variables, state variables, set-point inputs, disturbance inputs, and a physically measurable set of output variables.

During the FY 76 contract period, the most detailed simulation of such a combined-cycle plant was a dynamic power flow simulation having two major

PID controllers and two feedforward control blocks. The digital computer simulation to be developed in the current contract period will expand the number of dynamically controlled variables in the system to obtain a high-order and more accurate simulation which can be used to study the effect of alternative system control strategies on the system outputs.

Several general control philosophies will be considered, ranging from basic proportional rate and reset control through state variable formulations that are extensions of standard single-input, single-output frequency domain controls to complete optimal control strategies based on quadratic cost functions. Time invariant optimal control has been used previously on a steam turbine generator plant.

The validity and usefulness of a combined-cycle dynamic simulation depends on the accuracy with which major subsystems are characterized. In particular, the detail in combustor modeling must be increased; both a high-temperature equilibrium subprogram and a pulverized coal combustor simulation are to be developed on the basis of recent experimental and theoretical results. Also, the number of independent time-variable inputs to the combustor/nozzle/channel/diffuser (CNCD) subsystem must be increased; the electrical loading parameter will be included in this category. As for the bottoming plant, additional control loops will be introduced for feedwater control, superheat attemperator control, and turbine speed. To accomplish these objectives, many dynamic models for boiler-turbine combinations and related topics will be evaluated.

The scope of the work has broadened during the year to include component modeling for the CDIF. In particular, a detailed two-stage combustor program now is operational for the CDIF.

II. SUMMARY OF PROGRESS TO DATE

The cycle analysis and control efforts have been directed to several related areas. First, work continued on the overall combined-cycle dynamic simulation models; results[1,2,3] of this work were presented at the 1977 winter meeting of the IEEE Power Engineering Society, at the 16th Symposium on Engineering Aspects of MHD, and at the 1977 Power Plant Dynamics, Control, and Testing Symposium. Design values for 16 controller parameters were obtained on the basis of the combined-cycle simulation of system model III. Basic dynamic models for steam-bottoming plant components were developed for system model IV. An investigation was made into ways of incorporating compressor control, boiler feedwater control, and superheat attemperation in the combined-cycle simulation.

For the combustor and high-temperature chemical properties, two computer programs were developed. One of these, the chemical equilibrium program, is especially formulated to deal with seeded combustion gases as they exist within MHD combustors and channels. The program is fully debugged and is useable in a stand-alone mode. A report[4] is available on the conductivity modeling that is included in the program. The second combustion program is a pulverized coal combustor simulator in the form of a one-dimensional, plug-flow model.

A detailed two-stage combustor model was made operational, and the source cards and code were delivered to MERDI. Updates will be delivered as they are made. The model was constructed to fill needs related to control policy generation; a large family of input-output models can be produced from this single, rather detailed, parent combustor model, and a wide range of output variable sensitivities can be evaluated as a function of input variable variations and system parameter variations. For example, the sensitivities of combustion gas enthalpies, conductivity, or composition can be evaluated as functions of oxidant preheat temperature and composition, of coal composition, of combustor geometry, etc.

Features of the combustor model include the following:

One-stage or two-stage operation;

Thermal inputs from about 5 Mw to 4000 Mw;

Variable geometry (lengths, diameters, seed injection point);

Variable oxidant preheat and composition, combustion pressure (1-8 atm), and stoichiometric ratios; and

Axial profiles of temperature, velocity, gas density, heat loss, char particle burnout, electrical conductivity, gas composition, and gas enthalpy.

Emissivity calculations constitute an important part of combustor modeling. An accurate model of gas emissivities was developed and implemented in the overall combustor program. Appendix A contains a detailed description of the two-stage combustor model.

For input-output modeling of the combustor/nozzle/channel/diffuser (the CNCD), the electrical loading parameter was incorporated as an additional independent input, along with fuel feed rate and preheat air temperature. In order to observe the effect of a varying loading parameter on the channel, computer runs were made with varying thermal input and loading parameter. Consideration was given to a channel design in which the area variation of the channel results in a predetermined Hall voltage distribution, with the objective of minimizing arcing. A report[5] documents the approach.

Several trips were made during the year. Both principal investigators attended the 16th Symposium on Engineering Aspects of MHD. A visit to Colstrip, Montana was made to evaluate present-day operating procedures for modern coal-fired steam plants; a trip report on this was prepared, as were reports on visits to Argonne, AVCO, GE, and MIT. Contacts were made with scientific and engineering personnel from the major institutions that are working on MHD. As system components are advanced in form and are realized in hardware, these people will be consulted with regard to the control aspects of the components. Discussions were held with MHD channel modellers from MIT and Argonne National Laboratory; these discussions resulted in a better understanding of the relative accuracy of quasi one-dimensional models in comparison to the accuracy of three-dimensional models of channel phenomena. At this time, it appears that the trade-off of added accuracy

versus increased computational cost does not favor the use of three-dimensional models in establishing overall control system models for combined-cycle plants.

Although the original efforts of the cycle analysis and control task were directed at commercial size MHD systems, many of the results that have been and are being generated can be modified to apply to smaller systems such as the CDIF and the ETF. During the year, discussions were held with MERDI personnel to determine the type and amount of cooperative effort that would be appropriate. In January, 1977, a work-plan modification for Task H3 was agreed upon by MSU and MERDI. This modification was approved by ERDA in March 1977, and resulted in the development of the two-stage combustor model.

III. DETAILED DESCRIPTION OF TECHNICAL PROGRESS

Component characterizations have been extended beyond those previously developed. In the previous combined-cycle model[1,2,3] controllers were incorporated for fuel feed and turbine valve area, and these controlled values influenced throttle pressure, steam flow, and electrical power output. The new control model will make use of other important physical parameters (steam temperature, feedwater flow rate, superheater pressure and temperature, and turbine speed) as feedback and feedforward signals.

The overall control model is of the coordinated type with control loops for air-fuel, feedwater, superheat attemperator, and turbine valve area. To accomplish these objectives, many dynamic models for boiler-turbine and related topics have been studied and compared. The scheme used to complete the new model involves two phases:

Phase I. The Development of the Model

a) Develop equations that characterize the process dynamics.
b) Combine various parts of the model and coordinate their respective controllers.
c) Develop a block diagram representation of the model.

Phase II. Computation and Evaluation

a) Assign values for coefficients and constants; then calculate initial conditions.
b) Place the equations in state space form and prepare the corresponding FORTRAN model.
c) Run a series of solutions to determine desirable control configurations and parameters.

In the above phases, the start-up operation of a steam plant has not been included. In particular, a steam flash tank and bypass steam is not included.

Concerning control aspects of the steam subsystem, Laubli and Fenton[6] suggest an approach in which megawatt error and throttle pressure are used as feedback signals to the boiler and turbine valve. These two signals also

are compensated by main steam temperature error and oxygen error. The presence of an oxygen analyzer and an air-feed controller in the boiler unit permits the control of excess air. A certain percent of excess air is desirable at some fixed stack temperature; the relationship of excess air to boiler efficiency is discussed by Robnett.[7] Louis[8] is concerned mainly with superheater outlet pressure and temperature. The superheater pressure is controlled by feedback and feedforward signals. The load demand is fed to throttle valve position demand, fuel-air demand, and feedwater demand through three nonlinear blocks. The work of McDonald and Kwatny[9] is used to form part of the general block diagram of the control mode. However, their study assumes perfect air flow and feedwater flow, and the boiler is of the drum type instead of the once-through type to be used in the combined-cycle plant.

The GE combined-cycle configuration[10] and the more recent work of Jackson, et al.,[11] have been considered as benchmark systems for which control systems are to be developed. The initial task was to formulate, in a suitable mathematical way, the dynamic operating characteristics of the individual components of this system. For the bottoming plant components, the works of Kwan and Anderson[12] and Robles[13] have been followed with minor modifications and with expansion to include feedback control variables.

The dynamics of each component of the bottoming plant are governed by conservation equations for mass, momentum, and energy. For example, a one-lump version of the equations for the radiant boiler is as follows (symbols used are defined in Table 1):

Mass Conservation

$$\dot{\rho}_o = \frac{1}{V}(W_i - W_o) \tag{1}$$

Momentum Conservation

$$P_o = P_i - f\frac{W_i^2}{\rho_i} \tag{2}$$

Energy Conservation

$$\dot{h}_o = \frac{1}{\rho_o}\left[-h_o\dot{\rho}_o + \frac{1}{V}(W_i h_i - W_o h_o + Q)\right] \tag{3}$$

In addition, equations of state and of heat transfer are:

$$T_m = T(h_m) \tag{4}$$

$$\rho_o = \rho(h_o, P_o) \tag{5}$$

$$T_o = T(h_o, P_o) \tag{6}$$

$$Q_{ms} = \text{constant} \cdot (W_i)^{0.8}(T_m - T_o) \tag{7}$$

$$Q_{gm} = \text{constant}\cdot(T_{gi}^4 - T_m^4) + \text{constant}\cdot(W_g)^{0.6}(T_{gi} - T_m) \tag{8}$$

$$T_{go} = T_{gi} - \frac{Q_{gm}}{C_g W_g} \tag{9}$$

$$\dot{h}_m = \frac{1}{M} (Q_{gm} - Q_{ms}) \tag{10}$$

Equations (5) and (6) are evaluated by use of curve-fits of data obtained from appropriate regions of the steam tables. Equation (4) is evaluated in similar fashion from data relating metal temperature to enthalpy. Equations (3) and (10) are coupled first-order differential equations; in the simulation, $\dot{\rho}_o$ is approximated by use of (5) and past values of ρ_o, and W_o is determined by a slight rearrangement of (1).

In addition to the above one-lump version of the radiant boiler, both a two-lump and an averaged one-lump version were simulated. In all cases, in response to a 100 K increase in inlet gas temperature, steam output response time constants were comparable, on the order of 50 seconds. Robles has used a four-lump approximation with essentially the same result. The nominal steady-state operating point of the radiant boiler was the same as that given by Jackson, et al.[11]

Even though system model IV represents a significant advance over system model III, system model III is still being used to develop design criteria. Simulation runs have been conducted to determine the effect that a heat capacitor[14] will have on the electrical output. Without such a unit or other control to smooth temperature fluctuations in the preheated air, a significant ripple (10 Mw peak-to-peak on a basis of 1560 Mw) occurs in the electrical output of a particular combined-cycle plant.[1] This occurs despite the fact that the loading parameter for the MHD generator is assumed to be maintained constant.

The simulation of system model IV is to contain dynamic control characteristics of the air compressor and the boiler feed pumps. Static characteristics of compressors and boiler feed pumps are well-documented in engineering handbooks but dynamic characteristics are not. The high-pressure, high-volume compressor (either centrifugal or axial) must supply air at some ten times the mass flow rate of the coal and at pressures from five to nine atmospheres. The dynamic operating range of these units is limited by surge phenomena: flow must be maintained above limiting values (typically 75 percent of design flows) in order to avoid unstable pulsating flow; and therefore, the method of controlling flow is of concern. In general, flow control by throttling the inlet air stream is not advisable. More reliable control is obtained by use of a variable speed drive, such as an auxilliary steam turbine drive. In system model IV, coupled dynamics of a steam turbine driving an associated air compressor will be included.

From the standpoint of reliability, large MHD plants undoubtedly will employ a bank of compressors operating in parallel. When reduced load operation is required, some of the units will be shut down and isolated from the remainder by appropriate valves. The active compressor units will be operated well above respective surge lines. Maintenance and repair work

will be performed on out-of-service units without requiring plant shutdown. For the same reason, a battery of high-pressure boiler feed pumps will operate in parallel to supply the radiant boiler.

A key subsystem of system model IV is a new input-output model of the combustor/nozzle/channel/diffuser (CNCD). This model will be produced on the basis of the latest results in coal-combustor modeling, and a quasi one-dimensional channel model will be used. Variable inputs will include fuel feed, air feed, seed feed, preheat air temperature, and channel loading parameters. Outputs will include feedwater enthalpy, exit gas enthalpy, and electrical power output. Distinct dynamic controllers will be modeled for each of the feed systems. The seed feed controller will be implemented as a ratio controller, with air feed as the basis variable. Air and coal feed controllers will be coordinated on the basis of megawatt load demand and boiler pressure.

More effort is required to extract a simplified, but relatively accurate, combustor model to be included in system model IV. The available detailed combustor models will be used for this purpose.

The introduction of recirculated gas and gas tempering to control gas and steam temperature is attractive, but it complicates the problem formulation. Recirculated gas may be used in the seed condenser; the flow rate of this recirculated gas must be controlled to minimize temperature variations in the seed condenser.

In order to observe the effect of a varying loading parameter on the channel, computer runs were made with varying thermal input and loading parameters. At first, the thermal input was left constant at 3500 Mw (design center for system model III) and the loading parameter was varied from 0.6 to 0.8 (0.7 is the design center value). Above 0.79 the channel went into shock but for increased loading (smaller loading parameters), this problem did not occur. However, the Hall voltage increased dramatically for increased loading. As the loading was increased the following trends (on the average) were observed:

Current density	increased
Velocity	decreased
Inverter Voltage	decreased
Hall Voltage	increased

Next, the thermal input was varied from 3000 MW to 4000 MW in steps of 250 MW. At each value of thermal input, three values of loading parameter were tried (0.65, 0.70, and 0.75). In every case, the lightest loading (0.75) produced the largest power output. The Hall voltage peaked at the end of the channel for the heavier loadings and high thermal input. At 4000 MW thermal input and a loading parameter of 0.65, the Hall voltage exceeded 40 v/cm, which is definitely excessive.

In an attempt to decrease the Hall voltage, a varying loading parameter (as a function of x) was tried. The loading parameter was varied linearly along the length of the channel. Several computer runs indicated that this did not produce the desired effect.

Work was done to design an MHD channel for a predetermined Hall voltage distribution. This is accomplished by assigning a specific profile in the channel that will produce the assigned distribution. One channel has been designed using this technique, and the results look promising. This channel design was done with a loading parameter of 0.75 instead of 0.70 as was done in previous work. The lighter loading not only produces greater usable power output but also decreases the Hall voltage and peak electrode current.

The following programs were developed to aid in modeling of chemical properties: 1) a chemical equilibrium program, and 2) a pulverized coal combustor simulator, both one-stage and two-stage.

The equilibrium program is formulated especially to deal with seeded combustion gases as they exist within MHD combustors and channels. It is intended for use in the 1800-3000 K range and accomodates a range of pressures from zero to 10 atmospheres. Twenty-eight species are included. These are the elemental forms of C, H, O, N, S, K, and A, several compounds and ions of importance, electron concentration, and ash vapor. Electrical conductivity also is calculated. Inputs required are temperature, pressure, and initial concentrations of species. The program is fully debugged and functional, and is useable in a stand-alone mode.

During the contract period, work was completed on coding and testing of a digital computer model for two-stage, pulverized-coal-fired combustors and on documentation of the combustor model. Pre-publication drafts of the documentation have been delivered to several sites; the complete documentation appears as appendix A of this report. Making what will be a large number of combustor program runs to establish sensitivity of combustor outputs to inputs, physical parameters, and operating points also has begun. The result will be a set of input-output models of combustor behavior, suited to control policy synthesis requirements. They will have no detail of internal combustor behavior, being a set of multivariate curve fits of outputs as functions of inputs, physical parameters, and operating point. Execution speeds will be about two orders of magnitude greater than the relatively detailed combustor model mentioned above. The input-output models will be matched to nozzle, channel, and diffuser models of a similar nature in the study of system response to various control configurations.

Discussion with representives of Argonne National Laboratory revealed that they had achieved independently very similar combustor results. They had made some different assumptions regarding devolatilization and char burnout, but it appears gasifier temperature profiles are not highly sensitive to such assumptions. Arrangements have been made to exchange codes, and some identical check problems have been run on each code.

Because of the very high temperatures in MHD combustors, most of the heat lost is the result of radiation. This makes the accurate calculation of emissivities very important.

Gas emissivity is based on the radiation of two gases, H_2O and CO_2, although other gases are present. This is justified because only H_2O and

CO_2 have appreciable radiation in the combustion gases. The model used to calculate the emissivities of H_2O and CO_2 is based on the work of Leckner.[15] In the model, calculations first are performed to find the emissivities of H_2O and CO_2 taken separately at the desired temperature and partial pressure, with the total pressure assumed to be one atmosphere. Because of the above-atmospheric pressures encountered in the combustor, spectral line broadening of H_2O and CO_2 (which increases the emissivities) becomes important. Therefore, the emissivities of both gases are corrected for total pressure. The last step involves combining the emissivities to produce an emissivity for the mixture. The separate emissivities cannot simply be added because of the spectral overlap of the components.

The calculation of soot emissivity follows that described by Taylor and Fostor.[16] The total emissivity of soot can be calculated as

$$\varepsilon_s = \frac{1}{\sigma T^4} \int_0^\infty E_{\lambda,T}\, \varepsilon_\lambda \, d\lambda$$

where σ is Stefan's constant, $E_{\lambda,T}$ is the Planck distribution of the emissive power of a black body, ε_λ is the spectral emissivity of soot, and λ is the radiation wavelength. This integration has been performed over temperatures and soot densities of interest. It was found that the integration limits could be reduced to 0.1 to 20 microns with almost all of the radiation occurring in this wavelength range. A two-variable curve fit (temperature and soot density) is required to use the soot emissivity data.

In the first stage of the combustor, the combustion product has such a high temperature and contains such a large amount of unburned coal particles that the emissivity is close to 1. It would be simpler, and probably as accurate, to assign the emissivity of the first stage as 1. This possibility requires further study. The second stage ideally contains few particles, and a complete calculation is required.

Present heat loss calculations for radiation assume an isothermal gray gas radiating to an isothermal gray enclosure. Because of the high emissivity of the gas in the first stage, these assumptions will give reasonable results even though the gas is not isothermal. Using these same assumptions for the second stage would give a larger error in total heat loss because temperature gradients in the gas are unaccounted for. At this time, the feasibility of using a more complex model for the second stage is being considered. It will account for temperature gradients in the axial direction of the combustor.

IV. CONCLUSIONS

Control system models of combined-cycle MHD-steam power plants have been developed. Most of the reported results to date[1,2,3] have been obtained on the basis of system model III, which is structured on the basis of a dynamic power flow model. A more desirable form of combined-cycle control simulation is one in which detailed process variables (e.g., steam temperature, pressure, and flow rate) appear in the simulation, and simulated control actions are based on the available system outputs and command

signals. During the year, advances have been made in modeling key components of such an overall dynamic system simulation. A detailed two-stage combustor model was completed and the computer program was delivered to MERDI. This code, along with developed channel analysis and design routines, now is being used to obtain multivariable input-output models of the combustor/nozzle/channel/diffuser. Also, detailed steam bottoming plant equations have been formulated. Computer code for some of the bottoming-plant components has been written, and computer runs of individual components have been made to verify the approach.

MILESTONE CHART

STATUS DATE _____

TASK H3

PROGRESS

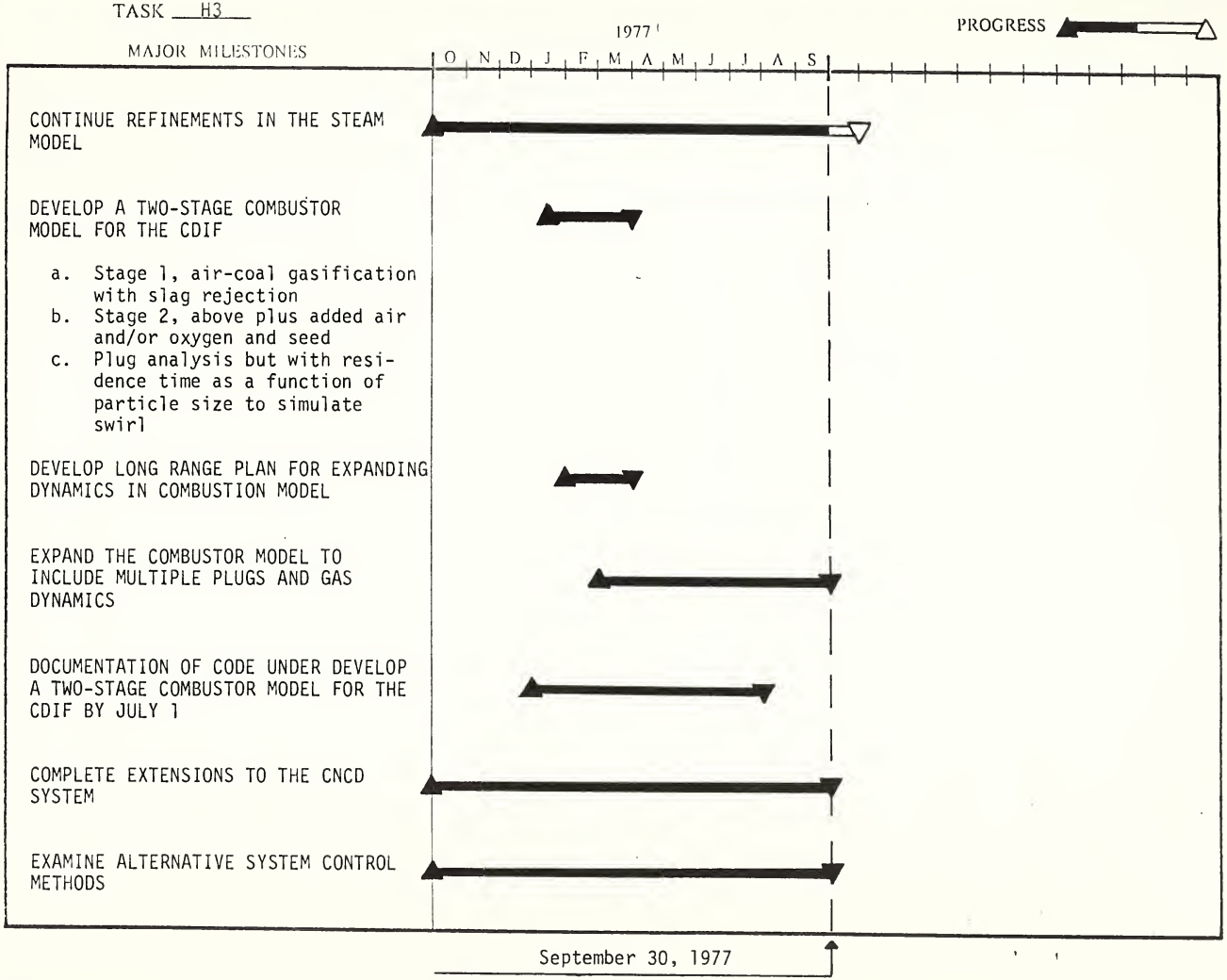
MAJOR MILESTONES
1977
O N D J F M A M J J A S
CONTINUE REFINEMENTS IN THE STEAM MODEL
DEVELOP A TWO-STAGE COMBUSTOR MODEL FOR THE CDIF
a. Stage 1, air-coal gasification with slag rejection
b. Stage 2, above plus added air and/or oxygen and seed
c. Plug analysis but with residence time as a function of particle size to simulate swirl
DEVELOP LONG RANGE PLAN FOR EXPANDING DYNAMICS IN COMBUSTION MODEL
EXPAND THE COMBUSTOR MODEL TO INCLUDE MULTIPLE PLUGS AND GAS DYNAMICS
DOCUMENTATION OF CODE UNDER DEVELOP A TWO-STAGE COMBUSTOR MODEL FOR THE CDIF BY JULY 1
COMPLETE EXTENSIONS TO THE CNCD SYSTEM
EXAMINE ALTERNATIVE SYSTEM CONTROL METHODS
September 30, 1977

TABLE I.--Notations Used for Bottoming Plant Equations

Symbols

h: enthalpy (Joules/Kg)

P: pressure (Newton/m^2)

T: temperature (K)

W: mass flow rate (Kg/sec.)

ρ: mass density (Kg/m^3)

Q: heat transfer

V: volume

C: specific heat (Joules/Kg degree K)

f: friction factor

M: metal mass (Kg)

Subscripts

g: gas

i: inlet

o: outlet

m: metal

ms: metal to steam

gm: gas to metal

go: gas outlet

gi: gas inlet

REFERENCES

1. J. Aspnes and D. A. Pierre, "Dynamic Modeling and Control of MHD/Steam Electrical Power Generating Plants," 16th Symposium on Engineering Aspects of MHD, May 1977.

2. J. Aspnes and D. A. Pierre, "Dynamic Modeling and Control of Magnetohydrodynamic/Steam Systems," IEEE Power Engineering Society, Winter Meeting, paper published in IEEE special publication 77CH1215-3-PWR, Energy Development III, February 1977.

3. J. Aspnes and D. A. Pierre, "Simulation and Control of Magnetohydrodynamics/Steam Combined-Cycle Power Plants," Proceedings of the Third Power Plant Dynamics, Control and Testing Symposium, September 7-9, 1977.

4. D. J. Miller and D. A. Pierre, Conductivity of Coal Combustion Gases, ERL Report No. 1876, Electronics Research Laboratory, Montana State University, Bozeman, October 1976.

5. C. H. Dudding and D. A. Pierre, MHD Channel Design Code to Obtain a Specified E_x Variation, ERL Report No. 177, Electronics Research Laboratory, Montana State University, Bozeman, Montana, January 1977.

6. F. Laubli and F. H. Fenton, Jr., "The Flexibility of the Supercritical Boiler as a Partner in Power System Deisgn and Operation; Part I: Theoretical Relationships; Part II: Application and Field Test Results," IEEE Transactions on Power Apparatus and Systems, Vol. PAS-90, No. 4, pp. 1719-1733, July-August 1971.

7. J. D. Robnett, "Boiler Controls Keep Energy Use From Going Sky High," Control Engineering, Vol. 23, pp. 36-38, October 1976.

8. J. R. Louis, "Controls for a Once-Through Boiler," Instruments and Control Systems, Vol. 44, pp. 77-80, January 1971.

9. J. P. McDonald and H. G. Kwatny, A Mathematical Model for Reheat Boiler-Turbine-Generator Systems, IEEE paper 70 CP 221-PWR, 1970.

10. G. R. Seikel and L. P. Harris, A Summary of the ECAS MHD Power Plant Results, NASA Technical Memorandum X-73491, October 1976.

11. W. D. Jackson, R. L. Lawit, R. A. Stoudt, M. G. Klett, J. C. Cutting, and C. D. Maxwell, "Status of the Reference Dual-Cycle MHD-Steam Power Plant," 16th Symposium on Engineering Aspects of MHD, May 1977.

12. H. W. Kwan and J. H. Anderson, "A Mathematical Model of a 200 MW Boiler," International Journal of Control, Vol. 12, pp. 977-998, June 1970.

13. T. C. Robles, A Simulation Approach to a Magnetohydrodynamic-Steam Electrical Power Generation System, Ph.D. Thesis, Montana State University, Bozeman, August 1975.

14. T. C. Robles and R. M. Johnson, "A Heat Capacitor for MHD Electric Power Generation Systems," Proceedings 16th Symposium on Engineering Aspects of MHD, May 1977.

15. B. Leckner, "Spectral Emissivity of Water Vapor and Carbon Dioxide," Combustion and Flame, Vol. 19, pp. 33-48, 1972.

16. P. B. Taylor and P. J. Foster, "The Total Emissivities of Luminous and Non-Luminous Flames," International Journal of Heat and Mass Transfer, Vol. 17, pp. 1591-1605, 1974.

17. D. A. Rudberg, A Digital Computer Model and Simulator for Pulverized Coal-Fired MHD Combustors, ERL Report No. 677, Electronics Research Laboratory, Montana State University, Bozeman, August 1977.

APPENDIX A

A Digital Computer Model and Simulator for Pulverized-Coal-Fired MHD Combustors

A1. INTRODUCTION

The program described herein is a steady-state, plug-flow model designed to predict the operating states of single-stage or two-stage pulverized-coal-fired combustors operating in the 1800 K to 3000 K range, which is appropriate for MHD generators. It calculates axial profiles of temperature, velocity, chemical composition, enthalpy, and electrical conductivity of the combustion gas, plus axial profiles of char particle burnout, heat loss, and residence time. Thus, it is possible to predict the effect on performance of air preheat temperature, oxidant composition (vitiated air, ambient air, oxygen enriched), relative humidity, coal composition, coal particle size distribution, seed type and injection technique, stoichiometric ratio in first and second stages, combustion pressure, combustor dimensions, and sidewall temperature.

The program is intended as a tool for predicting behavior of already designed combustors rather than for analysis of detailed internal behavior as a part of the combustor design process. A rigorous treatment would call for information on fluid flow and swirl patterns, slag particle size distribution and trajectories in the first stage [A1], kinetics of ash vaporization [A2], and kinetics of rapid devolatilization [A3,A4]. None of these are embodied in the model but it is conceivable that they could be added, particularly the topics of ash vaporization and devolatilization.

The model basically is intended as an aid in system analysis and control policy synthesis. It can be used either (1) in a stand-alone mode to make fairly detailed studies of combustor behavior under variations of inputs and operating conditions, (2) in conjunction with equally detailed models of other components, e.g., channel, nozzle, diffuser, to make more extensive system studies, or (3) as a parent model from which can be derived a family of models having the same relations between input variables and output variables but with no internal information calculated. Hence, they are given the name "input-output models". They most probably will omit chemical behavior also. Likely forms of input-output models are a set of multi-dimensional curve fitting routines or table lookup routines with interpolation algorithms. Their calculational speed will be greatly in excess of the parent model described in this report, making them much more suited to overall system analysis; but the necessity of understanding, to engineering satisfaction, what occurs within a system component and of having a widely descriptive parent model from which to generate input-output models is well recognized. The program described here deals in fair detail, offering insight into a wide range of combustor behavior and a facility for extracting other models.

The basic assumptions are:

(1) Plug flow exists with perfect mixing in the radial direction and with no significant mixing in the axial direction.

(2) Devolatilization and combustion of volatiles are instantaneous.

(3) Char particles are spherical, composed of carbon, perfectly entrained in the combustion gas, and are at the same temperature as the combustion gas.

(4) Chemical equilibrium exists at every point in the combustor.

(5) Sidewall temperatures are uniform throughout each combustor stage.

(6) Gases conform to the perfect gas law.

(7) Velocities are low so that the difference between actual pressure and stagnation pressure is insignificant.

(8) A temperature gradient exists in the axial direction only.

(9) Specified slag rejection can be attained with no change in plug flow properties by assuming that swirl flow combustion causes uniform plug rotation with no change in axial or radial properties of the plug (except slinging of larger slag droplets to the combustor walls).

(10) Non-rejected slag consists of a vapor-droplet mixture and is perfectly entrained in the combustion gas.

The report is organized as follows: Section A2 is a brief description of programs and their inter-relations; and Section A3 is a technical description of programs; and Section A4 gives treats pertinent variable descriptions.

A2. BRIEF PROGRAM DESCRIPTIONS

A2.1 Main Program

Input: Combustor geometry and internal operating conditions; ambient conditions; second stage geometry and operating conditions (if second stage exists); oxidant composition if other than ambient air; coal physical properties and chemical analysis; seeding level and injection point; oxygen enrichment.

Output: Axial profiles of combustion gas temperature, velocity, chemical composition, enthalpy, and electrical conductivity; axial profiles of char particle burnout, heat loss, and residence time.

Special features: Either single-stage or two-stage operation.

Subroutines called: EQUILZ, COMBU, QLOSS

A2.2 Subroutine EQUILZ

Purpose: To calculate chemical equilibrium of combustion gas products and to calculate enthalpies and standard heats of formation of both input reactants and output products.

Subroutines called: CONDUCT, CORRCT, ROOT

A2.3 Subroutine ROOT

Purpose: To calculate the root of each chemical reaction equation.

Functions called: FWD, REV

A2.4 Subroutine CORRCT

Purpose: To adjust component concentrations in accord with the results from ROOT.

Functions called: None.

A2.5 Subroutine COMBU

Purpose: To calculate the fraction of char burned in a given time interval.

Subroutines called: None.

A2.6 Subroutine QLOSS

Purpose: To calculate radiative and convective heat loss from the combustor.

Subroutines called: None.

A2.7 Subroutine CONDUCT

Purpose: To calculate electrical conductivity of the combustion gases.

Subroutines called: None.

A2.8 Function FWD

Purpose: To evaluate the equilibrium expression for each reaction proceeding in the forward direction.

A2.9 Function REV

Purpose: To evaluate the equilibrium expression for each reaction proceeding in the reverse direction.

Figure A2.1 shows the hierarchical relations between the various programs and functions.

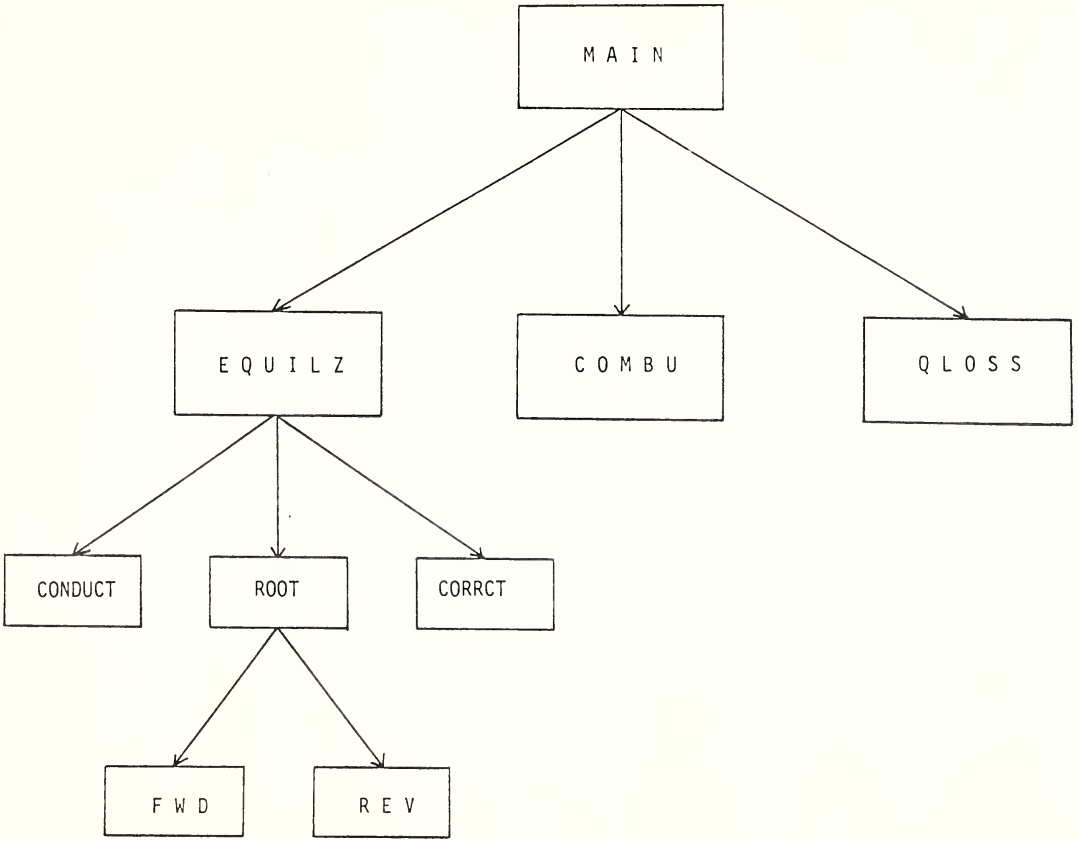

FIGURE A2.1

A3. TECHNICAL DESCRIPTION OF PROGRAMS

A3.1 Main Program

The main program has three general functions: (1) input-output, (2) fuel and oxidant chemistry calculations, and (3) energy balance calculations. Input and output are described in the preceding section, leaving the latter two functions to be described below.

A3.1.1 Fuel and Oxidant Chemistry Calculations

Heating value of coal:

Heating value of coal is calculated according to the Dulong formula [A5]:

$$QCOAL = 1.027 \times 10^7 (3.591C + 15.316(H - O/8) + S) \text{ joules/kg} \qquad (A3.1)$$

which gives results to within 3 percent for most coals. The symbols represent the results of an ultimate analysis of the fuel for carbon, hydrogen, oxygen, and sulfur, respectively. The only use of QCOAL in the program is in calculation of fractional heat loss (FHLOS).

Ambient air calculations:

Water vapor has significant effect on combustion and electrical conductivity in MHD generators so it is necessary to account for water vapor in the oxidant. Oxidant may include either ambient air or vitiated air. The following deals with ambient air since vitiated air composition, including moisture content, is known from specifications. Dry ambient air contains the following fractions by weight: nitrogen (78.03%), oxygen (20.99%), and argon (0.98%). Moist ambient air contains moisture expressed in relative humidity, which is the percentage of actual water vapor pressure compared to saturation vapor pressure. PSAT is a series expansion for saturation vapor pressure as a function of temperature. Its coefficients were calculated from steam tables via a least-squares procedure, giving the equation

$$PSAT = \frac{\left[\begin{array}{l} 604.376 + 456.609\left(\frac{T - 273}{10}\right) + 140.785\left(\frac{T - 273}{10}\right)^2 \\ + 24.293\left(\frac{T - 273}{10}\right)^3 + 3.2214\left(\frac{T - 273}{10}\right)^4 + .28079\left(\frac{T - 273}{10}\right)^5 \end{array}\right]}{101325.0} \qquad (A3.2)$$

where T is temperature in °K.

Results are accurate to 1 percent over the range 273 K to 323 K. If conversion to newtons/m^2 is desired, omit division by 101325.

The remaining values in the program segment are for the density of water vapor in moist ambient air

$$DENSVAP = PVAP/(454.16*TAMB) \text{ kg/m}^3 \qquad (A3.3)$$

where PVAP = the actual vapor pressure in atmospheres,
for the density of moist ambient air [A6]

$$DENSAIR = 1.2929\left(\frac{273.13}{TAMB}\right)(PAMB - .3783\ PVAP)\ kg/m^3 \qquad (A3.4)$$

where PAMB = ambient pressure in atmospheres,
and for the density of the oxygen fraction of moist ambient air

$$DENSO2 = .2315(DENSAIR - DENSVAP)\ \ kg/m^3 \qquad (A3.5)$$

Calculation of coal chemical formula

A molecule of coal is defined on the basis of one carbon atom per coal molecule with sufficient fractional atoms or molecules of H, O, N, S, H_2O, and ash to be consistent with the wet basis ultimate analysis. The coal formula is

$$CH_{XH}O_{XO}N_{XN}S_{XS}(H_2O)_{XM}(ASH)_{XA} \qquad (A3.6)$$

where:

$XH = \frac{HYD}{CAR/12}$ kg-moles H/kg-mole coal

$XO = \frac{OXY/16}{CAR/12}$ kg-moles O/kg-mole coal

$XN = \frac{NITROGEN/14}{CAR/12}$ kg-moles N/kg-mole coal

$XS = \frac{SULFUR/32.1}{CAR/12}$ kg-moles S/kg-mole coal

$XM = \frac{MOISTURE/18}{CAR/12}$ kg-moles water/kg-mole coal

$XA = \frac{ASH/70.27}{CAR/12}$ kg-moles ash/kg-mole coal

and HYD, OXY, NITROGEN, SULFUR, MOISTURE and ASH are from the coal ultimate analysis. The molecular weight of a representative ash molecule has been calculated at 70.27. A typical analysis of Rosebud seam coal is given in Table A3.1. From these results molecular weight is calculated for wet, ash-free coal

$$FUELMW = 12 + XH + 16*XO + 14*XN + 32.1*XS + 18*XM \qquad (A3.7)$$

and for wet coal with ash

$$COALMW = FUELMW + 70.27*XA \qquad (A3.8)$$

These will be used in succeeding sections. FUELMW is used in calculations involving stoichiometry while COALMW is used in calculations involving mass flows.

Calculation of fuel composition

The basis of all calculations stoichiometry, energy balances, enthalpy, heats of formation, and moles in chemical equilibria, is the kg-mole of fuel. A kg-mole of fuel is that mixture of wet, ash-free coal, of dry seed, and of mixing water for the seed such that (1) the prescribed level of potassium seeding is reached and (2) the sum of the mole fractions of wet, ash-free coal, of dry seed, and of mixing water add to one, i.e., Avogadro's number (6.023×10^{26}) of molecules are present in a kg-mole of fuel . A kg-mole of oxidant is defined in a similar manner (see below).

It also contains the proper fraction of potassium by weight and its mole fractions sum to one. By defining kg-moles of fuel and oxidant in this manner, any stoichiometric ratio can be chosen and the resultant combustible mixture will always have correct seeding levels. Of course, this is only a computational procedure since all seed is injected at the point specified by SEEDINJ and is not actually divided between fuel and oxidant.

TABLE A3.1 Colstrip Subbituminous Coal

Proximate

Moisture	23.9%
Volatile matter	30.9%
Fixed carbon	37.6%
Ash	7.6%

Ultimate

Moisture	23.9%
Carbon	50.3%
Hydrogen	3.4%
Nitrogen	.7%
Sulfur	.4%
Oxygen	13.7%
Ash	7.6%

Ash

SiO_2	36.4%	CaO	22.7%
Al_2O_3	17.6%	MgO	9.4%
Fe_2O_3	4.6%	Na_2O	.3%
TiO_2	.4%	K_2O	.5%
P_2O_5	.8%	SO_3	14.9%

As an example, consider a coal with an ultimate analysis as shown in Table A3.2.

Table A3.2 Example Coal Ultimate Analysis

Constituent	Percent by Weight
C	59.832
H	3.964
O	14.187
N	0.875
S	0.903
Ash	15.237
Moisture	5.003
Total	100.000

It represents a typical Rosebud seam coal of Table A3.1 dried to about 5 percent moisture giving a molecular weight of 17.000 (FUELMW) without ash and a molecular weight of 20.056 (COALMW) with ash. Its equivalent coal formula is

$$CH_{.79501}O_{.17783}N_{.01253}S_{.00564}ASH_{.04349}(H_2O)_{.05574}$$

Since stoichiometric calculations are involved, FUELMW is used in the example.

Now assume that SEED=0.01 is specified as the seeding level, requiring that sufficient seed must be added, together with desired mixing water (WET = kg mixing water/kg dry seed), so that the coal-seed-water mix contains precisely 1 percent potassium by weight and the remaining 99 percent is composed of coal, mixing water, and the non-potassium components of dry seed. Also to make 1 kg-mole of fuel, COALMOLE + SEEDMOLE + WATERMOLE = 1.0, where the variable names are self-explanatory.

Continuing the example, suppose potassium carbonate is to be the seed and is to be mixed with water in a 1:1 ratio by weight (WET = 1.0). K_2CO_3 has a molecular weight of 138.2 and contains two potassium atoms having a total molecular weight of 78.2. The equation for SEEDMOLE is

$$\text{SEEDMOLE} = \frac{\text{SEED*FUELMW}}{78.2 + \text{SEED}(1 + 7.677778\text{WET})\text{FUELMW} - 138.2(\text{SEED}(1+\text{WET}))} \quad \text{(A3.9)}$$

in kg-moles K_2CO_3/kg-mole fuel. The required mixing water is

$$\text{WATERMOLE} = 7.677778 * \text{SEEDMOLE} * \text{WET} \quad \text{(A3.10)}$$

in kg-moles H_2O/kg-mole fuel. The value 7.677778 is (kg seed/kg-mole seed)/(kg water/kg-mole water). Results for this example are shown in Table A3.3.

Table A3.3 Constituents of 1 kg-mole Fuel

Constituent	Kg-moles	Kg
Coal	.98082	16.67392
K_2CO_3	.00221	.30542
Water	.01697	.30548
Total	1.00000	17.28482

Of the seed, 56.59 percent or .17284 kg is potassium, meeting the seeding requirement. Calculations for potassium sulfate (K_2SO_4, molecular weight = 174.2) and potassium hydroxide (KOH, molecular weight = 56.1) are of the same form with obvious modifications.

The final calculation associated with fuel is that for the feedrate

FUELRATE = COAL/(COALMW * COALMOLE) kg-moles fuel/sec (A3.11)

With oxygen enrichment and/or water vapor present, new values of mole fractions result, so that a normalization procedure is required. The results of this normalization are YMO2, YMN2, YMAR, and YMW which are mole fractions of O_2, N_2, Ar, and water vapor, respectively, per mole of moist (possibly oxygen enriched) air. If vitiated air is used, YM values are read directly from the input device and the normalization is omitted. In either case, molecular weight of oxidant is then calculated and subsequently is used in calculation of dry seed and mixing water mole fractions in a mole of oxidant.

Calculation of Oxidant Composition

A kg-mole of oxidant is that mixture of moist ambient air (possibly oxygen enriched) or of vitiated air, of dry seed, and of mixing water such that (1) the prescribed level of potassium seeding is reached and (2) the sum of all mole fractions in the ambient (possibly enriched) air or of vitiated air, of dry seed, and of mixing water is one. As in the definition of a kg-mole of fuel, Avogadro's number of molecules are present in a kg-mole of oxidant. The composition of a kg-mole of dry ambient air is .2099 kg-mole O_2, .7803 kg-mole N_2 and .0098 kg-mole Ar, which accounts for not only argon but all other trace elements in air.

Continuing the example above, in which a 1 percent potassium seeding level and a 1:1 dry seed-water mix was specified, assume ambient air at 1 atmosphere, no oxygen enrichment and 40 percent relative humidity at 293 K. Values of YMO2 = .208186, YMN2 = .773933, YMAR = .009722, YMW = .008159 and AIRMW = 28.8673 result. Calculations for mole fractions of dry seed and mix water are similar to those for a kg-mole of fuel

$$\text{ASEEDMOL} = \frac{\text{SEED} * \text{AIRMW}}{78.2+\text{SEED}(1+7.677778\text{WET})\text{AIRMW}-138.2\text{SEED}(1+\text{WET})} \qquad \text{(A3.12)}$$

and

$$AWATRMOL = 7.677778\ ASEEDMOL * WET \qquad (A3.13)$$

Finally, values of AIRMOL (kg-moles air, either ambient or vitiated/kg-mole oxidant) and the composition of ambient or vitiated air are calculated. Results for the example are shown in Table A3.3.

Table A3.3 Constituents of 1 Kg-mole Oxidant

Constituent	Kg-moles	Kg
Ambient Air (AIRMOL)	.967866	27.939709
K_2CO_3 (ASEEDMOL)	.003703	.511757
Water (AWATRMOL)	.028431	.511757
Total	1.000000	28.957580

The seed is 56.59 percent potassium or .289603 kg potassium, again meeting the seeding level specifications, within roundoff accuracy. A further breakdown of the constituents of ambient air is given in Table A3.4.

Table A3.4 Constituents of Air in 1 Kg-mole Oxidant

Constituent	Kg-moles	Kg
Oxygen (OXYMOL)	.201496	6.447872
Nitrogen (NITMOL)	.749063	20.973764
Argon (ARMOL)	.009410	.375930
Water Vapor (WMOL)	.007897	.142146
Total	.967866	27.939712

Calculation of Stoichiometric Oxygen Requirements

Stoichiometric oxygen is based upon requirements for complete combustion of C to CO_2, of H to H_2O, and of S to SO_2. Specifically,

$$STOICOXY = COALMOLE\ (1 + XH/4 + XS - XO/2)\ \frac{\text{kg-moles } O_2}{\text{kg-moles fuel}} \qquad (A3.14)$$

where, as before, the mole fractions are those contained in a kg-mole fuel. The total oxidant requirements are given by

$$SOXIDANT = STOICOXY/OXYMOL \text{ kg-moles oxidant/kg-mole fuel} \qquad (A3.15)$$

Completing the example, we find STOICOXY = 1.09408 $\frac{\text{kg-mole } O_2}{\text{kg-mole fuel}}$

and SOXIDANT = 5.42980 $\frac{\text{kg-moles oxidant}}{\text{kg-mole fuel}}$

Coal Particle Sizes and Distribution

Coal particles are assumed to be spherical and to be distributed in size according to the Rosin-Rammler equation [A7] whose distribution function is

$$f(x) = bsx^{s-1} \exp(-bx^s) \tag{A3.16}$$

and cumulative function is

$$R(x) = \int_0^x f(z)dz = 1 - \exp(-bx^s) \tag{A3.17}$$

where $R(x)$ = mass fraction of material having diameters less than x

$b = (\frac{1}{\bar{x}})^s$

s = distribution constant, a measure of the spread of particle sizes. Low values (1.0-2.0) indicate a wide size distribution. High values (6.0-15.0) indicate a tight size distribution.

$\bar{x}$ = size constant, that diameter such that $1 - \frac{1}{e}$ mass fraction of particles have diameters less than $\bar{x}$ (or $\frac{1}{e}$ have diameters greater)

A truncated distribution of twenty piecewise constant segments is assumed. Each segment has f(x) evaluated at its center point, giving a cumulative distribution that is a piecewise summation of rectangles rather than a true integration. The smallest segment is centered at XD; the largest is centered at XL; and they are of length (XL-XD)/19. Since the summation will not equal one (whereas the integration will), normalization is done to give this condition. The result of each rectangular integration is called WFRAC(I) and the number of coal particles, /kg-mole fuel, in each segment is W(I).

A3.1.2 Preparation for Energy Balance and Temperature Determination

After printing initial conditions, geometry, and other values calculated above, complete fuel and oxidant compositions are calculated. At this time XH, XO, XN, XS, XA, and XM are converted to kg-moles component/kg-mole fuel from kg-moles component/kg-mole coal. XFIX is introduced as kg-moles fixed carbon/kg-mole fuel. Gaseous components of oxidant are loaded into the CONC array, which is otherwise empty. This is done in preparation for calculation of enthalpy and chemical composition of preheated air by subroutine EQUILZ. Seed and mixing water are not transferred to CONC since they will be retained for injection at the proper point specified by SEEDINJ. Slag rejection is also calculated so that only carryover slag remains in calculations. Fuel and oxidant information is then printed.

The first call to EQUILZ is made to calculate enthalpy of preheated air in joules/kg-mole fuel* and the chemical composition of preheated air at preheat temperature. Typically, there are traces of NO_x and dissociation of other gases. A calculation is then made of the heat of vaporization required for moisture in the coal and of the enthalpy (sensible heat) of the moist coal at COALTEMP. A conversion factor of 1 kcal/g-mole=4186 joules/kg-mole appears through this section.

All components of coal with the exception of fixed carbon and slag are assumed to be volatiles. It is further assumed that devolatilization of combustibles is instantaneous, leaving a set of more or less spherical, perhaps swelled, char particles, composed of carbon and slag. Their burnout is controlled by particle size, temperature, and oxygen availability, in a process described in section 4. Volatile species are complex and a complete analysis of their forms and concentrations is beyond the scope of this program. However, calculations show that standard heats of formation of CO_2, H_2O and SO_2 [A8] are within about 1% of the Dulong formula [A5] so that when combustion is complete, use of standard heats of formation will yield an acceptably accurate result. Hence, the volatiles are treated as monatomic carbon and sulfur; and diatomic hydrogen, oxygen and nitrogen.

The CONC array is loaded with these molar concentrations (kg-moles/kg-mole fuel) along with moisture in the coal and carryover ash. CONC(31) is reserved for fixed carbon (char) in kg-moles/kg-mole fuel and is not used in calculating equilibrium. Seed and mixing water from both fuel and oxidant are then combined in a single variable for seed (SEEDMOLE) and a single variable for mixing water (WATERMOLE). Both are in kg-moles/kg-mole fuel.

A combustion temperature is assumed (TEMP = 2500 K is a typical value) and EQUILZ is called. The results of EQUILZ are: (1) chemical equilibrium concentrations (in kg-moles species/kg-mole fuel) of volatiles and preheated air at TEMP, (2) standard heats of formation (in joules/kg-mole fuel) of incoming reactant species and outgoing product species, giving a measure of heat release, and (3) enthalpy of the resultant combustion gas-char particle mixture (in joules/kg-mole fuel). This call to EQUILZ is intended only to give a starting point for char burnout and energy balance calculations and is not theoretically necessary in computing burnout and energy balance. But it does reduce the number of iterations required in EQUILZ when char burnout takes place. EQUILZ allows only 50 major iterations in determining chemical equilibrium before it takes the last values as the output, regardless of whether convergence criteria are satisfied. Since the number of major iterations is dependent upon the nearness of input concentrations to final concentrations, it is reasonable to precalculate the results of volatile combustion.

A3.1.3 Temperature Determination

Temperature determination is done by finding zeros of an energy balance vs. temperature curve. The entire plug of fuel, oxidant and combustion

---

*Units of joules/kg-mole fuel appear frequently. The set of dimensions implied are (joules/kg-mole species)(kg-moles species/kg-mole fuel).

gases is partitioned into slices and an energy balance is calculated for each slice, beginning at the input and progressing along the combustor. Slice thickness is determined by the time of passage (DT) through that slice. An initial burning time of 2 msec is tried and adjusted up or down by multiples of 2 or .5 such that between 2 percent and 5 percent of the original char is burned in each slice. As char burnout progresses there is a tendency to produce very thick slices with the 2 percent minimum burnout criterion so an additional constraint is imposed, which limits slice thickness to 10 percent of total first stage length.

The energy balance is quite straightforward. Energy supply to a slice is composed of (1) enthalpy output from the previous slice and (2) the heat of formation appearing in a slice (HFDIFF), which is the difference between heat of formation of input reactants (HF298FST) and output products (HF298OUT). Since JANAF tables [A8] or their equivalent are used for all enthalpy and heat of formation calculations, enthalpies are positive but heats of formation are negative if net positive heat is produced. Hence HFDIFF=HF298FST-HF298OUT. This reversal of terms gives a positive value for heat release and is used throughout.

Energy demand by a slice to achieve a given temperature is composed of (1) its final enthalpy (HOUT), (2) its heat loss to the walls (HLOSRATE), and (3) heat loss of its rejected slag (HSLAG). Slag heat loss is assumed to be uniform throughout, with each slice losing slag in proportion to its thickness. The temperature of rejected slag is assumed to be sidewall temperature (TS). Some adjustment of dimensions is necessary since HINPUT, HDIFF, HOUT and HSLAG are in joules/kg-mole fuel and HLOSRATE is in watts. This is done by multiplying the former by FUELRATE in kg-mole fuel/sec so that the energy balance term (HRATE) is in watts.

In order to get a correct value of HFDIFF it is necessary to preserve the heat of formation and enthalpy of input reactants to a slice. These values are stored in HF298FST and HINPUT, respectively. Since the heat of formation of char (carbon) is zero, the amount of carbon calculated by COMBU as available has zero effect on heat of formation and it is correct to use the heat of formation of the preceding slice final products as HF298FST for the next slice. The final HOUT of the preceding slice is used as HINPUT. Energy balance calculations involve calls to COMBU, EQUILZ and QLOSS. COMBU uses the current char particle sizes (X(I)), partial pressure of O_2 and O (PTERM), and temperature (TEM) to calculate the amount of char that would be burned in the given time interval (DT). EQUILZ calculates heats of formation of input reactants and output products, i.e., the chemical composition of products (CONC(I)), enthalpy of output products (HOUT), in joules/kg-mole fuel, and electrical conductivity of combustion products (SIGMA) in mhos/meter. QLOSS calculates heat loss in watts from the slice in question.

The general shape of the energy balance vs temperature curve is shown in Figure A3.1. Zero finding of the curve is done by selecting two temperatures separated by 10 K and calculating an energy balance term for each. The initial temperature used in a given slice is the final temperature from the preceding slice (TEMP) and is stored in TEM. TLOOP = 1 is used to

$T = T + DT$ Total residence time, msec. (A3.23)

$DIST = DIST + DDIST$ Total axial distance, meters (A3.24)

$FHLOS = HLOSS/HSUPPLY$ Fractional heat loss in watts cumulative loss/watts coal thermal input (A3.25)

$$HTOT = \frac{HOUT}{AVMW*CONC(30)*PRESS+CONC(31)*12.0}$$ specific enthalpy joules/kg gas-char mix (A3.26)

Preparation for next slice calculations is done by the equations

$HINPUT = HOUT$ joules/kg-mole fuel (A3.27)

$HF298FST = HF298OUT$ joules/kg-mole fuel (A3.28)

$UOLD = US$ mass fraction char unburned, cumulative (A3.29)

$DUOLD = 0.0$ a temporary variable used in calculating mass fraction char burned in current slice (A3.30)

and

$$PTERM = \frac{(CONC(2)+CONC(3))}{CONC(30)}$$ Partial pressures of O_2 and 0 atm (A3.31)

The first two equations are well-known by this time. US is returned from the call to COMBU and is the mass fraction of original char that remains unburned. It is stored in UOLD to use in calculating DU, the mass fraction of char burned in the current slice. DUOLD is a temporary variable used in calculating char burned in a slice. It is explained in the section on COMBU. PTERM is used in COMBU to calculate char particle burnout. The last operations are the storage of XOLD(I) into X(I) and the printing of slice results.

A3.1.4 Testing and Program Flow After Temperature Determination

Next Slice Thickness and End of First Stage

Several tests are made after temperature determination is complete. The first establishes whether calculations have been made for the last slice of the first stage (KEND = 1 for no; KEND = 2 for yes). The possibilities under the yes condition (KEND=2) will be considered later. They are (1) that the just completed temperature determination was for the final slice of the first stage or (2) that it was for the second stage. If the result is no (KEND = 1), the next slice thickness is adjusted if necessary to keep it at 10 percent or less of first-stage length. Thickness adjustment begins with prediction of next slice thickness, made by multiplying current slice thickness (DDIST) by the multiplier constant of the time slice (MCDT, which is either 1.0 or 2.0). The clear assumption is that velocity changes slowly along the combustor and this is supported by experience in using the model.

If the predicted slice thickness exceeds 10 percent of the first stage length, MCDT is set to 1.0 so that the next slice will be approximately the same as the current slice in thickness (which has satisfied the thickness constraint). If the 10 percent constraint is met, no change is made in MCDT.

In any event, a new value of DT is calculated by DT = DT*MCDT and a temporary prediction of total plug length (DX) is made to see if the extreme boundary of the plug extends beyond the first stage exit. If so, the next slice will be the final one of the first stage and KEND is set to 2. DT is modified on a proportional basis to give a value that will take the plug boundary to the first-stage exit, assuming negligible velocity change.

$$DT = \frac{1000(LENGTH-DIST)}{VEL} \text{ msec.} \qquad \text{(A3.32)}$$

Otherwise no action is taken and the succeeding test is made.

Seed Injection

The next test is of KINPUT to see if seed has been injected (KINPUT = 1 if not; KINPUT = 2 if so). If seed has been injected, TEM is set to TEMP, TLOOP is set to 1 and a return is made to the temperature determination loop. Before re-entering the actual energy balance-temperature calculations, a test is made to see if first stage calculations should be continued, or if first stage calculations are complete and preparations should be made for second stage calculations (NEND = 1 for re-entry of first stage calculations; NEND = 2 for completion of first stage and preparation of second stage calculations). Second stage preparation and program flow are convered in a subsequent section.

If seed has not been injected, a test is made to see if DX, the predicted plug boundary exceeds the seed injection point (SEEDINJ). If not, TEM is set to TEMP, TLOOP is set to 1 and the temperature determination loop is re-entered through the test of NEND just described.

If DX≥SEEDINJ, seed injection is indicated, and CONC(15+KSEED) is set to SEEDMOLE in kg-moles dry seed/kg-mole fuel. Note that KSEED=1 for K_2CO_3, KSEED=2 for K_2SO_4 and KSEED =3 for KOH so that we are dealing with CONC(16), CONC(17), or CONC(18), respectively. CONC(11) is set to CONC(11)+ WATERMOLE, preserving previous water content of combustion gases and adding the seed mixing water in kg-moles water/kg-mole fuel. QVAP = 10500.8*WATERMOLE*4186 is the heat of vaporization of the mixing water in joules/kg-mole fuel. (The constant 4186 is a conversion factor from calories to joules.) QVAP is subtracted from HINPUT to give a new HINPUT, and HF298FST is adjusted by the heats of formation of seed and mixing water.

HF298FST=HF298FST+SEEDMOLE+HFSEED(KSEED)-WATERMOLE*57.978 (A3.33)

Because of the expected temperature drop after seed injection, TEM is set to TEMP-35.0 to being the next slice energy balance calculations. Finally, control variables are set to KINPUT=2 and TLOOP=1. Then the temperature determination loop is re-entered through the test of NEND.

A3.1.5 Second-Stage Calculations

If the last energy balance was for either the last slice of the first stage or for the second stage (KEND=2 in both cases) a test is made of NEND to see which of these conditions holds: NEND=1 if last slice of first stage just completed; NEND=2 if second stage just completed. If the second stage computations are complete, the program returns to the input device for a new problem. If they are yet to be done, NEND is set to 2, indicating the next set of calculations are for the second stage. This is followed by a test of NCOMB to see if a second stage was specified (NCOMB=1 for single stage; NCOMB =2 for two stages). If NCOMB=1, the program returns for a new problem. If there is a second stage, KINPUT is tested to see if seed was or was not injected in the first stage. If seed has not been injected in the first stage, it is automatically injected in the second stage and the previously described sequence for adjusting seed and water concentrations, enthalpy, heat of formation, first trial temperature, and control variables is executed.

A return to the temperature loop determination is made through the test of NEND. This time NEND=2 and preparation is made for second stage combustion and heat loss calculations. It is assumed at this time that all remaining char will be burned, so the second stage is done in one pass rather than on a slice-by-slice basis. (Consideration is being given to changing this to a multi-slice procedure, rather similar to the first stage, but it is not of high priority.) In order to use the same temperature determination loop, the variables for geometry and parameters of the second stage are loaded into corresponding locations for first-stage variables. Then the remaining preheated oxidant components are added to the CONC array, along with the enthalpy of the oxidant, and the temperature loop is entered, this time bypassing COMBU since it is assumed that all char has been burned off.

Following temperature determination, the output values of component concentrations velocity, heat loss, mass flow, etc., for the second stage are calculated and printed. Tests are made of KEND and NEND, both of which are 2, and the program returns for a new problem.

A3.2 Subroutine EQUILZ

This subroutine calculates (1) the chemical equilibrium of combustion products in kg-moles component/kg-mole fuel, (2) the enthalpy of the char-gas mixture in joules/kg-mole fuel, (3) the total heat of formation of incoming reactants and outgoing products in joules/kg-mole fuel, and (4) the average molecular weight of gaseous products. It also calls subroutine CONDUCT which calculates the electrical conductivity of the seeded combustion gases in mhos/meter.

The program begins with several arrays of DATA statements. The first two are (1) coefficients for second order curve fits of cross-sections (for species required by CONDUCT) and (2) enthalpy. The enthalpy curve fits are for $H\text{-}H_{298}$ and are mostly from JANAF tables [A8]. Values for K_2CO_3, K_2SO_4, K^+ are from Howald and Eliezer [A9]. All enthalpy curves are fitted over the range from 1500 K to 3000 K with less than 1 percent error.

Arrays of heat of formation, ΔH°_{f298}, and molecular weights follow. Heat of formation data are from the same sources as the enthalpy curves.

The fifth DATA statement is for the equations themselves and contain all data for determining both the equations and associated reaction constants as functions of temperature. Each equation appears as a separate line and carries an identifier in cols, 73-80. The first entry defines the number of reactants in the equation; the next three entries identify the reactants from the COMNAM list and the next three entries are coefficients of the reaction. Entries eight through fourteen give similar information for the products with an additional datum as explained below. The last two entries are α and β, respectively, for the equilibrium constant, which is given by

$$Kp = 10^{\left(\frac{\alpha}{T}+\beta\right)} \quad , \; T \text{ in } ^{\circ}K \tag{A3.34}$$

for most reactions. Exceptions are those for the reactions

$$2KOH \rightleftarrows (KOH)_2$$

$$2K + O_2 \rightleftarrows K_2O_2$$

and

$$NO^- \rightleftarrows NO + e^-$$

which have the form

$$Kp = 10^{\left(\frac{\alpha}{T}+\beta\right)} T^{2.5} \tag{A3.35}$$

where T = temperature, degrees Kelvin.

As an example of interpreting equation coding, equation 1 has data fields

2, 5,2,0, 1.,.5,0., 1, 11,0,0, 1.,-.5,0., 13100.,-3.000

There are two reactants having identifiers 5 and 2 (the third reactant identifier is unused and, as are all unused identifiers, is set to zero as an aid in visual scanning of fields), and coefficients 1 and 1/2, respectively. Thus equation 1 deals with H_2 and $\frac{1}{2}$ O_2 as reactants. One product results and is recognized as H_2O through its identifier of 11. The coefficient array contains 1 and -1/2 which are interpreted to be (1) the product coefficient, and (2) the net change in total moles if mole fractions are reactants as specified by reactant coefficients are supplied and the reaction goes to completion. This change in total moles is present in every product coefficient set, giving one more entry in the set than there are products.

Finally, ALPHA(1) = 13100 and BETA(1) = -3.000. For a temperature of 2500 K, we get the equilibrium constant

```
EQUIL(1) = 10**(ALPHA(1)/TEMP + BETA(1))
         = 3181.0
```

The completely decoded reaction is

$$H_2 + \frac{1}{2} O_2 \rightleftarrows H_2O$$

with Kp = 3181.0 at 2500 K and a net loss of 1/2 mole for indicated moles supplied and the reaction carried to completion.

The mode of operation is to solve sequentially the complete set of equilibrium equations until the results of two successive solution passes through the entire set differ by less than some prescribed error for each equation. A value of 1 percent change has been used as the error. A flow chart of the overall program is given in Figures A.

Some description of the solution procedure for individual equilibrium equations is warranted. Assume that the reaction

$$aA + bB \rightleftarrows cC + dD \tag{A3.36}$$

if of interest. The associated mass action equation is

$$\frac{[C]^c\ [D]^d}{[A]^a\ [B]^b} = K_p \tag{A3.37}$$

where [A] is the partial pressure of component A in atmospheres and K_p is the equilibrium constant for the reaction (K_p is not actually constant but is instead a strong function of temperature. However, the name persists.).

Expanding (A3.37)

$$\frac{[C]^c\ [D]^d}{[A]^a\ [B]^b} = \frac{(\frac{N_C}{N_T} P_T)^c (\frac{N_D}{N_T} P_T)^d}{(\frac{N_A}{N_T} P_T)^a (\frac{N_B}{N_T} P_T)^b} = \frac{N_C^{\,c}\ N_D^{\,d}}{N_A^{\,a}\ N_B^{\,b}} (\frac{N_T}{P_T})^{[(a+b)-(c+d)]} \tag{A3.38}$$

Where N_A is the molar concentration of A; N_T is the total number of moles and P_T is the total pressure in atmospheres.

Now pick as a basis the reactant of least availability, i.e., the reactant that will be depleted first as the reaction proceeds toward completion. This is not necessarily the reactant of least concentration but is found from min $\{\frac{N_{A_o}}{a}, \frac{N_{B_o}}{b}\}$ (where N_{A_o} is the beginning of concentration of A) and is influenced by a and b. Assume the basis is A. Then for the forward reaction we can write the mass action equation as a function, f(x), of the fractional conversion of A, which is called x.

$$f(x) = \frac{(N_{C_o} + \frac{c}{a}xN_{A_o})^c (N_{D_o} + \frac{d}{a}xN_{A_o})^d}{(N_{A_o} - xN_{A_o})^a (N_{B_o} - \frac{b}{a}xN_{A_o})^b} \left\{\frac{N_{T_o} + \frac{[(c+d)-(a+b)]}{a}xN_{A_o}}{P_T}\right\}^{[(a+b)-(c+d)]} - K_p = 0 \quad \text{(A3.39)}$$

There is either a root of the equation for $0 \leq x \leq 1$ or the equation reverses.

It is important to note that (A3.39) is both a mass action equation and that it also implicitly demands safisfaction of the mass conservation equation of the elements involved through the proper addition or subtraction of the fractional conversion of the basis reactant. For reactions that reverse, the counter part of (A3.39) is

$$f(x) = \frac{(N_{A_o} + \frac{a}{c}xN_{C_o})^a (N_{B_o} + \frac{b}{c}xN_{C_o})^b}{(N_{C_o} - xN_{C_o})^c (N_{D_o} - \frac{d}{c}xN_{C_o})^d} \left\{\frac{N_{T_o} + \frac{[(a+b)-(c+d)]}{c}xN_{C_o}}{P_T}\right\}^{[(c+d)-(a+b)]} - \frac{1}{K_p} = 0 \quad \text{(A3.40)}$$

where C is assumed the basis and is found from $\min\{\frac{N_{C_o}}{c}, \frac{N_{D_o}}{d}\}$.

Before the equilibrium loop is executed a check is made to see if the temperature is less than 1800 K. If so, the last three ionization equations (for NO^-, NO_2^- and O^-) are skipped and the concentrations of NO^-, NO_2^- and O^- are zeroed because their concentrations at temperatures below 1800 K are negligible. The heat of formation, $\Delta H^\circ_{f_{298}}$, for the incoming reactants is calculated and converted from Kcal/g-mole to joules/kg-mole by the factor 4.186×10^6. Finally, any K_2CO_3 is broken into CO and K_2O_2 since it is assumed that K_2CO_3 completely decomposes at combustion temperatures.

The major equilibrium iteration loop is executed once for each equation and consists of an equation preparation section and a root finding section. Equation preparation makes a transfer of reactant concentrations and coefficients from the large CONC and RCOEFF arrays to the smaller REACT(J,1) and REACT(J,2) arrays that are used in the actual equation solution. Then a scan is made to find the basis identifier (IBASIS(I)) for the forward reaction. The transfer is done for products to PROD(J,1) and PROD(J,2) and the reversed reaction basis identifier (IBASIS(I+21)) is found. A root is first sought in the forward direction (CONTRL=1. in forward direction; CONTRL=-1. in reverse direction). If no root exists in the forward direction, the reaction reverses and a root is found for the reversed reaction. After the root (fractional conversion of basis) in the correct direction has been found, subroutine CORRCT is called to modify the component concentrations in the CONC array in accord with the conversion of the reaction under consideration. In the first call to CORRCT of a major iteration, the TEST array is loaded with initial CONC array values to provide a set of comparison values from the last major iteration for convergence testing.

The test section for approach to equilibrium begins with a check of the number of major iterations performed. If some maximum number have been done (the current number is 50) without reaching equilibrium in any preceding iteration, the program terminates the search for equilibrium and passes to the section in which mole fractions, (MOLEFR) partial pressures (PARTP) in atmospheres and average molecular weight (AVMW) of output products are calculated, using the results of the final iteration as output values. A check of total pressure (PPART) is made by summing all partial pressures. This is the value that appears in the output under total pressure. If the maximum number of major iterations have not been performed, the test is made to see if concentrations of the last two iterations (in CONC and TEST, respectively) differ by less than the prescribed error (currently 1%) for each equilibrium equation. Concentrations of less than 10^{-6} mole fraction are not tested for convergence since the effect of such small concentrations varying by more than 1 percent is negligible. If the test for every equation is passed, control passes to the section in which mole fractions, partial pressures and average molecular weight are calculated. If any equation fails the convergence test, the major loop is immediately repeated.

Following calculations of mole fractions, partial pressures and average molecular weight, the heat of formation of outgoing products is calculated as

$$\Delta H^{\circ}_{f298} = \sum_{i=1}^{n} \Delta H^{\circ}_{f_i 298} \, CONC_i \text{ Kcal/g-mole fule} \qquad \text{(A3.41)}$$

where $\Delta H^{\circ}_{f_i 298}$ is the heat of formation of the ith component in kcal/g-mole and $CONC_i$ is its concentration in moles component/mole fuel. The conversion to joules/kg-mole fuel is made through multiplying by 4.186×10^6.

Enthalpy of outgoing products is calculated by a similar summation in which the ith component is itself given by a series expansion

$$H\text{-}H_{298} = \sum_{i=1}^{n} \sum_{j=0}^{2} HCA(i,j)T^j \quad \text{kcal/g-mole fuel} \qquad \text{(A3.42)}$$

where HCA(i,j) is the jth coefficient for the enthalpy of the ith component and T is a defined temperature in °K/1000, used simply to get reasonable coefficients in the HCA array. The first calculations are enthalpy of gas only, followed by addition of char particle enthalpy to give total enthalpy of the gas-char mixture. The conversion to joules/kg-mole fuel is also made.

The final action of EQUILZ is to transfer appropriate concentrations from CONC to the SPEC array in preparation for calling CONDUCT, which calculates electrical conductivity.

A3.3 Subroutine ROOT

This subroutine evaluates the root of either reaction equation (A3.39) in the forward direction or equation (A3.40) in the reverse direction, depending on which direction the reaction proceeds.

The fractional conversion of basis, x, is the root desired. The first call to root assumes a forward reaction (CONTRL=1.0) and a test of f(0) is made to determine validity of this assumption. If $f(0) < 0$, the reaction is indeed forward; if $f(0)>0$ the reaction reverses; and if $f(o)=0$ the root is zero.

If the reaction is forward, the solution section is entered with FUNCTION FWD as the function called. If the reaction is reversed, ROOT returns to EQUILZ to have FUNCTION REV established as the function called and CONTRL set to -1.0. ROOT is entered again with program flow passing immediately to the solution section.

The solution procedure is to evaluate repeatedly and do interval halving in the proper direction, depending on the evaluation. If the evaluation is negative, increase x; if positive, decrease x. Some equations tend very strongly toward completion (either forward or reversed) so that a value of x=0.9 is tried first. If a greater value of x is indicated, rapid steps of x=0.99, x=0.999 etc. are attempted until a sign change is encountered in f(x). When the sign change is found, an interval halving routine is entered to establish the solution.

A solution is defined as the midpoint of two values of x (x_{high} and x_{low}) such that (1) f(x) undergoes a sign change for the two values, i.e. that $f(x_{low})*f(x_{high}) \leq 0$, and (2) that $x_{high}-x_{low}$ is less than some prescribed value, usually 10^{-6} for the test runs.

If no sign change occurs before x=0.999999, the value of x=0.999999 is used to replace the old concentrations with new ones and the root finding routine is entered again for that equation. If no root has been found after four such trials, i.e., if $x>1-10^{-24}$ is indicated, $x=1-10^{-24}$ is assumed good enough for that particular major iteration. Despite single precision arithmetic, the value of $x=1-10^{-24}$ is the effective value since x=0.999999 is used in four consecutive replacements of beginning concentrations by newly calculated concentrations.

If $x<0.9$ is indicated, x is decreased in steps of 0.1 until a sign change is encountered. At that point the interval halving routine is again used.

A3.4 Subroutine CORRCT

This subroutine adjusts the CONC array to reflect the fractional conversion, x, of the basis in the just solved reaction equation. It is appropriate for either forward or reversed reactions and also readjusts CONC(30), total kg-moles gas/kg-mole fuel. On the first call to CORRCT of a major iteration loop in EQUILZ, the TEST array is loaded with CONC array values, forming an array to be used in equilibrium convergence testing.

A3.5 Subroutine COMBU

This subroutine calculates the reduction in size of char particles during combustion and adjusts component concentrations as necessary prior to calling EQUILZ. Char burn off rate is a function of particle temperature and partial pressure of oxygen. Char particle size reduction is a function of burnoff rate, original particle size and residence time.

Both chemical resistance and diffusion resistance are used in calculating the burning rate

$$q = \frac{P}{\frac{1}{K_s} + \frac{1}{K_{diff}}} \qquad \text{(A3.43)}$$

where q = burning rate in gm/cm^2 sec

P = partial pressure of O_2 in atmospheres

K_s = chemical resistance

K_{diff} = diffusion resistance

The expression for chemical resistance was established by Field, Gill, Morgan, and Hawksley [A10] through curve fitting of data from several investigators

$$K_s = 8710 \exp(-35700/RT) \text{ gm/cm}^2 \text{ sec-atm} \qquad \text{(A3.44)}$$

where R = gas constant, 1.987 cal/g-mole °K

T = temperature, K

The value of diffusion resistance is

$$K_{diff} = 24\ \phi\ D/xRT \qquad gm/cm^2\ \ sec\text{-}atm \tag{A3.45}$$

where ϕ = mechanistic factor = 1 if product being transported from the surface to bulk is CO_2
= 2 if product is CO

R = gas constant, 82.06 atm cm^3/mole °K

x = particle diameter, cm.

T = temperature, K.

and D, the diffusion coefficient, is given as

$$D = 0.207\left(\frac{T}{300}\right)^{1.68} \tag{A3.46}$$

giving

$$K_{diff} = 0.083467\ T^{0.68}/x$$

where x is now in microns rather than cm, since coal particle sizes are given in microns. The combustion product is assumed to be CO. So the burning rate can now be written as

$$q = \frac{P}{1.148 \times 10^{-4}\ \exp(17967/T) + 11.971\ T^{-0.68} x}\ \frac{gm}{cm^2 sec} \tag{A3.47}$$

with x again in microns. It is now postulated that the coal not containing volatiles, i.e., the char, has a density of ρ gm/cm^3 and α is the factor giving change of diameter caused by volatiles combustion. Thus, after devolatilization, each char particle increases in diameter to a value α times that of the original coal particle. The new char particle diameter is called x. The rate of combustion of fixed carbon can be written as

$$qA = q\pi(x\cdot 10^{-4})^2 \quad gm/sec \tag{A3.48}$$

with x in microns.

The combustion rate can also be written in volume density terms as a differential equation

$$\frac{d\ char}{dt} = -\frac{d}{dt}\left[\frac{4}{3}\pi\left(\frac{x}{2}\cdot 10^{-4}\right)^3\rho\right] = -\frac{\pi}{2}\cdot 10^{-12}\ x^2\rho\frac{dx}{dt}\ \ gm/sec \tag{A3.49}$$

with x in microns, t in seconds. When these rates are equated

$$q\pi x^2\cdot 10^{-8} = -\frac{\rho\pi}{2}\ x^2\cdot 10^{-12}\ \frac{dx}{dt}$$

or

$$\frac{dx}{dt} = -2\cdot 10^4 \frac{q}{\rho} \qquad \frac{\text{microns}}{\text{sec}}$$

$$= -20 \frac{q}{\rho} \qquad \frac{\text{microns}}{\text{sec}} \tag{A3.50}$$

The latter units are used in the program.

Now the equation can be written

$$\frac{dx}{dt} = -20 \frac{q}{\rho} = \frac{-P}{\frac{\rho}{20}\frac{1}{K_s} + \frac{\rho}{20}\frac{1}{K_{diff}}}$$

or

$$\frac{dx}{dt} = \frac{-P}{A + Bx} \qquad \frac{\text{microns}}{\text{sec}} \tag{A3.51}$$

where $A = \frac{\rho}{20K_s}$

$$B = \frac{\rho}{20(0.093467)T^{0.68}}$$

The variables are separable to

$$\int_x^{x_n} (A+Bx)dx = \int_t^{t_n} - P_{O_2}\, dt$$

and integrating over small times (where P_{O_2} is assumed constant) results in

$$A(x-xn) + \frac{B}{2}(x^2-x_n^2) = P\delta t \tag{A3.52}$$

Particles below a critical size x_c will be annihilated. This critical size is that for which $x_n=0$, so that

$$A(x_c-0) + \frac{B}{2}(x_c^2 - 0) = P_{O_2}\delta T \tag{A3.53}$$

giving

$$x_c = \frac{A}{B}\left[\sqrt{1 + \frac{2BP\delta t}{A^2}} - 1\right] \tag{A3.54}$$

For $\frac{2BP\delta t}{A^2} < .001$, evaluation of the square root is done by a power series for greater computational accuracy, using the relation $\sqrt{1+\varepsilon}=1+1/2\varepsilon$ which is accurate to within .00002 percent when $\varepsilon<.001$. Then the critical size is

given by

$$x_c = \frac{P\delta t}{A} \text{ for } \frac{2BP\delta t}{A^2} < .001 \tag{A3.55}$$

For particles not completely burned, the new size is given by

$$x_n = \frac{A}{B}\left[\frac{B^2}{A^2}x^2 + \frac{2B}{A}x + 1 - \frac{2BP\delta t}{A^2} - 1\right] \tag{A3.56}$$

when $\frac{B^2}{A^2}x^2 + \frac{2B}{A}x - \frac{2BP\delta t}{A^2} < .001$

the expression for x_n is

$$x_n = \frac{B}{2A}x^2 + x - \frac{P\delta t}{A} \tag{A3.57}$$

The second portion of COMBU consists of checks to see if the mass fraction of char burned ranges between 2 percent and 5 percent of the original char. If more than 5 percent is combusted, X(I) is replaced by the original x value, XOLD(I), DT is halved, and the particle burn calculations are re-entered. If less than 2 percent is burned off, the main program is signalled to increase DT by setting MCDT=2, but the results of the charburn calculations are used in the current-slice energy balance. DT is not increased until the current energy balance is completed.

The third and final portion of COMBU adjusts concentrations of C, CO, CO_2, O_2, and fixed carbon in accord with the amount of char burnoff just calculated. The secant-line method of temperature determination requires establishment of two points on the energy balance-temperature curve for every new temperature (of which there may be several before convergence). Each such point requires distinct calculations of char burnoff and chemical equilibrium based upon conditions of char particle size and chemical composition existing at the input to the slice. Therefore, some means of preserving original conditions (or their equivalent) is necessary. Original char particle sizes for a slice are retained in an array called XOLD, which the main program loads with the X array prior to entering the temperature determination section for the slice. While in the temperature determination section, the MAIN program replaces X(I) with XOLD(I) before a call of COMBU. Partial oxygen pressure (PTERM) is not changed during temperature determination. Thus the only non-constant factor in determining char burn is temperature, which is a necessarily varied in seeking an energy balance.

To remain consistent with the policy of returning to original conditions of a slice, the CONC array should also be preserved prior to calculations for a slice. It would be restored upon the call to EQUILZ, with only the new carbon released by the charburn inserted into CONC(1). But it

is wasteful of computer time to continually make a major adjustment of equilibrium concentrations when a minor adjustment will yield identical ultimate results, and in less time. So, instead of resetting the entire CONC array to original conditions, only concentrations of C, CO, CO_2, O_2, and fixed carbon are adjusted in the final portion of COMBU.

The amount of char burned (kg-mole carbon/kg-mole fuel) in any call to COMBU is stored in DUOLD and is compared with the char burned in the next call to COMBU. DUOLD is set to zero by the MAIN program prior to temperature determination. Details of this procedure are given below.

The value

$$\text{DCHAR} = (\text{DU} - \text{DUOLD})*\text{XFIX}*\text{COALMOLE}\ \frac{\text{kg-moles carbon}}{\text{kg-mole fuel}} \qquad \text{(A3.58)}$$

is the difference between char burnoff calculations on two successive calls to COMBU. Action to be taken in adjusting CONC depends on the value of DCHAR.

If DCHAR is zero (highly improbable), both calls to COMBU caused the same char burn off and no adjustment of CONC is necessary.

If DCHAR is positive, the most recent call of COMBU produced more char burnoff than the preceding one (a higher temperature is the cause since X, PTERM, and DT are the same). CONC(1), the carbon, is increased by DCHAR and CONC(31), the fixed carbon, is decreased by DCHAR.

If DCHAR is negative, the most recent call of COMBU produced less char burnoff than the preceding one. Some carbon containing components must be reduced in concentration to give a starting point for EQUILZ. Because negative concentrations cannot be used by EQUILZ, CONC(1) must remain non-negative and cannot be reduced. The candidates for reduction are CO_2 and CO. CO_2 is the first to be reduced to C and O_2. If its concentration is sufficient to allow all of DCHAR to be used in conversion to C and O_2, COMBU returns to the calling point. If there is not sufficient CO_2 to accomodate all of DCHAR, all CO_2 is reduced to C and O_2, followed by sufficient reduction of CO to C and O_2 so that all of DCHAR is used. There is no provision for reduction beyond the CO_2 and CO reactions since it is unimaginable that such a condition could exist. Following the reductions, CONC(31) is increased by |DCHAR| to give the correct concentration of fixed carbon.

A3.6 Subroutine QLOSS

This subroutine calculates the combined radiative and convective heat loss of the combustor. Most of the subroutine is concerned with calculation of gaseous and particle emissivity. The most important gaseous emitters of radiant heat are H_2O and CO_2, and are the only gases considered here. The emissivity of these gases is calculated using the equations from Leckner [A11]. The general procedure is to calculate the emissivities of each gas separately at a specific path length and temperature. Leckner presents curve fits which have a maximum deviation of 5 percent from values

calculated with spectral data. These curves are valid at atmospheric pressure and zero partial pressure. Increased pressure causes the spectral lines to broaden, thus causing the emissivity to increase. By means of a pressure correction correlation, the actual emissivity is calculated. After the emissivity of each gas is independently calculated, their emissivities must be combined. This is done by adding the individual emissivities and then subtracting an appropriate quantity to account for the spectral overlap of H_2O and CO_2.

The particle emissivity (unburned char) is calculated using a simple model from Hottel and Sarofim [A12]. This is a theoretical formulation for emitting spheres which are much larger then the radiation wavelength; a condition satisfied by the char particles. The emissivities obtained from this formulation are usually lower than those measured. The discrepancy is probably due to the contribution of cracked hydrocarbons producing luminosity, as well as ash particles not accounted for in the theoretical derivation. However, the flame is so large that the emissivity is not far from unity. The gaseous and particle emissivities are combined to give the emissivity of the gas-char mixture.

$$EM = EP + EWEC - EP*EWEC \tag{A3.59}$$

where EP = particle emissivity

EWEC = combined emissivity of H_2O and CO_2

The heat loss due to radiation is calculated as if the combustion products were a gray gas. The combustor walls are assumed to be isothermal. The formulation used for this case can be found in Hottel and Sarofim [12]. Radiative heat loss rate per unit area is then given by

$$RRATE = \sigma \frac{1}{\frac{1}{EM} + \frac{1}{ES} - 1} * (TEMP**4 - TS**4) \text{ watts/m}^2 \tag{A3.60}$$

where σ = 5.669×10^{-8} watts/m^2-°K^4, Stefan-Boltzmann constant

ES = wall emissivity

TEMP = combustion gas temperature, °K

TS = wall temperature, °K

Multiplication of RRATE by the surface area of the slice (but only that area which includes the combustor wall) gives the radiative heat loss for that slice.

The convective heat losses are calculated as

$$CRATE = HCO*(TEMP-TS) \text{ watts/m}^2 \tag{A3.61}$$

where HCO = heat transfer coefficient, watts/m^2-°K

A value of HCO from 200 to 300 is suggested, based on private communication with persons having experience in the matter. This will yield convective losses that are about an order of magnitude less than radiative losses. As with RRATE, CRATE is multiplied by the appropriate surface area to calculate the convective heat loss per slice.

Calculations for velocity and slice thickness are also made in QLOSS. The velocity is based upon flowrate of gaseous components (FUELRATE*CONC(31))= kg-moles gas/sec), the perfect gas law, and cross-sectional area of the combustor.

$$\text{VEL} = \text{FUELRATE}*\text{CONC}(30)*\text{TEMP}*R/\text{AREA} \text{ m/sec} \qquad \text{(A3.62)}$$

where R=.082056 joules/kg-mole°K, gas constant .

A3.7 Subroutine CONDUCT

This subroutine calculates the electrical conductivity of ionized combustion gases. It has been fully reported by Miller and Pierre [A13] and the presentation here will be principally in connection with equations essential to computation rather than with theoretical aspects. A valuable reference is by Demetriades and Argyropoulos [A14].

Conductivity of a gas is the product of three terms:

$$\sigma = n_e e\mu \qquad \text{(A3.63)}$$

where n_e = charge carrier density, particles/m^3

e = 1.602×10^{-19} coulombs, electronic charge

μ = scalar mobility, mhos/m

The first two terms can be dispatched quickly. Charge carrier (electron density is calculated by

$$n_e = m_e \frac{N_A P}{RT} \text{ electrons/m}^3 \qquad \text{(A3.64)}$$

where m_e = mole fraction of electron gas

N_A = 6.0225×10^{26} particles/kg-mole. Avogadro's number

P = pressure, atmospheres

R = 0.08206 atm-m^3/kg-mole °K, gas constant.

Note that electrons are treated as an ideal gas. Concentration of species, including electrons, that are significant in conductivity are calculated by EQUILZ. They are transferred to CONDUCT by loading the SPEC array with mole fractions prior to calling CONDUCT.

Carrier charge is that of the electron, 1.602×10^{-19} coulomb. Positive ions are disregarded as charge carriers in coal combustion gas because their low mobilities contribute negligibly to conductivity.

The expression for scalar mobility is

$$\mu = \frac{3}{4}\left(\frac{1}{8}\pi\right)^{1/2} \frac{e}{(km_eT_e)^{1/2}} \frac{1}{Q_{sum}} \quad \text{mhos/meter} \qquad \text{(A3.65)}$$

where $k = 1.38054 \times 10^{-23}$ joules/°K, Boltzmann's constant

$m_e = 9.101 \times 10^{-31}$ kg, electron mass

T_e = electron temperature, °K

$e = 1.6021 \times 10^{-19}$ coulomb, electron charge

Q_{sum} = total collision cross-section per unit volume, m^2/m^3

It is assumed that no non-equilibrium ionization occurs so that electron temperature and gas temperature are the same. Thus Q_{sum} is the only term left to calculate and is given by

$$Q_{sum} = \sum_{\alpha} n_\alpha Q_\alpha \quad m^2/m^3 \qquad \text{(A3.66)}$$

where Q_α = collision cross-section of the αth species, m^2/particle. Both ionized and non-ionized species must be included.

n_α = density of the αth species, particles/m^3

For non-ionized particles, collision cross-section is temperature dependent and is given by a power series

$$Q_\alpha = Q(\alpha,1) + Q(\alpha,2)T + Q(\alpha,3)T^2 \quad \text{a } m^2 \times 10^{20}\text{/particle} \qquad \text{(A3.67)}$$

where T = temperature, degrees Kelvin

The array of $Q(\alpha,I)$ is given in a DATA statement at the beginning of EQUILZ. The index α is used here rather than k to avoid confusion with the Boltzmann constant. Q_α is multiplied by 10^{-20} to get results in m^2/ particle. Particle density is given by

$$n_\alpha = \text{spec}_\alpha \frac{N_A P}{RT} \quad \text{particles/m}^3 \qquad \text{(A3.68)}$$

where spec_α = mole fraction of species α.

Non-ionized species of consequence are CO, CO_2, H, K, KOH, OH, SO_2, H_2, H_2O, NO_2, O, and O_2.

The collision cross-section of ionized species is calculated considering only singly ionized species, and assumes that the ion cross-section depends not on the structure of the species, but only on its mass. The expression for cross-section involving collisions between species α and β is

$$Q_{\alpha\beta} = \frac{\pi}{2}\left[(e_\alpha e_\beta/4\pi\epsilon_o)(\gamma_{\alpha\beta}/\mu_{\alpha\beta})\right]^2 \ln(\Lambda_{\alpha\beta}) \text{ m}^2/\text{particle} \qquad \text{(A3.69)}$$

where e_α, e_β = charge of species involved. One of these refers to the electrons and the other to the ion.

ϵ_o = 8.854×10^{-12} farads/m, permittivity of free space

Only collisions between electrons and ions are considered. Ionized species are K^+, OH^-, NO_2^-, NO^- and O^- and are identified as SPEC(14), SPEC(15), SPEC(17), SPEC(18), and SPEC(19), respectively.

Several quantities in equation (A3.69) require explanation. The quantity $\gamma_{\alpha\beta}$ is a constant for Maxwellian energy distributions and is defined by

$$\gamma_{\alpha\beta} = \gamma_\alpha\gamma_\beta/(\gamma_\alpha + \gamma_\beta) \quad \text{kg/joule} \qquad \text{(A3.70)}$$

where $\gamma_j = m_j/(kT_j)$ kg/joule; $j = \alpha,\beta$

and m_j = mass of jth particle, kg; $j=\alpha,\beta$

The quantity $\mu_{\alpha\beta}$ is called the reduced mass and is defined by

$$\mu_{\alpha\beta} = m_\alpha m_\beta/(m_\alpha + m_\beta) \text{ kg} \qquad \text{(A3.71)}$$

Finally, consider the quantity

$$\Lambda_{\alpha\beta} = 3\lambda_D(4\pi\epsilon_o/|e_\alpha e_\beta|)(\mu_{\alpha\beta}/\gamma_{\alpha\beta}) \qquad \text{(A3.72)}$$

All of the terms in it have been defined except λ_D, the Debye shielding distance. For an electron embedded in a homogeneous distribution of ions, the coulomb attraction between the electron and a specific ion is lost in the mass interaction between the electron and all other ions unless the electron is within the sphere of influence of the particular ion. Within the sphere of influence, the force on the electron is dominated by the ion. The average radius of this sphere is the Debye shielding distance and is given by

$$\lambda_D = \sqrt{\epsilon_o/(\Sigma n_\alpha e_\alpha^2/kT_\alpha)} \quad \text{meters} \qquad \text{(A3.73)}$$

After calculating $Q_{\alpha\beta}$ in m^2/particle it is only necessary to use the results in arriving at a total value for Q_{sum} in equation (A3.66). The n_α are those for K^+, OH^-, NO_2^-, NO^-, and O^-.

A3.8 Functions FWD and REV

Functions FWD and REV are called repeatedly by ROOT in the evaluation of equations (A3.39) and (A3.40), respectively. Their execution is so straightforward that no explanation seems necessary.

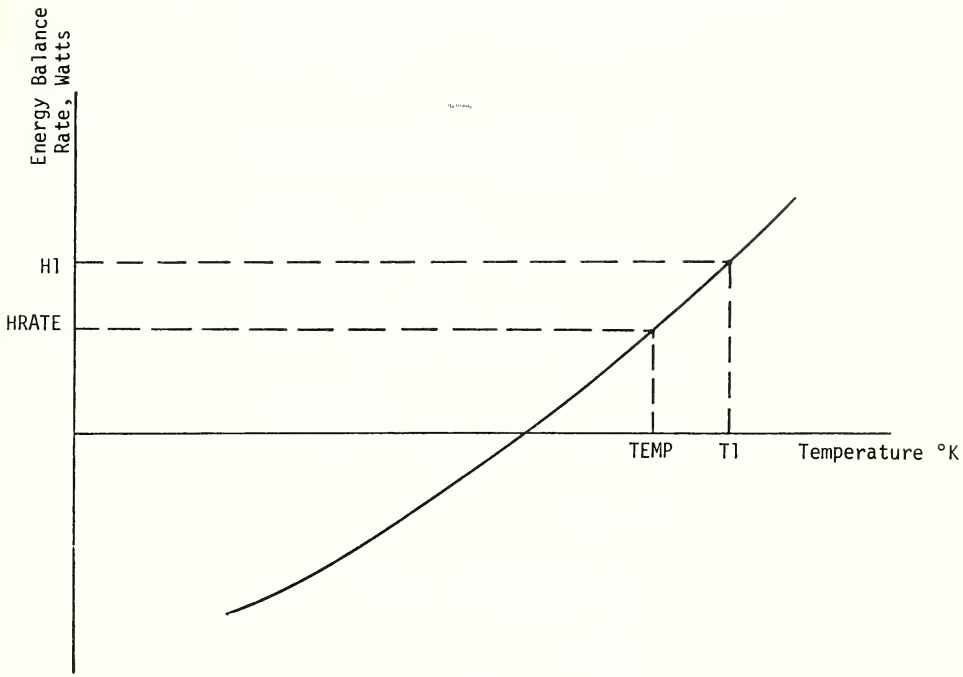

Figure A3.1--General shape of energy rate balance vs. temperature curve

A4. Description of Variables

Variables that appear in common blocks are indicated by /COMMON/ for blank common and /LABEL/ for labeled common. Labeled common blocks are used as follows: /CHARBURN/ is common to MAIN and COMBU, /HEATLOSS/ is common to MAIN and QLOSS, and /SET1/ is common to MAIN and EQUILZ.

Local variables having the same identifiers, but whose meanings vary between programs, are defined as many times as required. Their program associations are shown parenthetically. Variables declared as real or integer are shown parenthetically.

A(COMBU)	-	Reciprocal chemical resistance, adjusted for particle density and swelling factor
A(QLOSS)	-	Array for storage of intermediate results in H_2O emissivity calculation
A1	-	Variable associated with pressure correction of emissivity of H_2O
AIRMOL	-	Kg-moles air/kg-mole oxidant
AIRMW	-	Average molecular weight of either ambient air or vitiated air
AIRRATE	-	Air feed rate, kg/sec
ALFA/CHARBURN/	-	Swelling factor of coal particles after devolatilization
ALPHA(CORRCT)	-	Coefficient of the basis in the reaction equation
ALPHA(EQUILZ)	-	Array of inverse temperature coefficients of exponents used in calculation of equilibrium constants
ANUM	-	Numerator of the equilibrium equation
AREA	-	Combustor cross-section area, m^2
ARMOL	-	Kg-moles argon/kg-mole oxidant
ASEEDMOL	-	Kg-moles seed in oxidant/kg-mole oxidant
ASH	-	Kg-moles ash/kg-mole fuel. Average molecular weight of ash in Rosebud coal taken as 70.27
ASHREJCT	-	Fraction of ash rejected in first stage
AVMW/SET1/	-	Average molecular weight of combustion gas

AWAT - Kg-moles water in seed and water mixture of oxidant/ kg-mole fuel

AWATRMOL - Kg-moles water in seed and water mixture of fuel/ kg-mole fuel

B(COMBU) - Particle-size-independent portion of reciprocal diffusion resistance, adjusted for particle density and swelling factor

B(MAIN) - Rosin-Rammler parameter for coal particle sizing

B(QLOSS) - Array for storage of intermediate results in H_2O emissivity calculations

B1 - Variable associated with pressure correction of emissivity of H_2O

BASIS - Basis of the reaction equation

BETA - Array of constants for exponents used in calculation of equilibrium constants

CAR - Carbon fraction of coal by weight, wet basis ultimate analysis

CC - Array of constants used in curve fit of H_2O emissivity

CDIA - Second stage diameter, meters

CFIX - Fixed carbon, fraction by weight after devolatilization

CLENGTH - Second stage length, meters

CO2MOL - Mole fraction of CO_2 in vitiated air

COAL - Coal feed rate, kg/sec

COALMOLE - Kg-moles coal/kg-mole fuel

COALMW - Molecular weight of wet coal with ash, based on one atom carbon per coal molecule

COALTEMP - Temperature of incoming pulverized coal, °K

COMNAM - Alphameric array of chemical names for species treated

CONC/COMMON/ - Array of species concentrations in kg-moles species/ kg-mole fuel supplied, except CONC(30), which is kg-moles total/(kg-mole fuel*pressure)

CONTRL/COMMON/ - Control and computation variable indicating whether a reaction proceeds in the forward direction (CONTRL = 1.0) or the reverse direction (CONTRL = -1.0)

CRATE	-	Radiation heat loss rate, watts/m^2
DDIST/HEATLOSS/	-	Current slice thickness, meters
DEL	-	Search interval in root finding, used when $0 \leq x \leq 0.9$
DELTE	-	Overlap correction
DENOM	-	Denominator of the equilibrium equation
DENS	-	Wet coal density, kg/m^3
DENSAIR	-	Density of moist ambient air, kg/m^3
DENSO2	-	Density of oxygen in moist ambient air, kg/m^3
DENSVAP	-	Density of water vapor in moist ambient air, kg/m^3
DHLOSS	-	Heat loss of current slice, watts
DIA/HEATLOSS/	-	First-stage diameter, meters
DIST	-	Axial distance along first stage, meters
DT/HEATLOSS/	-	Time required in current slice, msec
DU	-	Fraction of original char burned in current slice
DUOLD/CHARBURN/	-	Fraction of original char burned in preceding trial calculation
DX	-	Predicted value of DIST for the next slice
EC	-	CO_2 emissivity for PT = 1.0 bar and PCO2 = 0.0 bar
EQUIL/COMMON/	-	Array of equilibrium constants for forward reactions
EM	-	Combined particle and gaseous emissivity
EP	-	Particle emissivity
EPEC	-	CO_2 emissivity with pressure correction
EPECMAX	-	Variable used in pressure correction of CO_2 emissivity
EPEW	-	H_2O emissivity with pressure correction
EPEWMAX	-	Variable used in pressure correction of H_2O emissivity
ES/HEATLOSS/	-	First-stage sidewall emissivity
ESCOMB	-	Second-stage sidewall emissivity

EW - H_2O emissivity for PT=1.0 bar and PH2O=0.0 bar

EWEC - Combined H_2O and CO_2 emissivity

FHLOS - Cumulative heat loss rate/enthalpy input rate of coal, exclusive of air preheat enthalpy

FLOWRATE - Combustion gas mass flow rate, kg/sec

FPLC - Variable used in pressure correction of CO_2 emissivity

FPLW - Variable used in pressure correction of H_2O emissivity

FTOT/SET1/ - Sum of all mole fractions in combustion gas. Should equal 1.00

FUELMW - Molecular weight of wet, ash-free coal

FUELRATE/HEATLOSS/ - Fuel input rate, kg-mole fuel/sec

H - Uniform spacing of size divisions in pulverized coal size distribution

H1 - Temporary storage for first energy balance term in secant-line method of combustion gas temperature determination

HA298IN - Dummy variable completing calling arguments for EQUILZ

HA298OUT - Same as HA298IN

HC - Array of second order curve fit coefficients for enthalpy ($H-H_{298}$), kcal/g-mole

HCA - Set of three coefficients, weighted by mole fractions of components and mass fraction of char, for calculations of enthalpy of combustion-gas char-particle mixture

HCO/HEATLOSS/ - Sidewall convective loss coefficient for both stages, watts/m^2-°K

HCOAL - Sensible heat or enthalpy of incoming coal at COALTEMP, joules/kg-mole fuel

HF - Array of standard heats of formation for each species in COMNAM, kcal/g-mole

HF298FST - Total standard heat of formation of all reactant species entering a slice, joules/kg-mole fuel

HF298I - Total standard heat of formation of all input components to the combustor, including coal, air, seed and mixing water, joules/kg-mole fuel

HF298IN - Total standard heat of formation of all reactant species when EQUILZ is called, joules/kg-mole fuel

HF298OUT - Total standard heat of formation of all product species when EQUILZ is finished, joules/kg-mole fuel

HF298RAT - Energy-release-rate density of current slice, watts/m^3

HFDIFF - Difference in total standard heat of formation of all reactant species entering a slice and total standard heat of formation of all product species leaving a slice

HFSEED - Array of the standard heats of formation of the three kinds of seed, kcal/g-mole

HINPUT - Enthalpy of all reactant species, including char, when EQUILZ is called, joules/kg-mole fuel

HLOSRATE(HEATLOSS) - Total heat loss rate from a slice, watts

HLOSS - Cumulative heat loss rate, watts

HOUT - Enthalpy of all product species, including char, when EQUILZ is finished, joules/kg-mole fuel

HOUTGAS - Enthalpy of gaseous product species when EQUILZ is finished, joules/kg-mole fuel

HRATE - Energy balance gain or loss rate, watts

HSUPPLY - Thermal input rate of coal, watts

HTAIROUT - Enthalpy of preheated air, joules/kg-mole fuel

HTOT - Specific enthalpy of gas-char mixture, joules/kg

HYD - Hydrogen fraction of coal by weight, wet basis ultimate analysis

IA - Basis identifier

IB - Temporary storage used in determination if IBASIS

IBASIS/COMMON/ - Identifier of reaction basis, the species that will be depleted first as the reaction proceeds to completion

JPROD - Identifying indices of product species in a reaction

JREACT - Identifying indices of reactant species in a reaction

KCC - Control variable telling whether more char remains to burn (KCC=1) or all char has been burned (KCC=2)

KEND - Control variable telling whether intermediate slice of first stage is being computed (KEND=1) or last slice is being computed (KEND=2)

KINPUT - Control variable telling whether seed has not been injected (KINPUT=1) or has been injected (KINPUT=2)

KOUNT - Count of major iterations done in EQUILZ

KPROD - Number of product species in a reaction

KREACT - Number of reactant species in a reaction

KSEED - Identifier of kind of seed used

LAMBDA - Log_{10}\{(partial pressure)*(mean beam length)\}

LENGTH - First-stage length, meters

LMAX - Variable used in pressure correction of H_2O emissivity

LO - 4*(volume enclosed)/(surface area), used in mean beam length calculation

LOGEC - Intermediate variable in calculation of CO_2 emissivity

LOGEW - Intermediate variable in calculation of H_2O emissivity

LOW(Real) - Temporary variable in determination of forward and reverse reaction bases

MCDT(Real) - Multiplier constant of DT, restricted to 1.0 or 2.0

MOISTURE(Real) - Moisture fraction of coal by weight, wet basis ultimate analysis

MOLEFR/SET1/(Real) - Mole fraction of gaseous species in combustion gas

MW(Real) - Coal thermal input rate, megawatts

NC1 - Number of terms on product side of reaction equations, one more than number of products to accomodate total moles/pressure term

NCOMB - Control variable telling whether single-stage operation (NCOMB=1) or two-stage operation (NCOMB=2) is desired

NEND - Control variable telling whether second stage is yet to be calculated (NEND=1) or has been calculated (NEND=2)

NEQS - Number of equations in reaction set, varying according to temperature

NITMOLE(Real) - Kg moles N_2/kg-mole oxidant

NITROGEN(Real) - Nitrogen fraction of coal by weight, wet basis ultimate analysis

NOMOL(Real) - Kg-moles NO/kg-mole oxidant

NPROD/COMMON/ - Number of product species in reaction

NREACT/COMMON/ - Number of reactant species in reaction

NSLICE/HEATLOSS/ - Number of current slice

OSEEDMOL - Kg-moles seed in oxidant/kg-mole fuel

OXIDANT - Kg-moles oxidant/kg-mole fuel

OXY - Oxygen fraction of coal by weight, wet basis ultimate analysis

OXYENRICH - Oxygen enrichment of ambient air, kg-mole O_2 enrichment/kg-mole O_2 in ambient air

OXYMOL - Kg-moles O_2/kg-mole oxidant

PAMB - Ambient pressure, atmospheres

PARTP,PARTPI,PARTPJ - Partial pressures of gaseous species, atmospheres

PCO2 - Partial pressure of CO_2, bars

PCOEFF - Array of coefficients of product species for entire set of reaction equations

PE - Equivalent pressure, used in pressure correction of H_2O and CO_2, bars

PH2O - Partial pressure of H_2O, bars

PHEAT - Oxidant preheat temperature, °K

PHI - Overall stoichiometric ratio, kg-mole O_2 supplied /kg-mole O_2 required for stoichiometric combustion

PHI1 - Stoichiometric ratio of first stage

PMW - Array of molecular weights of species

SEEDINJ	-	Axial distance along first stage at which seed is injected, meters
SEEDMOLE	-	Kg-moles seed in fuel/kg-mole fuel. Also kg-moles total seed/kg-mole fuel
SIGMA/SET1/	-	Average combustion gas conductivity, mhos/m
SLAG	-	Kg-moles slag rejected/kg-mole fuel
SOXIDANT	-	Oxidant required for stoichiometric combustion, kg-mole oxidant/kg-mole fuel
SPEC	-	Array of mole fractions of neutral and ionized species needed in conductivity calculations
STOICOXY	-	Oxygen required for stoichiometric combustion, kg-moles oxygen/kg-moles fuel
SULFUR	-	Sulfur fraction of coal by weight, wet basis ultimate analysis
SUM SUM1	-	Intermediate variablesin calculation of particle emissivity
SUMW	-	Normalizing term in calculation of WFRAC
T	-	Time, msec
T1	-	Temporary storage for first temperature term in secant-line method of temperature determination, °K
TAMB	-	Ambient temperature, °K
TAU	-	Defined temperature in QLOSS
TC	-	Defined temperature for calculation of PSAT
TEM	-	Current temperature in secant-line method of temperature determination, °K
TEMP(MAIN)	-	New temperature in secant-line method of temperature determination, °K
TEST/COMMON/	-	Array of original species concentrations when EQUILZ is called, used for convergence testing, kg-mole species/kg-mole fuel
TLOOP(Integer)	-	Control variable telling whether first point (TLOOP=1) or second point (TLOOP=2) is being calculated in secant-line method of temperature determination

TMOL - Total kg-moles ambient air/kg-mole O_2 in ambient air. Also total kg-moles oxygen enriched air/kg-mole O_2 in oxygen enriched air

TN - Defined temperature for calculation of enthalpy

TOTMOL/SET1/ - Total kg-moles combustion gas/kg-mole fuel

TS/HEATLOSS/ - Sidewall temperature of first stage, °K

TSCOMB - Sidewall temperature of second stage, °K

UOLD - Fraction of original char unburned at input to current slice

US - Fraction of char unburned at output of current slice

VEL/HEATLOSS/ - Combustion gas velocity, m/sec

VOL - Volatiles, fraction by weight

W - Number of coal particles in each size division/kg-mole fuel

WATERMOLE - Kg-moles water in seed-water mix of fuel/kg-mole fuel

WET - Kg mixing water/kg dry seed

WFRAC/CHARBURN/ - Array of mass fractions of coal particles appearing in each discrete size division

WMOL - Kg-moles water vapor/kg-mole oxidant

X(EQUILZ,ROOT,CORRCT,FWD,REV) - Fractional conversion of basis

X/CHARBURN/ - Array of current coal or char particle diameters, microns

XA - Molecules ash/molecule coal. Also kg-moles ash vapor/kg-mole fuel

XBAR - Size of pulverized coal particles for which particles composing ϵ^{-1}=.368 of the total coal mass are larger than XBAR

XC - Critical char particle size for annihilation, microns

XD - Smallest coal particle size division, microns

XFIX/CHARBURN/ - Kg-moles fixed carbon/kg-mole fuel

XH - Atoms hydrogen/molecule coal. Also kg-mole atomic hydrogen/kg-mole fuel

XHIGH	-	An upper bound of fractional conversion such that the root is less than XHIGH
XL	-	Largest coal particle size division, microns
XLOW	-	A lower bound of fractional conversion such that the root is greater than XLOW
XM	-	Molecules water/molecule coal. Also kg-moles water/kg-mole fuel
XMID	-	Midpoint of XHIGH and XLOW. Replaces XHIGH or XLOW during interval halving
XN	-	Atoms nitrogen/molecule coal. Also kg-moles atomic nitrogen/kg-mole fuel
XOLD/CHARBURN/	-	Char particle diameters at output of previous slice, microns
XO	-	Atoms oxygen/molecule coal. Also kg-moles atomic oxygen/kg-mole fuel
XS	-	Atoms sulfur/molecule coal. Also kg-moles sulfur/kg-mole fuel
XT	-	Test value for char particle sizes, microns
YAR	-	Kg-moles argon/kg-mole O_2 in ambient air
YMAR	-	Mole fraction of argon in ambient air, oxygen enriched air or vitiated air
YMCO2	-	Mole fraction of CO_2 in vitiated air
YMN2	-	Mole fraction of N_2 in ambient air, oxygen enriched air or vitiated air
YMNO	-	Mole fraction of NO in vitiated air
YMO2	-	Mole fraction of O_2 in ambient air, oxygen enriched air or vitiated air
YN2	-	Kg-moles N_2/kg-mole O_2 in ambient air
YO2	-	Kg-moles O_2 in ambient air or oxygen enriched air)/ kg-mole O_2 in ambient air
YW	-	Kg-moles water vapor/kg-mole O_2 in ambient air
Z/CHARBURN/	-	Original coal particle sizes, microns
ZAT	-	Temporary variable used in convergence testing

ZETA	-	Ratio of PH2O to PH2O + PCO2
ZOT	-	Temporary variable used in convergence testing

REFERENCES

[A1] TRW 25 MW$_t$ Staged MHD Coal Combustor Conceptual Design Study, TRW Defense and Space Systems Group, Redondo Beach, California, Document TID-27145, June 4, 1976.

[A2] A. Padia, "The Behavior of Ash in Pulverized Coal Under Simulated Combustion Conditions," Sc.D. Thesis, MIT, Department of Chemical Engineering, Cambridge, Massachusetts, 1976.

[A3] S. K. Ubhayakar, D. B. Stickler, C. W. von Rosenberg, and R. E. Gannon, "Rapid Devolatilization of Pulverized Coal In Hot Combustion Gases."

[A4] D. B. Stickler and R. T. Barnes, CDIF Combustor Design, Final Report, Avco-Everett Research Laboratory, Everett, Massachusetts, Document TID-27143, June 1976.

[A5] Steam/Its Generation and Use, 38th Edition, Babcock and Wilcox, New York, 1972.

[A6] Handbook of Chemistry and Physics, Chemical Rubber Publishing Co., Cleveland, Ohio.

[A7] P. Rosin and E. Rammler, "The Laws Governing the Fineness of Powdered Coal," Journal Inst. Fuel, Volume 7, October 1933, pp. 29-36.

[A8] JANAF Thermochemical Tables, Second Edition, National Bureau of Standards, U.S. Government Printing Office, June 1971.

[A9] I. Eliezer and R. Howald, "Thermodynamics of the Vaporization Processes for Potassium Sulfate," Journal Chem. Phys., October, 1976.

[A10] M. A. Field, D. W. Gill, B. B. Morgan, and P. G. W. Hawksley, Combustion of Pulverized Fuel, British Coal Utilization Research Association, 1967.

[A11] B. Leckner, "Spectral and Total Emissivity of Water Vapor and Carbon Dioxide," Combustion and Flame, 19, 1972, pp. 33-48.

[A12] H. C. Hottel and A. F. Sarofim, Radiative Transfer, McGraw-Hill, New York, 1972.

[A13] D. J. Miller and D. A. Pierre, Conductivity of Coal Combustion Gases, ERL Report 1876, Electronics Research Laboratory, Montana State University, Bozeman, Montana, October 1976.

[A14] S. T. Demetriades and G. S. Argyropoulos, "Ohm's Law in Multicomponent Non-isothermal Plasmas with Temperature and Pressure Gradients," The Physics of Fluids, Volume 9, No. 11, November 1966, pp. 2136-2149.

TASK M

Preliminary ETF Environmental Analysis and Site Study

Susan Brown

ABSTRACT

Baseline information based on existing data was compiled for each of the five candidate site areas (CSA) for the following items: surface and groundwater hydrology, geology, soils, terrestrial vegetation, wildlife, aquatic biology, ambient noise level, air quality, meteorology, electrical transmission networks, and transportation access. Areas where baseline information was deficient or non-existent were specified. A research strategy for social and socioeconomic analysis was developed but not implemented.

Primary data were determined insufficient in the areas of meteorology, air quality, noise level, and social/socioeconomic parameters. Therefore, FY 78 efforts should be directed at quantifying such parameters. Certain areas require further investigation before impact analysis proceeds: water availability, archaeology, and land use. Based on available information, it is premature to eliminate any of the five candidate site areas from further investigation.

I. OBJECTIVE AND SCOPE OF WORK

Public Law 93-404, Section 107, requires that ERDA construct an MHD engineering test facility (ETF) in the state of Montana. The purpose of this preliminary environmental impact analysis of the MHD ETF at candidate sites in Montana is as follows:

1. Determine what effects effluents and residuals from the MHD ETF plant construction and operation may have on the ecosystem of the selected candidate sites;

2. Determine whether these effects may be of positive or negative significance at particular candidate sites; and

3. Select several specific sites for the MHD ETF where the environmental impact effects are expected to be minimal.

A current program recently initiated by ERDA-FE-MHD is directed toward the definition and conceptual design of a pilot-scale ETF which is a combined coal-fired, open-cycle MHD steam power plant.

The overall research and development program goals of the ETF are to 1) test a combined MHD steam system on an integrated basis, 2) provide design data for scale-up to a commercial-sized demonstration plant, 3) evaluate component interfacing and control characteristics, endurance, and performance and resolve critical problem areas, 4) provide basic performance and parametric data for analytical and design improvements, and 5) define other major prob-

lem areas requiring further development. The ETF also will be utilized to sequentially test individual components and systems as they become available. Thus, the ETF will include the necessary flexibility to accommodate testing different component designs and sub-systems as well as different system configurations.

II. SUMMARY OF PROGRESS TO DATE

The site selection study for FY 77 was directed at identifying one or more suitable specific sites for an MHD engineering test facility in Montana. The identification of potential power plant sites requires the evaluation of engineering, environmental, social, and economic attributes related to the candidate areas. The particular process used on this project is shown schematically in Figure 1.

Phase I and a first cut at Phase II of this process were carried out in FY 76 as explained in the Task H5 annual report. The preliminary work on Phase II, carried out under Task H5, involved three arbitrarily selected constraint weighting schemes. These schemes were applied through the use of computer techniques to produce three distinct computer-printed composite maps for each of the six candidate regions of Montana. Figure 2 shows the relative definition of Phases I, II, and III. Refinement of the first portion of Phase II was completed the second quarter of FY 77. The analysis of the physical constraint maps yielded a total of 15 candidate site areas (CSA) as highly suitable.

During the third quarter, the second portion of Phase II was completed. The 20 CSA's were evaluated on the following basis: 1) any existing government or ERDA site would be considered; 2) the site must be located in an area with a population density of 15,000 within a 20-mile radius; and 3) the site must be near a 161 KV or comparable line. Five CSA's, suitable from this analysis, include the following: 1) Billings, 2) Butte-Anaconda, 3) Glasgow Air Force Base, 4) Great Falls, and 5) Livingston-Bozeman (see Figure 3).

This quarter's Phase III effort focused on literature review and limited field confirmation of existing baseline data for each CSA. The subcontracting firm of Sawyer-Waring and Associates completed an assessment of surface hydrology, geology, soils, terrestrial vegetation, wildlife, and aquatic biology characteristics.

MERDI personnel completed an assessment of groundwater hydrology, electrical transmission grid availability, transportation networks, air quality, meteorology, and noise level data. Preliminary analysis of available information was initiated concerning land use, resource availability, demographic, and infrastructure characteristics. Methodologies for conducting social and socioeconomic analysis were examined, and a research strategy was formalized. Impact analysis has been limited to gross levels of analysis in order to narrow potential candidate site areas. A more detailed environmental impact site analysis cannot proceed until receipt of ETF design criteria or certain design parameters are quantified. The following is a list of publications completed under Task M during FY 77:

1. Montana Energy and MHD Research and Development Institute, A Plan for the Preliminary Environmental Impact Analysis of the MHD-ETF at Candidate Sites in Montana, January 1977.

2. Montana Energy and MHD Research and Development Institute, Preliminary Evaluation of Montana Candidate Areas for the MHD-ETF Site, Draft Topical Report, January 1977.

3. Montana Energy and MHD Research and Development Institute, Selection of Tentative MHD-ETF Candidate Site Areas, Second Draft Interim Report, April 1977.

4. Sawyer-Waring and Associates, Baseline Environmental Evaluation of Five Montana Sites, August 15, 1977.

5. Montana Energy and MHD Research and Development Institute, Groundwater Resources in Five Montana Candidate Site Areas, available October 31, 1977.

6. Montana Energy and MHD Research and Development Institute, Legal Aspects of Water Availability in Montana, available October 31, 1977.

7. Montana Energy and MHD Research and Development Institute, Air Quality Inventory of Five Montana Candidate Site Areas, available October 31, 1977.

8. Montana Energy and MHD Research and Development Institute, Air Pollution Meteorology of Five Montana Candidate Site Areas, available October 31, 1977.

9. Montana Energy and MHD Research and Development Institute, Transportation Facilities Available in Five Montana Candidate Site Areas, available October 31, 1977.

10. Montana Energy and MHD Research and Development Institute, Electrical Transmission Systems in Five Montana Candidate Site Areas and Their Suitability to Serve the Engineering Test Facility, available October 31, 1977.

DETAILED DESCRIPTION OF TECHNICAL PROGRESS

A. Acquisition of Existing Baseline Data on Five CSA's

In general, the study areas were limited to the 40-mile radii surrounding Billings, Butte-Anaconda, Glasgow Air Force Base, Great Falls, and Livingston-Bozeman. However, a 75-mile radius was used to investigate the fault zones and a 20-mile radius for slope investigations. The primary method of investigation consisted of a literature review and interviews with resource personnel. Since the goal was a comparative analysis to determine site suitability rather than a site specific environmental impact analysis (EIA), this level of detail was deemed appropriate. However, areas where no baseline data exists were identified, and recommendations to fill such voids were made.

The following sections summarize major findings for each subject area addressed:

1. Hydrology--surface water and groundwater: sources, availability, and quality

The primary objective for this section was to identify all rivers with an annual average flow greater than 750 cubic feet per second, lakes or reservoirs with a storage capacity of 2,000 acre-feet or more, and groundwater reservoirs. Water availability and water quality problems received emphasis.

a. Billings

The major surface water resource in the Billings area is the main stem of the Yellowstone River. The Clark Fork of the Yellowstone River enters the Yellowstone River mainstream within the Billings study area. Both streams have large variations in seasonal flow. Although surface water exists, the availability is questionable.

A major legal problem that may affect water availability is surface water moratoriums, such as those currently affecting the Yellowstone River. Under moratorium, further appropriation of waters from the river or from the drainage basin is prohibited. Furthermore, the surface water in a stream is known to be interrelated with the groundwater stored in the alluvium along the channel (bank storage); therefore, a large withdrawal of groundwater from the alluvium in the vicinity of the channel may lower the water level in the stream. In this manner, the use of groundwater also could be affected by a surface water moratorium. Water may be available from the Yellowstone River if development occurs in conjunction with the Montana Power Company's Frank Bird Power Plant.

The water quality of the Yellowstone River at Billings is considered good, even though there is a downstream increase in specific conductance from Gardiner to Billings. The Yellowstone River from Laurel to Billings has been classified as water quality limited by the Montana Water Quality Bureau, largely due to the discharge from the Laurel and Billings sewage treatment plants, oil refineries, sugar beet factory, and steam generating plant. The Clark Fork River also is noted to be water quality limited due to high sediment loads. Water quality information specific to Cooney Reservoir was not identified although it could be expected to be similar to that of the Clark Fork River.

Several reservoirs and lakes exist in the Billings CSA. However, they are used primarily for irrigation or hunting clubs or are shallow alkali lakes. As yet, it is undetermined whether sufficient water rights could be purchased in conjunction with agricultural land. The Bureau of Reclamation has water available at the Yellowtail Reservoir, although they are currently unable to quantify the amount.

The alluvium along the Yellowstone River and its tributaries is the best proven source of groundwater. However, withdrawing an industrial supply of groundwater from the alluvium may conflict with the surface water moratorium on the Yellowstone River.

Deeper aquifers have an undocumented potential for producing industrial supplies of groundwater. The Kootenai, although known to produce yields exceeding 500 gpm, has quality problems; on the other hand, the Madison is untested in the Billings area.

In the alluvium and terraces along the Yellowstone River, groundwater quality ranges from excellent to poor for domestic and irrigation use. Furthermore, water from the Kootenai Formation is high in dissolved salts and high in temperature. Groundwater in the Madison Formation, although untested, can be expected to be high in total dissolved solids.

b. Butte-Anaconda

In the Butte-Anaconda area, substantial surface water exists in both the Columbia and Missouri river basins. The major streams (Clark Fork, Big Hole, and Jefferson) however, are noted for low daily flow rates in the summer.

In addition, the Clark Fork River carries a high pollutant load of heavy metals and coliform bacteria from Silver Bow Creek. The Big Hole River is generally of excellent quality; however, elevated temperatures and dewatering caused by irrigation cause problems for cold water fish. The Jefferson River also has dewatering and temperature problems. Moreover, suspended solids may reach undesirable levels.

Adequate water is available from the Anaconda Company's Georgetown Lake-Silver Lake system. The cost of such water has not been determined. Water quality data will be obtained from the Anaconda Company.

Within the Butte-Anaconda CSA, the best proven potential for an industrial groundwater supply is the Deer Lodge Valley from Anaconda to Deer Lodge. The Whitehall and Silver Bow-Divide areas seem to have potential, but further studies are needed to substantiate an industrial groundwater supply (>500 gpm). Although the Butte valley should produce short-term industrial supplies of groundwater, a long-term sustained yield is questionable because of limited recharge to the aquifer.

Groundwater quality in the Butte-Anaconda CSA generally is considered excellent, but several pollution problems do exist. Along upper Silver Bow Creek, contamination of groundwater supplies by industrial wastes in the stream can be expected; furthermore, the Anaconda Company's settling ponds near Warm Springs also may pollute nearby aquifers. Domestic pollution, such as improper septic systems, may affect groundwater quality locally.

Site specific hydrogeologic and groundwater quality studies will be necessary if a location in the Butte-Anaconda area is selected.

c. Glasgow Air Force Base

The Glasgow area has three significant sources of surface water: the Missouri and Milk rivers and the Fort Peck Reservoir. The Milk River, however, is characterized by low summer flows. The Fort Peck Reservoir appears to be the most assured source of water where up to 300,000 acre-feet have been reserved for industrial users.

The major water quality problem in both the Milk River and the lower Missouri River basins is suspended sediment. Measurements from the water quality station below the Fort Peck Reservoir indicate that the water quality is good and constant throughout the year.

There are two potential sources of an industrial supply of groundwater in the Glasgow area: the stream channel and preglacial alluvium and the deep aquifers such as the Kootenai and Madison Formations. Yields exceeding 500 gpm have been obtained from the alluvium, but little is known about the deeper aquifers.

In the Glasgow CSA, groundwater quality generally can be classified as poor because of high levels of total dissolved solids. Both the alluvial and deeper aquifers yield water that is poor to fair in quality. Although it produces good water in central Montana, the Kootenai Formation is untested in the Glasgow area. Moreover, the Madison Formation, which also is untested, is thought

to be affected by an influx of saline water.

More study is necessary to determine the groundwater availability and applicability to an industrial process.

d. Great Falls

Four main streams exist in the Great Falls CSA: Missouri River, Sun River, Smith River, and Belt Creek. The latter three all have low summer flows which may make them unsuitable supply sources.

Requests for water use permits in the Missouri River Basin above Great Falls are being contested due to potential loss of hydro-electrical power generation. However, below Morony Dam east of Great Falls, water use permits are being issued without being contested.

The principal water quality problems near Great Falls are related to agricultural and mining activities. East of Great Falls, the Missouri River has high levels of iron, zinc, and turbidity.

A number of potential sources of an industrial supply of groundwater exist in the Great Falls CSA. The Missouri River and Sun River alluvium are proven sources of moderate yields of groundwater; moreover, large yields (up to 500 gpm) should be available to properly located and constructed wells. Deeper aquifers, such as the Kootenai and Madison Formations, are also potential sources of a groundwater supply exceeding 500 gpm. However, these aquifers are between 250 and 2000 feet deep; therefore, the supply from the Kootenai and Madison Formations should be confirmed before wells are drilled.

Except for isolated areas of domestic pollution, groundwater quality in the Sun River and Missouri River alluvial aquifers is considered to be excellent for both domestic and irrigation use. Quality of the groundwater in the deeper aquifers ranges from poor to excellent depending upon the formation penetrated and local conditions.

Because of the wide ranges of the quantity and quality of groundwater available in these aquifers, further studies will be needed to assure a supply suitable for industrial use.

e. Livingston

Like Billings, the major water resource in the Livingston area is the main stem of the Yellowstone River. The problem of water availability at this site is the same as for Billings. In the Livingston area, the water quality is relatively good with low concentrations of dissolved solids.

Based on the available information, the Yellowstone River alluvium is the best source of a large groundwater supply in the Livingston CSA. However, like the Billings area, the moratorium on

withdrawals of surface water from the Yellowstone River may affect the utilization of the alluvial aquifer.

The Shields River alluvial valley has some potential, but the chances for a large, sustained yield of groundwater seem questionable. Deeper aquifers in the Livingston area are untested.

Although exceptions may exist, the quality of the groundwater in the alluvial aquifers is considered to be good.

f. Conclusions

Once a water supply of the necessary quantity and quality has been documented by detailed hydrogeologic studies, the legal aspects of water availability must be considered. The following paragraph summarizes the procedures necessary to appropriate groundwater or surface water in Montana.

According to the Montana Water Use Act, any new appropriation of more than 100 gpm of water undertaken after July 1, 1973 must be accompanied either by a "Permit to Appropriate Water" or a "Certificate of Water Right." Both are granted by the Montana Department of Natural Resources and Conservation (DNRC) following the payment of an application fee and a review process. Since the water requirements of the ETF are surely greater than 100 gpm, a permit to appropriate water will be necessary. Furthermore, the water needs of the facility may be sufficient to qualify it as a large appropriation; consequently, the burden of proving that the water rights of prior appropriators will not be affected adversely may be MERDI's responsibility. In addition, an environmental impact statement will be needed if the appropriation is determined to be a major action significantly affecting the quality of the human environment.

2. Geology and Soils

Within this section, the following site characteristics are discussed: slope, soils, and faults. Only the candidate site areas with specific limitations are highlighted.

The slope analysis was restricted to identifying areas having less than a 10 percent slope within 20 miles of the study area centers. This data was mapped for each CSA. Slope information, when interrelated to soils data, may influence the following: 1) erodibility, land stability, compactibility, moisture handling, and soil temperatures; 2) building development and road construction; and 3) subsurface moisture characteristics which are important for road and dam construction or for drainage and sanitary facilities. Soil association data is available for all five CSA's although information regarding soil properties significant to engineering design is limited for Butte-Anaconda and Great Falls. Once specific sites have been selected, more detailed soil information will be collected.

Faults and related seismic activity were identified for a 75-mile radius within each CSA. The major faults that could cause a destructive earthquake are located mainly in the Butte and Livingston areas (see Figure 4). Any of these, including those that have not been active since the mid-Pleistocene age, could produce a major quake. A statistical study of earthquakes in Montana indicates that structures planned for the Butte or Livingston areas should be designed to withstand earthquakes of magnitude seven. The chances of a major earthquake occurring in the Billings, Glasgow Air Force Base, or Great Falls areas are low.

3. Terrestrial Vegetation

Terrestrial vegetation is an important resource due to its role in primary productivity, soil development and stability, and habitat for wildlife. For each of the five CSA's, the baseline analysis focused on four objectives: 1) to identify any endangered or threatened plant species; 2) to indicate on maps the location of major vegetative types; 3) to identify dominant plant communities and the prominent species of these communities; and 4) to identify those areas that support relic stands of undisturbed natural vegetation or those which are disturbed only slightly.

The only endangered plant species known to occur in Montana are the Phlox missoulenis wherry (also referred to as P. Kelseyi var. missoulenis (wherry) Crong.), Silene Spaldingii Wats., and Trisetum orthochaetum Hitch. The known range and locations of each of these species is outside all of the study areas.

Comparative, broad-scale climax vegetative unit maps of the CSA were developed. In addition, a large number of vegetative maps at different levels of detail are available for certain CSA's, and plant community data has been accumulated.

Relic stands of natural vegetation occur where the vegetation remains undisturbed or only slightly disturbed by man's activities. Figure 5 indicates natural areas which are known to exist within the CSA's. Since these provide valuable baseline information to scientists, those areas in the vicinity of the final ETF site should be preserved.

4. Aquatic Biology--Wildlife

Since most wildlife and bird populations enjoy a wide distribution within Montana, only rare or endangered species are highlighted in this summary. Endangered species, as listed by the U. S. Fish and Wildlife Service, that may be found in Montana include the black-footed ferret, the Northern Rocky Mountain wolf, the whooping crane, and the American peregrine falcon. The grizzly bear is classified as threatened by the U. S. Fish and Wildlife Service. Species under study to determine their status (threatened or not threatened) include the Northern bald eagle, the river otter, the swift fox, the bobcat, and the lynx.

Major fisheries are mentioned and related to their required habitats. An interesting phenomena noted in this study is the presence of both warm and cold water fisheries within the same CSA. The type of

fishery in an area will be important in determining the effects of a thermal discharge; warm water fisheries probably will be less sensitive to water temperature changes. Waterfowl habitats and important migratory routes also are mentioned. Furthermore, aquatic organisms and their relationship to water quality are treated briefly.

More complete information on the wildlife and aquatic biology of the five CSA's can be found in the report, Baseline Environmental Evaluation of Five Montana Sites.

a. Billings

Within the Billings candidate site area, a number of endangered wildlife species are thought or known to exist. Of the endangered species, only the peregrine falcon is known to exist (breeding grounds) in Yellowstone County. This CSA is a former range for black-footed ferret; therefore, the species may occur potentially. Whooping cranes are only migrants in Yellowstone County.

A number of the species under review also are known or thought to exist. The swift fox could potentially exist, whereas the lynx is suspected to exist in the area. Bald eagles are a migrant; however, winter residence in the region is indicated. Known breeding grounds of the prarie falcon are present, and winter occupancies have been reported.

Fish populations undergo a significant change in this study area. From above to below Billings, the fish composition changes from predominantly cold water species like brown trout and white suckers to warmer water species such as ling, goldeye, channel catfish, and sauger.

There are three important waterfowl habitats in the study area: the Comanche Basin, the Big Lake Basin, and the river bottoms of the Yellowstone and Clark Fork of the Yellowstone rivers. Ducks, geese, and other waterfowl use these areas as breeding (production) and migratory stopover (staging) areas. Furthermore, Halfbreed and Hailstone National Wildlife Refuges are located in the Big Lake Basin northwest of Billings.

As demonstrated by the depression in the number of benthic (bottom dwelling) organisms, the Billings metropolitan area has an effect on the water quality of the Yellowstone River. Furthermore, the percentage of pollution-sensitive benthic organisms was found to decline in relation to the more tolerant groups.

b. Butte-Anaconda

In the Butte-Anaconda candidate site area, no endangered species are known to exist. This CSA formerly served as the range of the Northern Rocky Mountain wolf; therefore, the species potentially could occupy the area. The peregrine falcon is classi-

fied as a migrant (non-breeder) in Silver Bow County. Grizzly bears, a threatened species, are not recorded as residents of the Butte study area; however, rumors of sightings have been reported in surrounding mountain ranges. The lynx is suspected to exist, and the prarie falcon has known breeding grounds in the CSA.

The Butte-Anaconda CSA also has substantial populations of big game species including black bear, Rocky Mountain goat, Rocky Mountain bighorn sheep, and moose.

Numerous lakes and streams in the CSA support cold water fish, including such species as rainbow, brook, golden trout, and arctic grayling. Georgetown Lake supports an excellent fish population, and considering its size, it is the most heavily fished lake in the state. The Clark Fork drainage does not support a large fish population in the study area, but the Big Hole River, a "blue ribbon" trout stream, and the Jefferson River support excellent fish populations.

Compared to the other study areas, only minor waterfowl habitat exists in the Butte-Anaconda area. The only protected habitat is part of The Anaconda Company's settling pond system near Warm Springs, Montana.

c. Glasgow Air Force Base

Although several endangered species could occupy the Glasgow CSA, no known occupations have been reported. The area is listed as the former range for both the black-footed ferret and the wolf, so both species potentially could occur. The peregrine falcon and the whooping crane are listed as migrants (non-breeders) in the area, and the peregrine falcon is reported to be a winter resident.

Species under status review in Valley County include the bald eagle, the prarie falcon, and the swift fox. However, the swift fox is not presently known to inhabit the region.

The Glasgow CSA contains three major fishery resources: Fort Peck Reservoir and the Milk and Missouri rivers. Fort Peck Reservoir is utilized for both recreational and commercial fishing, whereas the rivers provide mainly recreational fishing. In addition, a wealth of waterfowl habitat surrounds the Milk River bottom and many small ponds and reservoirs.

Glasgow is in the central flyway for migrating waterfowl, and many thousands of birds pass through each spring and fall. Two significant protected areas near Glasgow are the C. M. Russell National Wildlife Range and the Bowdoin National Wildlife Refuge (about 45 miles west of Glasgow).

Neither the Missouri River nor Fort Peck Reservoir are known to have water quality problems that affect the aquatic biota; however, the Milk River has problems with sediment and high water temperatures.

d. Great Falls

Cascade County (Great Falls CSA), which is similar to the other areas, is the former range of the wolf and black-footed ferret. The peregrine falcon also is suspected to have breeding grounds in this CSA. Although the swift fox was once a resident, no known occurrences are listed. Moreover, the lynx is suspected to exist in the area. Important birds, with known breeding grounds near Great Falls, include the bald eagle and the prarie falcon. Elk, moose, black bear, and mule deer are present in the mountainous areas surrounding Great Falls.

Fisheries in the Great Falls area, similar to those in the Billings area, are undergoing a transition from cold water to warm water species. The headwaters of the Sun and Smith rivers, and Belt Creek provide good fishing for cold water species (rainbow and brown trout); however, in the lower reaches of these streams, a cold and warm water fishery is present. The Missouri River at Great Falls is in a transition zone; above Great Falls, the species are primarily cold water, whereas warm water species are more prevalent downstream.

Two waterfowl concentration areas are found within forty miles of Great Falls at Benton and Freezeout lakes. Benton Lake, the site of Benton Lake National Wildlife Refuge, is an important area for the nesting and migration of ducks. Freezeout Lake has the largest waterfowl concentration area in the five study areas, especially for geese and swans. As many as 500,000 snow geese and a large portion of the continental population of Ross geese migrate through the area. Parts of both the Benton Lake and Freezeout Lake areas are closed to hunting.

The principal water quality problem affecting stream biota in this area is suspended sediment. High coliform levels also have been found in the Missouri River below Great Falls.

e. Livingston

Since the Livingston area includes the habitats of the plains and mountains, it has the greatest variety of game animals of the five candidate site areas. In assessing endangered species, it is noted that the black-footed ferret had former ranges near Livingston and the wolf is suspected to exist in parts of Park and Sweetgrass counties. Furthermore, the peregrine falcon is thought to have breeding grounds in the area and is reported as a winter resident. Grizzly bears, a threatened species, are present in the mountains surrounding Livingston, especially in areas adjacent to Yellowstone National Park.

A number of species that are currently under status review are known or potentially could exist in the Livingston CSA. The swift fox formerly inhabited the area, and the lynx is reported to be a

current resident. Both the bald eagle (which winters along the Shields and Yellowstone rivers) and the peregrine falcon are known or thought to exist near Livingston. Furthermore, numerous mountain-dwelling big game species, such as black bear, Rocky Mountain bighorn sheep, Rocky Mountain goat, and moose, are residents of the mountainous areas within and surrounding this CSA.

An excellent cold water fishery of national importance is provided by the Yellowstone River in the Livingston area. The Montana Fish and Game Department classifies the Yellowstone River as a "blue ribbon" trout stream throughout the study area. The river supports an excellent fishery for rainbow, brown, and Yellowstone cutthroat trout (the Yellowstone cutthroat trout is a unique species found only in the upper Yellowstone Basin). The Shields River supports a similar fishery.

Due to its geographic location on the edge of the Pacific Flyway, the Livingston area does not serve as a major flyway for migrating waterfowl. However, ducks and Canada geese use the bottoms of the Yellowstone and Shields rivers, and occasional fall concentrations do occur.

Although the water quality of the Yellowstone River is considered good, the Shields River has quality problems that have been detrimental to the younger age groups of fishes and, consequently, salmonid production.

5. Air Pollution Meteorology

A literature review of reports on air pollution meteorology in Montana provided the basis for this summary. A large amount of detailed meteorological data is available from the National Oceanic and Atmospheric Administration (NOAA); however, this information was not included in the report due to the expense and time required to reduce the data. Topics covered for the five CSA's include wind speed and direction, fog occurrences, and air pollution potential. Noise level information is available only for the Butte-Anaconda CSA. Consequently, future monitoring of noise levels at the other CSA's is required.

a. Billings

Wind records in the Billings area show a record high of 79 miles/hour (mph), an annual mean speed of 11.5 mph, and a prevailing direction from the southwest. Calm conditions were found to occur approximately 2.5 percent of the time on an annual basis. Winds 7 mph or less occurred 35 percent of the time during a 1966-67 study.

According to NOAA local climatological data, Billings has an average of 18 days of heavy fog per year, and most foggy days occur during the late fall-winter period.

In assessing the air pollution potential of the Billings area,

a number of sources were investigated, NOAA studies indicate a predominance of neutral atmospheric conditions (caused by wind and/or cloud cover) and a small amount of time in the stable and unstable categories. A predominance of neutral conditions can be expected in eastern Montana because of the frequency of moderate to high winds. On the other hand, Hosler's inversion studies suggest that inversions occur 50 to 45 percent of the time on an annual basis. Billings should experience between one and ten days of high meteorological potential for air pollution in a five-year period.

These general studies do indicate that the Billings area has meteorological conditions that contribute to an air pollution problem.

b. Butte-Anaconda

A limited amount of data indicates a record high wind of 40 mph and an annual mean speed of 7.9 mph in the Butte area. Wind data was not available for Anaconda or Whitehall. Wind roses for the Butte valley show that previaling winds are from the northwest; however, southerly winds prevail during the night. Wind roses for the Deer Lodge valley indicate a high occurrence of westerly winds. However, wind patterns vary widely in the Butte-Anaconda candidate site area, and these general directions cannot be applied to the whole area. For example, wind roses compiled at MERDI's meteorological station and at the Butte Airport (approximately two miles apart) differ substantially. Therefore, on-site monitoring will be necessary to accurately define wind patterns at specific sites.

Butte has an average of six days of heavy fog per year according to NOAA local climatological data. Similar to other areas, the highest frequencies are during fall and winter.

Based on the available information, the Butte-Anaconda area has the highest meteorological potential for air pollution of the CSA's. Butte has the largest percent of frequency in the stable category; moreover, an annual inversion frequency of 40 to 45 percent is estimated by Hosler's studies, and a high frequency (60 percent) of nighttime wind speeds are less than 7 mph. According to Holzworth's forecasts, an estimated 10 to 20 days of high meteorological potential for air pollution should occur in a five-year period.

Sampling of 11 sites in the vicinity of the Butte Industrial Park determined that there is a high level of noise in the TV band, FM band, and above. However, the TV and FM signals in the area are very high, such that a relatively large amount of high frequency interference can be generated without degrading nearby communications. No information is available in the Anaconda, Rocker, Deer Lodge, or Whitehall areas.

c. Glasgow Air Force Base

Within the Glasgow Air Force Base (GAFB) CSA, wind records are

available from two monitoring stations: GAFB and Glasgow Airport. Although wind roses developed for each station are similar, it is not determined whether all wind data may be positively correlated between stations. In addition, there is limited information available at GAFB. A 300-foot tower and meteorology lab currently are being installed at GAFB, and detailed meteorological data will soon be available.

Wind data collected at the Glasgow Airport indicates a record high wind of 46 mph, an annual mean speed of 11.0 mph, and northwesterly prevailing winds. Furthermore, a high percentage of wind speeds in the range of 0 to 7 mph were recorded for Glasgow Airport.

Glasgow Airport has an average of 12 days of heavy fog per year, but during the period 1968 to 1974, heavy fog surrounded the city an average of 14.3 days per year. The November through March period records the highest frequency of fog.

Available information indicates that the Glasgow area has a low potential for air pollution. A large percentage of the time is spent in the neutral atmospheric stability category. Furthermore, inversions occur 35 to 40 percent of the time annually based on a very general study by Hosler. Zero days of high meteorological potential for air pollution are expected in a five-year period.

Available data does indicate that Glasgow has meteorological conditions favorable to the dispersal of air pollutants.

d. Great Falls

Data from the Great Falls Weather Bureau Station shows a record high wind of 82 mph, an annual mean speed of 12.4 mph, and a southwesterly prevailing direction. Moreover, the Great Falls station shows a substantial percentage of time in the 8 to 23 mph and >23 mph wind speed ranges.

Based on 37 years of records, Great Falls has an average of 13 days of heavy fog per year (more prevalent during late fall, winter, and early spring).

Similar to most of eastern Montana, Great Falls shows a majority of the time in the neutral stability class, a class that promotes the dispersal of air pollutants. An annual inversion frequency of 35 to 40 percent is indicated; however, these figures are very general. Between zero and ten days of high meteorological potential for air pollution should occur in the Great Falls area during a five-year period.

These general studies indicate that the Great Falls area has a low potential for air pollution; however, more study is needed to substantiate this assumption.

e. Livingston

No wind roses have been compiled for the Livingston area; however, the necessary data are available from NOAA or Montana State University at considerable expense. A record high wind of 88 mph and an annual mean wind speed of 14.1 mph, the highest at any of the sites, were recorded at Livingston. The winds, which are predominantly from the southwest, spend a substantial percentage of time in the >23 mph wind speed range.

No data on fog occurrences are available because there is no national weather service station in Livingston.

Since air pollution is not considered to be a problem in the vicinity of Livingston, no work has been done on the air pollution meteorology of the area. The amount of wind in the area definitely decreases the air pollution potential.

f. Conclusions

Based on the above information, only the following general conclusion can be drawn: the Eastern Montana plains have meteorological characteristics better suited to handling air pollutants than the Western Montana valleys. The available data are taken only at weather bureau and flight service stations and may not apply to the entire CSA.

The lack of detailed information demonstrates the need for on-site meteorological monitoring at the candidate site. Until the meteorology of these areas is better defined, only rough approximations of potential environmental impact can be made.

6. Air Quality

The overall air quality situation at each of the five candidate site areas (CSA's) is concisely treated in this summary. Based on Air Quality Bureau (AQB) ambient air monitoring data available for 1971-77, specific pollutants that are exceeding standards are identified for each CSA. Furthermore, a matrix (Table 1) has been developed to display the relationship between the number of pollutants monitored and violations of air quality standards for each CSA. Point and non-point sources, as identified by the AQB, are mentioned and related to the overall pollution problem.

a. Billings

According to the data reviewed, the Billings-Laurel area has a substantial air pollution problem. Several pollutants have been and are exceeding Montana and federal ambient air quality standards. The following list gives the pollutants monitored by the AQB and describes their relation to ambient air quality standards:

1. Total suspended particulates (TSP) exceed state and federal standards in various parts of the area;

2. Sulfur dioxide (SO_2) levels have exceeded Montana and federal standards on numerous occasions during the period 1975 to 1977;

3. Sulfation rates (total reactive sulfur), available for only 1975, showed numerous violations of Montana standards;

4. Nitrogen dioxide (NO_2) levels are within federal standards;

5. Carbon monoxide (CO) levels exceeded the eight-hour federal primary standards several times during 1975 and 1976;

6. Hydrocarbon (HC) levels are above natural background levels, but they are not comparable with standards because of discrepancies in the AQB's monitoring techniques; and

7. Ozone levels often exceeded the federal standards during 1975 and 1976, but no violations were recorded during the first five months of 1977.

Briefly, the Billings area has high levels of suspended particulates and reactive sulfur compounds (including SO_2) in the ambient air. NO_2, CO, HC, and ozone contribute to the pollution load but to a smaller extent than TSP and reactive sulfur compounds.

Numerous point and non-point sources contribute to the air pollution problem. Point sources, including three oil refineries (Conoco, Cenex, Exxon), the Great Western Sugar Company, the Corette Power Plant, and the Montana Sulphur and Chemical Company, contribute large amounts of SO_2, particulates, nitrogen oxides, HC, CO, and fluorides. Furthermore, non-point sources, such as unpaved roads, agriculture, and transportation, contribute particulates as well as SO_2, CO, HC, and nitrous oxides.

Although the metropolitan area seems to be well covered with AQB monitoring stations, a lack of data for outlying areas demonstrates the need for additional monitoring.

b. Butte-Anaconda

With the exception of the Whitehall area, the Butte-Anaconda CSA has a history of air pollution problems. The results of this air quality review show that the problems, although lessened, still exist today.

A number of pollutants are monitored by the AQB, MERDI, and The Anaconda Company in the CSA. This report is based largely on AQB monitoring data; a small amount of MERDI's meteorological station data also was used. A list of the pollutants covered include TSP, SO_2, sulfation rate, dustfall, fluorides, CO, and NO_2.

A list of the pollutants and their relation to ambient air quality standards follow:

1. Total suspended particulates are a major pollution problem, especially in the vicinity of Butte and Anaconda where standards often are exceeded;

2. Sulfur dioxide often exceeds standards in the Anaconda area, but the Butte area has no SO_2 monitors so the levels of the gas presently are unknown (MERDI is installing an SO_2 automatic analyzer so data will be available in the future);

3. Sulfation rate state standards were exceeded near Anaconda during 1975, but MERDI's meteorological station near Butte recorded no violations during 1976 and 1977 to date;

4. Dustfall is recorded at MERDI's meteorological station, but not enough data was available for a comparison with standards;

5. Fluorides are a major problem in the Ramsay-Silver Bow area, and evidence indicates that standards are even exceeded in the Butte valley; and

6. Carbon monoxide and nitrogen dioxide monitoring was recently initiated in the Butte area, but not enough data was available for a comparison with standards.

Based on these findings, TSP, SO_2, and fluorides appear to be the major problems in the Butte-Anaconda CSA. The sulfation rate is also a problem near point sources of reactive sulfur compounds. Not enough data was available for dustfall, NO_2, or CO to accurately relate them to air quality standards.

The major point source in the vicinity of Butte is the Berkeley Open Pit Mine, from which large amounts of particulates, hydrocarbons, sulfur dioxide, and oxides of nitrogen are emitted. Other point sources in the area include a tepee burner, three asphalt hot mix plants, and a concentrator and crusher that process the Berkeley ore. Moreover, the Stauffer Chemical Company at Silver Bow, Montana emits significant quantities of fluorides, sulfur dioxide, and particulates. The Anaconda Company's copper smelter in Anaconda is the largest point source within any of the CSA's; it emits huge amounts of particulates and SO_2 every year.

Non-point sources in the CSA include incinerators, motor vehicles, agricultural burning and cultivation, and unpaved roads. The city streets in Butte may accumulate airborne particulates and thus be a major non-point source in the area.

Despite good coverage of several pollutants, more monitoring may be necessary to better define the air quality of the area. If the Whitehall area is under consideration, baseline air quality monitoring will have to be initiated.

c. Glasgow Air Force Base

Air quality in the Glasgow Air Force Base CSA generally is con-

sidered to be excellent. However, this assumption is poorly documented since only one air quality monitoring station lies within the CSA boundaries. The McCone County-Fort Peck AQB monitoring station is used because it is within the 40-mile radius and because it should have levels of air quality representative of the Glasgow area. Total suspended particulates, sulfur dioxide, and nitrogen dioxide are measured at the station. The following list describes the levels of these pollutants and their relation to ambient air quality standards:

1. Total suspended particulate levels usually were below standards; one violation occurred during the period 1975 through 1977, but it was an isolated case;

2. Sulfur dioxide, as measured by a gas bubbler, was not detected during 1976 or 1977; and

3. Nitrogen dioxide levels measured at the station were far below federal standards.

Low levels of these pollutants indicate the lack of population and industry in the area.

The only point source documented by the AQB in the Glasgow area is the Tumpane Company heating plant at Glasgow Air Force Base; it emits small amounts of SO_2 and particulates. Non-point sources in the area would include agricultural sources, transportation, unpaved roads, and natural sources.

Since only one air quality monitoring station lies within the CSA, a more extensive monitoring network certainly is needed.

d. Great Falls

The Great Falls area occasionally violates ambient air quality standards; however, the area does not appear to have a major air pollution problem. A number of AQB monitoring stations in the area record levels of total suspended particulates, sulfur dioxide, sulfation rate, and dustfall. These pollutants, their levels, and their relation to standards are listed below:

1. Total suspended particulate levels in the area occasionally violate standards, especially the 24-hour averages;

2. Sulfur dioxide levels have exceeded standards near the Phillips Oil Refinery in the past, but ambient air monitoring has been discontinued since 1975 because of non-detection of the gas;

3. Sulfation rates, available for only 1975, were exceeded only in the immediate vicinity of the oil refinery;

4. Dustfall data, again available for only 1975, indicated numerous violations of settleable particulates standards in Cascade County.

Based on the available data, particulates are considered to be the only significant air pollutant in the Great Falls area. Although SO_2 levels and sulfation rates are high near the oil refinery, the ambient air doesn't seem to be affected adversely.

Point sources in Great Falls include the Con-Agra Grain Mill, the General Mills Flour Mill, and the Phillips Petroleum Refinery; the mills emit only particulates, whereas the Phillips Refinery emits particulates, SO_2, nitrogen oxides, HC, and CO. A list of non-point sources would probably include agriculture activity, transportation, unpaved roads, incinerators, and other man-made and natural sources.

Further monitoring in the Great Falls CSA may be necessary to cover additional pollutants and to provide background air quality information for outlying areas.

c. Livingston

A substantial amount of wind and a lack of point sources in the Livingston area combine to give the CSA what is considered an excellent air quality. However, because no ambient air quality monitoring stations have been established in the area, this assumption is not documented. Therefore, ambient air quality monitoring is needed to establish a baseline air quality and to serve as an aid in siting of the ETF.

The only documented point source in Livingston is Burkland Studs, a lumber mill that emits small amounts of SO_2 and particulates. Another possible point source is the railroad repair shops, but it is not documented by the AQB. Non-point sources in the Livingston CSA would likely include agricultural activities, logging, slash burning, motor vehicles, unpaved roads, and natural sources (dust storms, hydrocarbon emissions from trees, etc.).

Since the Livingston area has no known air quality problems, there is no reason for the AQB to establish an air monitoring network. However, baseline air quality data is needed to conduct an environmental impact analysis; therefore, MERDI should proceed to set up an air quality monitoring program in the Livingston area.

f. Conclusions

To quickly summarize the ambient air quality data for the five CSA's, an ambient air quality matrix was constructed (Table 1). The number of pollutants monitored in each area and their relation to air quality standards is demonstrated. As shown in Table 1, the Billings and Butte-Anaconda areas have significant air pollution problems. Great Falls has a problem with particulates but not with sulfur oxides. Mainly, this matrix points out the need for additional air quality monitoring, especially in the Glasgow and Livingston areas.

7. Electrical transmission systems

Estimates of the electrical characteristics of the Engineering Test Facility (ETF), based on the draft preliminary design criteria reports prepared for ERDA, are itemized in this report. This data describes the input power requirements and the output power load which will be produced by the ETF.

The electrical utilities in each CSA which can supply the needed input power and which can accept the output load are identified. The companies which are being considered for serving the electrical needs of the ETF are the Montana Power Company (MPC), the U.S. Bureau of Reclamation (USBR), the Bonneville Power Administration (BPA), the Pacific Power and Light Company (PPL), and various rural electric cooperatives (REA's).

a. Criteria

The following list describes the basic electrical characteristics of the conceptual ETF:

A. Power level $\simeq$ 250 MW_t;

B. MHD power out $\simeq$ 33 MW_e;

C. Steam power out $\simeq$ 95 MW_e;

D. Start-up and auxiliary input power requirement $\simeq$ 15-20 MW_e;

E. Start-up duration $\simeq$ 28 hours;

F. Start-up energy requirements $\simeq$ 24 hours @ half load followed by $\simeq$ 4 hours @ full load;

G. Construction input
   1. power requirement $\simeq$ 450-700 KW @ peak demand
   2. energy requirement $\simeq$ 150,000-250,000 KWh/month; and

H. Generating time $\simeq$ 2000 hours/year @ 1-100 hour duration intervals.

During this phase of the ETF site suitability study, 1983 was assumed as the earliest date that power output would be generated. Reconfirmation of available service will have to be made as the ETF construction schedule is altered.

b. Construction input power

The construction input power conceivably could be furnished by any of the electric cooperatives serving the CSA's; however, only one REA has responded affirmatively at this time.

Of the utilities shown in Figure 6 , only the USBR has stated that it definitely cannot furnish this input. In the upper Missouri

region, the USBR has marketed all of its firm hydrocapacity and, therefore, cannot make additional commitments for firm power sales.

c. Start-up and auxiliary input power

In each CSA, transmission line capacity should be available to supply the start-up and auxiliary power requirements of the ETF. Lines rated at 69 to 100 KV presently are routed throughout the areas, and local utilities have indicated that overloading should not occur in attempting to distribute 15 to 20 MW by this means.

Start-up cycles may have to be limited to off-peak periods if the start-up input is supplied by the USBR. Their surplus capacity during these periods then could be utilized without disrupting their firm power commitments.

d. Output power

Transmission lines in the range of 100 to 230 KV will probably be required to transport the output energy. Available line capacities, line efficiencies, and service interruption insurance are all factors which lead to this decision by the utilities. Transmission lines within each CSA that presently can accept the 128 MW output are designated in Figure 6.

Currently, no transmission line in the Glasgow Air Force Base CSA is available to receive the output. Although the USBR has constructed 115 KV, 161 KV, and 230 KV lines within this CSA, these lines already are loaded heavily with the output of hydrogeneration at Fort Peck and Yellowtail dams. At this time, it would be necessary to construct an additional 230 KV transmission line between the site and lines with capacity in either the North Dakota/South Dakota area or the Havre/Great Falls area. However, the Army Corps of Engineers has proposed to add additional peaking capacity to the Fort Peck Reservoir between 1985-87, which would require the construction of a new transmission line. The draft environmental impact statement on this proposed action has been released, and authorization from the executive branch for construction may occur within FY 78. Should this development proceed, it is feasible that the ETF could utilize this transmission network.

Construction of a 230 KV transmission line could cost $55,000 per mile or more. A permit must be secured from the Department of Natural Resources if the construction distance is over ten miles; two years is normally required to obtain this permit.

8. Transportation Facilities

This section describes the transportation facilities available in the five candidate site areas (CSA's). The railroad lines, the airlines, the bus lines, and the interstate highway system are the four means of travel addressed.

a. Rail service

Freight currently is being transported throughout the state by seven railroad companies. The strength ratings of each line presently are being examined with regard to their capacities to transport coal and heavy supplies. Preliminary estimates indicate that costs of $35 to $40 per track foot may be required to upgrade any lines of insufficient quality. Furthermore, if new track must be laid, construction costs may range from $500,000 to $1,000,000 per mile depending on the type of terrain and many other factors.

Amtrak provides Montana with passenger train service along both a northern and southern route.

More detailed information about the rail services available in the CSA's is tabulated in the complete transportation report.

b. Air service

Four major commercial airlines supply Montana with passenger and cargo transportation.

Along with numerous smaller air strips, one commercial airport is located within each CSA. The busiest airport, Logan Field International, is located two miles north of Billings. It presently accommodates 32 flights per day; this is almost twice the number of flights routed to Great Falls International, the next busiest airport.

Glasgow Air Force Base (GAFB) is not maintained for commercial or military air traffic; therefore, Glasgow International, fifteen miles south of the air base, provides the passenger and cargo service for this CSA.

In the Livingston-Bozeman CSA, Gallatin Field, seven miles west of Bozeman, is utilized by the major airlines. The Bert Mooney/Silver Bow County Airport, four miles south of Butte, similarly accommodates commercial flights for the entire Butte-Anaconda CSA.

c. Bus service

Bus service is available between all major cities in the state. Butte and Billings are the only communities in the CSA's with intracity bus lines.

d. Interstate highway system

The construction of 1187 miles of multi-lane divided controlled-access interstate highway is planned in Montana. Seventy-one percent presently is completed, and the remainder tentatively should be finished by 1990.

Information is being gathered on the scheduled completion dates for the unfinished sections between Butte and Great Falls and between Butte and Billings. These routes are of particular interest because of the need for information transfer between the Engineering Test Facility and the Component Development and Integration Facility located in Butte. It should be noted that no interstate highway has been constructed or is scheduled for construction in the vicinity of Glasgow Air Force Base.

9. Work Forecast

Several topical areas describing the existing environment need to be assessed during FY 78: 1) archaeological, historical, religious, and cultural sites; 2) background signal/noise levels; 3) attitudes of local residents toward siting an MHD facility; 4) socioeconomic parameters including chronic, cyclic, and seasonal unemployment by occupation and land use; and 5) site area meteorological baseline characterization including wind speed and direction and background air quality.

Potential environmental impact of the ETF on the candidate site areas will be assessed upon receipt of final design criteria. Effects on the natural and human environment will include the parameters diagramed in Figure 7.

A determination of waste heat utilization options relevant to siting the ETF should be conducted. Such an effort would be initiated with a literature search on waste heat utilization. The state of Montana then would be canvassed to determine locations of existing industries and communities capable of utilizing waste heat. Determination will be made as to whether the siting process will be reopened and expanded to include this criteria.

IV. CONCLUSIONS

Table 2 is a summary analysis of the existing conditions of certain baseline parameters at each candidate site area. Its purpose is to identify problem areas at each site concisely but not to rank one site against another. Since individuals will consider one constraint significantly more important than another, the relative standing of each CSA will shift. Until the other baseline data (e.g., social acceptability, socioeconomic parameters, noise level, land use, and archaeology) are quantified and impact analyses are conducted, the relative benefits or deficiencies of each site will be incomplete.

Table 1.--Ambient Air Quality Matrix

Candidate Site Areas	Total Suspended Particulates (TSP)	Sulfur Dioxide (SO_2)	Sulfation Rate	Nitrogen Dioxide (NO_2)	Carbon Monoxide (CO)	Hydro-carbons (HC)	Ozone (O_3)	Fluorides	Dustfall (Settleable Particulates)	Remarks
Billings	e	e	e	ne	e	NC	e	NM	NM	
Butte-Anaconda	e	e	e	NM[c]	NM[c]	NM	NM	e	NM[d]	[c]monitoring just initiated [d]not enough data available
Glasgow	ne[b]	ne	NM	ne	NM	NM	NM	NM	NM	[b]only one isolated violation was recorded
Great Falls	e	ne	e[a]	NM	NM	NM	NM	NM	e	[a]exceeded only around oil refinery
Livingston	NM	NM	NM	NM	NM	NM	NM	NM	NM	

e - exceeding Montana or federal ambient air quality standards
ne - not exceeding standards
NM - not monitored for
NC - not comparable with standards

Table 2.--Summary Evaluation of Siting Criteria

CSA / Parameters	Butte-Anaconda	Billings	Glasgow Air Force Base	Great Falls	Livingston-Bozeman
Water Availability	+	-	+	+	-
Air Quality Meteorology	-	-	0	+	+
Transmission Capability	+	+	-	+	+
Geology/Soils	0	+	+	+	0
Vegetation	0	0	0	0	0
Wildlife & Aquatic Biology	0	0	0	+	-
Access	+	+	0	+	+

\+ No problems are foreseen to meet this criteria
0 Potential problems exist but can be solved by engineering design
\- Definite problems exist and must be resolved

Figure 1.--MHD Power Plant Siting Process

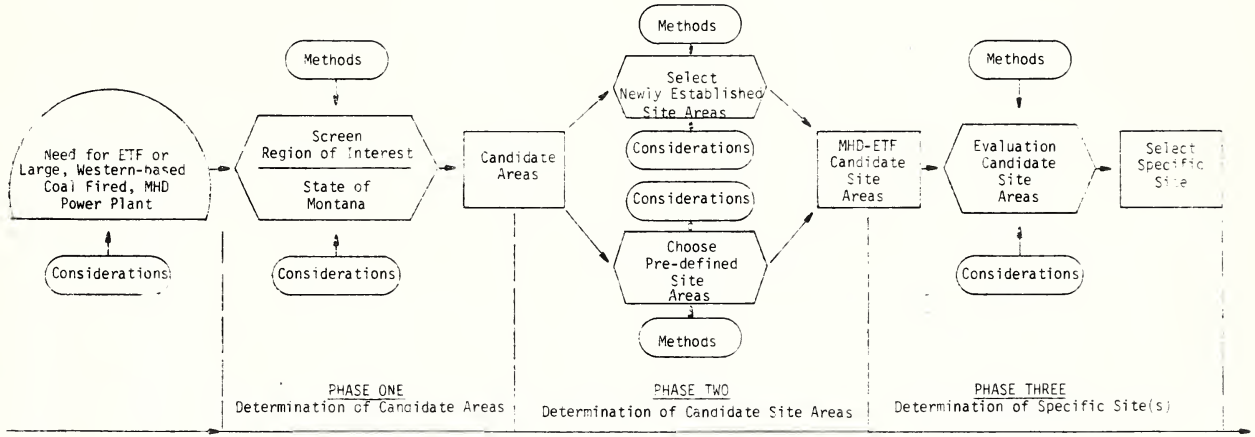

SUBSEQUENT STAGES ARE:

Stage Three: Pre-construction licensing of site and plant design

Stage Four: Construction and operation

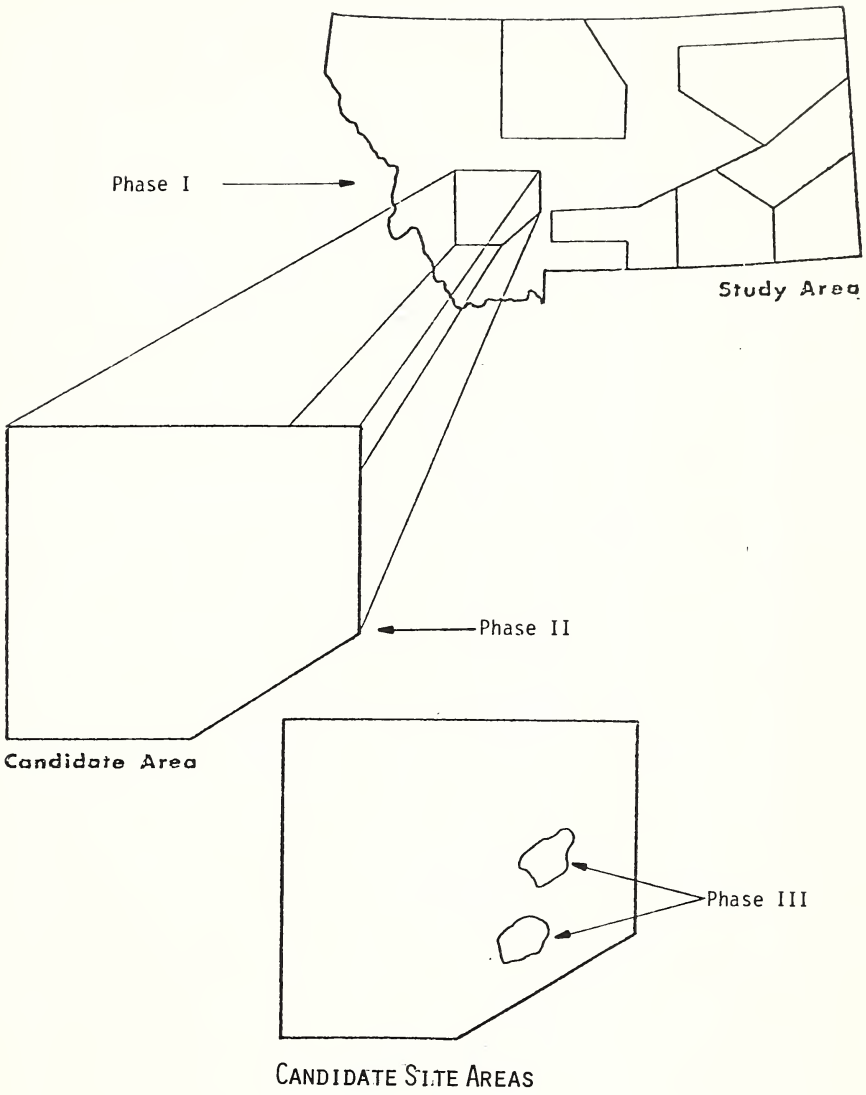

Figure 2.--The Site Selection Process

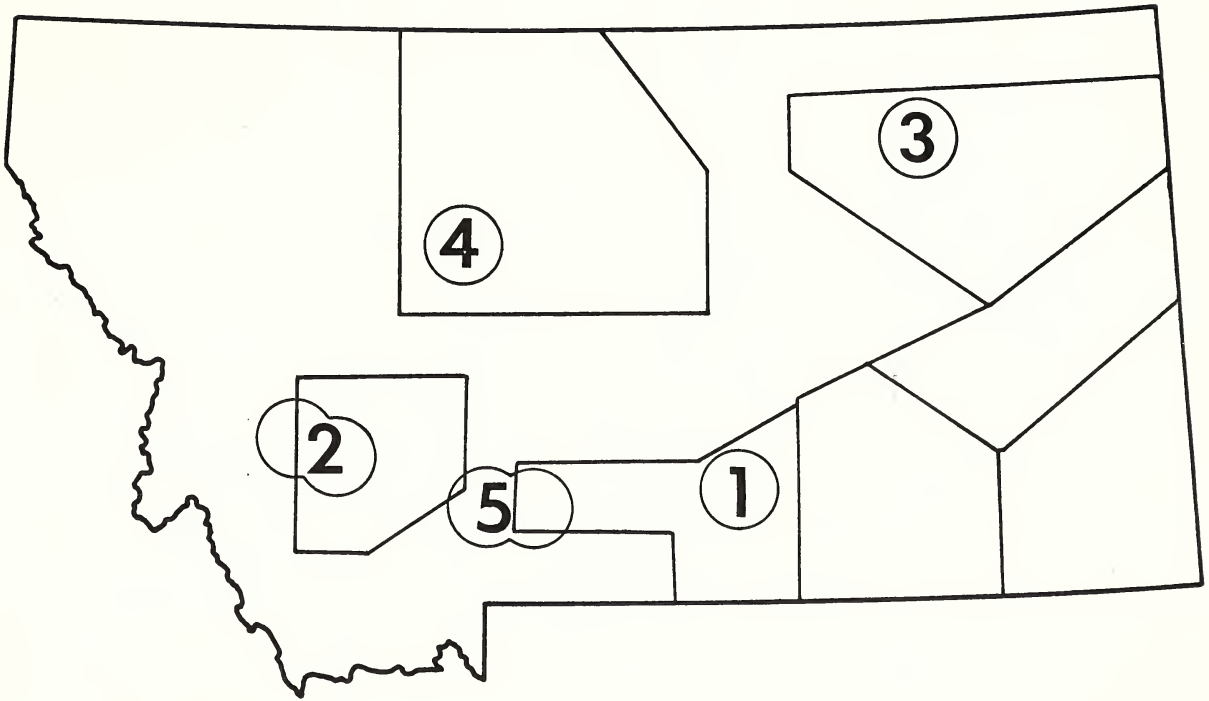

Figure 3.--Tentative Selection of MHD-ETF Candidate Site Areas

3
4

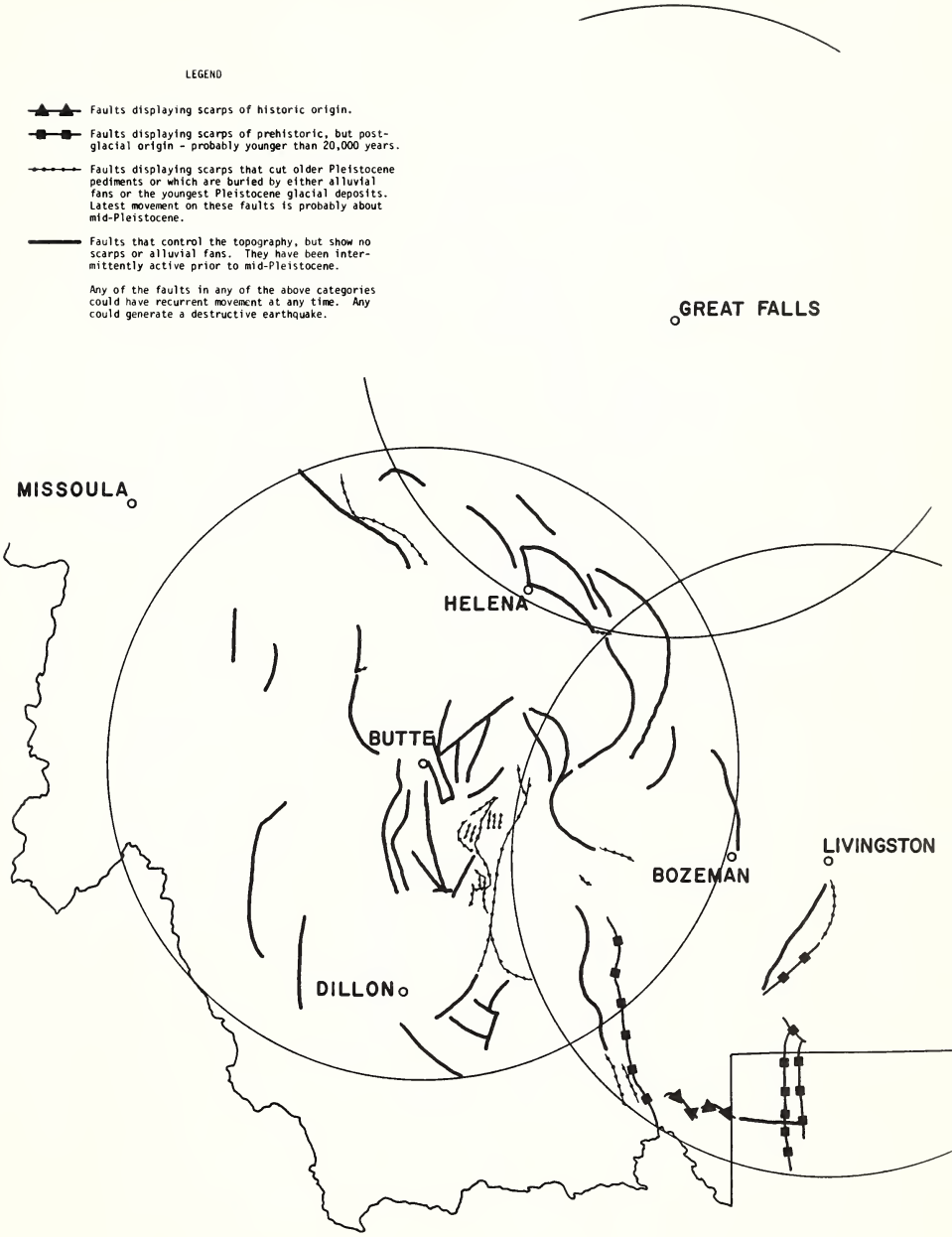
LEGEND
Faults displaying scarps of historic origin.
Faults displaying scarps of prehistoric, but post-glacial origin - probably younger than 20,000 years.
Faults displaying scarps that cut older Pleistocene pediments or which are buried by either alluvial fans or the youngest Pleistocene glacial deposits. Latest movement on these faults is probably about mid-Pleistocene.
Faults that control the topography, but show no scarps or alluvial fans. They have been intermittently active prior to mid-Pleistocene.
Any of the faults in any of the above categories could have recurrent movement at any time. Any could generate a destructive earthquake.
GREAT FALLS
MISSOULA
HELENA
BUTTE
BOZEMAN
LIVINGSTON
DILLON

Figure 4.--Study Area Faults

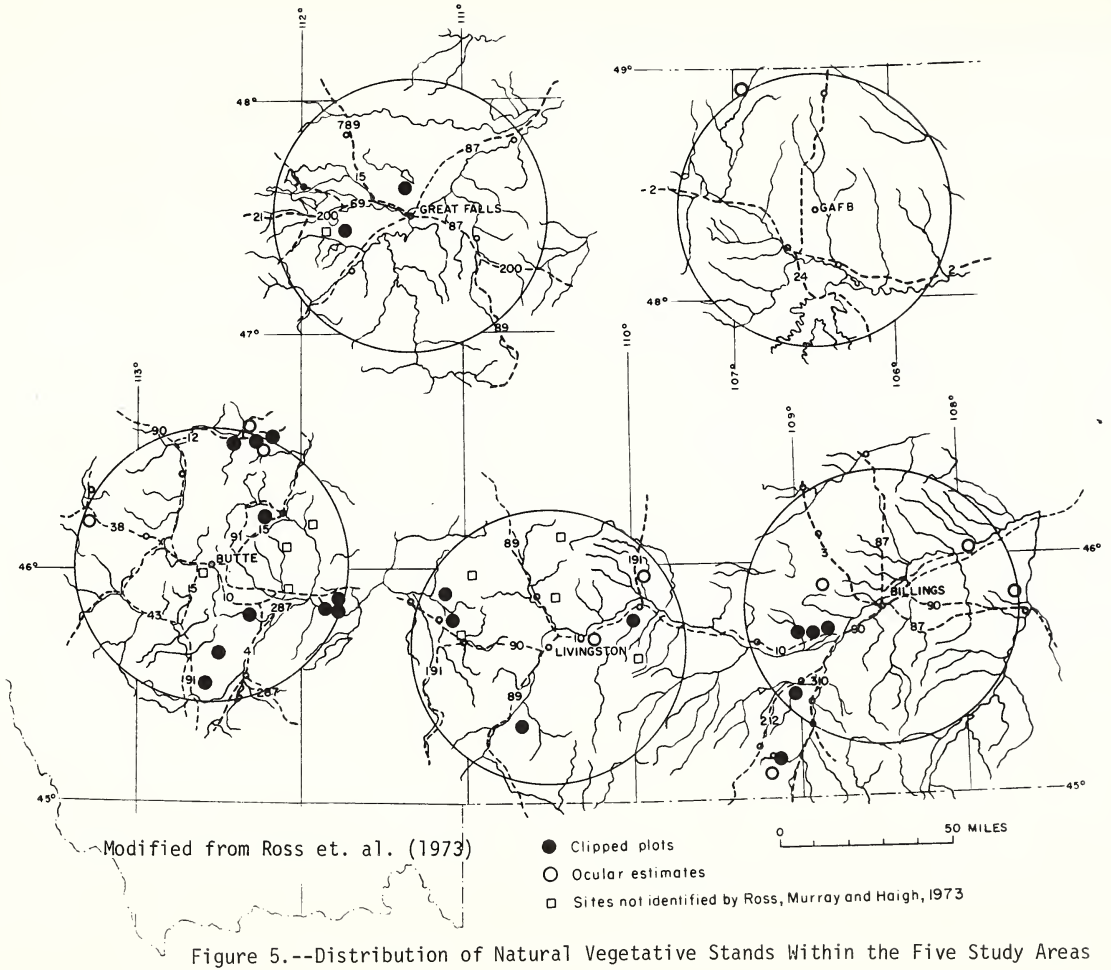

Figure 5.--Distribution of Natural Vegetative Stands Within the Five Study Areas

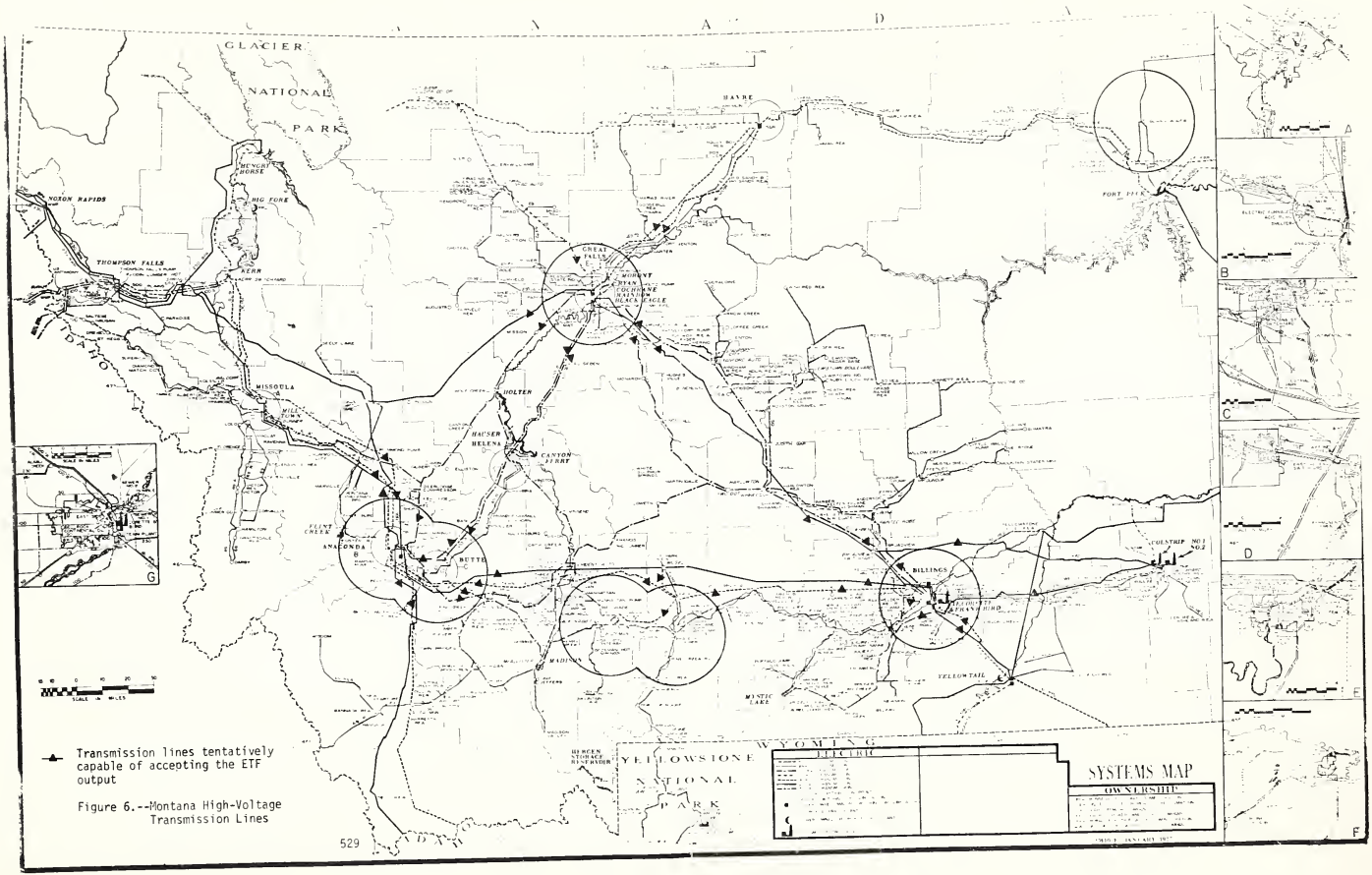

Figure 6.--Montana High-Voltage Transmission Lines

Figure 7.--Impact Assessment Parameters

NATURAL ENVIRONMENT

Meteorology/Noise	Topography	Geology/Soils	Hydrology	Ecology	Resource Availability
air currents & stability	slope	soil condition	water quantity & availability	wildlife	coal
air quality	land form	seismic activity	water quality	vegetation	oil
air temperature			flood zones	rare & endangered species	oxygen
					nitrogen

HUMAN ENVIRONMENT

MHD program requirements	Utility corridors	Transportation access	Land use	Archaeology	Socio-economic	Social acceptability
existing government sites	electrical grids	highway	ownership	historical sites	employment	cultural characteristics
program continuity	available start-up & output capability	railway	natural areas	archaeology sites	income	historical conditions
		airways	recreational	religious sites	under utilized labor force	social profile
			wildlife refuge		financial resources & expenditures	
			wilderness & primitive areas		community facilities & services	
			residential		population characteristics	
			commercial			
			irrigated			
			dryland			
			rangeland			
			forest			
			zoning regulations			
			waste disposal			

MILESTONE CHART

STATUS DATE Sept. 30, 1977

TASK M

PROGRESS

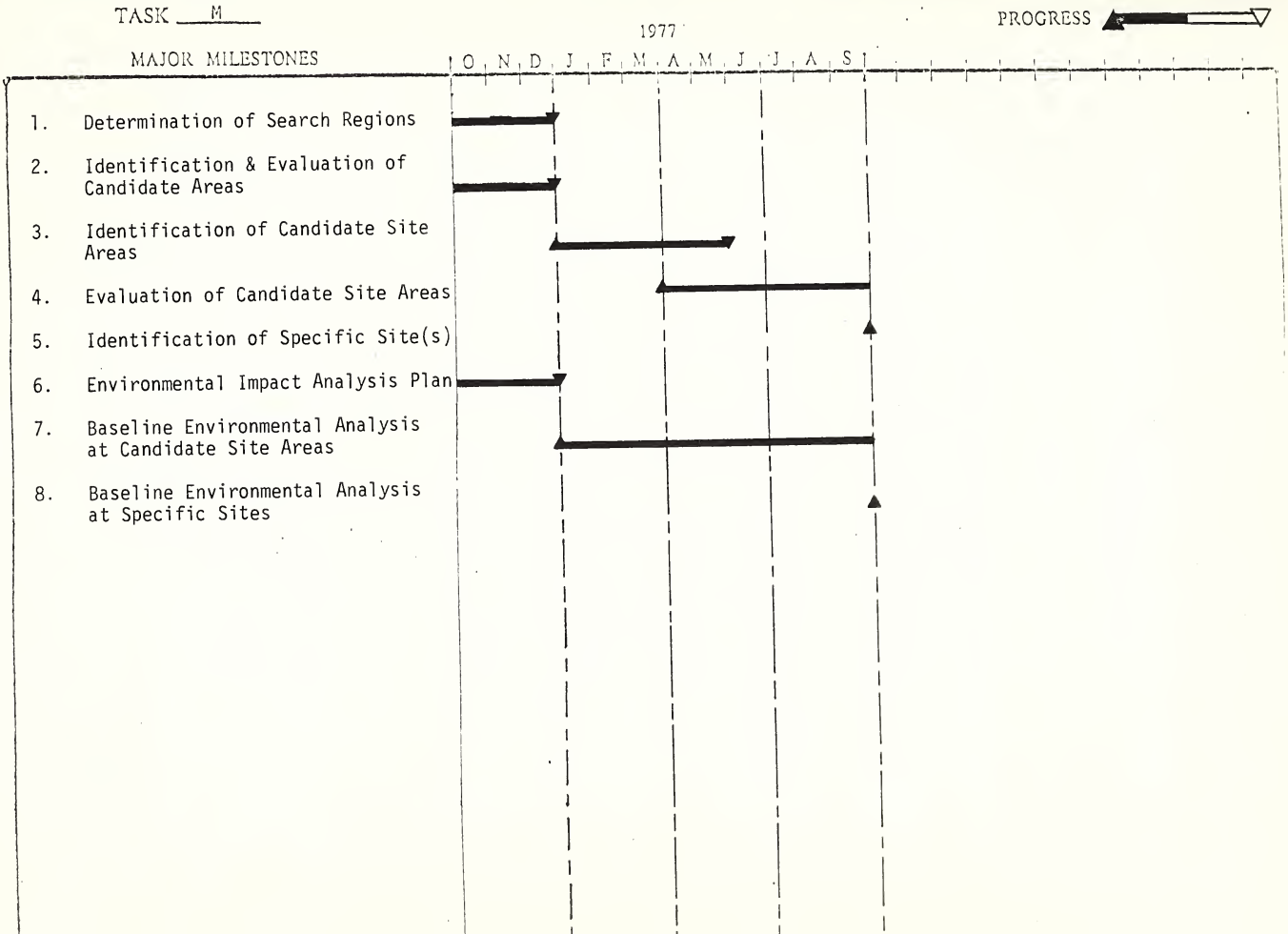
1977
O N D J F M A M J J A S
MAJOR MILESTONES
1. Determination of Search Regions
2. Identification & Evaluation of Candidate Areas
3. Identification of Candidate Site Areas
4. Evaluation of Candidate Site Areas
5. Identification of Specific Site(s)
6. Environmental Impact Analysis Plan
7. Baseline Environmental Analysis at Candidate Site Areas
8. Baseline Environmental Analysis at Specific Sites

TASK N
Materials Evaluation and Management of University and MERDI Supporting Science and Technology

J. J. Rasmussen

ABSTRACT

The design of the MERDI ceramic fabrication and characterization laboratory is described. Equipment for the laboratory was obtained, installed, and checked-out. Programs to study the thermal conductivity and diffusivity of MHD materials, to develop and fabricate controlled-structure MHD materials, and to study the wettability characteristics of MHD materials by slag-seed mixtures were initiated.

In collaboration with other MHD contractors at FluiDyne Engineering Corporation and Montana State University, the thermal transport properties of a preheater refractory (Corhart RFG) exposed to simulated MHD operating conditions were studied. The determined thermal diffusivity and conductivity data were expressed in analytical form to provide input for engineering design purposes.

High-purity and dense ceramic rods are being fabricated at MERDI to be used in Task B slag-corrosion studies. Initially, two spinel compositions (50 m/o MgO / 50 m/o Al_2O_3 and 65 m/o Mgo / 35 m/o Al_2O_3) are being fabricated and characterized. Substrate samples of α-Al_2O_3 and the two spinel compositions listed above are being made for in-house wettability studies. A development program to fabricate ceramic of controlled porosity was initiated.

Measurements of the surface tension of synthetic coal slags and characterization of the interaction boundary between the slags and ceramic substrates were carried out.

I. OBJECTIVE AND SCOPE OF WORK

The objective of Task N is to supply the technical manpower and facilities required to serve as a principal MHD materials evaluation and development capability for ERDA in conjunction with the MHD Component Development and Integration Facility (CDIF) in Butte, Montana. As directed by ERDA, this task will evaluate and develop the materials and materials' systems used in MHD power generator components including combustors, heat-exchangers, channels, electrodes and insulators, seed-recovery systems, pollution systems, and waste-disposal systems. This task also will provide the technical and administrative management of MHD supporting science and technology efforts at units of the Montana university system.

The MERDI in-house research program will include the following subtasks:

- Selection, evaluation, and characterization of MHD materials, including testing under simulated MHD conditions;
- Pre- and post-test analysis of MHD materials and components; and
- Materials and specimen fabrication facilities and analytical service to assist other experimental investigators in obtaining data on well-characterized materials.

Specific activities which are being initiated to meet these objectives include the following:

- Studies of the thermal conductivity and diffusivity of MHD materials;
- Development and fabrication of controlled-structure MHD materials; and
- Studies of wettability of MHD materials by slag-seed mixtures.

II. SUMMARY OF PROGRESS TO DATE

A. Thermal Conductivity and Diffusivity of MHD Materials

During the first half of the year, the laboratory was designed and the necessary equipment was purchased and checked out. During the third quarter, emphasis was placed on evaluating the thermal transport properties of a variety of ceramics and glass-ceramics which would provide a data base necessary to characterize MHD materials effectively. During this same period, the experimental components and techniques were upgraded continuously.

During the fourth quarter, in collaboration with other MHD contractors at FluiDyne Engineering Corporation and Montana State University, the thermal transport properties of a preheater refractory (Corhart RFG) exposed to simulated MHD operating conditions were studied. The thermal transport properties of primary interest are the thermal conductivity and the specific heat capacity values of cored refractory, both as a function of slag exposure and as a function of temperature in the range of operation of a typical regenerative preheater (1000° to 1700°C). The data are expressed in analytical form to provide input for engineering calculations of the magnitudes of thermal stresses and of overall heat energy balance and efficiency for particular preheater designs.

B. MHD Materials Development and Fabrication

During the first half year, equipment for a ceramics fabrication facility was obtained and installed. Equipment in operation at present includes a roller mill, two drying ovens, a bisque furnace, a 10 kpsi isostatic press, a high-temperature controlled atmosphere sintering furnace, a Mettler balance, a sample

mounting press, sample grinding and polishing equipment, a metallograph (magnification to x1000), and an optical microscope with camera attachments (magnification to x500). When possible, government surplus equipment has been obtained and reconditioned for use in materials fabrication or characterization work. Raw materials and chemicals such as high purity oxide powders and a variety of binders, dispersants, and mixing aids were purchased.

During the third quarter, a recirculating water cooling system for both high temperature furnaces was designed and built in-house. High-purity, high-density substrate materials were fabricated and characterized for the in-house slag wettability studies.

During the fourth quarter, a program was initiated to supply high-purity and dense ceramic rods for the Task B slag-corrosion studies. Fabrication techniques will be varied to provide materials of different grain sizes. Initially, two spinel compositions (50 m/o MgO / 50 m/o Al_2O_3 and 65m/o MgO / 35 m/o Al_2O_3) will be fabricated and characterized. Fifteen rods have been furnished to Task B personnel to date.

Also during the fourth quarter, a program to develop techniques for fabricating ceramic of controlled porosity was initiated. Specialized ceramicware necessary for fabrication of other ceramic pieces are being made in-house as well.

C. Wettability of MHD Materials by Slag-Seed Mixtures

During the first half year, a high temperature furnace was purchased, installed, and checked out. During the third quarter, substrate materials of high-purity, high-density alumina and magnesium aluminate spinel were prepared and characterized. A computer program designed to evaluate surface tensions from the curvature of the molten slag surface was debugged.

During the fourth quarter, measurements of the surface tension of synthetic coal slags and characterization of the interaction boundary between the slags and potential MHD materials were carried out. Nineteen slag-substrate combinations, including seven synthetic slag compositions with three different substrates, were tested. The contact angles were determined from photographs from the slag deformation point to 1550°C. The same photographic data is being processed to determine slag surface tension as a function of temperature using a computer program.

The contact angles were found to depend on slag composition, substrate composition and surface preparation, temperature, and time. The time dependence appears to be due mainly to corrosive attack of the substrate by the slag. Even at the highest test temperatures, contact angles remained greater than 10° in general.

Computer analyses of the surface tension data are in progress.

III. DETAILED DESCRIPTION OF TECHNICAL PROGRESS

A. Thermal Conductivity and Diffusivity of MHD Materials

1. Introduction

Efforts during this past year were directed primarily toward designing and checking out a test system for the rapid evaluation of thermal transport properties of real MHD materials--particularly those subjected to the hostile MHD environment of high and cyclic temperatures and of slag/seed exposures for various lengths of time. It is anticipated that these data will provide input for the various mathematical models which simulate MHD operations as well as additional criteria for evaluating a material's long-term suitability for use in a particular component. The MHD system is dynamic. The operating efficiency and long term durability depend directly on a component's thermal transport properties. This is particularly true since many physical properties such as electrical conductivity, viscosity, diffusion, reaction rates, creep rates, stress magnitudes, etc. are so sensitive to temperature or temperature gradients. Perhaps the most critical area where thermal transport properties are needed is in the area of ceramic MHD electrode and insulator design.

2. Experimental Procedure

Radiation losses and long measurement times encountered during high temperature steady-state methods of measuring thermal conductivity dictate that the thermal conductivity (λ) be calculated from the thermal diffusivity (α), density (ρ), and specific heat capacity (C_p) by the equation

$$\lambda(T) = \alpha(T) \cdot \rho(T) \cdot C_p(T). \qquad (1)$$

All of the terms are functions of temperature (T).

a. The laser-flash diffusivity technique

The laser-flash diffusivity technique was selected as the primary method for determining the thermal diffusivity, $\alpha(T)$. This method has been demonstrated to be rapid and convenient and to give reproducible results up to temperatures as high as 2500°K.[2-7] Furthermore, this technique uses a very small and simple specimen geometry.

Specifically for this program, the laser used was of the glass-neodymium type* which fires a single pulse (pulse width of $\approx$ 800 nsec) of 1.06 μm radiation. The laser flash is directed at one face of a disc-shaped specimen, measuring 1/2 inch diameter by <0.1 inch thick, and mounted on a suitable specimen holder within a cylindrical graphite chamber. In turn, the graphite chamber is contained in a high-temperature furnace[x] capable of attaining a temperature in excess of 2500°C. Specimens are coated with a thin

---

* Korad #K-1, Korad Division of Hadron, Inc. Santa Monica, CA 90406.

x Astro #1000A, Astro Industries, Inc. Santa Barbara, CA 93101.

layer of carbon[+] in order to make them opaque to the laser radiation and to make the emittance/absorptance characteristics of all specimens the same. The transient temperature response of the opposite face of the specimen is monitored either with an infrared (InSb) detector[o] or with a chromel-constantan thermocouple attached to the specimen with a small amount of ceramic cement.[†] The ambient sample temperature is determined by a Pt-Pt 13% Rh thermocouple placed next to the graphite chamber. This thermocouple is cross-checked periodically by signting on the chamber with an optical pyrometer and, at times, by measuring the temperature inside the chamber with the thermocouple attached directly to the sample. The transient signal from either detector is recorded on a storage oscilloscope.[*] All measurements were made in an inert atmosphere of dry nitrogen.

Figure 1 is a schematic diagram of the appartus for measuring the thermal diffusivity by the laser-flash technique. Figure 2 is a photograph of the apparatus. The thermal diffusivity (α) is calculated from the time ($t_{\frac{1}{2}}$) required for the transient temperature change (ΔT) of the backface of the specimen to reach half of its maximum value (ΔTm), which is also the steady-state value, from

$$\alpha = A\ell^2 / t_{\frac{1}{2}}. \qquad (2)$$

where ℓ is the specimen thickness and A is a dimensionless constant. The value of A depends on the rate of heat loss from the specimen during the time of measurement. Assuming linear heat flow normal to the face of the heated disc and no heat losses, A has a value of 0.1388.[4] When heat losses occur, the value of A is reduced in a manner described by Heckman.[8]

The normal procedure for determining $\alpha(T)$ consists of firing the laser at least three times at each temperature in order to get an average value for α. The heat-loss correction is estimated at each temperature by firing one additional laser pulse and recording the transient temperature change with a slower sweep time. The relative temperature rise ($\Delta T/\Delta Tm$) of the back surface is compared for times up to $10t_{\frac{1}{2}}$ with tabulated values given by Heckman,[8] and from which the constant A can be estimated.

Earlier results[1] showed that although the heat loss correction was only a few percent at 100°C, it increased to about 14% at 800°C when using a thermocouple monitor. With remote temperature sensing using an infrared dector, the heat loss is reduced and the correction factor at 800°C is only about 5%. In addition, the temperature range of observation was extended to 1500°C with remote sensing.

+ Miracle(R) dgf 123 dry graphite film lubricant, Miracle Power Products Corp., Cleveland, Ohio 44109

o Temptron #1T-7B, Barnes Engineering Co. Stamford, Conn. 06904

† Omega cc cement (sodium silicate), Omega Engineering, Inc. Stamford, Conn.

* Storage oscilloscope - #5111 mainframe (2MHz) #5A22N differential amplifier.

SCHEMATIC OF APPARATUS FOR MEASURING THE THERMAL DIFFUSIVITY BY THE LASER-FLASH TECHNIQUE.

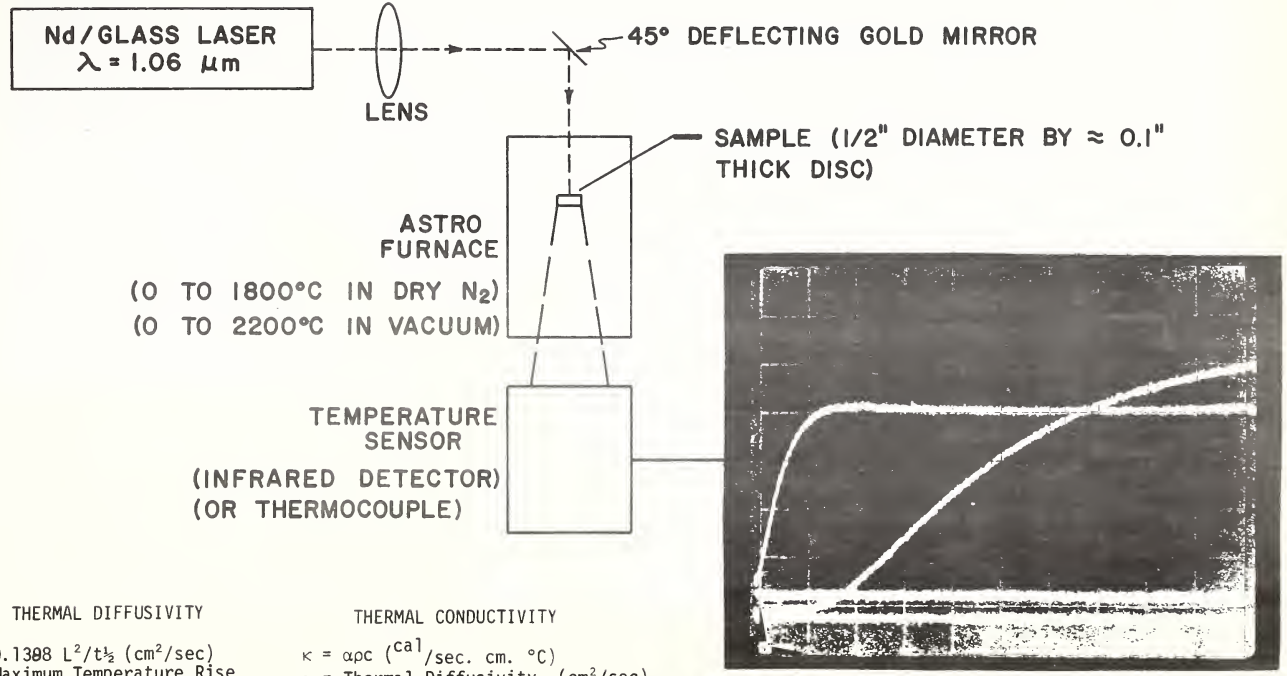

THERMAL DIFFUSIVITY

α = $0.1398\ L^2/t_{½}$ (cm^2/sec)
ΔT_m = Maximum Temperature Rise
L = Sample Thickness (cm)
$t_{½}$ = Time to reach $½\Delta T_m$ (sec)

THERMAL CONDUCTIVITY

$\kappa = \alpha\rho c$ ($^{cal}/_{sec.\ cm.\ °C}$)
α = Thermal Diffusivity (cm^2/sec)
ρ = Density (gm/cm^3)
c = Specific Heat Capacity ($^{cal}/_{gm°C}$)

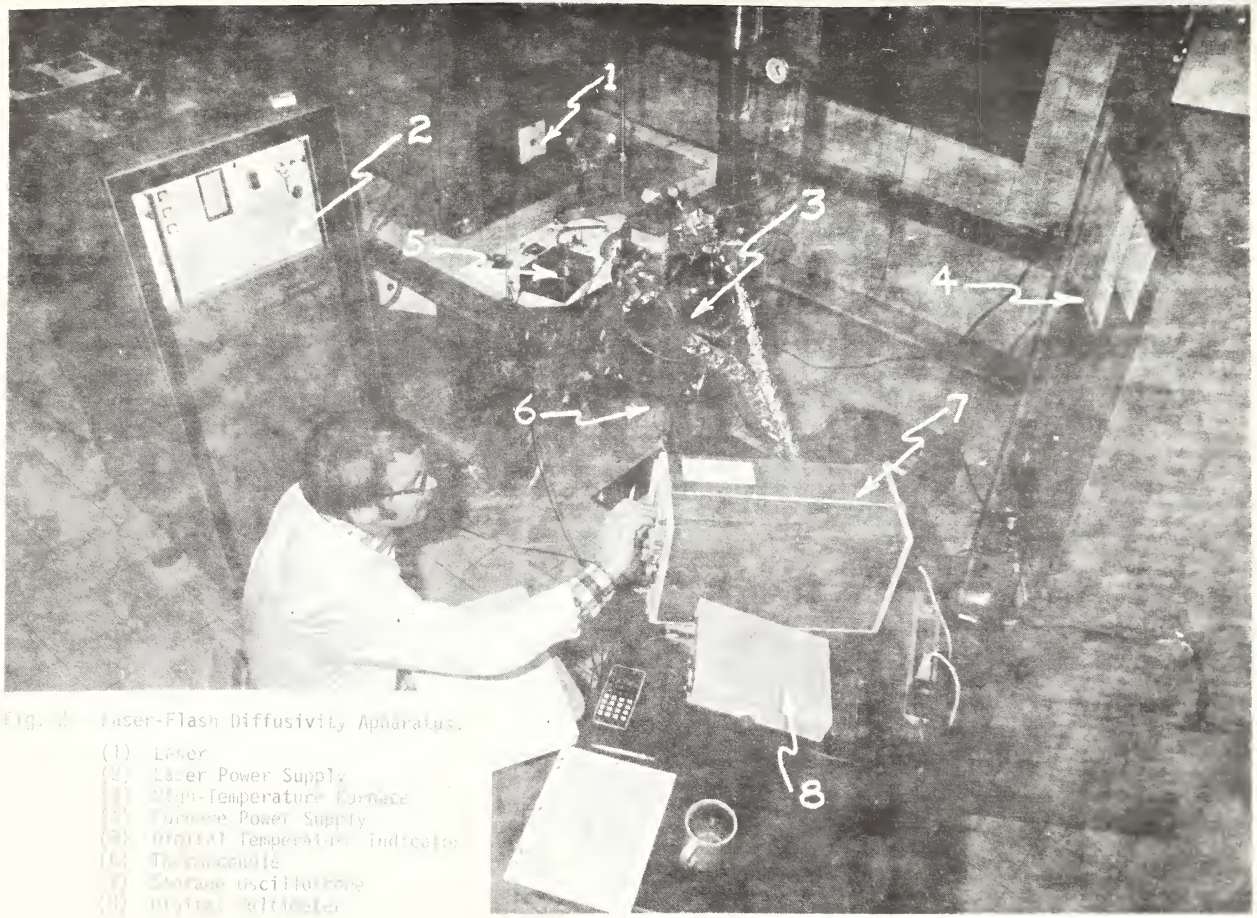

Fig. 4. Laser-Flash Diffusivity Apparatus.

(1) Laser
(2) Laser Power Supply
(3) High-Temperature Furnace
(4) Furnace Power Supply
(5) Optical Temperature Indicator
(6) Thermocouple
(7) Storage Oscilloscope
(8) Digital Voltmeter

In Figure 3, utilizing a common reference sample,[x] thermal diffusivity data from thermocouple monitoring are compared to data determined from infrared detector monitoring after correction for heat loss. These corrected data are compared to those of Gibby[9] for similar material. The thermocouple data are 10 to 20% lower than the infrared data. This indicates that a substantial time lag connected with our thermocouple monitoring system yields absolute values of thermal diffusivity that generally are too low. On the other hand, good correlation of the infrared data for the C9606 material with thermal diffusivity values determined by Gibby for similar material were obtained.

In Figure 4, recent measurements of the thermal diffusivity of Armco iron are compared to accepted reference values.[10] The excellent correlation with reference values indicates that our present technique using infrared monitoring gives good absolute determination (to ± 3%) of the thermal diffusivity in the 200 to 1000°C temperature range. It is noted that the Curie point at 769°C and the α-γ transition at 910°C are well defined in both temperature and magnitude of the thermal diffusivity by the experimental data.

b. Density measurements

Densities are determined by the liquid immersion technique. Normally, distilled water is used for the immersant; 1,3-dibromopropane is used for materials which are hygroscopic. The open porosity is estimated from wet weight after the samples have soaked in the boiling liquid for about 15 minutes.

If thermal expansion data are available, the density $\rho(T)$ is corrected for volume change as function of temperature by

$$\rho(T) = \rho_0 \, (1 - 3\alpha \, \Delta T) \qquad (3)$$

where ρ_0 is the measured room temperature density, α is the linear thermal expansion coefficient from the literature, and ΔT is the temperature difference between T and room temperature. This approximation holds for ideal isotropic materials only, so care must be used in its application. For many polycrystalline oxides, α is about 10×10^{-6} /°C. Therefore, a ΔT of 1000°C leads to only about a 3% decrease in the room temperature density. Due to this generally small correction, $\rho(T)$ is assumed equal to ρ_0 in cases where thermal expansion data are not available. Again, care must be taken that no higher temperature phase changes take place which could change ρ significantly.

Unless noted otherwise, density or thermal conductivity values were not corrected to the state of zero porosity.

---

[x] Corning C9606 glass-ceramic.

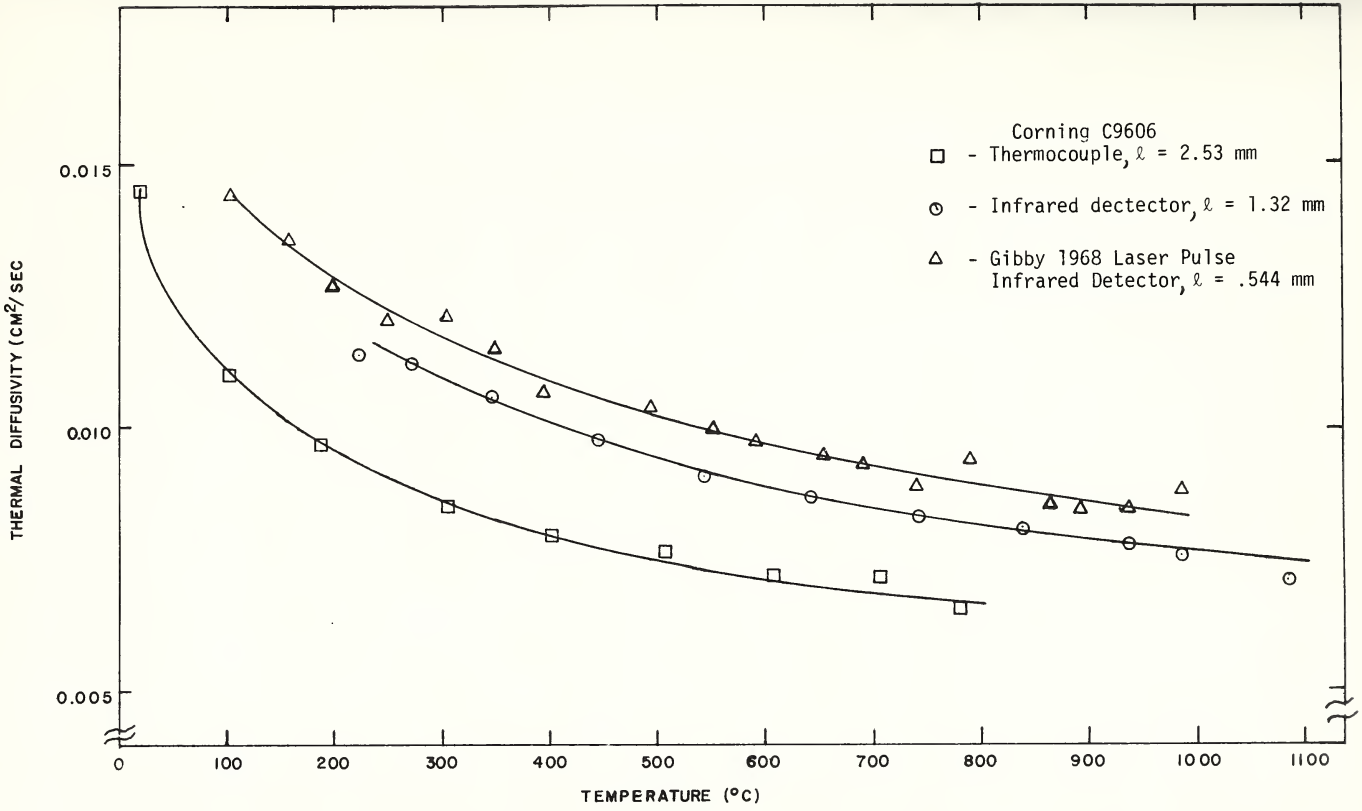

Fig. 3. Thermal diffusivity of C9606 by two methods of temperature detection.

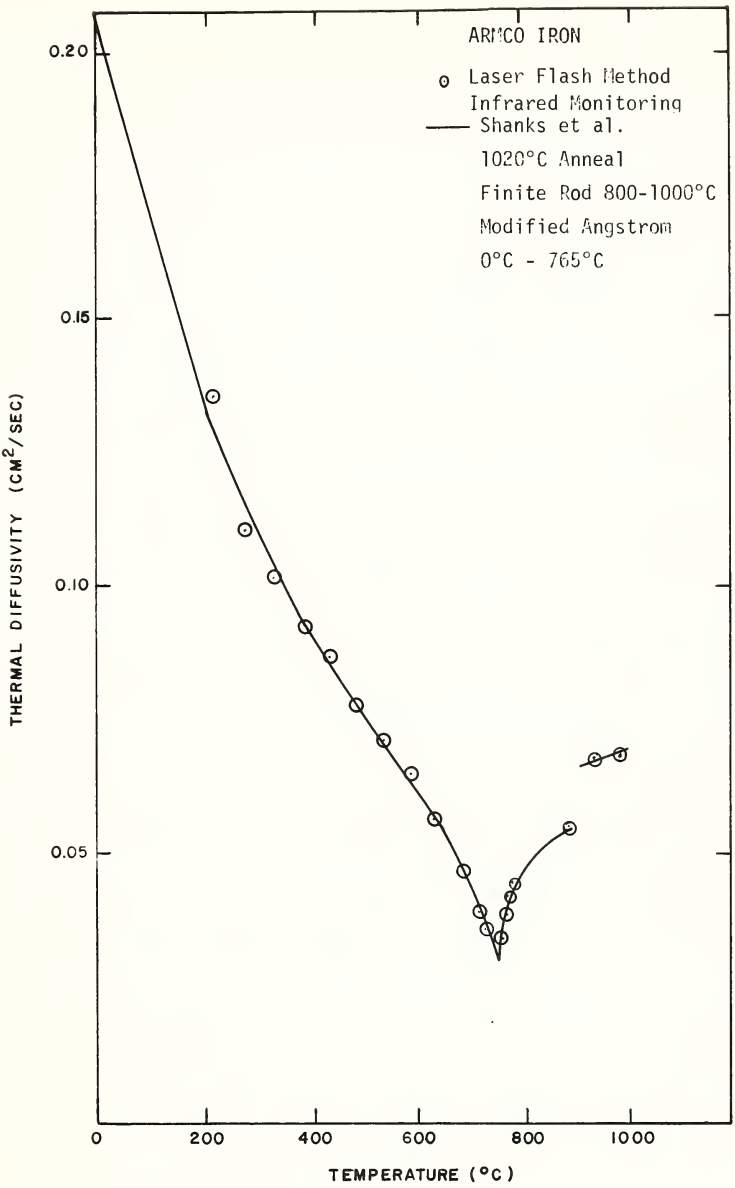

Fig. 4. Measured thermal diffusivity of Armco Iron compared to accepted values.

c. Heat capacity determinations

The specific heat values $C_p(T)$ were obtained from the literature or calculated using the law of mixtures, i.e.,

$$C_p = \sum_{i=1}^{n} X_i (C_p)_i. \quad (4)$$

Here X_i and $(C_p)_i$ are weight fractions and specific heats of constituents i, respectively. The law of mixtures (Equation 4) is used only when a material is composed of two or more well-defined phases. A more general formulation is the Kopp-Neuman Law which has the same form as Equation 4 except that now C_p is the molar specific heat of a compound or alloy, while $X_i(C_p)_i$ is the product of the number of moles and the atomic specific heats of the constituent elements.

The heat capacity at constant volume (C_v) approaches 3R above the Debye temperature and C_p is given by

$$C_p = C_v + a^2 V_o T \beta^{-1}. \quad (5)$$

where a is the volume thermal expansion ($a \simeq 3\alpha$ for isotropic bodies), V_o is the molar volume, and β is the compressibility. For a compound,

$$C_v = 5.96 \text{ cal /g-atom °C x (number of atoms/molecule)}. \quad (6)$$

Therefore, to a good approximation above the Debye temperature (300 to 700°C for most ceramics), heat capacity data can be fit to the expression

$$C_p = a + bT. \quad (7)$$

Equation 7 can be extended to a lower temperature range by the more general form found to hold for solids

$$C_p = a + bT + cT^{-2}. \quad (8)$$

Ordering type transformations cause rapid changes in heat capacity, but only over a limited temperature range. Also, heat capacity values are not sensitive to changes in crystal structure or ceramic microstructure, and Equations 7 or 8 generally are found adequate over a wide high temperature range.

The heat capacities of most oxide glasses have steeper temperature dependences than crystalline ceramics. On passing through the glass transition to the liquid state, the heat capacity can increase by a factor of 1.3 to 3.[11] Hence, exact heat capacity values and temperature dependence of slag or slag-ceramic mixtures should be determined experimentally rather than by mixture type formulas.

d. Analysis

As already mentioned, the main program effort is directed at obtaining reliable thermal conductivity values for various MHD component materials before and during service. At present, this is done by determining $\alpha(T)$ and $\rho(T)$ experimentally, estimating $C_p(T)$ from literature values and/or theoretical considerations, and then calculating $\lambda(T)$ by Equation 1 over the temperature range of interest.

In many cases, thermal transport is primarily via phonon conduction where $[\lambda(T)]^{-1}$ varies linearly with temperature so that over a large temperature range

$$[\lambda(T)]^{-1} = A + BT \tag{9}$$

where A and B are constants. In addition, where the temperature variations of the specific heat and density are linear and small, a similar expression for the thermal diffusivity is found to fit the data. Thus,

$$[\alpha(T)]^{-1} = A' + B'T \tag{10}$$

Good fits generally are obtained for T near or above the Debye temperature.

In dielectric crystals, thermal conduction is dominated generally by phonon-phonon interactions which lead to a $\sim 1/T$ temperature dependence at room temperature or above. Lattice imperfections (impurities, vacancies, faults, boundaries, etc.) are effective phonon scatterers also and lead to a temperature independent term-term A in Equation 9.

Deviations in $[\lambda(T)]^{-1}$ from the simple form of Equation 9 are observed in many materials-particularly those with complex molecular or anisotropic structures. Extrinsic microstructural features such as porosity, microcracking, impurity reactions or phase transformations also can introduce large deviations from Equation 9. In fact, at higher temperatures, photon conduction can contribute a term which is generally proportional to T^3 and can cause the thermal conductivity to increase again after reaching a minimum value at some intermediate temperature (often observed in transparent amorphous materials around 400°C). In highly porous insulators, the thermal conductivity may have a positive temperature dependence at all temperatures.

It is our intention then to explain deviations in $[\lambda\ (T)]^{-1}$ from the form of Equation 9 when encountered. In some cases, the linear form of Equation 9 will remain, but the coefficients A and B will change as a function of thermal environment or history. We will attempt to explain this also. Microstructural or phase composition analysis, thermal expansion, temperature cycling effects, or experimental heat capacity measurements will be made to corroborate the explanation. Hopefully, for a particular component one

then can predict changes in thermal transport properties as a function of MHD operating conditions.

Previous work in the MERDI Applied Research laboratories or elsewhere has examined many of the features which influence thermal transport. These will be reviewed briefly in order to classify the potential magnitudes of their influence in various MHD materials. The details are available in open literature.

In Figure 5, the effect on the thermal diffusivity when Al_2O_3 is alloyed with various amounts of Cr_2O_3 is shown.[12] The following analytic expressions were found to fit the data:

0m/o	Cr_2O_3	:	$]/\alpha$	=	(0.0437)T	+	8.349	,	r =	0.99
1m/o	Cr_2O_3	:	$]/\alpha$	=	(0.0421)T	+	13.465	,	r =	0.98
5m/o	Cr_2O_3	:	$]/\alpha$	=	(0.0475)T	+	16.630	,	r =	0.98
10m/o	Cr_2O_3	:	$]/\alpha$	=	(0.0452)T	+	25.202	,	r =	0.97
20m/o	Cr_2O_3	:	$]/\alpha$	=	(0.0354)T	+	40.887	,	r =	0.95
30m/o	Cr_2O_3	:	$]/\alpha$	=	(0.0343)T	+	45.512	,	r =	0.95

For up to 10m/o Cr_2O_3 additive, the slope of $[\alpha(T)]^{-1}$ varies little, but the intercept A' is roughly proportional to the amount of Cr_2O_3 additive. This is the expected behavior for phonon lattice conduction and phonon scattering by isolated point defects.

In Figure 6, the thermal diffusivity of titanium dioxide of various stoichiometries is examined.[13] It is noted that only ~1.8% oxygen sites are vacant for the most reduced rutile shown, which suggests that on the basis of concentration these lattice imperfections influence α far more effectively than do solid-solution atoms (such as were examined in the previous reference).

The effect of textured porosity on the thermal diffusivity/conductivity of a fibrous alumina is displayed in Figure 7.[14] The material's microstructure is shown in Figure 8. The data were analyzed using the semi-emperical equation

$$\lambda / \lambda_o = \frac{1 - P}{1 + \beta P} \qquad (11)$$

where λ and λ_o are the thermal conductivities of porous and non-porous materials, respectively; P is the fractional porosity; and β is a parameter which depends upon pore shape, P, and T.[15] The type of gas present in the pores or which can permeate the open porosity influence β strongly. The principle conclusion from this work was that at a given density the connected open pores in a fibrous microstructure are more effective in lowering the thermal diffusivity/conductivity of a ceramic material than the isolated isometric pores found in normally sintered or hot-pressed materials.

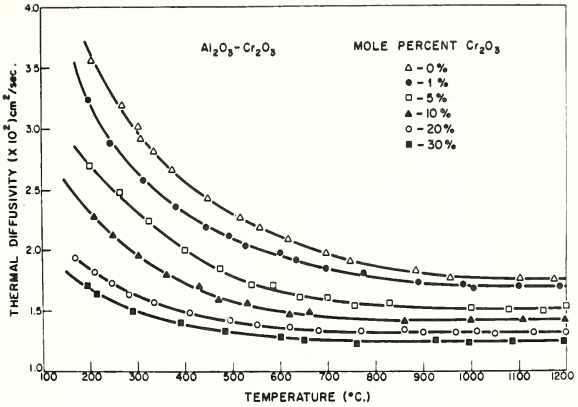

Fig. 5. Thermal diffusivity of alumina-chromia solid solutions.

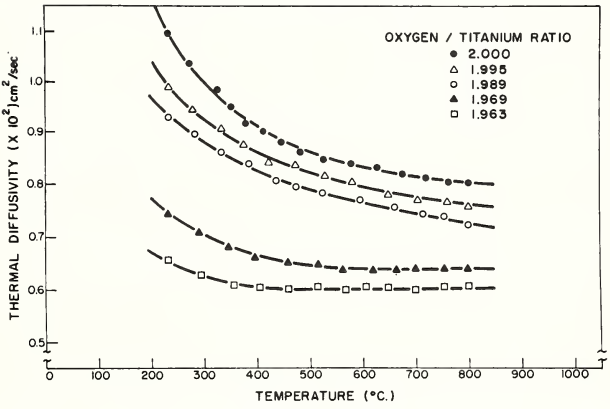

Fig. 6. Thermal diffusivity of nonstoichiometric titanium dioxide.

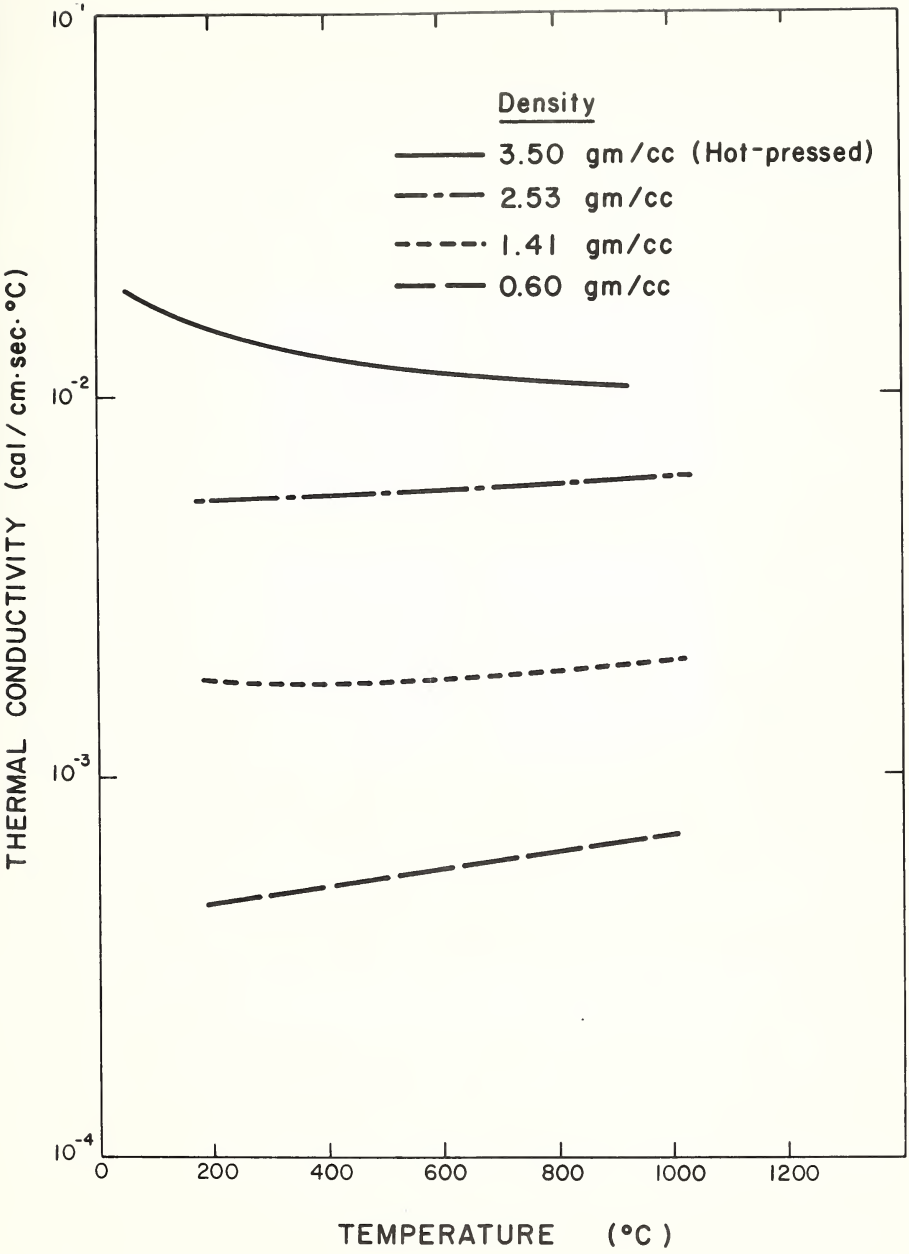

Fig. 7. Calculated thermal conductivity of fibrous alumina as a function of temperature and density.

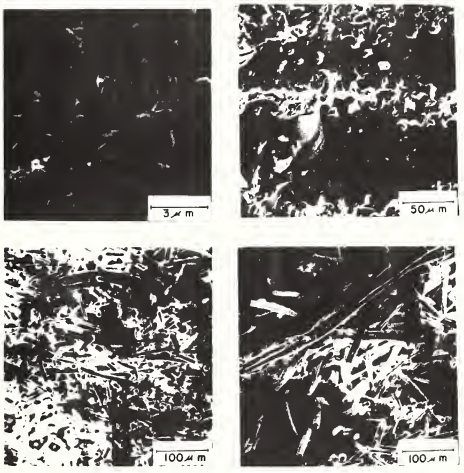

Fig. 8. Scanning electron micrographs of fibrous alumina: (a) hot-pressed, 3.50 gm/cc, (b) 2.53 gm/cc, (c) 1.41 gm/cc, and (d) 0.60 gm/cc

In Figure 9, experimental data are shown for the thermal diffusivity of a glass-ceramic with increasing degrees of crystallization.[16] Crystallization within a glassy matrix increases the thermal diffusivity at lower temperatures ($\lesssim$ 600°C) and decreases it above. This can be explained in terms of the mean free paths for phonon and photon conduction. It is expected that the thermal conductivity/diffusivity of slags, depending on their temperature and thermal history, will exhibit similar behavior.

The effects of microcracking on the thermal diffusivity of iron titanate,[17] magnesium ditanate,[18] and aluminum niobate[19] are reviewed in Figures 10, 11, and 12, respectively. Basically, anisotropic thermal expansion/contraction in these crystals cause stresses large enough to open microcracks along grain boundaries. The fractional porosity introduced is small, but the microcracks in series with the heat-flow path are very effective thermal transport barriers. The opening or propagation of cracks during cooling and the closing and even healing of cracks during heating results in the hysteresis loops as depicted in the data of Figures 10 through 12.

In Figure 13, the effects of microcracking on the thermal diffusivity/conductivity of an alumina matrix containing a dispersed phase of non-stabilized zirconia are shown.[20] Both the zirconia second phase addition and the microcracks in the system decrease the thermal conductivity. The dashed line indicates the composite thermal conductivity K_m, calculated from the Maxwell-Eucken relation

$$k_m = k_c \left\{ \frac{1 + 2\,V_d \left[\frac{1 - K_c / K_d}{1 + 2\,K_c / K_d} \right]}{1 - V_d \left[\frac{1 - K_c / K_d}{1 + 2K_c / K_d} \right]} \right\} . \qquad (12)$$

In this expression $K_c(K_d)$ is the conductivity of the continuous matrix (dispersed) phase and V_d is the volume fraction of the inclusions. It is clear that the largest part of the decrease in the thermal conductivity must be attributed to the presence of microcracks in this system.

There is a complete absence of any hysteresis effect for the alumina-zirconia system, in sharp contrast to the results discussed previously for materials with anisotropic thermal expansion. The reason for this difference is that in the alumina-zirconia system, the microcracked structure is supported by the zirconia inclusions. The inclusions expanded during the tetragonal to monoclinic phase transformation when the sample was cooled after hot-pressing. Once formed, the size and density of the microcracks apparently are independent of cyclic heating and cooling so that a hysteresis in the thermal diffusivity/conductivity is not observed.

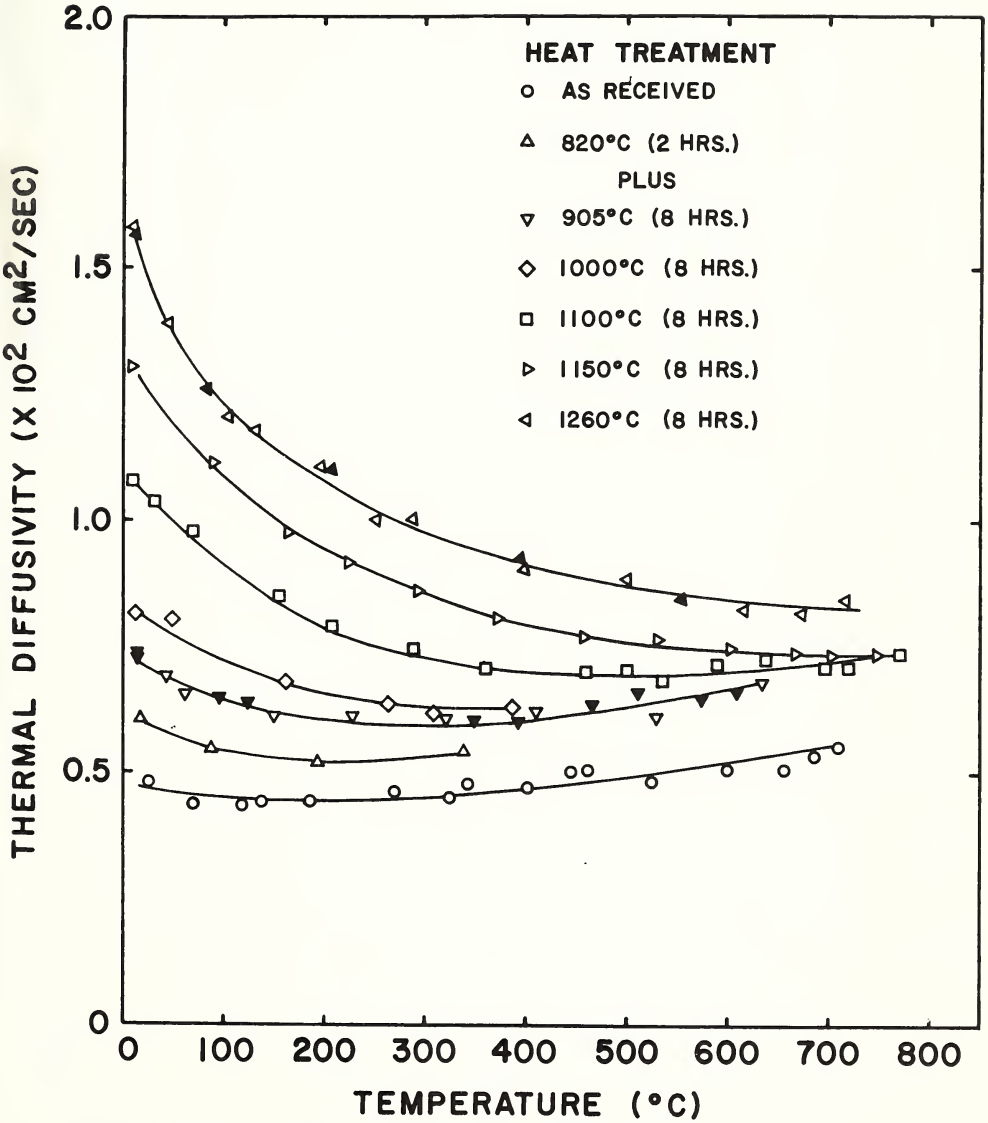

Fig. 9. Effect of crystallization on the thermal diffusivity of a Cordierite Glass-Ceramic. (open (solid) symbols indicate measurements made during heating (cooling).

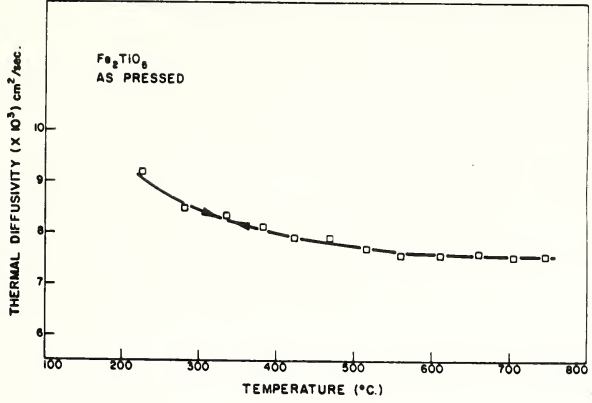

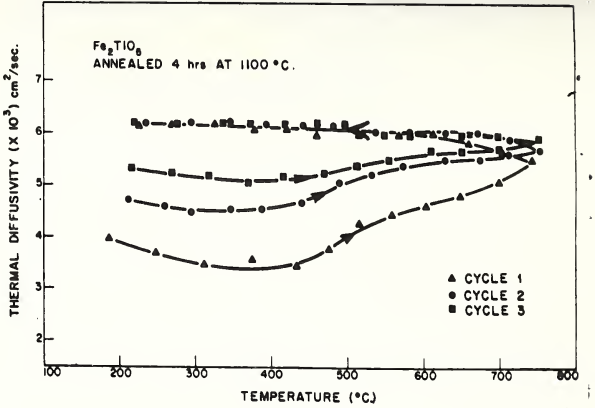

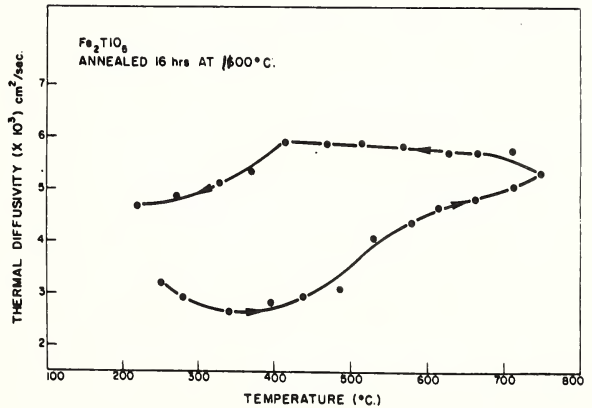

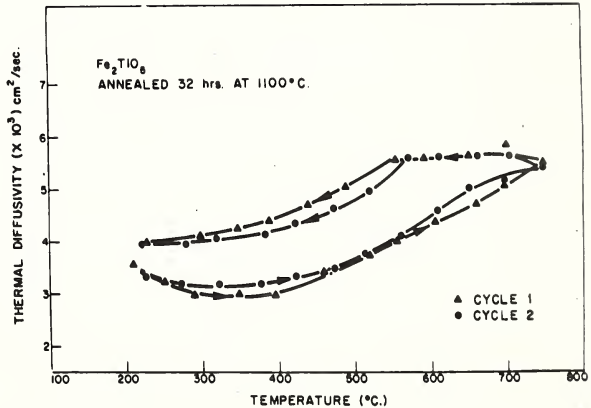

Fig. 10 Thermal diffusivity of Fe_2TiO_5 for various annealing treatments.

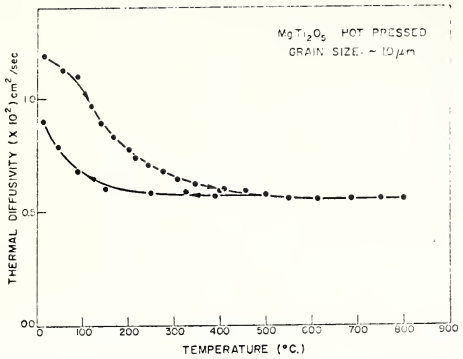

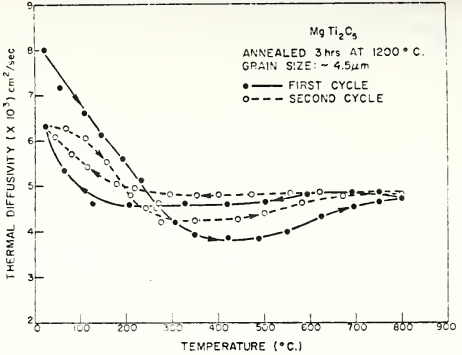

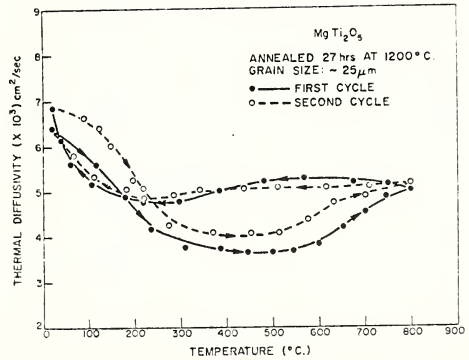

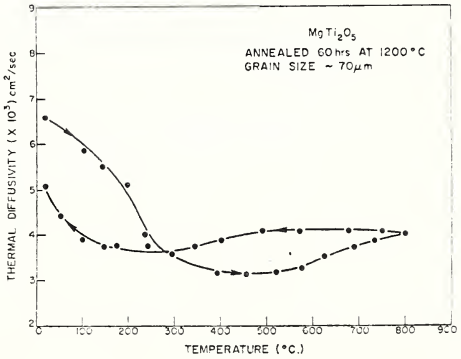

Fig.11 Thermal diffusivity of $MgTiO_5$ for various annealing treatments.

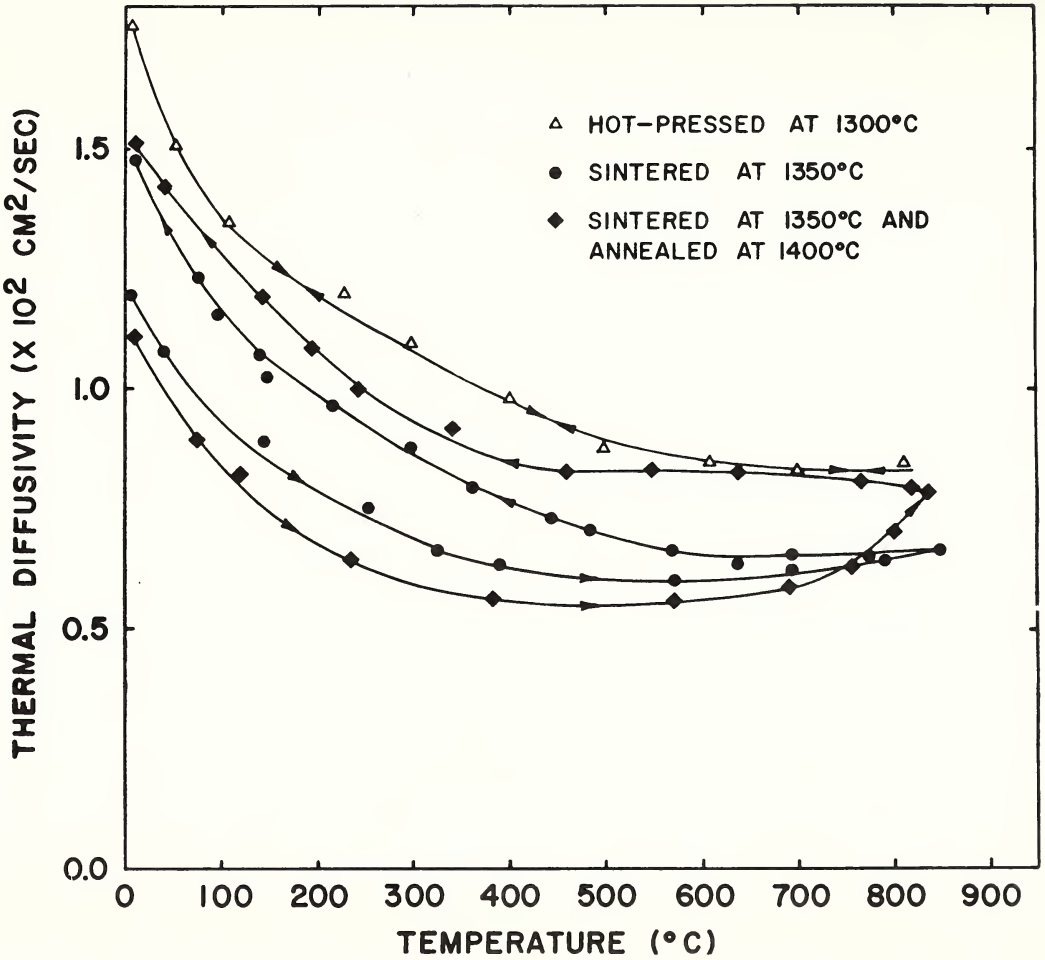

Fig. 12 Thermal diffusivity of polycrystalline aluminum niobate for various heat-treatments.

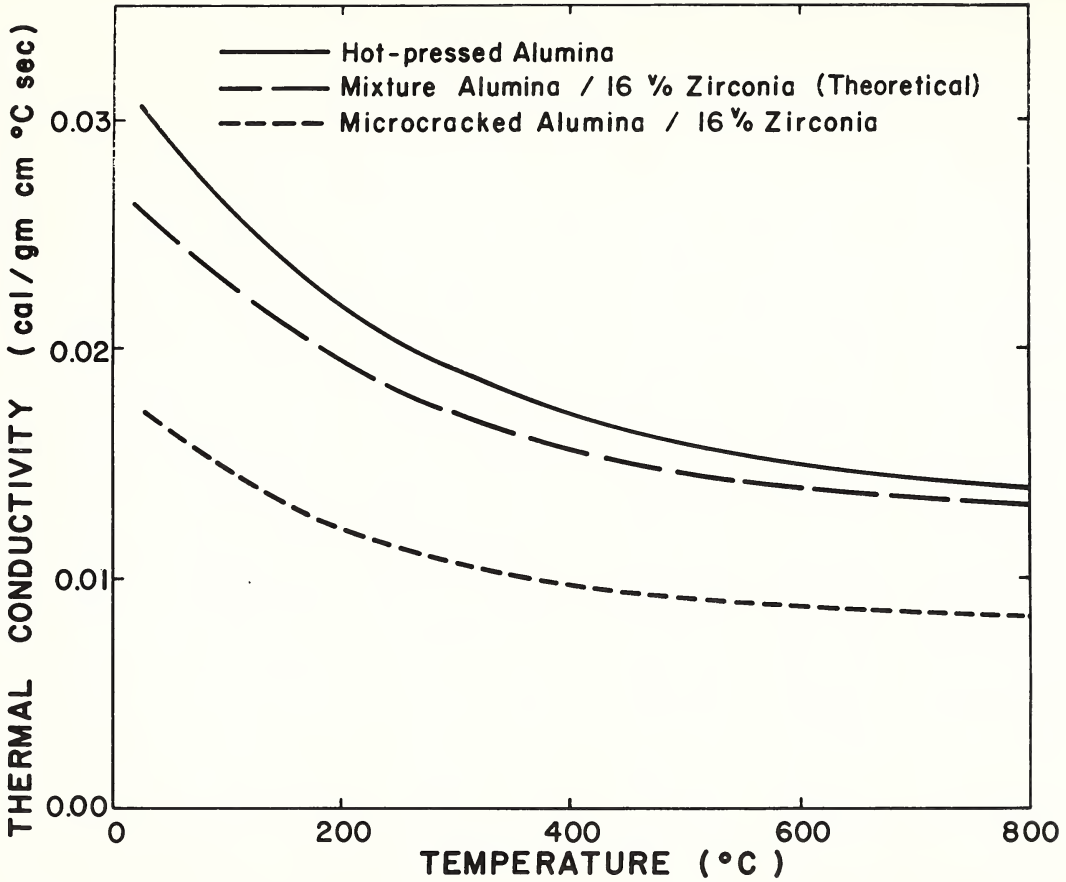

Fig. 13 Comparison of the Calculated Thermal Conductivity. Three cases: 1) Hot Pressed Alumina, 2) An Alumina with 16 percent Zirconia Dispersed Phase calculated using the theoretical relation of Maxwell-Eucken, and 3) A microcracked Alumina with 16 percent Zirconia Dispersed Phase.

The lack of hysteresis in the thermal diffusivity of the alumina-zirconia composite also should be observed for mechanical properties such as fracture toughness or thermal expansion. It has been reported [21] also that the fracture toughness can be enhanced by a factor of three over that of dense polycrystalline alumina. In addition to having high thermal shock resistance and good thermal insulating properties, this material should be highly corrosion resistant since it does not contain open porosity. Furthermore, one should be able to introduce a controlled amount of microcracks into other compatible oxides or ceramics by this technique. Such properties should make this ceramic (or similar zirconia composites) a candidate MHD insulator material.

Often thermal transport properties of a ceramic depend on the fabrication details. Texture in a single-phase compound with anisotropic thermal conduction (i.e., graphite or BN) or in the structural features of a composite material can introduce wide variations in the thermal conductivity and its temperature dependence.

It is clear that a proper analysis of thermal conductivity data will require a combination of experimental techniques and background information. The next section reports such an analysis; a preliminary one of the thermal transport properties of a candidate MHD preheater material subjected to slag exposure.

3. Preheater Materials--Corhart RFG

A fused grain magnesia chromite ceramic, Corhart RFG,* has been selected at Montana State University for initial heat exchanger experiments in the moderate temperature slag flow facility (MTSFF), which is designed to study the effects of coal slag and MHD seed material on the flow passages of high temperature air preheaters. The generally high temperature strength and corrosion resistance properties of RFG formed the basis for FluiDyne Engineering Corporation selecting the same material for their preheater tests.[22]

However, data concerning the effects of slag and seed on the thermal properties of RFG are generally not available. For this reason, material was obtained from researchers at FluiDyne for thermal characterization. The samples included a standard size (9" x 4½" x 3") brick and two samples of brick which had various time-temperature slag and seed exposure. Specifically, one brick had been exposed for about 100 hours and the other for about 200 hours in the FluiDyne hot gas flow test rig.[23] The temperature varied between 1400 and 1900°K during each of the exposures.

* Corhart Refractories Co., Louisville, Kentucky 40210.

The density and amount of open porosity were determined by liquid immersion. The bulk density of the unexposed RFG brick was found to be 3.29 g/cm^3 with an open porosity of 13.6 v/o, agreeing well with the manufacturer's values of 3.275 g/cm^3 and 16 v/o, respectfully. The brick, however, was found to be very inhomogeneous, As an example, the open porosity varies from about 11 v/o - 15 v/o. Generally, the open porosity is greatest in the center region and less near the outer surfaces.

Room temperature values of the thermal diffusivity of the raw RFG brick are also indicative of nonhomogeneity. Table 1 lists density and thermal diffusivity values for ten (10) samples cored from various locations in the brick. The first five (5) samples were cut in such a manner that the direction of heat flow was parallel to the 9" direction. Similarly, the other five had heat flow parallel to the 3" direction, presumably the direction of maximum pressure application during brick fabrication. With only one exception, the values of the thermal diffusivity for those samples with heat flow perpendicular to the pressing direction are higher than for those parallel to the pressing direction. Apparently, the open porosity is more likely to form thermal barriers parallel to the pressing direction. For the samples measured, the average difference in the thermal diffusivity due to porosity texture was 22%. Microstructural examinations are in progress to verify if there is porosity texture in RFG bricks generally.

In Figure 14, thermal diffusivity data as a function of temperature up to 1500°C are plotted for one of the raw RFG samples. Figures 15 and 16 show similar data for the RFG samples after exposure to molten slag for 100 and 200 hours, respectively. The data points marked with open circles were measured during heating, closed circles were measured during cooling.

The sample exposed to molten slag for 100 hours had a density of 3.55g/cm^3, indicating a ∿11% slag addition. The sample exposed to slag for 200 hours had a density of 3.39 g/cm^3, indicating a 7% slag addition. The slag only partially fills the available open porosity in the brick. Apparently, the higher mean temperatures during the 200 hour slag exposure results in a smaller amount of slag being entrapped for this sample.

Although the differences are small between all these samples, there apparently is a contribution to the thermal diffusivity at higher temperatures due to the slag addition. In addition, a slight hysteresis effect was observed for both the raw RFG and the 100 hour slag sample.

The strength of RFG brick exposed to slag at high temperature has been shown to decrease dramatically.[24] Additional cracking or separation of the grains, which can occur during thermal cycling, could account for both the loss in strength and hysteresis in the thermal transport.

Table 1. Measured Room Temperature Density and Thermal Diffusivity of Disc Samples Exhibiting Porosity Texture

Sample No.	Density (gm/cm^3)	Thermal Diffusivity (cm^2/sec)
a		
1	3.30	.0199
2	3.29	.0201
3	3.30	.0198
4	3.25	.0170
5	3.26	.0190
b		
6	3.34	.0168
7	3.26	.0132
8	3.27	.0122
9	3.27	.0120
10	3.35	.0207

a) The direction of heat flow was parallel to the 9" brick edge for this group.

b) The direction of heat flow was parallel to the 3" brick edge for this group.

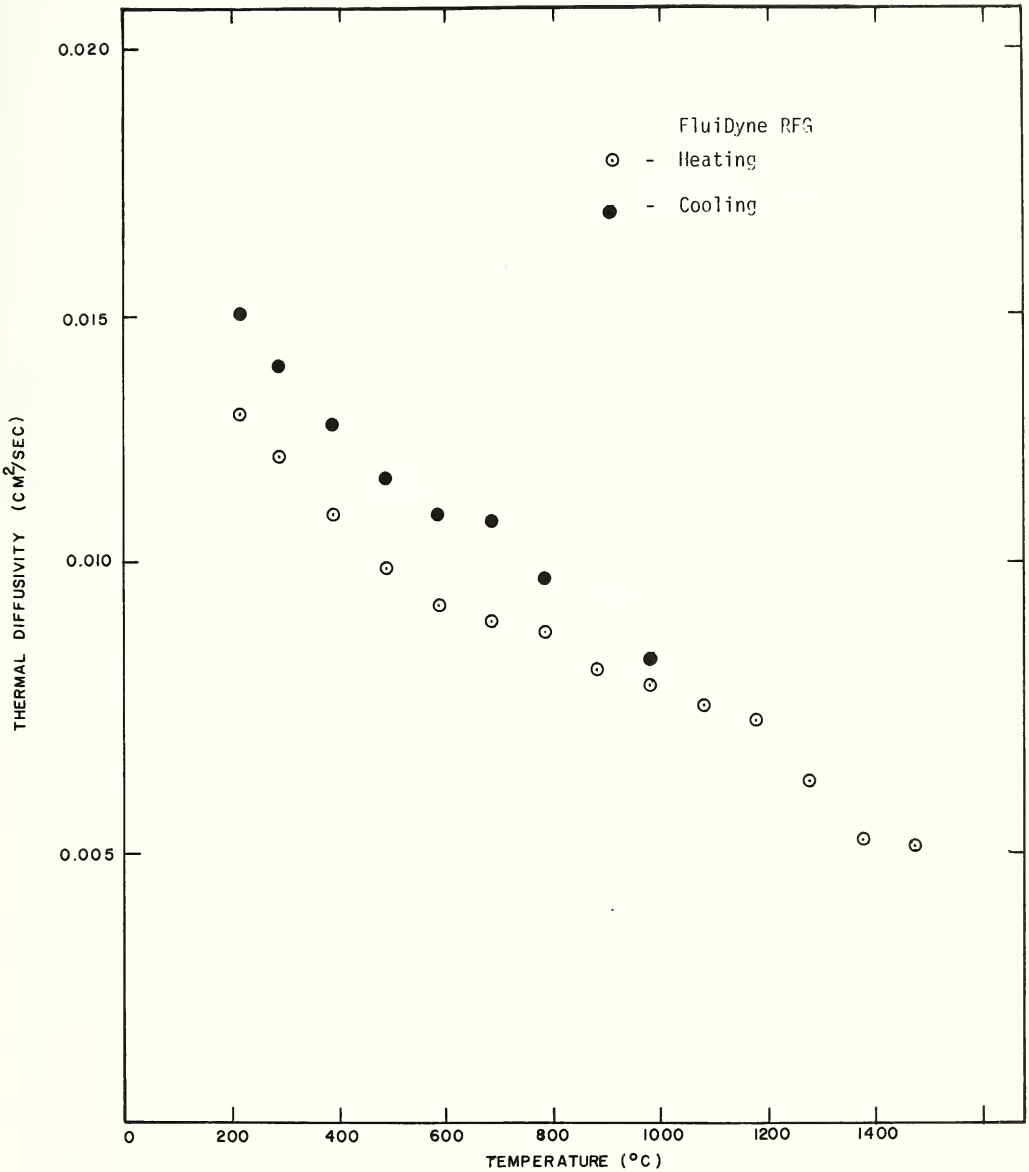

Fig. 14. Thermal diffusivity of CORHART RFG as a function of temperature.

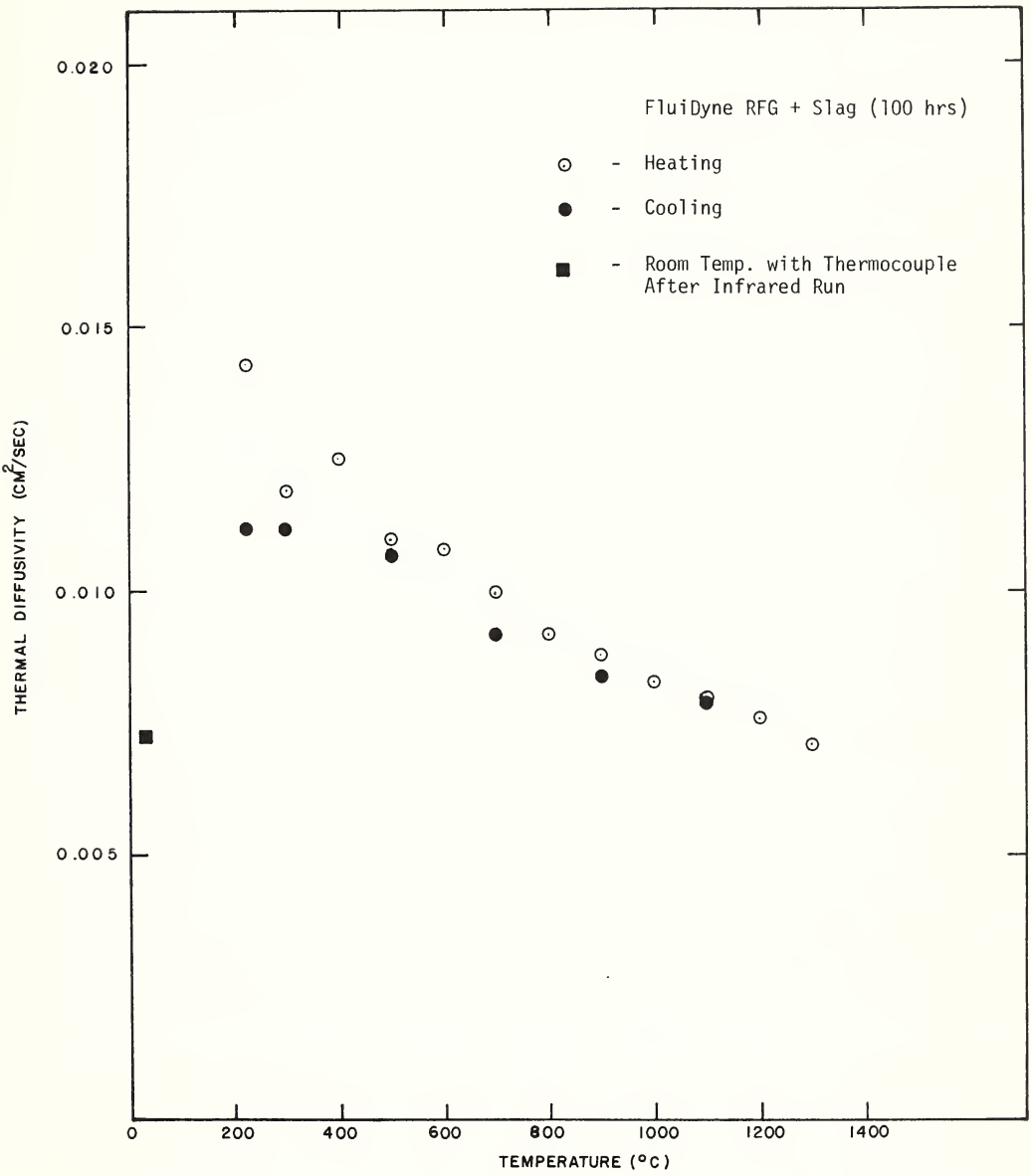

Fig. 15. Thermal diffusivity of CORHART RFG with 11 ^{V}/o slag (100 hours exposure).

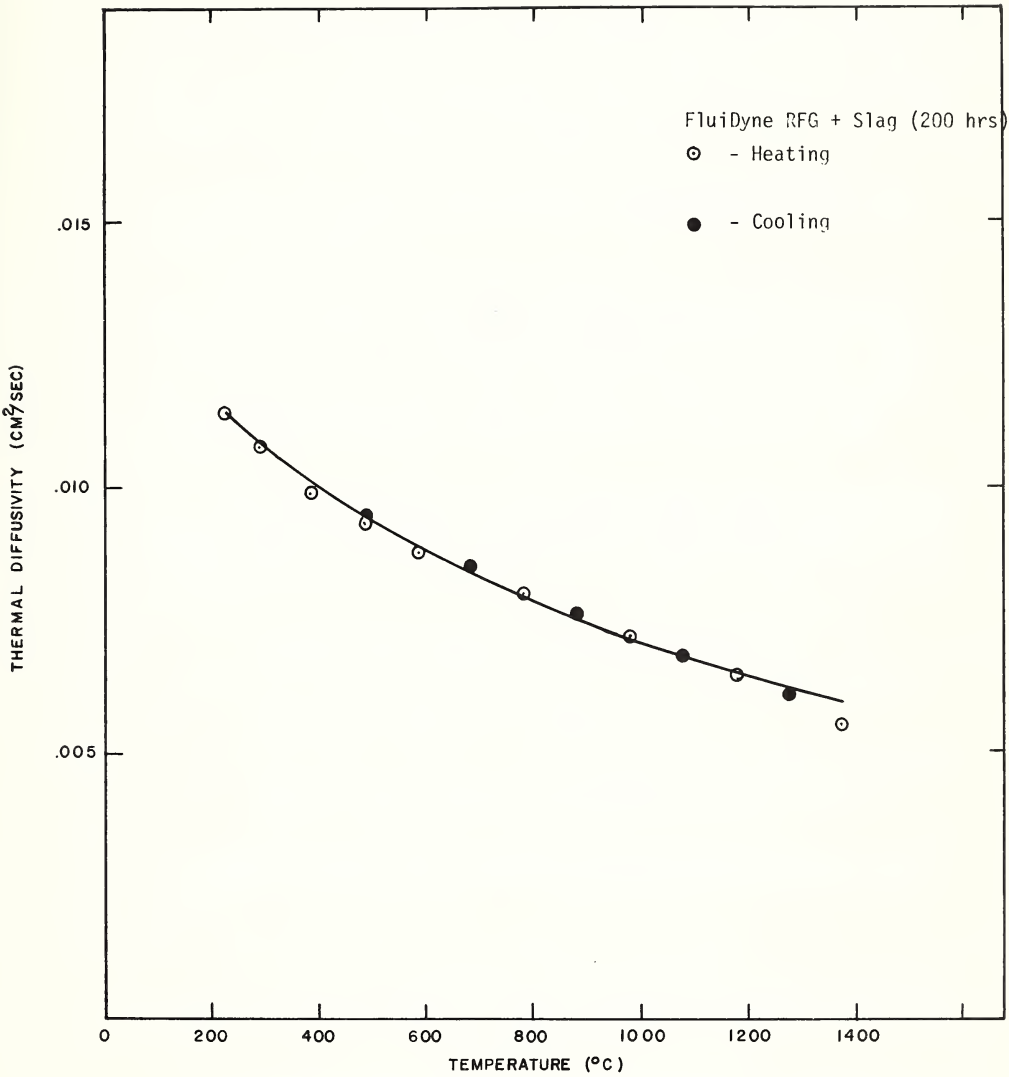

Fig. 16. Thermal diffusivity of CORHART RFG with 7 ^{v}/o slag (200 hours exposure).

However, the sample exposed to slag for 200 hours, but which contained a smaller quantity of entrapped slag, did not show hysteresis when diffusivity measurements were made during a temperature cycle to 1400°C. The hysteresis effect in the thermal transport and perhaps the mechanical strength will depend on the details of the slag exposure (i.e., temperature and time as well as slag composition).

The specific heat capacity for each sample was calculated as a function of temperature using Equation 4 and reference values of specific heat for each constituent.[25] The thermal conductivity was calculated from Equation 1.

Numerical results are listed in Table 2 for temperatures above 400°C, and a graphical form for the thermal conductivity is presented in Figure 17. Since the temperature dependence of the specific heat, thermal diffusivity and thermal conductivity are approximately linear for these materials, linear least-squares lines were fit to the data and are given in Table 3. The correlation factors for the thermal conductivities and specific heats were better than 0.99 and 0.98, respectively.

As discussed earlier, the differences in the thermal conductivity of raw RFG and RFG exposed to slag are not great, except that the slag-exposed samples have higher conductivities at high temperatures. The reasons for this are not clear at this time, but the following must be considered:

1) An additional contribution from photon conduction in an amorphous slag that fills pores in the RFG brick;

2) Slag layers actually bond some of the grains more tightly and phonon conduction is enhanced; and

3) Additional cracking of slag-exposed samples lowers the thermal conductivity at the lower temperature, and crack healing at higher temperatures enhances the conductivity.

Additional measurements on RFG or other refractory bricks exposed to slagging conditions will have to be analyzed before definite conclusions can be reached.

4. Future Work Plans

The following steps are planned to continue to upgrade experimental capabilities of the thermal transport properties laboratory this coming year.

A modified circuit designed for higher temperature ranges (600°C to 1600°C) will be added to the Temptron infrared detector to enhance its sensitivity. A photomultiplier detection system is planned for very high temperatures (>1000°C).

A thermal analysis station which consists of a differential scanning calorimeter (DSC), differential thermal analysis (DTA), and thermal

Table 2.: Thermal Transport Properties of CORHART (R) RFG Brick and RFG after Slag Exposure.

	Raw RFG			RFG + 11% Slag (100hrs)			RFG + 7% Slag (200hrs)		
(°C) Temp	cm^2/sec α	(cal/g°C) Cp	(cal/cm°Csec) λ	cm^2/sec α	(cal/g°C) Cp	(cal/cm°Csec) λ	cm^2/sec α	(cal/g°C) Cp	(cal/cm°Csec) λ
400	.0132	.253	.0109	.0125	.251	.0107	.0099	.251	.0083
500	.0122	.259	.0103	.0110	.257	.0100	.0094	.257	.0081
600	.0115	.262	.0097	.0108	.262	.0095	.0088	.262	.0077
700	.0116	.265	.0091	.0100	.266	.0091	.0084	.266	.0074
800	.0103	.268	.0086	.0092	.270	.0087	.0080	.270	.0071
900	.0093	.271	.0080	.0088	.274	.0084	.0076	.274	.0069
1000	.0088	.274	.0075	.0083	.277	.0080	.0072	.277	.0066
1100	.0079	.277	.0070	.0080	.280	.0077	.0068	.280	.0062
1200	.0076	.281	.0064	.0076	.282	.0073	.0065	.282	.0060
1300	.0065	.284	.0059	.0071	.284	.0071	.0061	.284	.0056
1400	.0054	.287	.0056				.0056	.287	.0052
1500	.0053	.290	.0049						
Bulk Density		3.29 g/cm^3			3.56 g/cm^3			3.39g/cm^3	

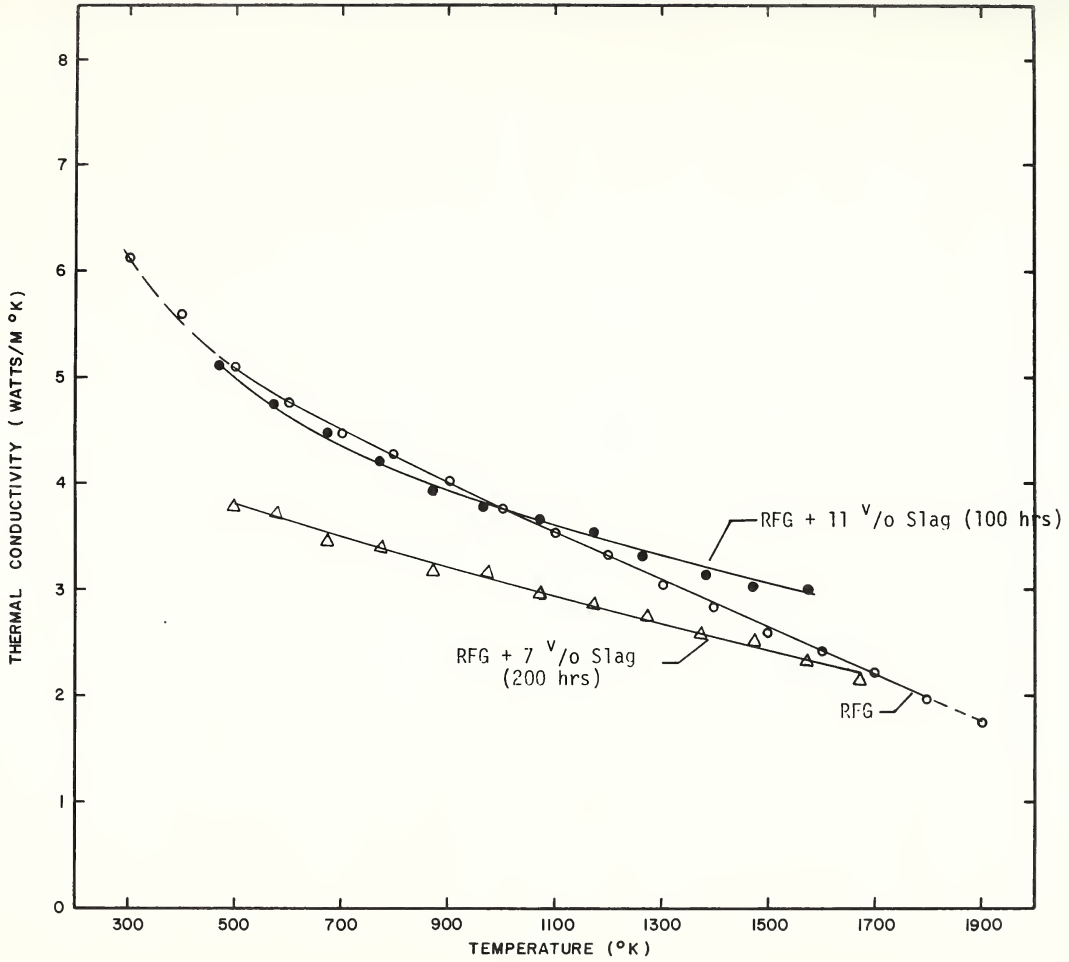

Fig. 17. Calculated thermal conductivity of CORHART RFG with and without slag.

Table 3. Linear Least Squares Representation of the Thermal Properties of Raw CORHART RFG and RFG after Slag Exposure.

Raw CORHART RFG — 673°K < T < 1773°K

$\alpha = 0.0181 - (7.36 \times 10^{-6}) \times (°K)$ cm^2/sec

$Cp = 0.233 + (3.23 \times 10^{-5}) \times (°K)$ cal/g°K

$\lambda = 0.0145 - (5.44 \times 10^{-6}) \times (°K)$ cal/cm°K sec

RFG + 11% Slag (100 hours) — 673°K < T < 1573°K

$\alpha = 0.0156 - (5.57 \times 10^{-6}) \times (°K)$ cm^2/sec

$Cp = 0.229 + (3.63 \times 10^{-5}) \times (°K)$ cal/g°K

$\lambda = 0.0130 - (3.87 \times 10^{-6}) \times (°K)$ cal/cm°K sec

RFG + 7% (200 hours) — 673°K < T < 1673°K

$\alpha = 0.0126 - (4.18 \times 10^{-6}) \times (°K)$ cm^2/sec

$Cp = 0.229 + (3.63 \times 10^{-5}) \times (°K)$ cal/g°K

$\lambda = 0.0105 - (3.05 \times 10^{-6}) \times (°K)$ cal/cm°K sec

gravimetric analysis (TGA) modular units is planned for purchase. With this station, direct measurements of a material's specific heat capacity from 100 to 765°C (DSC unit) and from 100 to 1500°C (DTA unit) will be made. Reliable heat capacity data are necessary to calculate the thermal conductivity for complex materials--especially those that have been exposed to seed/slag mixtures. The experimental values will be correlated with those values estimated by the present technique of calculating heat capacities from constituent values taken from the literature.

As part of a cooperative program to characterize the thermal transport properties of materials that have been subjected to real or simulated MHD operation environments, arrangements have been made to exchange samples with the followimg MHD researchers:

- Dr. Ron Smyth (FluiDyne Engineering Corp.)--preheater materials, Corhart RFG, and Taylor spinel.
- Dr. Al Kummick (Montana State University)--preheater materials.
- Dr. Richard Pollina (Montana State University)--synthetic and real coal slags.
- Dr. William Callister (Montana College of Mineral Science and Technology)--synthetic coal slags and refractory ceramics exposed to slag corrosion.
- Dr. W. R. Hosler (NBS)--Hoskins 875 metal mesh compressed to various densities.
- Dr. Calude Petersen (UTSI)--real porous coal slags from MHD channel tests.

In addition, thermal transport studies of other materials systems of interest will be carried out. The following systems are presently on hand:

- microcracked alumina with different concentrations of a dispersed zirconia phase;
- α-Al_2O_3 of controlled porosity fabricated in-house;
- composite materials with an inclusion phase that has a controlled orientation such as BN in α-Al_2O_3 and Ba mica in α-Al_2O_3; and
- cermets such as hot-pressed nickel coated alumina particles and a glass with various degrees of bonding to nickel inclusions.

B. MHD Materials Development and Fabrication

1. Introduction

The MERDI materials processing facility is being established for two main purposes:

1) to fabricate and characterize technical ceramics and thereby gain a more thorough understanding of the effects of various processing variables on the physical properties of such materials; and

2) with this knowledge, to fabricate test samples of specific materials of known and reproducible properties in support of other MHD research tasks at MERDI or the Montana schools.

In the future, the test equipment and techniques developed will be utilized for materials characterization which will be needed for quality control and diagnostics in direct support of the MHD CDIF test facility operations.

The properties of most classes of engineering materials are controlled by a variety of variables at the microstructural level such as porosity, grain size, impurity levels and distribution, phase composition and inclusions, dopants, and textural effects. Even minor changes in these variables can bring about major differences in the engineering behavior. An understanding of the influence on these variables on the key engineering parameters leads to the potential control or modification of a material's properties during fabrication so that a material is tailored to fulfill a specific engineering task.

2. Ceramic Fabrication and Characterization Facilities at MERDI

It is possible currently to form ceramic wafers, rods, and labware by dry-pressing, isostatic pressing, and slipcasting, respectively. Special tooling required for fabrication of parts of a specific geometry are made in-house.

Additional equipment obtained through government surplus has been reconditioned and placed into operation. Major items acquired from surplus this past year are listed below:

- American Optical Company metallograph (Model 2400),
- Lab Con fume hood,
- Buehler dual grinding and polishing table plus wheels,
- Precision Scientific forced air drying oven (Model 835), and
- Autoclave 50 kpsi isostatic press (soon will be operational).

Two recirculating water cooling systems, necessary for cooling the two high temperature furnaces, were designed and built in-house. These systems provide stable and safe cooling independent of the city water supply which is subject to pressure fluctuations and a high algae growth content at various times of the year. Both systems have been checked out and are in regular operation.

a. Powder preparation

The following ceramic oxide raw materials have been purchased:

α-Al_2O_3 - Reynolds RC-HP-DBM, 99.95% pure + .023% MgO,
" - Alcoa A-14,
" - J. T. Baker, 99.0% pure,

γ-Al_2O_3 - Union Carbide Linde B, 0.05 micron,
MgO - GEM ground and sintered, 99.5% pure,
" - J. T. Baker, food grade,
ZrO_2 - Magnesium Electron, Inc., 'S' grade, and
Y_2O_3 - Molycorp, 99.99% pure.

Powders routinely are dry or slurry-mixed and ground by roller milling using high-density alumina or zirconia media. A full line of binders, waxes, dispersants, and antifoams are available for ceramic body formulation. The effects of selected additives on final sintered body properties have been reported earlier.[26] Ceramic labware is fabricated routinely by slip-casting and sintering.

b. Isostatic pressing

Polyurethane bags are molded in-house to the correct size for fabricating ceramic rods. A Carver flat-plate press has been modified for isostatic pressing by adding a home-made reservoir and plunger system. Wet-bag pressing of small parts can be carried out up to 10 kpsi with this system.

c. Sintering

High temperature sintering is carried out primarily in a graphite element furnace* equipped with a muffle tube for air or controlled atmosphere sintering. In this mode of operation the furnace has a uniform hot zone (8 inches long by 3 inches in diameter) and an upper temperature limit of 1760°C. Soak times and heating and cooling rates are preprogrammed and automatically controlled. Temperatures are monitored with an optical pyrometer through a side viewing port or a Pt-Pt/13% Rh thermocouple. This furnace also is used for the wettability studies (see Section III-C). The furnace and power supply and control are pictured in Figure 18.

A similar furnace† is used for the thermal conductivity/diffusivity studies except that it is equipped with manual temperature control (see Section III-A).

d. Microstructural and density examination

Sample sections generally are cut from sintered rods with a diamond cut-off wheel. Densities are determined from these sections by liquid immersion using either water of 1,3-dibromopropane. Both open and closed porosities are estimated from weight measurements and are correlated with visual microstructural observations.

Cut specimens then are mounted in Bakelite and surfaces are ground and polished by a series of diamond or other abrasives and then viewed by reflected light microscopy. Grain structures normally are revealed by thermal etching.

---

* Centorr Associates, Inc. Model 10-4x8-G-G - EkO. Suncook, New Hampshire 03275.
† Astro Model A1000, Santa Barbara, Calif.

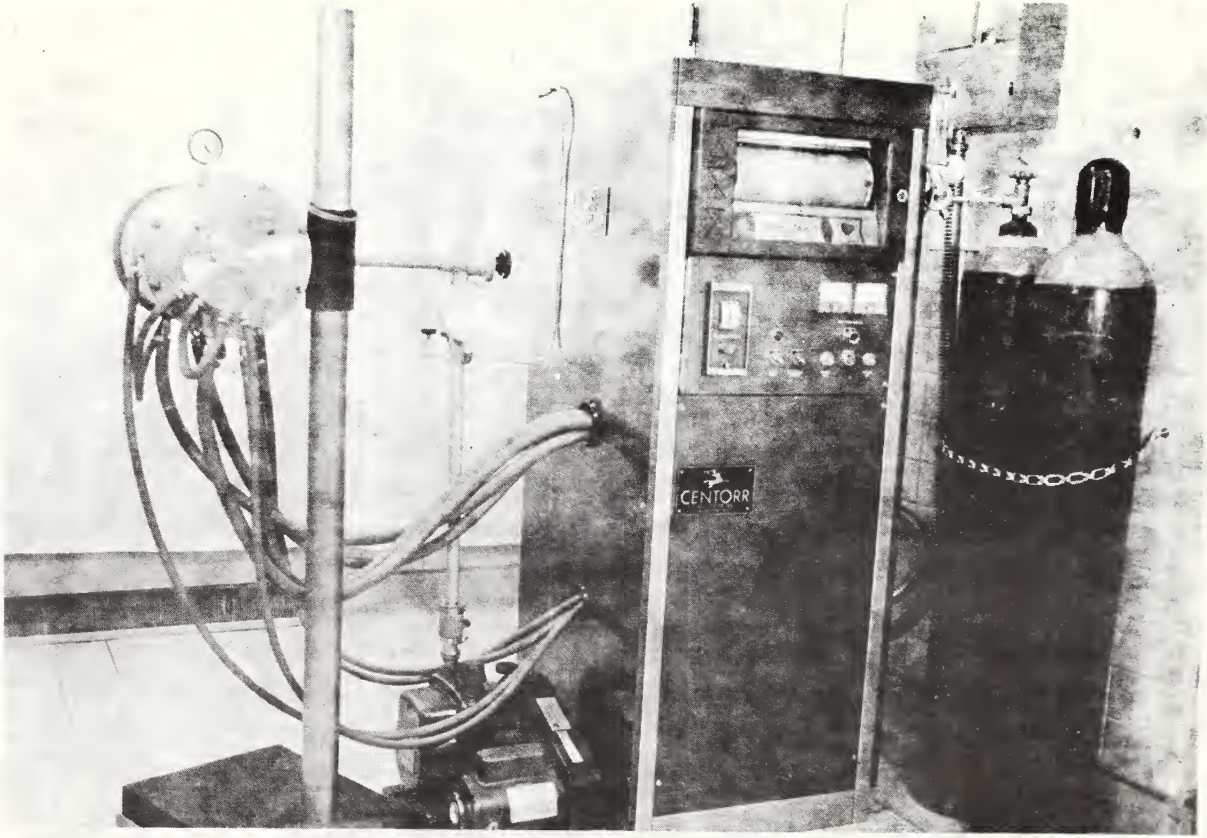

Fig. 18 Centorr firing furnace and power supply.

Optical microscopy is carried out utilizing a Leitz Orthoplan (R) largefield microscope equipped with either Polaroid(R) or 35 mm camera attachments. This microscope is equipped also for viewing by transmitted light (Xenon light source) and bright field/dark field illumination. A heated stage will be added in the future. An upper magnification of x500 is possible with present lenses. Also available is a reconditioned American Optical metallograph which is capable of x1000 magnification.

e. X-ray and SEM examination

Phase identification and relative composition are determined from X-ray diffractometer[x] scans of either powder or dense plate specimens. Some SEM fractographs have been made on dense specimens for grain size determinations.

For elemental composition determinations and determinations of diffusion profiles in solid ceramics, an SEM equipped with EDAX (energy dispersive X-ray analysis) is essential. At present, some of this analysis is performed by outside vendors. However, for fast turn-around thorough analysis, it is imperative that this capability be available in-house.

3. Fabrication Procedures and Sample Characterizations

The facilities described in the proceeding section have been used to fabricate controlled density aluminum oxide (Al_2O_3), stoichiometric magnesium aluminate spinel ($MgAl_2O_4$), and magnesium rich spinel (65m/o MgO : 35m/o Al_2O_3), both in rod and wafer geometries. After microstructural and density characterization, the rods are used in slag corrosion tests as part of Task B (Montana College of Mineral Science and Technology). The wafers are used as substrates for slag wettability studies and for evaluation of thermal transport properties as part of Task N in-house research. Techniques for fabricating alumina with a controlled porosity are under investigation. Variations of pressing pressure and sintering schedules in combination with the addition of organic fillers which are burned out of the green bodies prior to sintering are the techniques being used.

The following two sections describe in detail the procedures developed in this laboratory during the last year to fabricate ceramic materials.

a. Spinel Rods for Task B corrosion studies

Stoichiometric spinel (50 m/o MgO / 50 m/o Al_2O_3) and magnesia rich spinel (65 m/o MgO / 35 m/o Al_2O_3) rods (3¼" long by 1/2" diameter) are fabricated at the MERDI facilities. Initially,

---

x At present the Montana Tech X-ray machine (Norelco) which is equipped with a CuK_α tube is being used.

+ The ISI Super II SEM at Montana State University was used.

these rods are being made by a technique which yields small grains (< 10μm) and high densities (> 98% of theoretical). The densities, microstructures, and phase composition are being checked in order to guarantee uniform starting properties prior to corrosion testing of the rods.

Initially, various powder preparation techniques and sintering schedules were tried to develop an acceptable end-product. The following formulation has been adopted.

A 2000 gram batch of raw oxide powders, an amount sufficient for fabricating 40 rods, was prepared by weighing out 1433.40 gms α-Al_2O_3* and 566.6 gms MgO.+ Previous drying tests on the as-received MgO powder indicated that it contained additional water of hydration. Therefore, 20.4 gms of MgO were added to the batch to compensate for weight loss on ignition. The raw powders were wet-ground in a 6-liter polyurethane lined ball-mill with 50% of the volume filled with 3/4" high-purity Al_2O_3 grinding media and 500 gms of anhydrous alcohol. The mixture was milled for a period of 24 hours. The slip was spread over evaporation dishes and oven-dried. The powders were pre-calcined at 1200°C in air for 4 hours. On cooling, the powders were remilled for 10 hours, then calcined at 1350°C in air for 4 hours. The powders were then remilled for 10 hours and calcined at 1350°C in air for 5 hours. The powder was broken down to -80 mesh with mortar and pestle followed by wet-ball milling for 20 hours. During this milling period, Carbowax 20000 (1½ weight percent) was added. After final drying and seiving (-80 mesh), the powders were sealed and stored in individual one-liter plastic jars. Although this procedure has many steps, it yields a high-quality end product. Dopants have been tried to enhance the sinterability of spinel,[27] but tests in this laboratory indicate powder preparation is the most important factor.

A 500 gram batch of magnesia-rich spinel powder (65 m/o MgO/ 35 m/o Al_2O_3) was prepared in a similar manner and stored for future use.

Powder specimens were selected at the end of each calcine treatment for X-ray diffraction analysis. Less than 10% unreacted MgO remained at the end of the pre-calcine, and only stoichiometric $MgAl_2O_4$ peaks were observable after the second calcine.

Powders were weighed out, poured, hand-tapped into a home-made polyurethane bag,x and isostatically pressed at 10,000 psi. The green rods were ∿ 6½" long by 0.65" diameter. Generally, a uniform taper resulted so that the base of the rod was ∿ 0.05" larger in diameter than the top.

---

* - Reynolds Aluminum Co. (RC-HP-DEM) manufacturer's specification 99.95% pure--0.023% MgO, double ball-milled, 7.2m^2/g specific surface area.

\+ - J. T. Baker Reagent Grade.

x - Devcon Flexane,(R) Devcon Corp., Danvers, Mass.

An automated powder filler and tapper, under construction at the present time, however, will limit the amount of taper. Wafers (1.125" diameter by 1/4" thick) were dry-pressed from the same powder at 10,000 psi. Both the green rods and wafers were bisque-fired at 1200°C for $\sim$ 1½ hours in order to remove all organics. They then were stored in sealed plastic bags for final sintering.

Three rods and three discs were sintered at one time. The heating anc cooling rates were maintained at or below about 150°C/hr to minimize thermal stresses in the muffle tube. The samples were soaked at 1750 ± 10°C for four hours. Typically, the pieces experienced 18-20% shrinkage during sintering.

Table 4 lists the final dimensions and densities measured for the 15 spinel rods fabricated to date. The $\sim$ 5" sintered rods were cut into two 2¼" rods, and a 0.10" thick disc was removed from between the two rod sections for density, microstructural, and X-ray examination. Two of the rods were cut into 20 sections to check uniformity of density, microstructure, and phase composition along the length of the rod.

One sintering run of the magnesia-rich spinel has been performed which followed the same procedures as were followed for the stoichiometric spinel. The end-products were high-quality also.

The sintered densities of the stoichiometric spinel rods were 3.52 ± 0.01 g/cm^3 or 98.5% of theoretical density. A fairly uniform variation in the density of 0.006 g/cm^3 along the length of the sectioned rods indicates that a slight temperature gradient probably exists in the sintering furnace. A similar variation occurred in the sectioned magnesia-rich rod. This variation amounts to no more than 0.2%.

Figure 19 (a-b) shows typical micrographs of polished and thermally etched surfaces for the 50/50 and 65/35 spinel samples, respectively. The grains are isomorphic and generally range in size from 5 to 10 microns with a few 15 micron grains for both compositions.

No second phases are evident in the 65/35 micrograph; however, the X-ray diffraction scan of this sample shows strong MgO peaks as well as $MgAl_2O_4$ peaks. Only $MgAl_2O_4$ peaks were observed for the X-ray scans of the 50/50 spinel material.

Fabrication and characterization of more of these rods and wafers is ongoing. EDAX profiles will be run on selected samples of 65/35 spinel to ascertain where the MgO second phase exists.

An attempt will be made next quarter to lower the sintering temperature $\sim$ 50°C for these materials. Hot spots develop at two locations near the front end of the muffle tube and have led to muffle tube failure after three or four runs. In addition, at 1750°C, the muffle tube creeps excessively and eventually may damage the graphite heating element. In order to reduce the load

Table 4. Dimensions and Densities of Spinel (50m/o MgO / 50 m/o Al_2O_3) Rods Fabricated to Date

Rod No.	Soak Temp and Time	Mean + Diameter (Green)	Mean + Diameter (Sintered)	Density*	Comments
	°C (hrs)	(in.)	(in.)	% theory	
1	1750 (4)	0.597	0.469	98.6	5-10 μm grains
2	1750 (4)	0.581	0.468	98.4	" " "
3	1750 (4)	0.609	0.483	98.4	" " "
4	1750 (4)	0.610	0.485	98.1	micros. not completed
5	1750 (4)	0.609	0.487	98.0	" " "
6	1750 (4)	0.615	0.486	97.8	" " "
7	1750 (4)	0.665	0.531	98.0	" " "
8	1750 (4)	0.656	0.518	98.0	" " "
9	1750 (4)	0.656	0.520	97.8	" " "
10	1750 (4)	0.677	0.536	97.9	" " "
11	1750 (4)	0.690	0.549	97.9	" " "
12	1750 (4)	0.687	0.544	97.9	" " "
13	1750 (4)	0.669	0.532	98.1	" " "
14	1750 (4)	0.682	0.548	98.0	" " "
15	1750 (4)	0.686	0.539	98.0	" " "

+ Since the rods have a uniform taper, the average of the end diameters is recorded.

* Theoretical density is taken as 3.5755 gm/cm^3

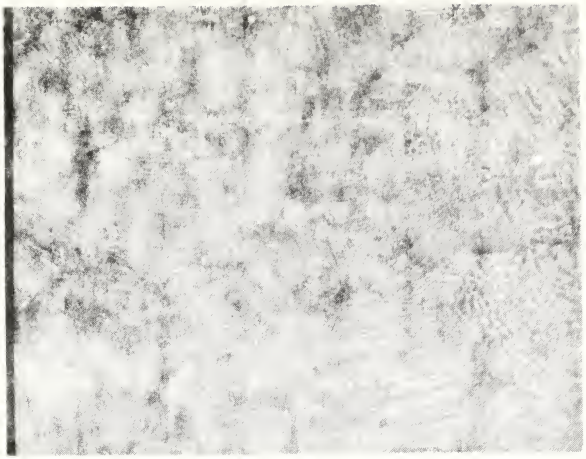

Fig. 19-a. Thermally etched 50/50 $MgAl_2O_4$ spinel.

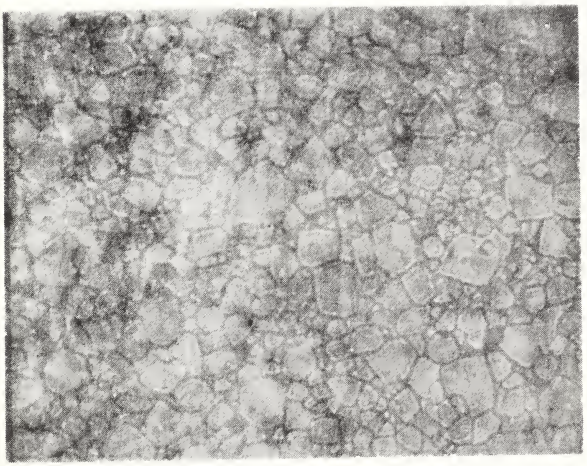

Fig. 19-b. Thermally etched 65/35 $MgAl_2O_4$ spinel.

in the critical hot-zone region of the muffle-tube, a Dee tube which bridges the hot-zone will be installed.

b. Disc substrates for wettability studies

Disc substrates (final dimensions of ∿ 1.125 inches diameter by 1/4 inch thick) of dense, high-purity α-Al_2O_4 and magnesium aluminate spinel ($MgAl_2O_4$) of two compositions--50/50 and 65/35 magnesia to alumina mole ratios--were prepared for the in-house wettability studies. Powder preparation for both spinel compositions was the same as for rods described in the previous section. Wafers from twice-calcined powders were pressed uniaxially at 10 or 20 kpsi, bisque-fired, and sintered along with the rods. The sintered densities ranged from 97.4 to 97.9% of theoretical with no dependence on the pressing pressure noticed.

The alumina* powders were wet-milled for eight hours using high-purity alumina media and anhydrous alcohol and then dried and pressed without a calcining step or a binder addition. The wafers were fired in a N_2 atmosphere at 1510°C for one hour. The final densities all were over 3.94 gm/cc (98.9% of theoretical).

c. Controlled pososity α-Alumina

The effect of pressing pressure on the porosity level in α-alumina prepared from the Reynolds RC-HP-DBM powders (powder preparation described in the previous section) was examined initially. Wafers (∿1/4 inch thick) were pressed uniaxially to different pressures and sintered in ambient atmosphere at 1510°C for one hour. Table 5 shows the resulting values of porosity, and Figure 20 (a-b) shows typical microstructures.

From the photomicrographs, it is observed that the porosity was distributed uniformly and consisted primarily of large voids of ∿ 20-25 μm size in addition to smaller-sized pores within the alumina grains. Future work will examine the effect of the additional organic fillers which can be burned out of the green body prior to sintering.

4. Future Work Plans

The MERDI materials development, fabrication, and characterization laboratory will be upgraded continuously this coming year. The acquisition of additional equipment that will allow the utilization of specialized techniques will extend materials processing capabilities further.

In support of other MHD and fuel-cell research tasks, fabrication of test samples of specific materials with controlled properties will be continued. Spray drying of pre-pressed powders when available will provide greater materials quality control and is a key item which is required. The Autoclave isostatic press with 50 kpsi pressing pressure capability will be operational soon, augmenting the 10 kpsi capability already in use. The addition of organic fillers to control microstructural variables will be studied in greater detail.

* Reynolds RC-HP-DEM + 0.023% Mgo.

Table 5. Measured Porosity of Alumina Wafers for Various Pressing Pressures.

Pressing Pressure (psi)	Porosity (%)
2000	15.6
3000	11.3
4000	7.7
5000	7.2
6000	5.5
7000	5.6

Table 6. Nominal Slag Compositions from Task B Investigations

Slag	Composition
B-0	5% Fe_2O_3, 45% SiO_2, 25% CaO, 25% Al_2O_3
B-15	(B-0 composition) x .85 + .15 K_2SO_4
B-30	(B-0 composition) x .7 + .30 K_2SO_4
B-C (after Al_2O_3 corrosion run)	Al_2O_3, SiO_2, CaO
B-C (after MgO corrosion run)	Al_2O_3, SiO_2, CaO, MgO
B-M (after MgO corrosion run)	Al_2O_3, SiO_2, MgO

Techniques for examining materials microstructure will be upgraded. Thermal and chemical etching procedures for enhanced photomicrographic imaging will be refined with the need for in-house SEM capability becoming more crucial as the limits of optical methods are reached.

C. Wettability of MHD Materials by Slag-Seed Mixtures

1. Introduction

The basic experiment consisted of photographing sessile drops of molten slags on several solid ceramic substrates at temperatures above the slag deformation point. Photographs of the slag profile were used to determine the wetting contact angle and the slag surface tension as a function of temperature. Post-test analyses were made to characterize the amount and mode of slag-substrate reaction at the interface.

2. Experimental Procedure

The synthetic slag specimens were obtained from Task B researchers at the Montana College of Mineral Science and Technology. The nominal slag compositions are listed in Table 6. Slags B-C and B-M are slags which have been used in Task B corrosion tests. The slag compositions in these samples have increased amounts of either Al_2O_3 or MgO depending the type of rod which has been tested. The other slags were virgin materials which had not been subjected to corrosion tests. A description of each of the three ceramic substrate materials used is listed in Section B-3b where fabrication and characterization of these substrate materials is discussed. Substrate surfaces were polished flat on a 70μm diamond wheel followed by ultrasonic cleaning in acetone prior to the wettability tests.

Tests were performed in the high temperature sintering furnace in air. The furnace temperature was increased at a rate of 2°C/min. The thermal time constant for the specimen to reach ambient temperature was estimated to be less than 10 seconds.

Since thermal history of the slag-ceramic interface appeared to be important, identical slag samples were tested simultaneously on two different substrates. At five-degree temperature intervals, the slag profiles were photographed.+ Prints with up to x5 magnification were obtained. Figure 21 shows a typical sample arrangement with a side-by-side view of slag B-C on Al_2O_3 (right side) and on 50/50 MgO-Al_2O_3 spinel (left side).

The wetting contact angles were determined from the photographs. They were taken as the angle formed by the tangent of the liquid surface at the point of contact with the solid. Using the technique of Bashforth and Adams[28] as modified by Butler and Bloom,[29] the surface tensions are being determined from the slag profiles. The technique is described further by Bates and Rasmussen.[30]

Upon cooling, the samples were sectioned, mounted in Bakelite holders, polished to 3μ diamond paste, and photographed at x100 to x500.

+ 35 mm single lens reflex camera with a 200 mm telephoto lens and bellows.

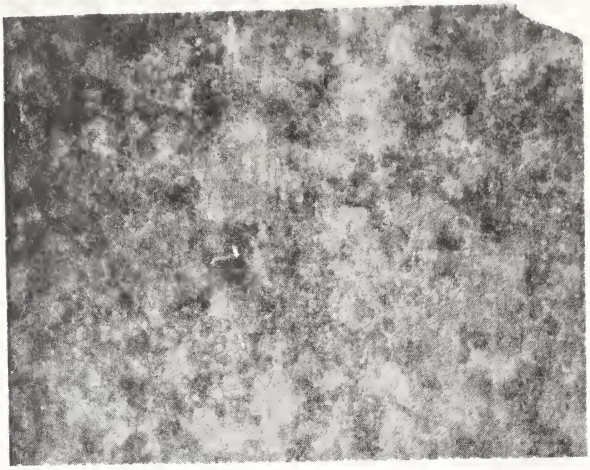

Fig. 20-a. Alumina pressed at 4000 psi.

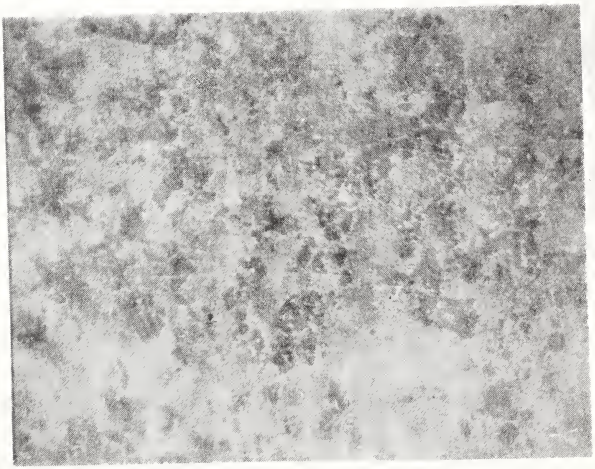

Fig. 20-b. Alumina pressed at 7000 psi.

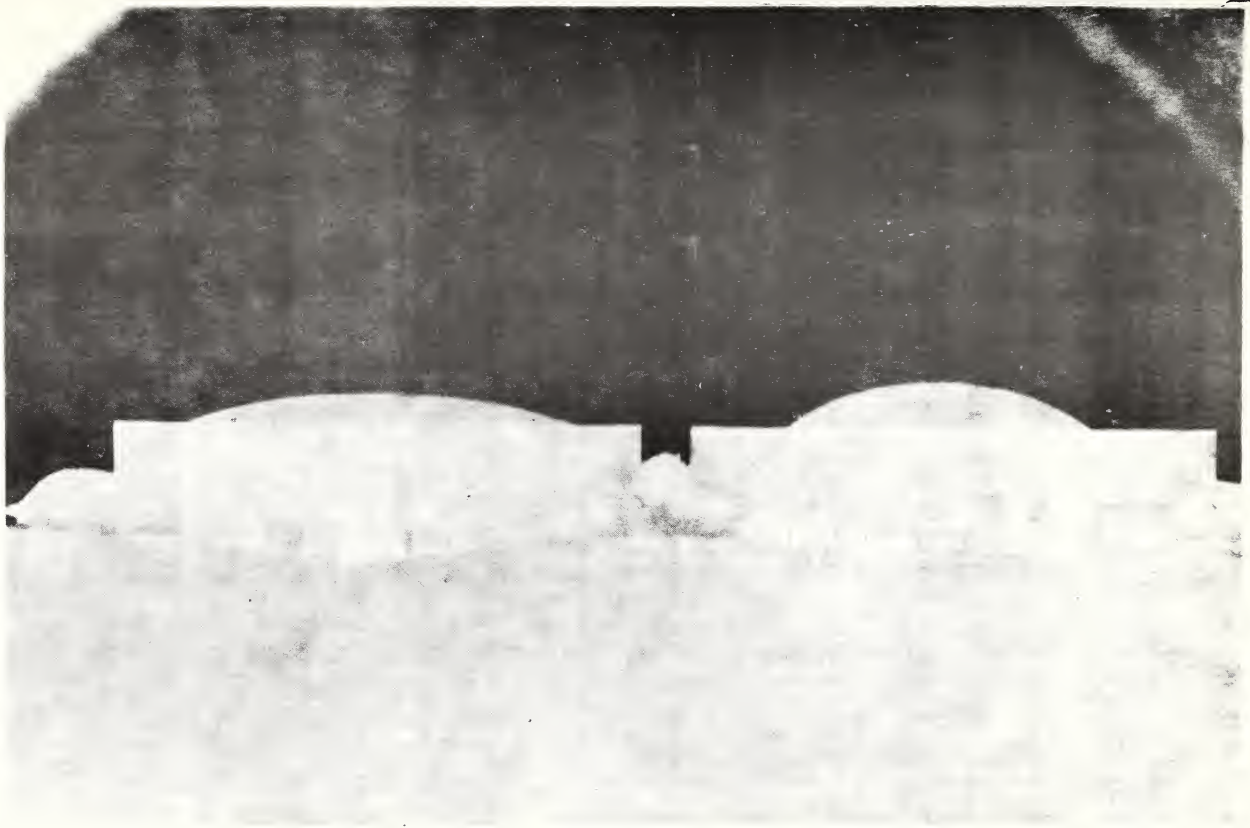

Fig. 21. Sample arrangement for Wettability Test
Slag B-C on Al_2O_3 (right side), B-C on $MgAl_2O_4$ (left side).

3. Results and Discussion

The range of wetting contact angles observed at various temperatures are summarized in Table 7. With the exception of slag BC(MgO) all other slags had higher contact angles on Al_2O_3 than on either 65/35 or 50/50 m/o MgO / Al_2O_3 spinel.

Typical temperature dependences of the contact angle are shown in Figures 22 and 23.

Potassium seed concentration had a mixed effect on the contact angle; compare slags B-0 (no potassium), B-15 (15w/o K_2SO_4), and B-30 30 w/o K_2SO_4) on AR#2. B-15 had a much lower deformation point and a somewhat higher contact angle. B-30 displayed a nearly constant contact angle over a wide range of temperatures. Post-test analyses indicated that B-30 reacted less with the substrate than did either B-15 or B-0. This is in agreement with Task B corrosion results.[31] The nearly constant contact angle for B-30 may be related to its lower corrosiveness.

Comparison of slag BC (with and without MgO) on alumina and spinel show the affinity of MgO for Al_2O_3. Namely, BC with MgO wets the Al_2O_3 more than BC without MgO.

Figure 24 shows the effect of surface roughness on the contact angle. This test was a side-by-side comparison of slag B-15 on stoichiometric spinel. One substrate was polished to 3μm, and the other was polished on a 70μm diamond wheel. The slag slumped on the 3μm substrate 15°C before the 70μm substrate. However, the temperature dependence of the contact angle was greater on the 70μm substrate and at the higher temperature; the 70μm substrate had the lower contact angle.

Figures 25 and 26 are photographs from the post-test analyses. The slag reaction with an Al_2O_3 substrate showed grain boundary attack with swelling of the substrate. The slag reaction with the $MgAl_2O_4$ spinel appears in part to be a dissolution of the substrate. These observations are in agreement with those of Oh.[32]

Surface tension results are in the process of being calculated. These values have been delayed because of problems with data transmittal between the MERDI computer and the larger facility at Argonne National Laboratory required to do the computation.

4. Plans for Future Work

Future programs on the wettability and surface tensions of molten coal slags in contact with MHD materials will include the following:

- Evaluation of additional slag-substrate combinations,
- Determination of the effects of potassium seed concentration on wettability and surface tension,
- Computation of surface tension values as soon as the computer inter-connect problems are solved,
- Conduction of constant temperature tests to determine the time dependence of wettability caused by slag-substrate reactions,

Table 7: Range of Slag Contact Angles as a Function of Temperature (°C) on Alumina and Spinel Substrates.

Substrate / Slag	Al_2O_3 (AR#2)		MgO rich $MgAl_2O_4$ (65/35 m/o MgO/Al_2O_3)		Stoichiometric $MgAl_2O_4$ (50/50 m/o MgO/Al_2O_3)	
	Temp. Range	Angle Range	Temp. Range	Angle Range	Temp. Range	Angle Range
B-0	1453 - 1511	26 - 16				
B-15	1226 - 1436	63 - 20	1226 - 1436	42 - 9	1225 - 1504	54 - 9
B-30	1375 - 1450 1400 - 1511 1422 - 1500	37 - 14.6 20 - 22 14 - 15				
B-C(Al_2O_3)	1490 - 1530	49 - 21			1490 - 1530	32 - 14
B-C(MgO)	1405 - 1550	41 - 15			1405 - 1550	42 - 16
BM(MgO)	1375 - 1550	68 - 16			1375 - 1550	56 - 16
B-30	1420 - 1500	37 - 13.5	1430 - 1550	15 - 6		
(After-View)	1430 - 1550	37 - 11-4				

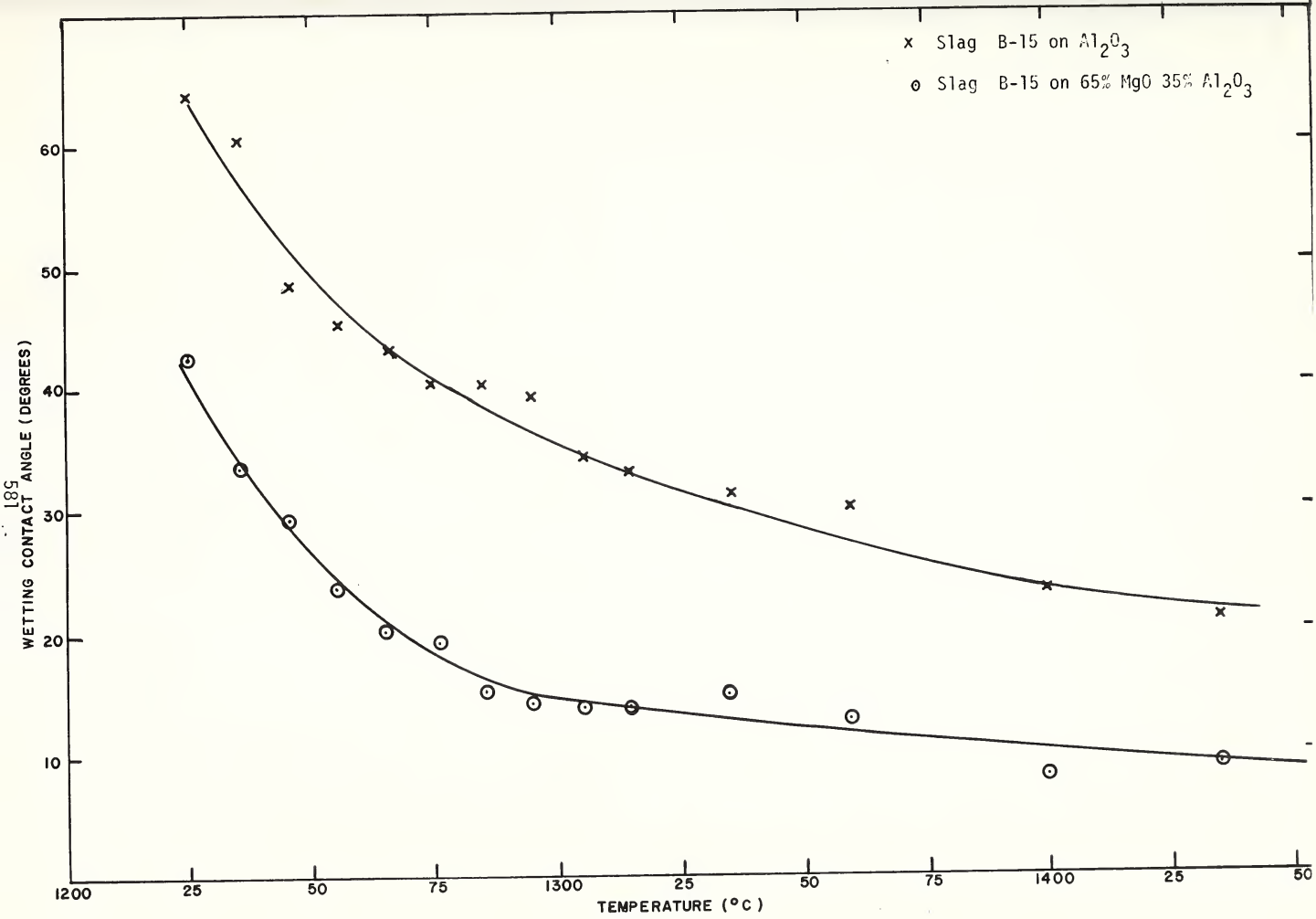

Fig. 22 Typical Temperature Dependence of Contact Angle.

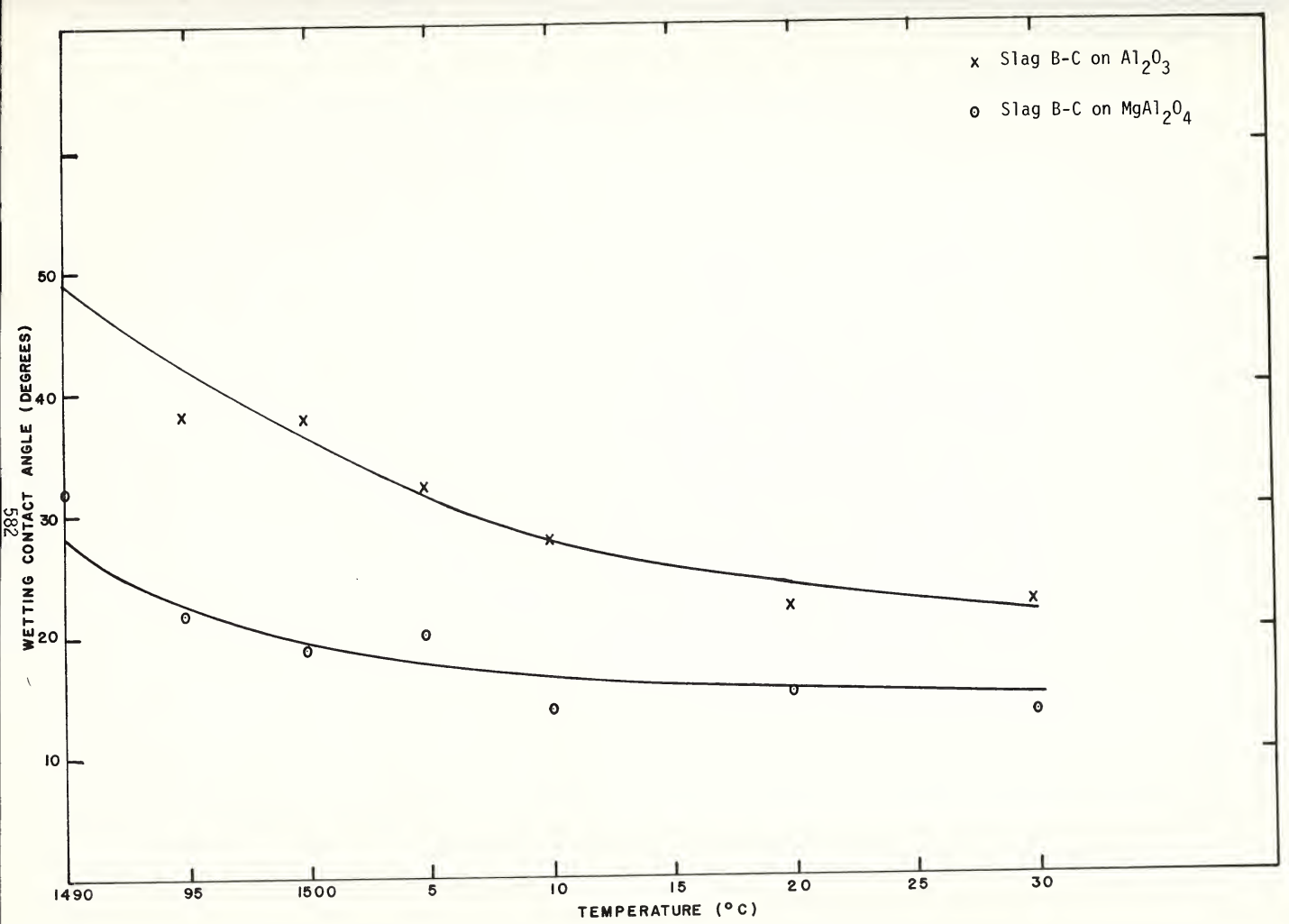

Fig. 23 Typical Temperature Dependence of Contact Angle.

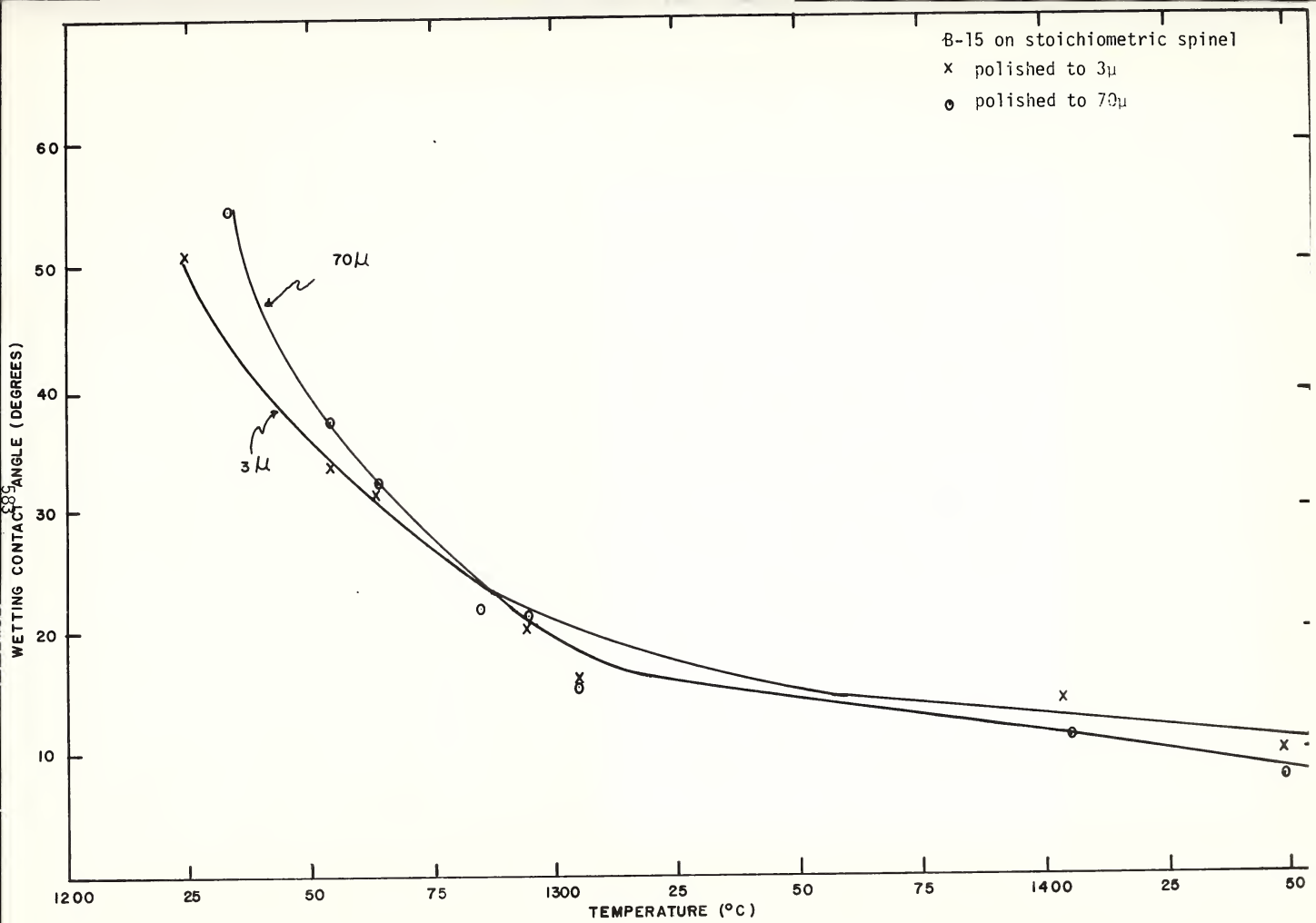

Fig. 24 Effect of Surface Roughness on Contact Angle.

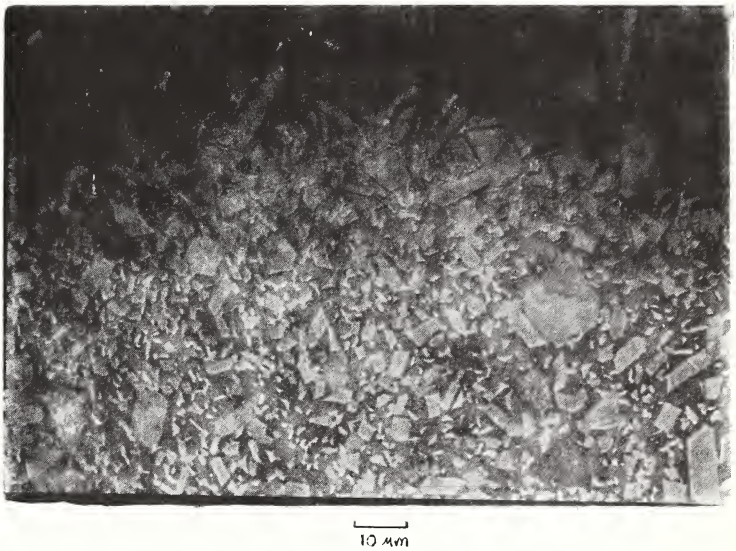

Fig. 25. Boundary reaction region between slag B-15 (top layer) and α-Al_2O_3 substrate (lower layer). B-15 is a 4-component slag with 15% K_2SO_4 added.

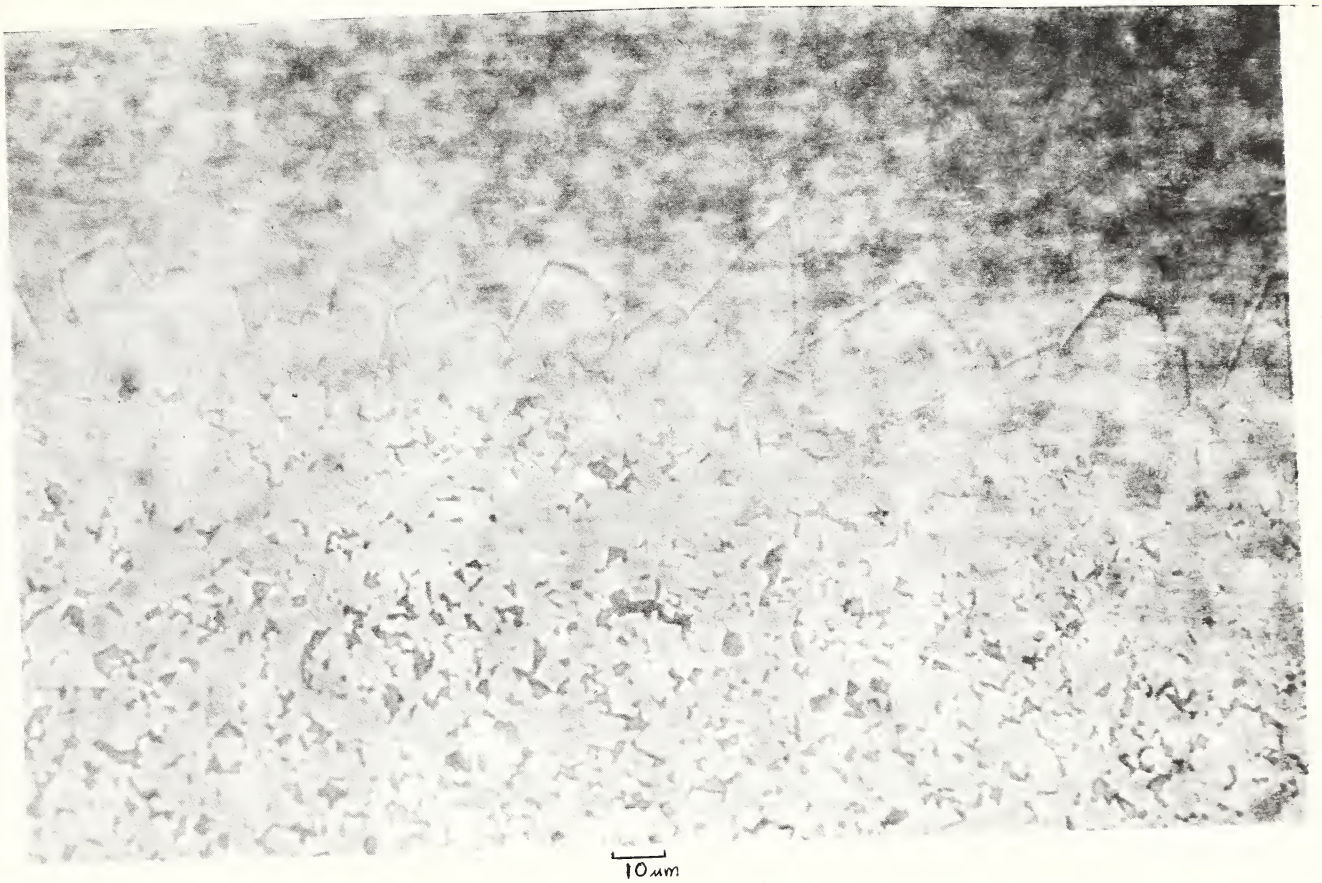

Fig. 26. Boundary reaction region between slag B-15 (top layer) and 65/35 MgO/Al_2O_3 spinel substrate (lower layer). B-15 is a 4-component slag with 15% K_2SO_4 added.

- Determination of the effect of atmosphere on the wettability and surface tension, and
- Continuation of materials characterization to evaluate the relationship between substrate corrosion, wettability, and slag components diffusion into the substrate.

REFERENCES

1. Montana Energy and MHD Research and Development Institute, MHD Power Generation: Research, Development and Engineering, Quarterly Progress Report prepared for ERDA, Contract EF-77-C-01-2524-12, pp. 201-208, June 1977.

2. D. R. Elynn and B. A. Peary, Jr., (eds.) Thermal Conductivity, NBS Special Publication #302, 1968.

3. N. S. Rasor and J. D. McClelland, "Thermal Property Measurements at Very High Temperature," Review of Scientific Instruments, 31, p. 595, 1960.

4. W. J. Parker, R. J. Jenkins, C. P. Butler, and G. L. Abbott, "Flash Method of Determining Thermal Diffusivity, Heat Capacity, and Thermal Conductivity," Journal Applied Physics, 32, pp. 1679-1689, 1961.

5. R. D. Cowan, "Pulse Method of Measuring Thermal Diffusivity at High Temperatures," Journal Applied Physics, 34, pp. 926-927, 1963.

6. R. E. Taylor and J. A. Cape, "Finite Pulse-Time Effects in the Flash Diffusivity Technique," Applied Physics Letters, 5, pp. 212-213, 1964.

7. R. Righini and A. Cezairliyan, "Pulse Method of Thermal Diffusivity Measurements (A Review)," High Temperatures - High Pressures, 5, pp, 481-501, 1973.

8. R. C. Heckman, "Finite Pulse-Time and Heat-Loss Effects in Pulse Thermal Diffusivity Measurements," Journal Applied Physics, 44, pp. 1455-1460, 1973.

9. Y. S. Touloukian, R. W. Powell, C. Y. Ho, and M. C. Nicolson, (eds.) "Thermal Diffusivity," vol. 10 of Thermophysical Properties of Matter Series, IFI/Plenum, New York, 1973.

10. H. R. Shanks, A. H. Klein, and G. C. Danielson, "Thermal Properties of Armco Iron," Journal Applied Physics, 38, pp. 2885-2892, 1967.

11. W. D. Kingery, H. K. Bowen, and D. R. Uhlman, Introduction to Ceramics, 2nd edition, John Wiley & Sons, New York, p. 589, 1976.

12. J. E. Matta and D. P. H. Hasselman, "Thermal Diffusivity of Al_2O_3 - Cr_2O_3 Solid Solutions," Journal American Ceramic Society, 58, p. 458, 1975.

13. H. J. Siebeneck, W. P. Minnear, R. C. Bradt, and D. P. H. Hasselman, "Thermal Diffusivity of Nonstoichiometric Titanium Dioxide," Journal American Ceramic Society, 59 (1-2), p. 84, 1976.

14. H. J. Siebeneck, R. A. Penty, D. P. H. Hasselman, and G. E. Youngblood, "Thermal Diffusivity and Thermal Conductivity of a Fibrous Alumina," Ceramic Bulletin, 56 (6), p. 572, 1977.

15. G. P. Marino, "The Porosity Correction Factor for the Thermal Conductivity of Ceramic Fuels," Journal Nuclear Materials, 38, p. 178, 1971.

16. G. E. Youngblood, K. Chyung, and D. P. H. Hasselman, "Effect of Crystallization on the Thermal Diffusivity of a Cordierite Glass-Ceramic," (in preparation).

17. H. J. Siebeneck, W. P. Minnear, R. C. Bradt, and D. P. H. Hasselman, "Effect of Micro-cracking on the Thermal Diffusivity of Fe_2TiO_5," Journal American Ceramic Society, 59 (5-6), pp. 241-44, 1976.

18. H. J. Siebeneck, J. J. Cleveland, D. P. H. Hasselman, and R. C. Bradt, "Effect of Micro-cracking on the Thermal Diffusivity of $MgTi_2O_5$," Journal American Ceramic Society, 60 (7-8), pp. 336-37, 1977

19. W. R. Manning, G. E. Youngblood, and D. P. H. Hasselman, "Effect of Microcracking on the Thermal Diffusivity of Polycrystalline Aluminum Niobate," Journal American Ceramic Society, 60 (9-10) p. 469, 1977.

20. D. Greve, N. Claussen, D. P. H. Hasselman, and G. E. Youngblood, "Thermal Diffusivity/Conductivity of Alumina with a Zirconia Dispersed Phase," Ceramic Bulletin, 56 (5), p. 414, 1977.

21. Nils Claussen, Max-Planck Institute for Metallforschung, private communication.

22. FluiDyne Engineering Corporation, "Support Testing and Design Study Evaluation of Regenerative Air Heaters," Progress Report for the period January 1977 - March 1977, Minneapolis, Minnesota.

23. J. E. Fenstermacher, Jr., L. R. White, and R. R. Smyth, "Progress in the Testing of Refractories for Directly-Fired MHD Air-heater Service, Part II," Conference on High Temperature Sciences Related to Open-Cycle, Coal-Fired MHD Systems at Argonne National Laboratory, Argonne, Illinois, April 4-6, 1977.

24. A. Kumnick and W. Beezhold, "Thermal Shock Behavior of Magnesia Chromite Ceramic Exposed to Coal Slag, Conference on High Temperature Sciences Related to Open-Cycle, Coal-Fired MHD Systems at Argonne National Laboratory, Argonne, Illinois, April 4-6, 1977.

25. Y. S. Touloukian and E. H. Buyco, (eds.) "Specific Heat-Nonmetallic Solids," vol. 5 of Thermophysical Properties of Matter Series, IFI/Plenum, New York, 1970.

26. Ted Morse and J. J. Rasmussen, "Evaluation of Binders, Lubricants, Dispersants and Antifoams for Use in Ceramic Body Formulation," Report 4D19 : Montana Energy and MHD Research and Development Institute, January 21, 1977.

27. E. Kostic and I. Momcilovic, "Reaction Sintered $MgAl_2O_4$ Bodies from Different Batch Compositions," Ceramugria International, 3 (2), pp. 57-60, 1977.

28. F. Bashforth and J. O. Adams, An Attempt to Test Theories of Capillary Action, Cambridge University Press, 1883.

29. J. M. Butler and B. H. Bloom, "A Curve Fitting Method for Calculating Interfacial Tension from the Shape of the Sessile Drop," Surface Science, 4, pp. 1-17, 1960.

30. J. Lambert Bates, Properties of Molten Coal Slags Relating to Open Cycle MHD, Progress Report No. 1, July 1974 to January 1975 to NSF (RANN), Battelle-Pacific Northwest Laboratory, February, 1975.

31. W. E. Seymore, Materials Engineer, Montana College of Mineral Science and Technology, private communication.

32. Tae-I Oh, Lewis N. Shen, Roland W. Ure, Jr., and Ivan B. Cutler, "Slag Penetration into Oxide Refractories," American Ceramic Society Bulletin, 56 (7), p. 649, 1977.

TASK Q
CDIF Environmental Monitoring and Evaluation

E. Kukay

ABSTRACT

The monitoring and evaluation program under Task Q will ensure that the operation of the MHD CDIF adheres to existing environmental regulations and standards. In addition, the program will verify the MHD CDIF environmental impacts through documentation and comparison between baseline (pre-operational) and future (operational) environmental parameters.

The total ambient environmental surveillance program for the MHD CDIF has been implemented. Construction of a permanent air quality/meteorological station and site preparation for the first mobile station have been completed. Meteorological and air quality data for 1977 will be compiled in a data reference manual.

Computer interfacing of the air quality and meteorological data handling systems will provide a data base for assessing and predicting air pollution potentials and environmental impacts of the MHD CDIF.

I. OBJECTIVE AND SCOPE OF WORK

The objective of this program is to ensure that the design, construction, and operation of the MHD component development and integration facility (CDIF) complies with the applicable environmental protection standards concerning air pollution, water pollution, solid waste disposal, and noise.

In-plant environmental monitoring for air quality, noise safety, stack gas emission, and solid/liquid waste treatment and disposal is in the planning stage. Evaluations and recommendations will be provided to the CDIF A and E contractors and ERDA project management as deemed appropriate.

Meteorological and air quality investigations will be performed for the CDIF site and the surrounding area to determine the potential for air quality degradation associated with the CDIF operation. Baseline air quality data and climatological data can be used to assess the effects of the CDIF on the environment. Investigations will be implemented by designing and constructing a fixed meteorological station and several air quality monitoring stations. The system will be adequate for investigating the impact of the engineering test facility (ETF), provided Butte is chosen as a potential site.

II. SUMMARY OF PROGRESS TO DATE

A total ambient environmental surveillance program (TAESP) has been designed for the MHD CDIF in the Industrial Park south of Butte, Montana.

The proposed program will serve a three-fold purpose regarding CDIF environmental impact: a) it will establish an environmental baseline; b) it will provide continuous surveillance during CDIF operation; and c) it will provide necessary data to predict the environmental impact of future coal-fired MHD facilities accurately.

The meteorological/air quality mobile unit is completely operational (Figures 1 and 2). The unit has been located near the site of the permanent meteorological station since December 1976. The 40-meter meteorological tower installation was completed the end of November 1976 (Figure 3). Wind, temperature, and humidity sensors were placed on the tower during September 1977. Tower installation is now complete, and data are being recorded on magnetic tape.

An acoustic radar unit used to study the thermal stratification of the atmosphere was installed at the location of the permanent air quality/ meteorological station during October 1976. Additional data concerning the atmospheric thermal stratification was gathered on a limited basis throughout the year by aircraft temperature soundings.

An airflow study of wind data gathered from the Butte airport for the period 1971-1975 was completed, and a draft interim report was submitted to ERDA during February 1977.

A comparison of wind data between the MHD CDIF and the Butte airport during December 1976 and January/February 1977 was completed and submitted to ERDA during March 1977. The preliminary study showed that general wind directions vary as much as 80 degrees between the CDIF and airport data. Instrumentation must be available at other locations since airport data is not a reliable indicator of airflow throughout the Butte valley.

A daily weather log (visual observations) has been pursued since the summer of 1976. Five major sources of air pollution have been noted:

1. The Anaconda Company open pit mining operations;

2. Gilman Excavation operation approximately half a mile south-southeast of the pit;

3. Silver Bow County asphalt plant and rock crusher about one mile south of Gilman's operation;

4. The Montana Pole and Treatment Plant along the west edge of Butte; and

5. Transportation influences.

Analysis of the wind data obtained at the meteorological/air quality site and the acoustic radar data were completed and submitted to ERDA in June 1977.

The air quality sampling program initiated during January 1977 from a mobile unit located at the permanent meteorological site is continuing. High-volume particulate samples are collected every two days. Impinger sampling for SO_2 and NO_x is conducted every six days to correspond to the schedule of the national ambient sampling network. Other parameters such

as settleable particulate and static air sampling are determined on a monthly basis. All analytical work, including trace element analysis of collected particulate, is being conducted by the Mineral Research Center (MRC) of the Montana Tech Alumni Association. The collaborative intra-laboratory study between MRC, the Montana Air Quality Bureau, The Anaconda Company, and Stauffer Chemical is being continued to assure quality results of ambient air samples.

A sample and calibration procedure manual relative to the CDIF monitoring program has been prepared and currently is being revised. Analytical procedures used in the air quality program were compiled by MRC personnel. Updates and/or modifications will be introduced as new procedures become necessary with the acquisition of new instrumentation.

Aerial infrared photographs were taken from eleven selected sites at approximately two-week intervals from May through September 1977. A total of seven fly-overs were conducted. Documentation of the real color and false color photographs will depict the 1977 growing season.

Construction of the permanent air quality/meteorology station was completed in September 1977. All of the meteorology/climatology instrumentation has been installed.

Design and implementation of the meteorological data handling system, a portion of the environmental data base systems, on MERDI's computer has been completed, and the system is operational. The data entry portion of the air quality data handling system has been completed, and the data file structures have been finalized and documented.

III. DETAILED DESCRIPTION OF TECHNICAL PROGRESS

A. Meteorology/Climatology

1. Daily Weather Log

During the summer of 1976, a log concerning pertinent air pollution weather features was begun. Although the log is not continuous, it does help in establishing an air pollution climatology for Butte. It was found that Butte frequently experiences nighttime radiation inversions. The top of the haze layer imbedded in the temperature inversion typically is 200 meters (m) above the valley floor. The height of the layer does not show appreciable variation except during periods of strong winds which limit its height to less than 200m. Also, during these windy periods when the inversion does form, its destruction seems to be accomplished through a downward flux of momentum which initiates sufficient turbulence to destroy the inversion. During quiescent periods, the destruction is caused by the fumigation process (thermally induced turbulence). It has been noted that the destruction of the inversion through mechanical turbulence (windy conditions) usually occurs a few hours before its destruction by thermal turbulence. During the summer, the radiation inversion normally was gone by 1000 MST; however, records to date indicate cases in which the radiation inversion had attained sufficient depth and strength to persist the entire day. Significant air quality deterioration accompanied this persistence. The frequency of this occurrence increased during

the winter because of decreased insolation and the associated reduction in surface heating.

During the year, several different sources of air pollution were noted, and a seasonal dependence for some of the sources was discovered. The major pollution sources within the Butte valley are listed below.

a) The Anaconda Company open pit mining operations--These operations are continuous throughout the year and result in a bluish-black haze hovering over and near the pit. Normally, the bluish-black haze produced by the haulage vehicles does not visibly extend to the CDIF area.

b) Gilman Excavation and Silver Bow County rock crushers--The Gilman rock crusher lies about half a mile south-southeast of the pit and frequently operates during summer and fall mornings. Little wintertime activity was seen. This crusher produces a visible cloud of particulates. Frequently, particulates from this crusher pervade the eastern portion of the valley until the nocturnal inversion is destroyed and good atmospheric mixing disperses the particulates. This plant seems to produce the greatest visual air quality deterioration when it operates. The county rock crusher lies about half a mile south of Gilman's and is much smaller. Summer and fall operations are much more intermittent but still produce a visible particulate cloud. Little winter activity was noticed.

c) A pole treatment plant at the west edge of the city--This plant operates all year and produces a yellowish-brown haze. Normally, this haze seems restricted to the western portion of the valley and was not seen at the southern portion where the CDIF is located.

d) Transportation--The effects of automobile emissions seem most pronounced during the winter. Frequently during winter, a bluish haze with a top 100m above ground at most was seen during the warmer months, possibly because during morning rush hour there was a greater degree of atmospheric mixing during warmer months than during winter when the inversion was strongest and no vertical mixing occurred during rush hour.

Other minor sources of visual pollution are no doubt present, but their contribution to the overall visual pollution at Butte is minimal. The haze layer seems worse during fall and summer mornings when all the sources are operating. During winter, the haze seems less obvious since the rock crushers do not operate at that time.

2. 1971 to 1975 Wind Data Analysis

The hourly weather observation data gathered at the Butte airport presently is being analyzed to develop a series of wind roses to describe airflow patterns during each month and season in Butte. Figures 4, 5, and 6 illustrate the airflow using the five years' data. Figure 4 shows the wind rose for an entire 24-hour period. Figures 5 and 6

show the data for the daytime and nighttime periods, respectively. It should be noted that the frequencies are expressed as a percentage of total observations for the given time period of interest, not necessarily the 43,000 + total observation for all times. Hence, one merely cannot add daytime and nighttime percentages to arrive at the 24-hour rose. Figure 5 shows that during the day, the predominant wind direction is northwest. Figure 6 shows that the predominant direction is south during the night. The reason for a southerly wind at night is cold air drainage from the higher terrain immediately south of the Butte airport. During the day, the wind shifts to a northwesterly direction in response to the destruction of the nighttime radiation inversion, which causes the general circulation pattern to override local circulation patterns.

Figures 7, 8, and 9 depict the wind roses compiled from wind observations taken when the temperature was 0^{0}F or less. It is seen that both the day and night roses show a mostly southern wind component. In addition, during the day (Figure 7), the percentage of calm conditions is much greater than during the night (Figure 8). Overall, there is a high percentage of calms during these cold episodes.

3. Wind Data Comparison

Data from a temporary portable unit (MRC) for December 1976 and January/February 1977 were compiled for the MHD CDIF and the airport wind sensor locations. The data for these three months were combined to form a winter wind rose. Airport data consisted of hourly observations of wind velocity, while CDIF data were integrated for one-half hour prior to observation. The CDIF wind sensor had a speed threshold of 0.3 $msec^{-1}$, while that of the airport was about 1.5 $msec^{-1}$. Since the CDIF sensor had a lower threshold, calms were chosen arbitrarily as those speeds $\leq$0.9 msec. If a higher cut-off speed had been utilized, the number of CDIF calm periods undoubtedly would have approached the percentage reported at the airport.

The airport data exhibits a bimodal frequency distribution. The dominant directions are south-southeast and northwest (Figure 10). The CDIF data also exhibits a bimodal distribution; however, the northwesterly direction is overshadowed greatly by the southwesterly direction (Figure 11). The northwesterly frequencies at both locations are similar; however, the airport's southeasterly component has been replaced by a large southwesterly component at the CDIF site two miles southwest of the airport. A comparison of these roses illustrates the necessity of having airflow detection instrumentation at the CDIF and other locations since airport data is not a reliable indicator of airflow throughout the Butte valley.

4. Acoustic Radar Data

An acoustic radar was installed at the site of the future CDIF meteorological station location at the Butte Industrial Park during October 1976. Data collection began October 23, 1976.

At present, there are three areas of concern with respect to inversions in the Butte valley which can be investigated using the records supplied by the radar. They are the determination of the time

of formation, time of destruction, and height of the nocturnal radiation inversion. The nocturnal inversion is a surface-gased inversion caused by infrared radiational cooling of the earth's surface. It normally extends from the surface to several hundred meters above it. The depth of the radiation inversions typically ranged from 300m to 1100m, with an average depth of 600m. The onset of the inversions seems to follow the setting of the sun closely. However, during the passage of synoptic scale weather systems, the inversions frequently did not form. There appears to be no correlation between time of onset and maximum inversion depth.

Aircraft soundings obtained during radar operation showed inversion heights which are similar to those determined by radar. Differences in height of up to 100m were common during periods when gravity waves were present within the inversion layer. Frequently, weak, shallow inversion layers were present in the atmosphere that went undetected by radar; however, aircraft observations uncovered their presence.

5. Aircraft Temperature Soundings

Beginning in August 1976, a Cessna 150 aircraft, equipped with a thermometer placed within the cabin air vent, was used to study the vertical temperature structure of the atmosphere over Butte. Most of the soundings were taken prior to 0900 MST. More than 40 soundings were obtained during the year, and it was determined that the average height of the top of the inversion was 1600 feet. Frequently, the temperature gradient through the layer was in excess of 10°C. A thermocouple and digital readout system was utilized during the latter part of the year; however, radio frequency noise and static electricity in the atmosphere produced erroneous data.

6. Correlation of Acoustic Radar and CDIF Wind Data

Analysis of the wind data obtained at the CDIF meteorological site and the acoustic radar data were completed. A definite correlation was found to exist between the temperature inversion formation and destruction times and the character of the wind during those periods. It was found that when no inversion formed during the night, there was no particular wind direction or speed which consistently occurred from one episode to the next. The wind speed and direction reflected the general airflow pattern over the region. When a nighttime inversion did form, airflow generally was from the southwest at 2 to 3 m sec^{-1}. Prior to inversion formation after sunset, the afternoon winds frequently were from a specific direction and often exceeded 4 m sec^{-1}. After the inversion formed, however, the wind shifted to a southwesterly direction and decreased to a speed of 2 to 3 m sec^{-1}. They normally remained at this speed throughout the night when an inversion layer was present. When the nocturnal inversion was destroyed during the morning, the wind speed normally increased from 2 to 3m sec^{-1} to greater than 4m sec^{-1}, provided the general atmospheric circulation was of sufficient magnitude to warrant surface wind speeds of that strength. Frequently, a wind shift accompanied the speed increase because the general circulation pattern no longer was decoupled from surface airflow by the inversion's presence. The direction became quite consistent following the destruction. During the daytime when the convective motions were insufficient to destroy the upper portion of the inversion, surface winds remained light. A local circulation

pattern within the valley dominated the airflow features at such times. Frequently, wind speeds were less than 1m sec^{-1}, and the direction was quite variable. If the inversion happened to break during late afternoon, the speed generally increased and the direction became fairly consistent.

7. Meteorological Data

Computer reduction of all meteorological data collected since December has begun. The current data format is presented in Table 1. Included on the data printout is a daily 36-point wind rose. Other parameters measured and included in the printout are station identification, location, elevation, date, time (mountain standard), in-coming solar radiation (langleys per minute) integrated for one hour, instantaneous temperature (°C), instantaneous dew-point (°C), precipitation (inches) integrated for one hour, instantaneous barometric pressure (millibars), both integrated and instantaneous wind direction (degrees), speed (meters per second), and the standard deviation of the direction (degrees). Daily averages and standard deviations are available for most of the parameters.

B. Air Quality

1. Air Quality/Meteorological Stations

The CDIF air quality/meteorological station in the Butte Industrial Park was completed during September 1977. The station is located within an 80' x 80' fenced area surrounding the 40-meter meteorological tower. All tower instruments have been installed, and the system is fully operational. Instruments were placed on the tower at 10-meter and 40-meter levels. The upper level sensors measure the horizontal and vertical wind direction, wind speed, and temperature. The lower level sensors measure the horizontal wind direction, wind speed, temperature, and dew point. Standard deviation of both vertical and horizontal wind direction will be determined by a microprocessor. All meteorological and climatological data currently are being recorded on digital paper tape and magnetic tape for entry to the Data General Eclipse C-330 computer. Air quality instrumentation which has been received will be installed by mid-October 1977.

Site preparation has been completed for establishment of the first satellite air quality/meteorological station near Terra Verde about 2.4 kilometers (1½ miles) southeast of the CDIF. The mobile unit will be moved to this site, and data collection for both air quality and meteorological parameters will begin by mid-October 1977. Establishment of the second satellite meteorological/air quality station to be located 1.6 kilometers (1 mile) north-northeast of the CDIF has been initiated. Site lease will be negotiated with the Montana Power Company.

2. Aerial Infrared Photography

Selection of eleven control sites in the Butte valley was completed and bi-monthly fly-overs were conducted during the 1977 growing season. The selected areas are listed on the following page.

a) CDIF (looking east)

Sand Creek/Little Basin Creek

b) East Ridge (looking east)

Old Columbia Gardens

Mode-S Canyon/Continental Drive Interchange

Lucky Strike Gulch--Northern Pacific Railroad Trestle

Ueland Ranch/Homestake Pass

c) Highlands (looking south)

Janney/Chicago, Milwaukee, St. Paul, and Pacific Railroad

Lions Camp

d) West of CDIF (looking west)

Middle Fork of Little Basin Creek

e) North of CDIF (looking north)

Timber Butte

Mountain View Cemetery

Country Club/Evel Knievel Residence

The FY 77 series started May 13, 1977 and continued through September 9, 1977 with approximately two-week intervals between fly-overs. Reprints of the color slides have been made, and documentation and compilation of the prints is in progress.

The infrared slides taken on May 13, 1977 of the Lion's Camp show an area of possible deterioration about ¼ mile southeast of the camp. A joint field inspection was performed by MERDI, Silver Bow County Resource Conservation and Development Committee, and the Lion's Club. Examination showed that the light area on the slide exactly coincided with the location of a fire approximately four years ago. While not visible from the air, ground reconnaissance revealed a number of dead trees in the area and a lessened undergrowth where the retardout had been dropped. Later slides in the year do not show this light area, indicating that growth was proceeding at a normal rate.

3. Air Quality Data

Air quality sampling at Butte Industrial Park (CDIF meteorology station) utilizing the mobile unit is continuing. The following parameters are being monitored:

a) High-volume sampling for total suspended particulate and trace element analysis, 24-hour samples every two days.

b) Impinger, gas bubbler type sampling for SO_2 and NO_x, 24-hour samples every sixth day to coincide with the national ambient air sampling network.

c) Static sampling for gaseous fluoride (calcium formate), sulfation rate (lead peroxide), and nitration rate (triethanolamine), 30-day exposure period.

d) Dustfall sampling for total settleable particulate and trace element analysis, 30-day sampling period.

e) Precipitation washout sampling with chemical analysis of the collected samples including trace elements, pH, and acidity determinations.

Air quality sampling equipment for the CDIF meteorology station has been received, and installation is in progress. When this equipment is fully operational, the mobile unit will be relocated to establish an air quality station at the Paxon Terra Verde site.

In addition to the above parameters, ambient monitoring at the CDIF meteorology station will include continuous analyzers for real-time SO_2 and NO_x concentrations. A Lundgren impactor has been ordered for the determination of particle size distribution. Installation of this equipment will be completed during the first quarter of FY 78.

A sample and calibration procedure manual relative to the CDIF monitoring program has been prepared. Current analytical methods used in the air quality program were compiled by Mineral Research Center (MRC) personnel. Updates and/or modifications of the manual will be introduced as new procedures become necessary with the acquisition of new equipment.

The intra-laboratory analytical study involving Montana Tech, the Mineral Research Center, The Anaconda Company, Stauffer Chemical, and the State of Montana Air Quality Bureau is continuing. Periodic cross checks of trace element and chemical analysis are conducted to assure quality results for the ambient air sampling program.

4. Environmental Computer Data Base

Design and implementation of the meteorological data handling system (MDHS) of the environmental data base systems on MERDI's computer has been completed and is operational. The computer programs to enter and report the data on Montana Tech's system have been converted, tested, and successfully implemented on MERDI's computer. All of the data from the cassette tapes has been input, edited, and placed in the appropriate data files.

Documentation of the MDHS has been completed. The conceptual design and the preliminary design documents have been issued.

Data entry sheets have been designed for the air quality data handling system (AQDHS). Parameters include static samples, dust fall, precipitation washout, and high volume air samples using Whutman #41 and type A/E fiberglass filter media. All previous data collected have been transferred to the appropriate data entry sheets. Figures 2-10 represent typical entry sheets for data input to the computer data file. Computer programs to input, verify, and/or edit each parameter have been coded, debugged, and tested.

5. Communication Measurements

Western Telecomputing Corporation, Bozeman, Montana, completed a communications quality survey at eleven locations relative to the CDIF. Density plots were made of the electro-magnetic spectrum from 10 KHz to 1000 MHz. Results from the preliminary survey support the conclusion that the CDIF can generate a relatively large amount of high frequency radio interference without degrading nearby communications. Distant AM radio reception, however, could be degraded because of the presently low noise level in the AM spectrum.

Normal transportation and aircraft traffic contributed audio noise at most of the recording sites. Sound level meter readings ranged from a low of 32 dBA to a high of 52 dBA.

Additional baseline data recorded at the same sites during different seasons of the year would be valuable. A second survey for electromagnetic and audio quality measurements will be arranged during December 1977.

6. CDIF In-plant Monitoring

Stack sampling requirements necessary to meet EPA new source performance standards (NSPS) for fossil fuel fired plants have been reviewed. Sampling equipment for determining SO_2 and particulate emission rates has been ordered. The equipment meets the specifications of the most recent EPA regulations for determining compliance with NSPS (Federal Register, Vol. 42, No. 160, NSPS Revision of Reference Methods 1-8, August 18, 1977). The equipment also can be used for accurately measuring emission rates for fluoride and several non-regulated chemical pollutants. A Cascade-type impactor can be attached to the sampling probe for in-stack particle size distribution.

C. Work Forecast

Ambient air quality monitoring efforts will continue at the CDIF meteorology station and Paxon Terra Verde site to establish a preoperational environmental baseline. Continuous analyzers for real-time monitoring of SO_2 and NO_x will be operational during the first quarter of FY 78. Equipment for ambient particle size distribution measurements has been ordered. A second satellite air quality/meteorological site at the Montana Power Company gas substation approximately one mile north-northeast of the CDIF will be established by the end of 1977. Procurement of the mobile unit and necessary instruments will be initiated during the first quarter of FY 78.

Development of the air quality data handling system (AQDHS) on the Data General Eclipse C-330 computer will be continued by implementing the data entry programs and designing the final report format. The AQDHS and the meteorological data handling system (MDHS) programs will be interfaced to allow correlation of meteorological conditions with air quality results. A data reference manual including all meteorological and air quality monitoring results for the CDIF and south Butte district for 1977 will be compiled and distributed during the second quarter of FY 78.

The acoustic radar data will continue to be compiled and analyzed as it is collected. A program to study the upper level airflow within the radiation inversion utilizing pilot balloons may be implemented. Objective forecasting techniques will be developed for the prediction of formation and destruction of the radiation inversion. Airflow and temperature characteristics in the lowest layer of the radiation inversion will be investigated using data obtained by the 40m tower. A comparison of wind data between the permanent station and Paxon Terra Verde site will be undertaken in an effort to describe local variations of the horizontal airflow patterns.

A CDIF environmental health and emission monitoring plan will be initiated and finalized for distribution during the second quarter of FY 78. The plan will be formulated to satisfy applicable federal and state regulations.

IV. CONCLUSIONS

The total ambient environmental surveillance program (TAESP) has been implemented for the MHD CDIF in the Industrial Park south of Butte, Montana. Construction of the permanent air quality/meteorological station has been completed. Instruments have been installed at the 10-meter and 40-meter levels. Site preparation has been completed for establishment of the first air quality/meteorological station near Terra Verde Heights.

As additional mobile units become available, meteorological data will be collected and correlated to define the air pollution dispersion potential within the Butte valley. Inversion characteristics and airflow patterns will establish data for a qualitative dispersion model. Mathematical models are currently available which will adequately predict dispersion in areas with complex terrain.

Aerial infrared photographs depicting the 1977 growing season in the Butte valley have been compiled, and documentation is in progress.

The air quality data handling system (AQDHS) and the meteorological data handling system (MDHS) will be interfaced to allow correlation of meteorological conditions with air quality results. This will enable accurate assessment and predictions of air pollution potential and environmental impact of the MHD CDIF.

MILESTONE CHART

STATUS DATE _____

TASK Q

PROGRESS

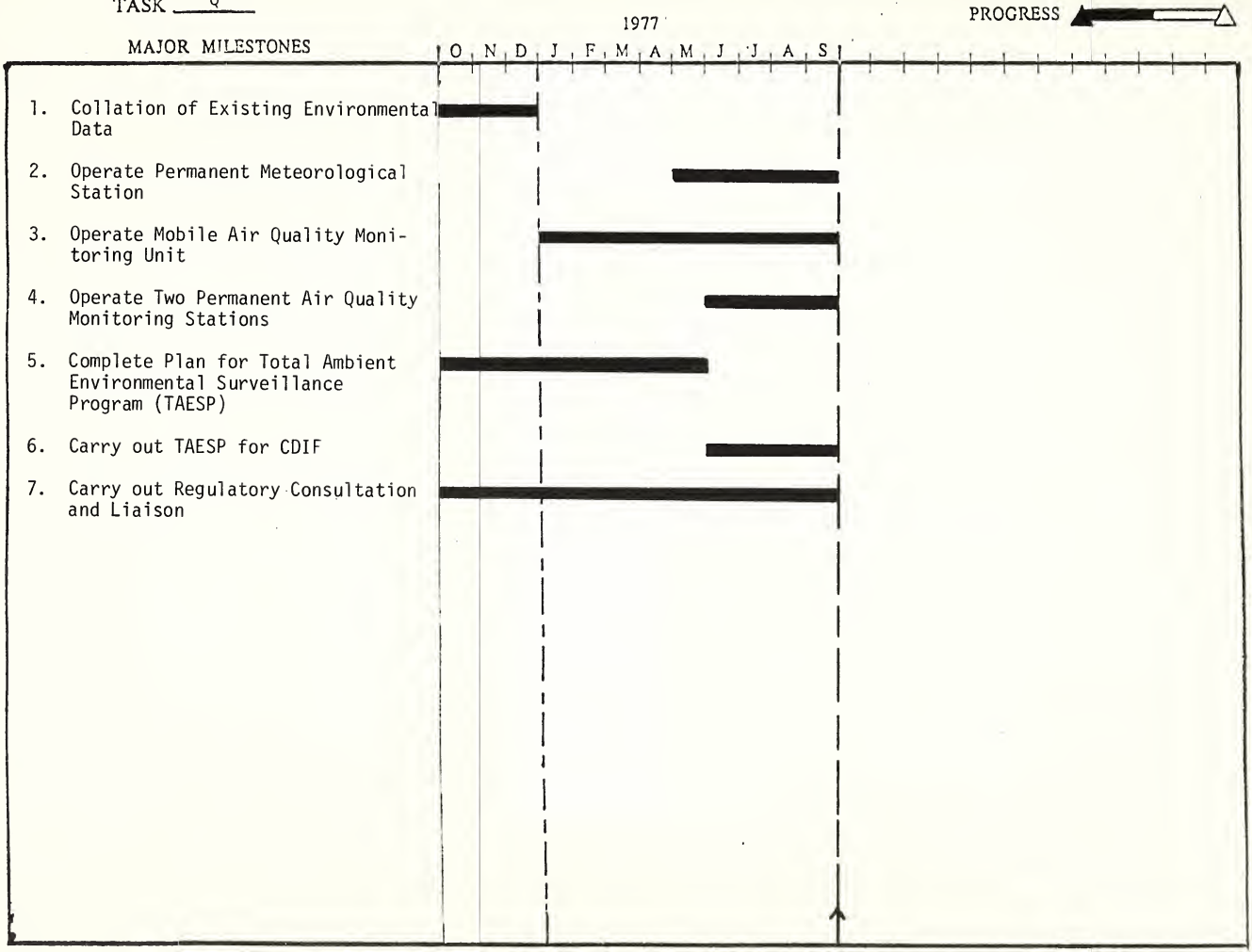
1977
MAJOR MILESTONES
O N D J F M A M J J A S
1. Collation of Existing Environmental Data
2. Operate Permanent Meteorological Station
3. Operate Mobile Air Quality Monitoring Unit
4. Operate Two Permanent Air Quality Monitoring Stations
5. Complete Plan for Total Ambient Environmental Surveillance Program (TAESP)
6. Carry out TAESP for CDIF
7. Carry out Regulatory Consultation and Liaison

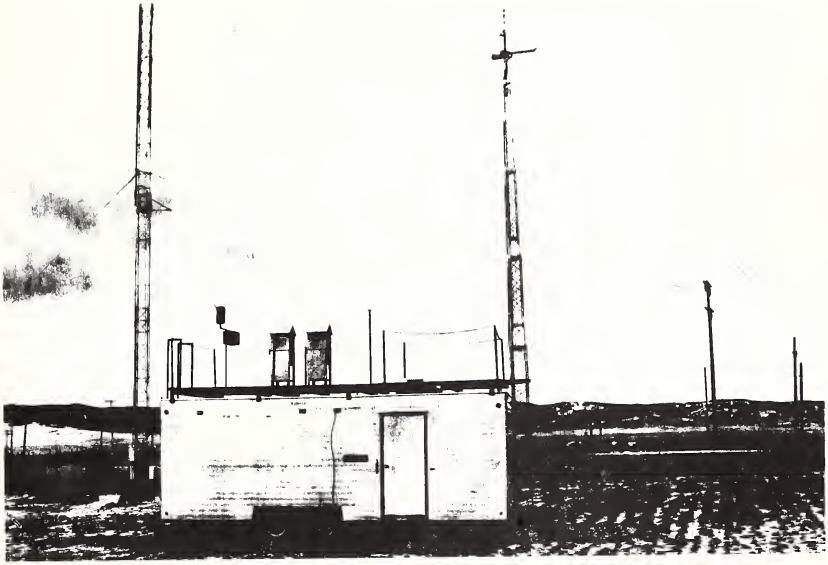

Figure 1--The meteorological air quality mobile unit with 10m wind and temperature mast extended. Two high volume air samples, a dustfall jar, and housing for sulfation and nitration plates are on top of the trailer.

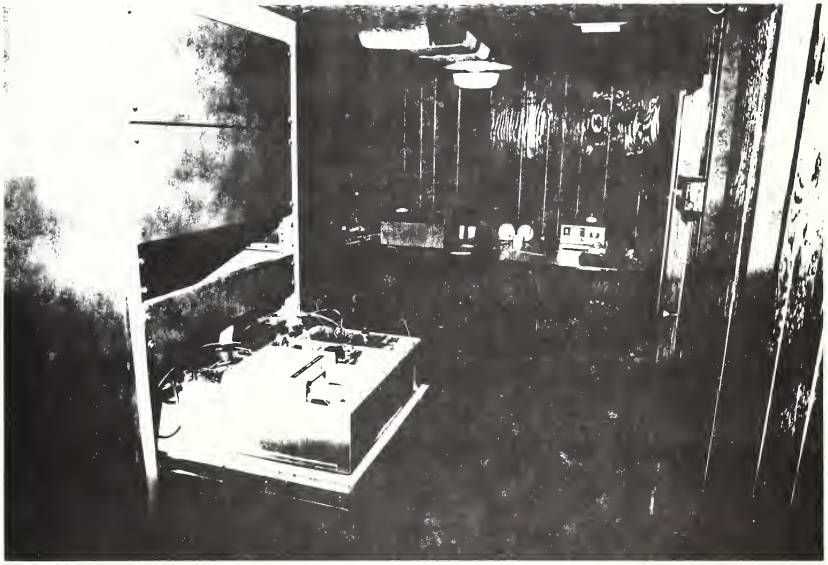

Figure 2--Inside the mobile unit is the meteorological data collection instrumentation system (foreground).

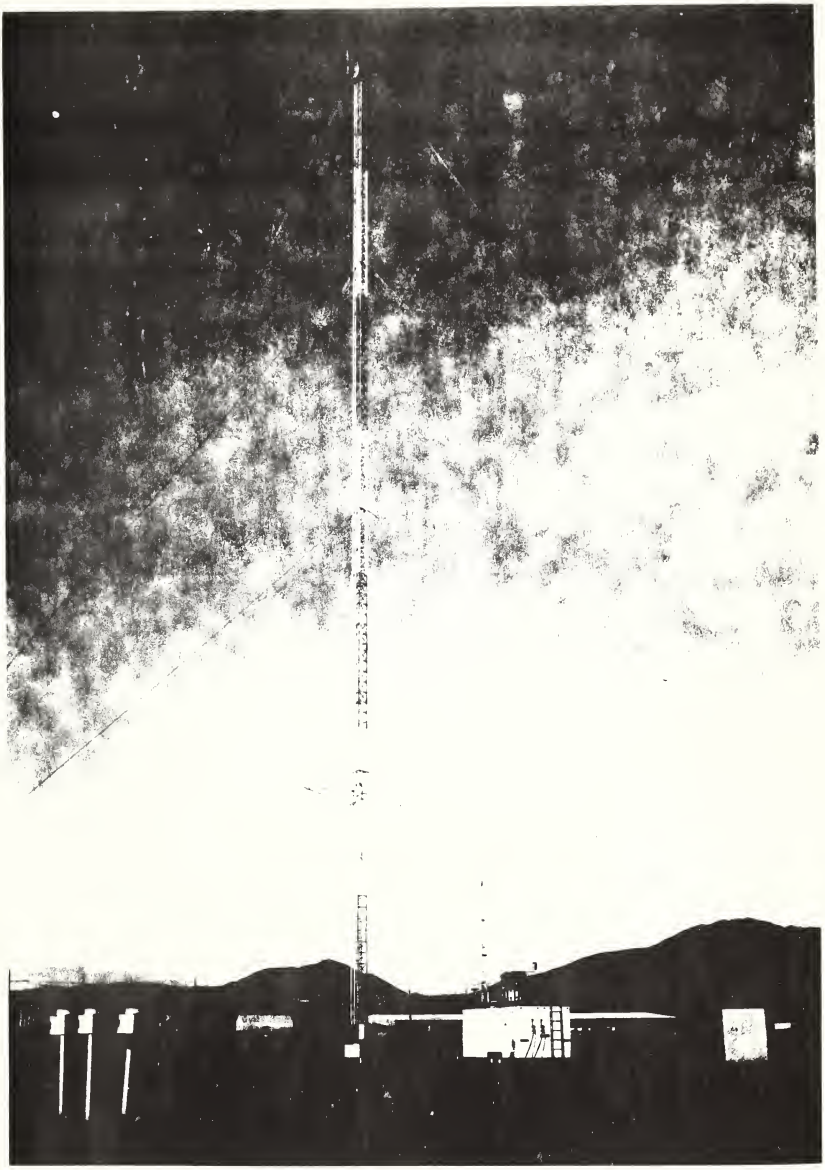

Figure 3--Pictured is the 40m meteorological tower capable of handling sensing systems at 10m and 40m to left of tower are acid rain sampling buckets. To right of tower are mobile unit and acoustic radar enclosure.

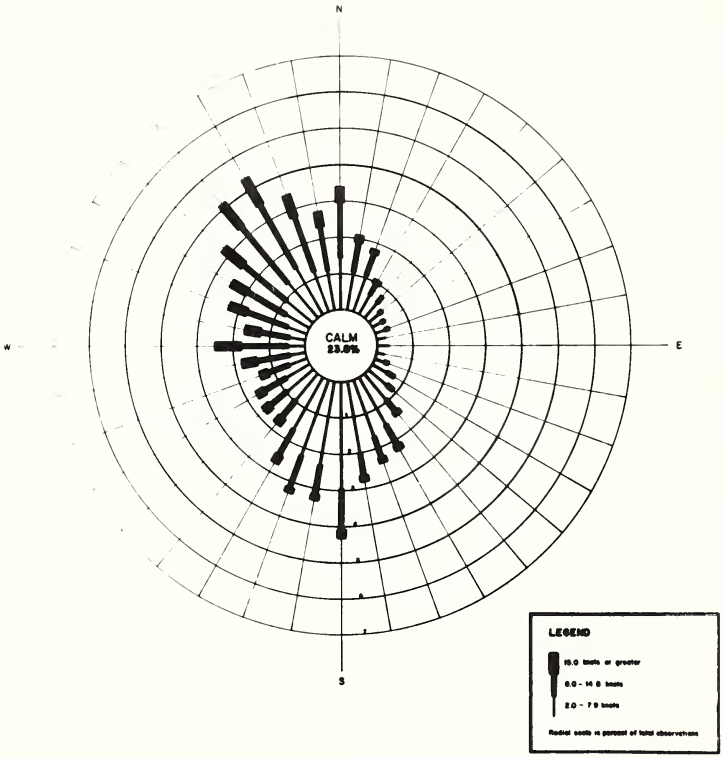

Figure 4--1971-1975 wind rose using all data.

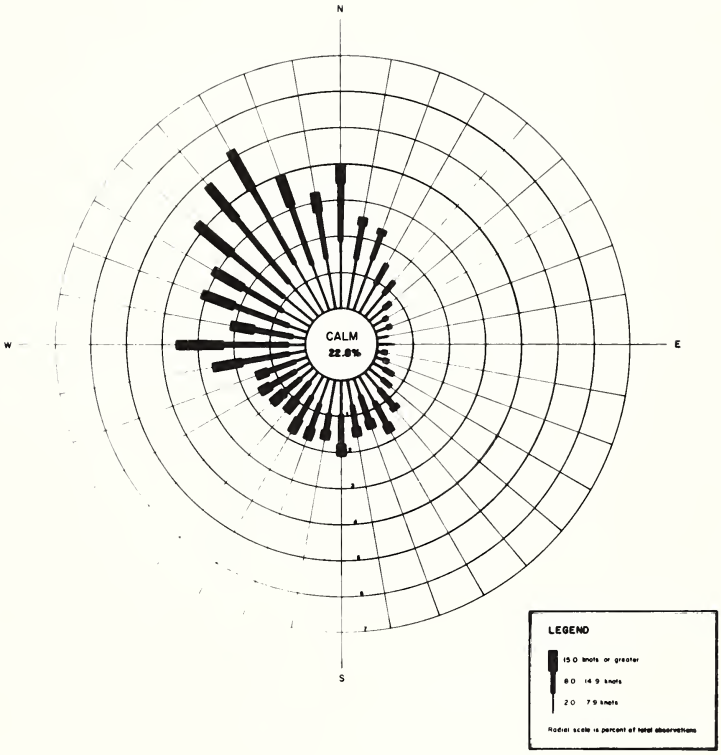

Figure 5--1971-1975 wind rose using daytime data only.

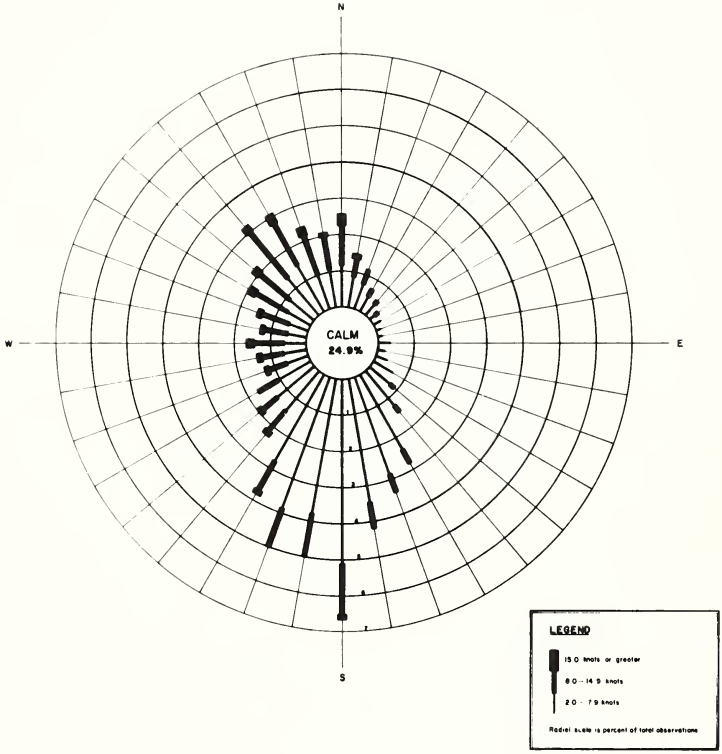

Figure 6--1971-1975 wind rose using nighttime data only.

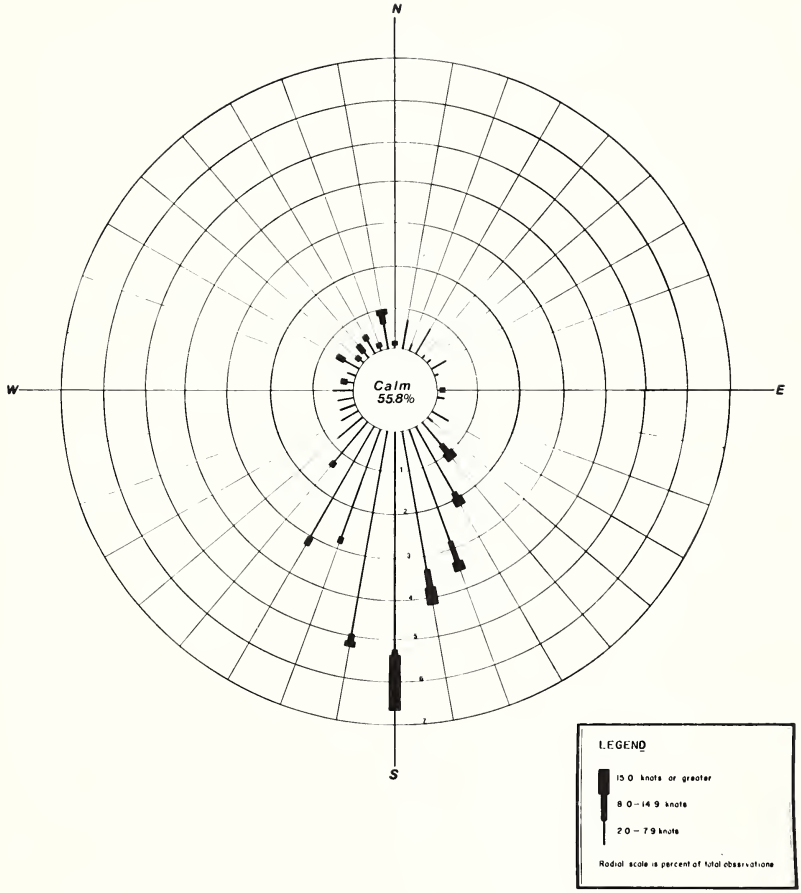

Figure 7--1971-1975 wind rose using data for 0°F and below and daytime only.

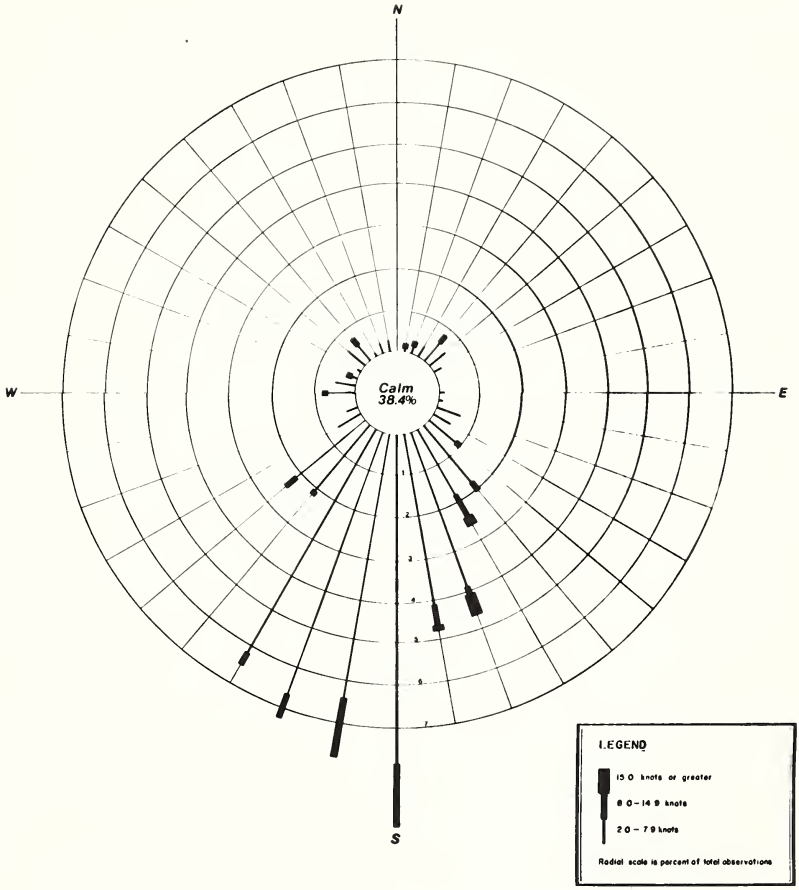

Figure 8--1971-1975 wind rose using data for 0°F and below and nighttime only.

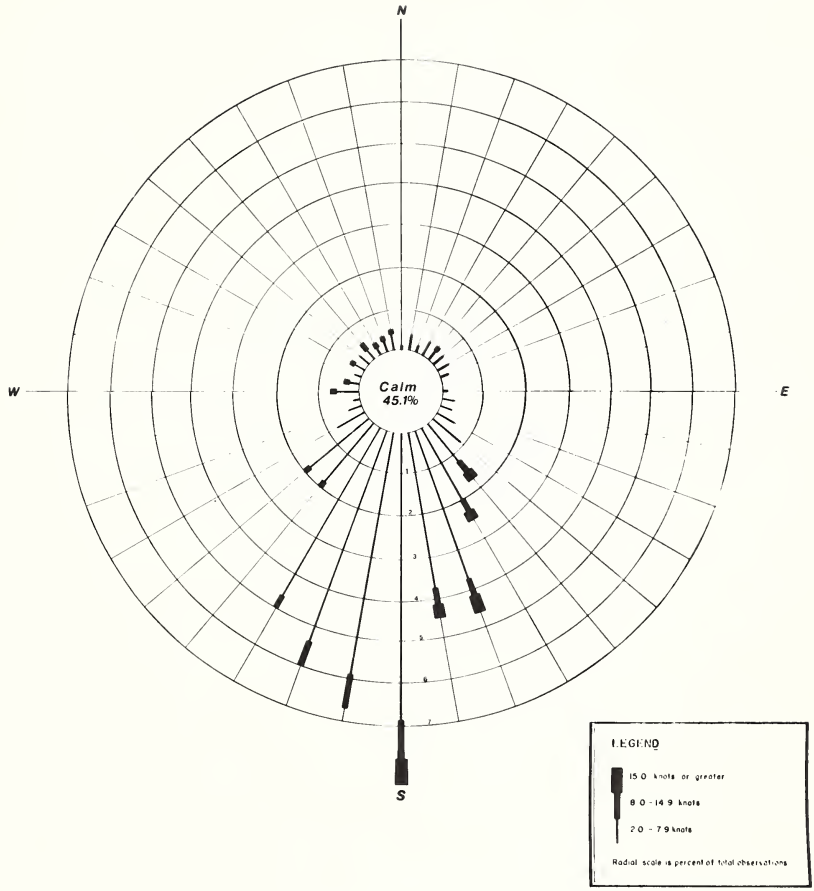

Figure 9--1971-1975 wind rose using all data for $0^{o}F$ and below.

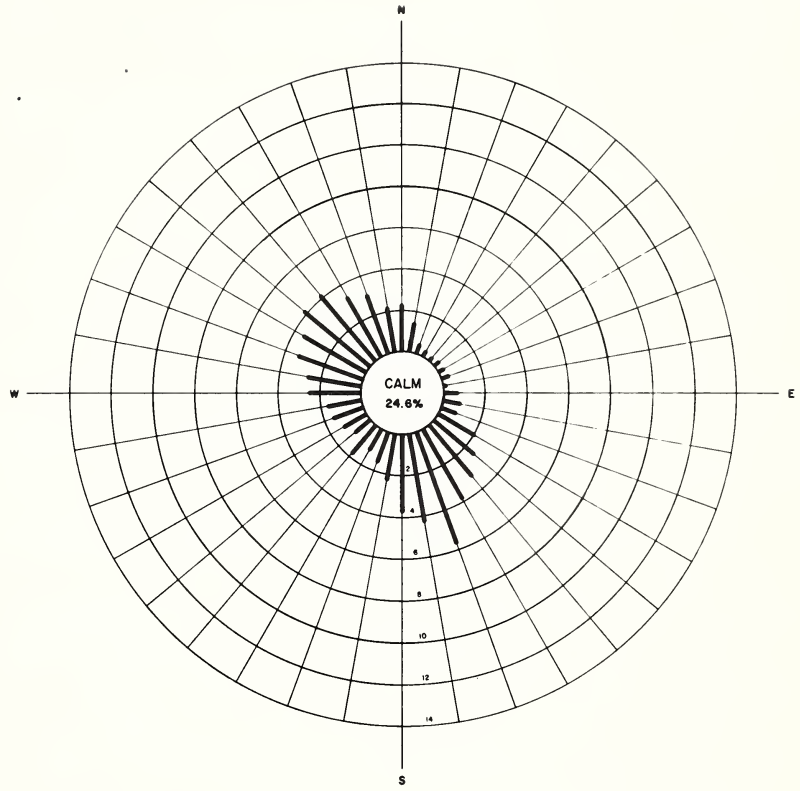

Figure 10--Winter wind rose compiled from airport data during December 1976 and January/February 1977 (Flight Service Station located at Butte, Montana)

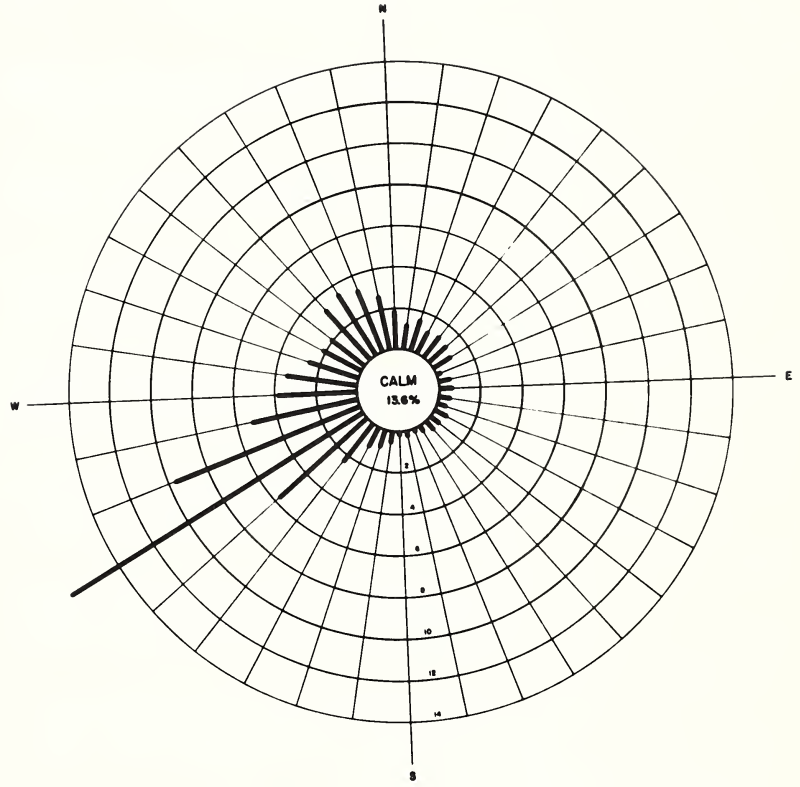

Figure 11--Winter wind rose compiled from MHD CDIF data during December 1976 and January/February 1977 (station located at Industrial Park, Butte, Montana)

Table 1--METEOROLOGICAL DATA

STATION: MET
LOCATION: 02NO7@18ACCD
ELEVATION: 1712 METERS
WIND/TEMP SENSORS AT 10 METERS
DATE: 1/21/77

TIME	SOLAR RADIATION (LY/MIN)	TEMPERATURE (C)	DEW POINT (C)	PRECIP-ITATION (IN)	BAROMETRIC PRESSURE (MB)	INTEGRATED WIND DIRECTION (DEGREES)	INTEGRATED WIND SPEED (M/S)	RESULTANT WIND SPEED (M/S)	INSTAN-TANEOUS WIND DIRECTION (DEGREES)	INSTAN-TANEOUS WIND SPEED (M/S)	SIGMA (DEG)
0000	0.00	-9.4	-13.4	0.00	830.1	240	2.7	2.5	240	2.2	21
0100	0.00	-9.9	-13.7	0.00	829.7	240	2.5	2.4	220	1.7	17
0200	0.00	-10.5	-14.0	0.00	829.1	230	1.8	1.6	240	2.8	24
0300	0.00	-10.2	-14.0	0.00	828.4	240	2.4	2.1	230	2.1	26
0400	0.00	-9.9	-14.2	0.00	828.0	240	2.2	2.0	230	1.7	23
0500	0.00	-9.3	-13.8	0.00	827.5	240	1.8	1.6	200	1.2	28
0600	0.00	-9.1	-13.9	0.00	827.0	230	2.0	1.8	220	2.6	28
0700	0.00	-8.6	-13.9	0.00	826.1	230	2.3	2.1	240	3.5	26
0800	0.00	-9.3	-13.9	0.00	825.9	230	2.3	2.1	220	3.0	21
0900	0.03	-10.0	-13.9	0.00	825.7	240	1.6	1.4	260	1.5	25
1000	0.18	-7.5	-12.4	0.00	825.9	240	1.3	1.0	160	1.0	37
1100	0.28	-5.8	-11.2	0.00	825.8	150	0.5	0.2	250	0.5	60
1200	0.36	-3.8	-9.7	0.00	825.1	180	0.6	0.2	90	1.1	66
1300	0.41	-0.7	-10.3	0.00	824.6	240	0.7	0.2	250	1.2	67
1400	0.28	-1.7	-8.7	0.00	823.5	50	0.9	0.5	210	0.5	54
1500	0.18	-0.3	-8.4	0.00	823.3	180	0.3	0.1	0	0.5	66
1600	0.13	-0.4	-9.2	0.00	823.5	30	1.0	0.7	***	0.8	46
1700	0.05	-0.8	-7.8	0.00	823.5	310	0.8	0.3	340	1.0	65
1800	0.00	-2.4	-7.4	0.00	823.9	250	1.4	1.1	250	2.1	35
1900	0.00	-3.6	-8.8	0.00	824.5	270	1.9	1.6	240	0.4	32
2000	0.00	-1.7	-8.7	0.00	825.0	250	1.7	1.4	250	2.6	36
2100	0.00	-2.2	-8.7	0.00	825.8	260	1.0	0.5	10	0.2	57
2200	0.00	-3.3	-8.7	0.00	825.4	180	1.1	0.5	330	1.5	60
2300	0.00	-3.7	-8.8	0.00	825.7	340	1.2	0.6	160	0.5	56
DAILY TOTAL	114.00**			0.00							
DAILY AVG	0.21*	-5.6	-11.1		826.0		1.5	1.2		1.5	41
STD DEV	0.13	3.8	2.6		2.4		0.7	0.8		0.9	18

* SOLAR AVERAGE IS FOR DAYLIGHT HOURS ONLY
** TOTAL LY/DAY

DAILY WIND ROSE
CALM (<.5M/S)= 4.2%
<4M/S>=4M/S
30 = 4.2% 0.0%
50 = 4.2% 0.0%
150= 4.2% 0.0%
180= 8.3% 0.0%
230=16.7% 0.0%
240=33.3% 0.0%
250= 8.3% 0.0%
260= 4.2% 0.0%
270= 4.2% 0.0%
310= 4.2% 0.0%
340= 4.2% 0.0%

Table 2--AIR QUALITY PROGRAM DATA SHEET

Precipitation Washout Sampling

Station ID Number	Met 1	
Starting Date of Sample Period	7/24/77	
Ending Date of Sample Period	7/25/77	
Starting Time of Sample Period	1:00 PM	
Ending Time of Sample Period	4:00 AM	
Date Sample Was Collected	7/25/77	
Time Sample was Collected	11:00 AM	
Field Temperature of Sample	14.4	^{o}C
Field pH of Sample	4.6	
Amount of Precipitation Collected During Sample Period	0.33	inches
Volume of Sample	1600	ml

ION CONCENTRATIONS(ppm)

Acidity	.097	Fe	16.4
Al	40	K	68
As		Mn	
Ca		Na	
Cr	4.0	Ni	4.0
Cl	.45	NO_3	.7
Co	<.1	Pb	4.0
Cu	8.8	PO_4	.02
F	.016	SO_4	1.0
		Zn	21.6

Table 3--AIR QUALITY PROGRAM DATA SHEET

Static Air Sampling

Station ID Number	Met 1	
Sampling Date	8/1 to 9/1/1977	
Exposure Days	31	
Concentrations of:		
Total SO_2	286.4	µg/plate
Total NO_2	45.0	µg/plate
Flouride from Ca Formate	17.9	µg/plate
Flouride of Na Formate	3.0	µg/plate

Comments:

Calcium Formate #1= 16.0
Calcium Formate #2= 16.8
Calcium Formate #3= 21.0

Calcium Formate BIK= 0

Table 4--AIR QUALITY PROGRAM DATA SHEET

High Volume Air Sampling
Whatman #41 Filter

Station ID Number	Met 1
Date	7/28/77
Filter Number	100096
Q_{std}	43.08 cfm
Initial Time (t_i)	33501.2
Final Time (t_f)	34918.9
Total Particulate Weight	32.8 mg/paper

Concentrations of:

Al	650	µg/paper	Hg		µg/paper
As		µg/paper	K	300	µg/paper
B		µg/paper	Mg		µg/paper
Be		µg/paper	Mn	15	µg/paper
Benzene Sol		µg/paper	Mo		µg/paper
Bi		µg/paper	Na		µg/paper
Ca		µg/paper	Ni	30	µg/paper
Cd		µg/paper	Pb	110	µg/paper
Cl		µg/paper	Sb		µg/paper
Co		µg/paper	Se		µg/paper
Cr	< 5	µg/paper	Sn		µg/paper
Cu	750	µg/paper	SO_4		µg/paper
F	5	µg/paper	V		µg/paper
Fe	900	µg/paper	Zn	50	µg/paper

Table 5--AIR QUALITY PROGRAM DATA SHEET

High Volume Air Sampling
Whatman #41 Filter

Station ID Number	Met 1
Date	7/30/77
Filter Number	100097
Q_{std}	43.11 cfm
Initial Time (t_i)	34952.8
Final Time (t_f)	36397.0
Total Particulate Weight	42.3 mg/paper

Concentrations of:

Al	900	µg/paper	Hg		µg/paper
As		µg/paper	K	300	µg/paper
B		µg/paper	Mg		µg/paper
Be		µg/paper	Mn		µg/paper
Benzene Sol		µg/paper	Mo		µg/paper
Bi		µg/paper	Na	1100	µg/paper
Ca	1000	µg/paper	Ni	25	µg/paper
Cd		µg/paper	Pb		µg/paper
Cl		µg/paper	Sb		µg/paper
Co	9	µg/paper	Se		µg/paper
Cr		µg/paper	Sn		µg/paper
Cu	600	µg/paper	SO_4	1178	µg/paper
F		µg/paper	V		µg/paper
Fe	1250	µg/paper	Zn	110	µg/paper

Table 6--AIR QUALITY PROGRAM DATA SHEET

Dust Fall Sampling

Station ID Number	Met 1	
Sampling Date	8/1 to 9/1/1977	
Exposure Days	31	
Concentrations of:		
Solubles	12.5	mg/jar
Insolubles	6.5	mg/jar
Total	19.0	mg/jar

Concentrations of:

Al	12.5	µg/jar	Hg		µg/jar
As	.292	µg/jar	K	125	µg/jar
B		µg/jar	Mg		µg/jar
Be	<.001	µg/jar	Mn	10	µg/jar
Benzene Sol		µg/jar	Mo		µg/jar
Bi		µg/jar	Na		µg/jar
Ca		µg/jar	Ni	25	µg/jar
Cd	<.01	µg/jar	Pb	<.1	µg/jar
Cl		µg/jar	Sb		µg/jar
Co	<.1	µg/jar	Se	<.001	µg/jar
Cr	<.1	µg/jar	SO_4		µg/jar
Cu	26.25	µg/jar	Sn		µg/jar
F		µg/jar	V		µg/jar
Fe	175	µg/jar	Zn	77.5	µg/jar

Table 7--AIR QUALITY PROGRAM DATA SHEET

High Volume Air Sampling
Fiberglass Filter

Station ID Number	Met 1	
Date	7/28/77	
Filter Number	000098	
Q_{std}	43.08 cfm	
Initial Time (t_i)	32130.5	
Final Time (t_f)	33548.7	
Total Particulate Weight	36.1	mg/paper

Table 8--AIR QUALITY PROGRAM DATA SHEET

High Volume Air Sampling
Fiberglass Filter

Station ID Number	_____	
Date	_____	
Filter Number	_____	
Q_{std}	_____	
Initial Time (t_i)	_____	
Final Time (t_f)	_____	
Total Particulate Weight	_____	mg/paper

Table 9--AIR QUALITY PROGRAM DATA SHEET

Impingers Sampling

Station ID Number	Met 1	
Sampling Date	7/28/77	
Exposure Days	24 hours	
Concentrations of:		
Total SO_2	210	µg/exposed sample
Total NO_2	19.2	µg/exposed sample

Table 10--AIR QUALITY PROGRAM DATA SHEET

Impingers Sampling

Station ID Number	_____	
Sampling Date	_____	
Exposure Days	_____	
Concentrations of:		
Total SO_2	_____	µg/exposed sample
Total NO_2	_____	µg/exposed sample

TASK S_1

MHD CDIF Pre-Operational Biological Baseline Surveillance Program

R. Portch, J. Cornish, S. Bentsen,
M. Griffin, D. Dolenc, and T. Pelletier

ABSTRACT

The pre-operational biological baseline surveillance program (PBBSP) was established in late May 1977. The goal of the PBBSP under Task S_1 was to initiate and carry forward an environmental research program capable of quantifying the potentially adverse impact of the CDIF trace element emissions on the surrounding biological communities within the general Butte, Montana area.

A preliminary "minimum but adequate" terrestrial-aquatic monitoring program is being implemented to accomplish the above goal. This preliminary program is being formulated in a manner that will allow development of a comprehensive monitoring design applicable (with possible modifications) to either the ETF location or other MERDI-MHD related research programs.

I. OBJECTIVE AND SCOPE OF WORK

Trace element biological monitoring is one phase of the MHD total ambient environmental surveillance program (TAESP). In this phase, the ERDA/CEQ requires that MHD engineering technology development be monitored continually and simultaneously for potentially adverse environmental impact. As stated in the Environmental Development Plan, "the immediate establishment of a detailed environmental research program is essential to maximize the chances of the availability of appropriate environmental data for informed decisions on commercialization, environmental standards, control technologies, and other mitigating measures."[1] Although the MHD CDIF will not reflect the conditions existing in the ETF or in the commercial process necessarily, it is MERDI's intention to produce an increasingly refined biological monitoring system. This would include improved sampling-analytical techniques and increasingly valid experimental design based on MHD CDIF data (gathered before, during, and after completion of its operation) that can be adopted readily to the larger MHD facilities.

The objective of the MHD CDIF surveillance is to provide the initial data base necessary to eventually allow a comprehensive study of trace element cycling in terrestrial-aquatic environments influenced by various anthropogenic pollutants. The end products would allow a disentangling of pollutant effects from the naturally occurring geographic variation of the target trace elements and general ecosystem dynamics. This will require accurate knowledge of the natural biogeographic variance including past human impact on the study area.

The PBBSP study will assume the "worst case" potential of chronic adverse impact[2] on the biogeochemical environment surrounding the CDIF as a result of its potential trace element emissions. The delineation-quantification of such effects from those previous acute anthropogenic impacts[3] (as determined by natural vs. existing vegetation patterns) remains uncertain; it is the responsibility of the PBBSP under Task S2 to accomplish this quantification of biological community response to the MHD CDIF potentially adverse trace element loading effects.

II. SUMMARY OF PROGRESS TO DATE

The progress of the PBBSP for the fourth quarter of FY 77 can be found in the milestone chart in Table 1 of the appendices; details of the separate phases of the program are given below.

A. Terrestrial

Candidate sampling areas have been located and inspected (i.e., "ground-truth" review) to determine their suitability for inclusion in the monitoring program. Specific site selection (within each candidate area) and consequent procurement of local land owner permission for such site access and use is underway. A review of the existing and proposed sampling sites and this quarter's data has been completed with changes, as warranted, being implemented in the study's sampling design.

B. Aquatic

Site selection and procurement of permission from local land owners for location of aquatic sampling sites has been completed. A review of existing sites and consequent data generated this quarter has been completed with changes, as warranted, being made.

C. Public Health

Data acquisition for the public health report for Butte and its environs is near completion. Final (i.e., FY 75) data banking sheets are on order from the Montana Department of Health and Environmental Sciences, Records Bureau, located in Helena. When received, the report will be finalized (up to 1976) and promulgated to the Records Bureau and to the Butte-Silver Bow County Health Department for inspection and review.

D. Trace Ion Analysis

Analytical progress for samples obtained from terrestrial and aquatic sites has been minimal; however, all samples not analyzed yet have been preserved and stored in MERDI's laboratory bureau. The subcontractor for this analytical work has informed MERDI that analysis of the CDIF-related samples is proceeding as scheduled. MERDI personnel currently are reviewing the analytical program in terms of economic cost-benefit factors in order to maximize-optimize this critical phase of the PBBSP at the current levels of funding.

III. DETAILED DESCRIPTION OF TECHNICAL PROGRESS

A. Work Accomplished

1. Terrestrial Study

The review of both meteorologic and emission inventory data to determine the general areas of CDIF emissions impact is almost complete.[4] The resulting preliminary sampling areas are defined in Figure 1. Past trace element studies in the vicinity of nonferrous smelters[5] and conventional coal-fired power plants[6,7] have demonstrated a considerable variance in their areas of trace element burdening. Mercury has a wide pattern of dispersal[8] according to Klein and Russell; thus, several "control" sites more distant from the CDIF ($\geq$ 8 km. downwind) will be included. At present, these will be located at or near the Moulton Reservoir (T4N, R7W) and the Basin Creek Reservoir (T1N, R8W) aquatic monitoring sites.

Plant species inventory lists[9] gathered at the existing sites have been updated and are included on a site-by-site basis in Table 2.

2. Aquatic Study

a. Surface water

Selected sampling sites on the three major drainage patterns (see Figure 2) have been reviewed; sites from Barry[10] and MERDI[11] will be utilized. They are delineated by drainage as follows:

1) Basin-Little Basin Creeks

a) S_6--Upper Basin Creek before confluence of Little Basin Creek and Basin Creek.

Latitude-Longitude: 45° 54' N, 112° 30' W

Topographical Map: Butte, South, Sec. #19

This is a perennial stream fed by intermittent feeder rivulets and overflow from the Basin Creek Reservoir.

Water Use: livestock

b) S_4--Little Basin Creek, NW of confluence of Little Basin Creek and Basin Creek.

Latitude-Longitude: 45° 55' N, 112° 30' W

Topographical Map: Butte, South, Sec. #18

The Little Basin Creek drainage, although intermittently flowing in late summer, is a major tributary of Basin Creek.

Water Use: livestock

c) S_{11}--Lower Basin Creek, 100 m. north of runway at airport, south of Elizabeth Warren Way.

Latitude-Longitude: 45° 57' N, 112° 29' W

Topographical Map: Homestake, Sec. #32

This site is above the confluence with Blacktail Creek and after the confluence with the Sand Creek bypass.

Presumed Water Use: livestock

2) Blacktail-Little Blacktail Creeks

a) S_7--Upper Blacktail Creek at base of Thompson Park in Deer Lodge National Forest.

Latitude-Longitude: 45° 54' N, 112° 27' W

Topographical Map: Homestake, Sec. #22

This site is located on the main Blacktail Creek drainage, originating north and west of the Continental Divide in Deer Lodge National Forest.

Water Use: recreational purposes

b) S_8(F)--Little Blacktail Creek at "Beaver-Human Dam" and NE of confluence with Blacktail Creek.

Latitude-Longitude: 45° 54' N, 112° 27' W

Topographical Map: Homestake, Sec. #22

A perrenial tributary to Blacktail Creek, with lowest levels in August and September. The surrounding area currently is being developed with individual homes constructed on ca 0.4 to 2 hectare lots.

c) S_9--Lower Blacktail Creek, east of LDS Church on East Four Mile Road at culvert on south side.

Latitude-Longitude: 45° 57' N, 112° 28' W

Topographical Map: Homestake, Sec. #4

The site is located on Blacktail Creek before its confluence with Basin Creek.

Presumed Water Use: livestock

3) Sand Creek

a) S_1--NNW of CDIF site in a gully entering Sand Creek.

Latitude-Longitude: 45^{o} 55' N, 112^{o} 30' W

Topographical Map: Butte, South, Sec. #18

This site presently is dry but during operation of the CDIF, it could be a source of potential surface runoff or pond discharge.

b) S_2--ENE of CDIF site, west of RR tracks, labeled as discharge two from CDIF site.

Latitude-Longitude: 45^{o} 55' N, 112^{o} 30' W

Topographical Map: Butte, South, Sec. #18

This site presently is dry but during operation of the CDIF, it could be a source of potential surface runoff or pond discharge.

c) S_3--Sand Creek, North of CDIF site.

Latitude-Longitude: 45^{o} 56' N, 112^{o} 30' W

Topographical Map: Butte, South, Sec. #7

This site, located on the main drainage of Sand Creek, is subject to seasonal flow (e.g., storm runoff and snow melt). Sand Creek is channeled via a drainage ditch to Basin Creek, north of the CDIF and south of Holy Cross Cemetery, entering Basin Creek before Station S_{11}.

Water Use: unknown

The biological, chemical, and physical data gathered to date from the surface water sites are shown in Figures 6, 7, 8, 9, and 10.

b. Impounded water

Outside of the eight-kilometer radius of the CDIF location are two "control" stations intended to monitor possible wide-ranging trace ion emissions.[8] The first, G (see Figure 2), is located at the second holding dam below the Basin Creek Reservoir (which serves as a portion of the water supply for the city of Butte, Montana). This pool is accessable (courtesy of Butte Water Company) and usually has a steady flow from the reservoir year around. The second, E (see Figure 2), is located at the outfall from a beaver dam on Yankee Doodle Creek. The water flows from the Moulton Reservoir and is approximately 50 m. upstream from the intake for the Butte Water Company supply line.

The above two stations, E and G, have a two-fold use as sampling sites: 1) the watersheds should collect any potential trace element fallout that is dispersed widely from the MHD CDIF, and 2) therefore allow the PBBSP personnel to monitor for adverse trace ion concentrations in the municipal water supply for the city of Butte, Montana. This could allow monitoring of health hazards caused by the MHD CDIF operations on the potable water supply.

Site H (see Figure 2) is not situated on any of the three major surface drainage patterns designated in the study area. It is, however, a "sink" for the general area's groundwater flow and surface runoff because of its elevation (relative to the surrounding topography). The sampling site was located within the Butte Wildlife and Bird Sanctuary, a marshy area near Maryland and Majors streets in Butte.

The biological, chemical, and physical data gathered to date from the above impounded sites are shown in Figures 11, 12, and 13.

c. Groundwater(s)

Two sites have been selected (see Figure 3) for analysis of the above bio-chemical-physical parameters as was done for the surface water samples. The first, $S_5(I)$, is registered by John Krause with the Montana Bureau of Mines and Geology (MBMG); the 50-foot deep well (37 feet to groundwater) is located at 45^{o} 54' N latitude, 112^{o} 31' W longitude from the Butte South topographical map, Section #19. The registered land owners are Paul, Mary, and Bill Gozden. The water is used largely for domestic and livestock watering purposes.

The second, $S_{10}(J)$, located at 45^{o} 56' 14" N latitude, 112^{o} 31' 01" W longitude (within Section #8 of the above topographical map) is registered with the MBMG by Mr. L. Webster. The well is 134 feet deep (72 feet to groundwater) and is used by Mr. Webster for domestic water supply purposes.

The biological, chemical, and physical data gathered to date are shown in Figures 14 and 15.

3. Public Health Study

Progress continues to be made on the acquisition of human morbidity and mortality statistics (e.g., male vs. female, white vs. non-white, 0-64 years vs. $\geq$ 65 years) for Silver Bow County; limited data also has been obtained for regional livestock mortality figures. The available data to date have been collated in a manner similar to the format found in Appendix B of Reference 9. Records of local livestock and crop pathologies statistics have been included whenever available. A search

and review program of the relevant public health literature is being planned currently with initiation of the search phase beginning by late October 1977.

4. Trace Ion Analysis

Preliminary analytical results from the June aquatic sample set has been received from our subcontractor, the Mineral Research Center, Industrial Park, Butte; the data can be found in Table 3. At present, no terrestrial soil or plant samples have been processed or analyzed chemically.

B. Discussion

1. Terrestrial Study

In the process of reviewing the previous documentation[12,13] pertaining to the terrestrial site selection rationale, it became apparent that emphasis was placed on biotype variance (e.g., grassland vs. deciduous biomes--Figure 4) rather than on potential sensitivity to CDIF emissions impact. Comparison of William Barry's broadleaf and/or sage-juniper areas against those locations impacted by either past industrial activities or extrapolated air pollution meteorologic patterns (see Figure 5) imply that both sites (B and D) have been, or continue to be, disturbed by trace element emissions. It has been evaluated that such pollution effects were of sufficient magnitude to overshadow any CDIF emission-induced biological change in these two sites.

Until comprehensive data on the CDIF trace element emission characteristics, as well as a detailed model of the study area's airflow patterns become available, the PBBSP will employ methodologies largely developed for the study of air emission impacts arising from conventional coal-fired systems. The fundamental aspects of such hypothesis are given below.

a) The normal indigenous trace element concentrations might be elevated overtime as the result of cummulative CDIF emissions impact on the surrounding environment. The determination of this impact will be a function of accuracy in sample site selection and sensitivity of the given analytical methods in response to the existing environmental conditions.

b) The resulting trace element "loading," or accumulation, might be sufficient to change the ecological fate[14] of the naturally (or previously) occurring levels (e.g., a shift in a given element's pool size or changes in its rate of transfer-cycling between producer-herbivore trophic levels).

c) The added burden of CDIF trace elements might be of sufficient magnitude on the study area's vegetation to continue the elimination of sensitive native plant species. The present grazing disclimax or zootic climax condition would

continue to remain during the CDIF operation's lifetime, with possible increases in the percent occurrence (per unit area) of weedy annual plant species.

As suggested by Dr. Barry,[13] transect and/or quadrat methods were employed at the four terrestrial sites (see Figure 4); the site specific details are discussed below.

a) Site A, Thompson Park: Mature Pseudotsuga menziesii (douglas fir) were somewhat aggregated in the SE½ (25 m^2) and E½ (50 m^2) of the sampling plot at Site A. Reproduction was spotty, tending to be concentrated in the NE¼ and surrounding tree #7 in the SW¼. The near absence of Pinus contorta (lodgepole pine) seems to imply that this area has not been disturbed grossly (e.g., by fire) in the recent past. Mechanical disturbance (namely, trampling from recreational use) apparently has influenced the herbaceous phenologic characteristic. Vandalism also has necessitated the removal of the particulate air sampler located in the sampling vicinity.

   A partial list of the local flora, determined by Barry[9] and addended by biology technician Susan Bentsen, can be found in Table 2A. No quantitative vegetational analysis was accomplished at the site.

b) Site B, Woodville Hill: The sample area was located initially, and the corner boundaries were marked with survey stakes; a string grid pattern (1m intervals) was imposed on the area within the defined bounds. The results of the July 21, 1977 inspection revealed a slightly aggregated, approximately even-aged stand of Populus tremuloides (aspen) as overstory, being above the herbaceous groundcover growing in abundant leaf litter. The combined repeated vandalism and inappropriate site location necessitated the discontinuance of sampling after September 8, 1977. The flora list of Barry,[9] addended by Bentsen, can be found in Table 2B. No quantitative data relating to vegetational structure or composition is available for this site.

c) Site C, Grassland Site: A 1m^2 quadrat was located permanently and then sampled on June 22, July 12, and July 18, 1977. Inspection of the field notes revealed a sparse community apparently dominated by Agropyron spicatum (bluebunch wheatgrass) and Stipa comata (needle and thread grass). The forbs appear to show a slight seasonal phenologic dominance--i.e., Allium cernuum (nodding onion), Linaria vulgaris (butter and eggs), Achillea millefolium (yarrow), and probably Lupinus leacopsis (lupine); Chrysothamnus nauseosus (rubber rabbitbrush) was not flowering at the time of the above observation periods. The presence of human refuse within and nearby the quadrat site implied that this area has and continues to be disturbed by human activity. The flora list of Barry[9] which was addended by Bentsen can be found in Table 2C. The data was not in a form suitable for vegetational analysis; however, an

analysis can be extrapolated by reviewing the results of the heavily grazed sites 7, 8, and 9 from Paul Sawyer's study[15] of the local grassland types. Such an interpretation would suggest a native Agropyron spicatum: Festuca idahoensis (Idaho fescue) community for Site C, contrary to Barry's estimation of it as being a grass-sage vegetation type.

Minimal damage was exacted on the particulate fallout air sampler despite its visibility from the Basin Creek Road; however, the filter paper was contaminated by orthinogenic excretions.

d) Site D, Williamsburg: A $1m^2$ quadrat was located on this site with floristic analysis (lists) being compiled on June 23, July 18, and July 29, 1977. The area is sparsely populated by the apparently dominant species: Artemisia tridentata (big sagebrush) and Poa compressa (Canada bluegrass). Centaurea maculosa (spotted knapweed) appears to be a subdominant within the plot although it is widespread throughout the study site area. The flora list of Barry,[9] addended by Bentsen, can be found in Table 2D. No quantitative analysis or interpretation of the flora data is possible because of its form of collection.

The following sections (e, f, g, and h) are vegetative descriptions of four of the aquatic sampling sites.

e) Site E, Yankee Doodle Creek: The presence of tangled riparian vegetation growing above the water's surface level eliminated the use of quadrat sampling at this site. The stream-side shrub strata included (but was not limited to) Salix exigua (willow species), Rosa woodsii (rose species), and Rubus sp. (raspberry). The herb layer included Streptopus amplexifolius (twisted stalk) and Epilobium angustifolium (fireweed). The emergent flora included a genus of rush, Juncus, while duckweed (tentatively identified as a Lemna species) was included in the lotic flora. The list accumulated by Barry,[9] and addended by Bentsen, is given in Table 2E. Again, the data's quantity and format was insufficient for valid quantitative-statistical analysis.

f) Site F, Little Blacktail Creek: A partially immersed $1m^2$ quadrat was located at this site on June 23, 1977. The quadrat represents a microhabitat within an impounded portion-section of the creek. The riparian flora includes Populus trichocarpa (black cottonwood) and Salix sp. (willow species) among the overstory-shrub strata overlying a semi-mesic grassland herb layer. A successive floristic inventory on July 12 and 28, August 18, and September 7 revealed a general physiognomic replacement of Juncus balticus by Agrostis tenuis; this change in the community "structural dominance" appears to correspond with the observed drop of the surface water level. The destruction of the dam at Site F, with consequent drainage of the

impounded water to a lower level on or about September 8, 1977 caused the outfall-sample site to become dewatered. Thus, barring repair of the impoundment, a change in community type is expected, possibly an Agropyron spicatum-Festuca spp. (fescue) association.

The flora list of Barry,[9] as addended by Bentsen and Portch, can be found in Table 2F.

g) Site G, Basin Creek: The area's macrohabitat appears to be a Pseudotsugu menziesii-Populus tremuloides (douglas fir-aspen) association with a small number of maturing Pinus contorta (lodgepole pine) scattered throughout the stand. The shrub strata along the margin of the pond includes Alnus tenuifolia (alder) and Salix sp. (willow).

A partially immersed quadrat was established on July 13, 1977; the quadrat remained partially immersed throughout the observation period (July 13, August 17, and September 7) despite the reduction in surface water elevation. Numerous genera of composites (compositae), grasses (Gramineae), and thistle (Cirsiuum sp.) largely composed the terrestrial portion of the quadrat community. Several grass genera, most apparently Hordeum jubartum (foxtail barley) and Mentha arvensis (mint),extended into the emergent zone, their range corresponding to the seasonal reduction of the pond's water level.

The floristic list of Barry,[9] as addended by Bentsen and Portch, can be found in Table 2G.

h) Site H, Butte Wildlife and Bird Sanctuary: The macrohabitat can be described as a semi-artificial swamp with both standing and flowing water. Populus trichocarpa (black cottonwood) trees form the overstory, while the shrub strata includes both willow and rose species. Equisetum (horsetail) and Typha latifolia (cattails) dominate the emergent flora, with scattered Carex sp. (sedge) colonies throughout the area.

A partially immersed $1m^2$ quadrat was established on June 23, 1977 and observed on this date as well as on July 12 and 28, August 18, and September 9, 1977. A number of grass genera (e.g., Agropyron, Hordeum, Elymus, Agrostis) dominate the terrestrial portion of the quadrat. Mentha arvensis (mint) and Carex (sedge) species occupy the seasonally influenced soil-water transition zone, while scattered clumps of cattails occupy the emergent habitat. The quadrat was vandalized on or about August 18, with destruction of the cattail and sedge colonies very evident.

The floristic list of Barry,[9] as addended by Bentsen and Portch, can be found in Table 2H. No quantitative analysis of the data was attempted because of its insufficient volume and unappropriate format.

2. Aquatic

The tabulated aquatic site data has been converted to graphical form as presented in Figures 6 through 15; the preliminary nature of the generated data allows little more than a superficial discussion. The parameters listed per site were determined via standardized Hach Chemical Company procedures,[9] whether they were performed in the laboratory or in the field.

The five sampling periods listed in the above figures have been judged to be insufficiently small to allow statistical analysis or comments on the area's general water quality. However, the present and continuing improvement of laboratory instrumentation and facilities will increase both accuracy and precision of the given analytical determinations. It is hoped that the population size of the sample data will be large enough to document trends in water quality before the March quarterly report.

The aquatic flora, and especially the "water quality index species" of the Cyamophyta and Chlorophyta, have not been identified yet. The necessary facilities for the taxonomic work currently is being assembled with initiation of "keying" the sampled populations within the coming quarter.

Preliminary electronic data processing systems capable of handling the aquatic parameters have been initiated and should be operational when required to store the generated aquatic (and terrestrial) data as discussed in Exhibit 1 (Appendix).

3. Public Health

The Quality of Life Program was initiated by Dr. William Barry on June 6, 1977. The epidemiological data gathered by Tom Pelletier and Susan Bentsen have two interrelated purposes: 1) to protect the community of Butte from any adverse affects arising from the operation of the CDIF (e.g., the induction of any unanticipated pathology such as skin or bladder cancers from the trace element emissions), and 2) to consequently protect the facility and/or MERDI from spurious law suits arising from the potential problems noted in 1.

Information for the data accruement program is proceeding on schedule, with a summary report being prepared by the end of November 1977.

4. Trace Ion Analysis

The analytical work on all sample materials remains in a preliminary phase, with completed analysis limited to the aquatic samples gathered in June. At present, the cost-benefit economic analysis of the MRC analytical program (as found in the PBBSP files) has induced a reconsideration of sample analysis (e.g., the construction of comprehensive "in-house" laboratory facilities or the possible recontracting of the work to another organization, hopefully with the state of Montana).

C. Work Forecast

1. Terrestrial

As suggested by Dr. Barry,[13] a transect-quadrat methodology will be employed at each of the selected sampling areas; however, the sampling distance gradient (from the CDIF) will be more variably scaled.[16] The conifer Site A should receive greater pollution impact and thus serve as a more sensitive CDIF-emission indicator if moved to the vicinity of Terre Verde (approximately 5800 feet, msl) 1½ statute miles ESE of the facility. The yearly minimum inversion height is 400 meters;[17] thus, a sensitive measurement of fumigation impact must occur at elevations ≤6800 feet (above msl). Despite W. C. Hill's stated (yet hypothetical) grassland-conifer biotype transition at approximately 6500 feet,[18] inspection of both true color and infrared photographs of the Terre Verde site reveals the presence of coniferous tree species. Thus, this site would satisfy the characteristics of Barry's Site A. Also, a relocation of Site D to the lower slopes-foothills region ESE of Timber Butte would approximate Barry's sage-juniper community type as well as be more sensitive to CDIF-emission impact(s).

The criteria applied toward the selection of candidate terrestrial (and aquatic) study areas, as well as their general location (to the nearest section of a given township and range), is given in the PBBSP September progress report.[16] Detailed site descriptions will be listed in the PBBSP October progress report as soon as the present negotiations over land owner lease or easement agreements are procured. The October report will emphasize detailed terrestrial-aquatic sampling and analytic methodology; it is hoped that an appendix will be attached to such a report listing the preliminary data (as a means of validating-testing the methods). It is planned to gather detailed field data throughout the coming fall (i.e., through mid-December). The emphasis of the PBBSP then will shift to the static moss sampling-analysis system[16] until mid-March, with resumption of the full program at that time. The PBBSP program has been designed to collect approximately 1½ years (i.e., two summer periods of growth) of terrestrial-aquatic data before the anticipated initiation of CDIF operations in December 1978. The resulting data from the CDIF "impacted" vs. "background" sites then can be analyzed statistically to judge (or determine) the relative intersite emission(s) impact. A graphical or schematic presentation of change in trace ion concentrations to observed changes in biological community structure or function overtime could be mapped. Ideally, this "graphical" approach then could serve as a model in the design of an even more comprehensive (and sensitive) monitoring program applicable to the ETF site or elsewhere.

2. Aquatic

The parameters given in Figure 6 will continue to be sampled on a three-week frequency as is done at present,[10] while water and aquatic trace ion content will be sampled every six weeks. All parameters (including the target trace elements) will be determined on a more frequent basis once the CDIF becomes operational. Table 4 represents the first quarter's status of the PBBSP; as shown in the table, all deficiencies will be corrected by December 1977. Such delays in the

research progress resulted largely from the initial inertia involved with the "start up" of the program (e.g., the establishment of methods and purchase of the necessary facilities before data was generated).

3. Public Health

The final (or summary) report of this phase of the PBBSP will be completed by the end of October 1977. Reviews in June or July of 1978 for the priority or need for this program currently are anticipated.

4. Trace Ion Analysis

The sampling frequency mentioned in Part 2 (above) will continue throughout FY 78. The anticipated improvement and expansion of MERDI laboratory facilities for the PBBSP will allow greater diversification of the program into other research problems in the energy field.

IV. CONCLUSIONS

A. Terrestrial

This quarter, the laying-creation of the necessary technical "groundwork" for the establishment of a "minimum but adequate," yet sufficiently defensible, PBBS Program was accomplished. The data gathered to date was neither of sufficient size nor form to allow valid statistical analysis; thus, no quantitative conclusions can be made.

B. Aquatic

During this quarter, a defensible[4] sampling program was initiated. As is the case above, the data does not allow scientifically valid conclusions to be put forth; however, the anticipated progress of this phase of the PBBSP will allow the establishment of a quantified water quality baseline.

C. Public Health

Conclusions for this phase of the PBBSP will be given in the final report (November 1977).

D. Trace Ion Analysis

The present data is insufficient for statistical analysis; at this time, the critical review of past methods of analysis (for the target trace ion suite) as well as the source of the analyses if being undertaken.

LITERATURE CITED

1. U.S. Energy Research and Development Administration, Environmental Development Plan (EDP), September 1977.

2. J. E. Blodgett, Ecosystem Effects of Environmentally Dispersed Pollutants in O. E Teague (chm.), Effects of Chronic Exposure to Low-Level Pollutants in the Environment, Subcommittee on the Environment and Atmosphere, Committee on Science and Technology, U.S. House of Representatives, 94th Congress, First Session, U.S. Government Printing Office, Washington, D.C., November 1975.

3. Ronald D. Tasky, Soil Contamination at Anaconda, Montana: History and Influence on Plant Growth, Unpublished M.S. thesis, University of Montana, School of Forestry, 1972.

4. James E. Cornish and Rodney W. Portch, A Review and Critique of Previous Pre-Operational Baseline Biological Surveillance Program Siting Rational, Draft Interim Progress Report, Engineering Division, Montana Energy and MHD Research and Development Institute, prepared for ERDA, Report No. 319:77108, 1977.

5. Marilyn J. Buchauer, "Contamination of Soil and Vegetation Near a Zinc Smelter by Zinc, Cadmium, Copper, and Lead," Environmental Science and Technology, 7(2):131-5, 1973.

6. Barbara M. Anderson, John R. Keith, and Jon J. Conner, "Antimony, Arsenic, Germanium, Lithium, Mercury, Selenium, Tin, and Zinc in Soils of the Powder River Basin," pp. 50-57, in source 11, 1976.

7. Helen L. Cannon and Vernon E. Swanson, Contributions of Major and Minor Elements to Soils and Vegetation by the Coal-fired Four Corners Power Plant, San Juan County, New Mexico, USDI, Geological Survey Open File Report 75-170, 1975.

8. David H. Klein and Phillip Russell, "Heavy Metals: Fallout Around a Power Plant," Environmental Science and Technology, 7(4):357-8, 1973.

9. William T. Barry, MHD CDIF Pre-Operational Baseline Biological Surveillance Program, Draft Interim Progress Report, the Montana Energy and MHD Research and Development Institute, Report No. 3F19:77N08, July 1977.

10. William T. Barry, Pre-Operational Baseline Biological Surveillance Program Plan for the MHD CDIF, Draft Interim Progress Report, the Montana Energy and MHD Research and Development Institute, Report No. 3F19:77N06(2), June 1977.

11. The Montana Energy and MHD Research and Development Institute, Basic Environmental Data for the CDIF and Butte Vicinity, Draft Interim Report, Task Q, 3H19:77N1, December 1976.

12. William T. Barry, Pre-Operational Baseline Biological Surveillance Program Plan for the MHD CDIF, Draft Interim Report for ERDA, 3F19:77N02, February 1977.

13. William T. Barry, MHD CDIF Pre-Operational Baseline Biological Surveillance Program--Procedures and Data Manual for Field and Laboratory Investigations, Draft Topical Report for ERDA, 3F19:77NO7, July 1977.

14. G. M. Woodwell, "Effects of Pollution on the Structure and Physiology of Ecosystems, Science 168:429-422, 1970.

15. Paul Sawyer, "Preliminary Report of Plant Community Studies in the Butte Vicinity," Appendix 3-A, Baseline Environmental Data for the CDIF and Butte Vicinity, prepared for ERDA, 3H19:77NO1, January 1977.

16. James E. Cornish and Rodney W. Portch, Terrestrial and Aquatic Site Selection Criteria and Preliminary Sampling Parameters and Methods, prepared for ERDA, September 1977, 319:77I09.

17. Gilbert Associates, Incorporated, Montana MHD Component Development and Integration Facility, Siting Survey, prepared for ERDA, Office of MHD, GAI Report No. 1895, Reading, Pennsylvania, Table 3-2, 1975.

18. William Calvin Hood, Weathering of Butte Quartz Monzonite near Butte, Montana, Unpublished Ph.D. thesis, Department of Geology, Montana State University, Missoula, 1963.

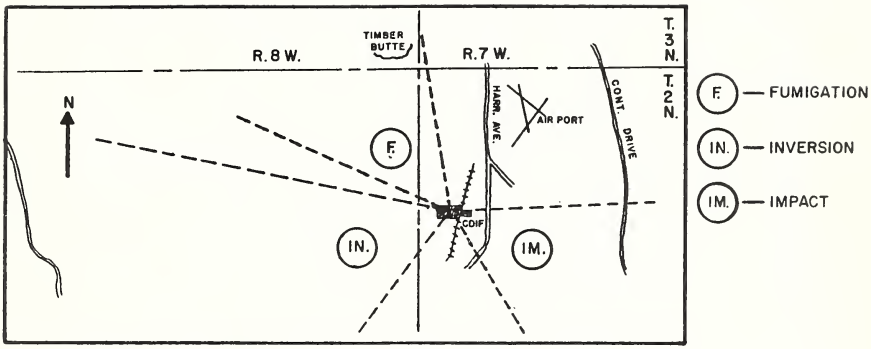

Figure 1. Characterization of Trace Element Sampling Areas (Deerlodge N.F., Butte Ranger District, Base 1967 Forest Series Map)

(1) Fumigation (F) - NNW to N. of the CDIF site, being largely contained within sections 35 and 36 in T3N, R8W and sections 1 and 2 in T2N, R8W.

(2) Impact (Im) - E to ESE of the CDIF site, being largely within sections 15-17, 20 and 21 of T2N, R7W.

(3) Inversion (In) - WSW of the CDIF site, being largely within sections 13, 23-7 of T2N, R8W.

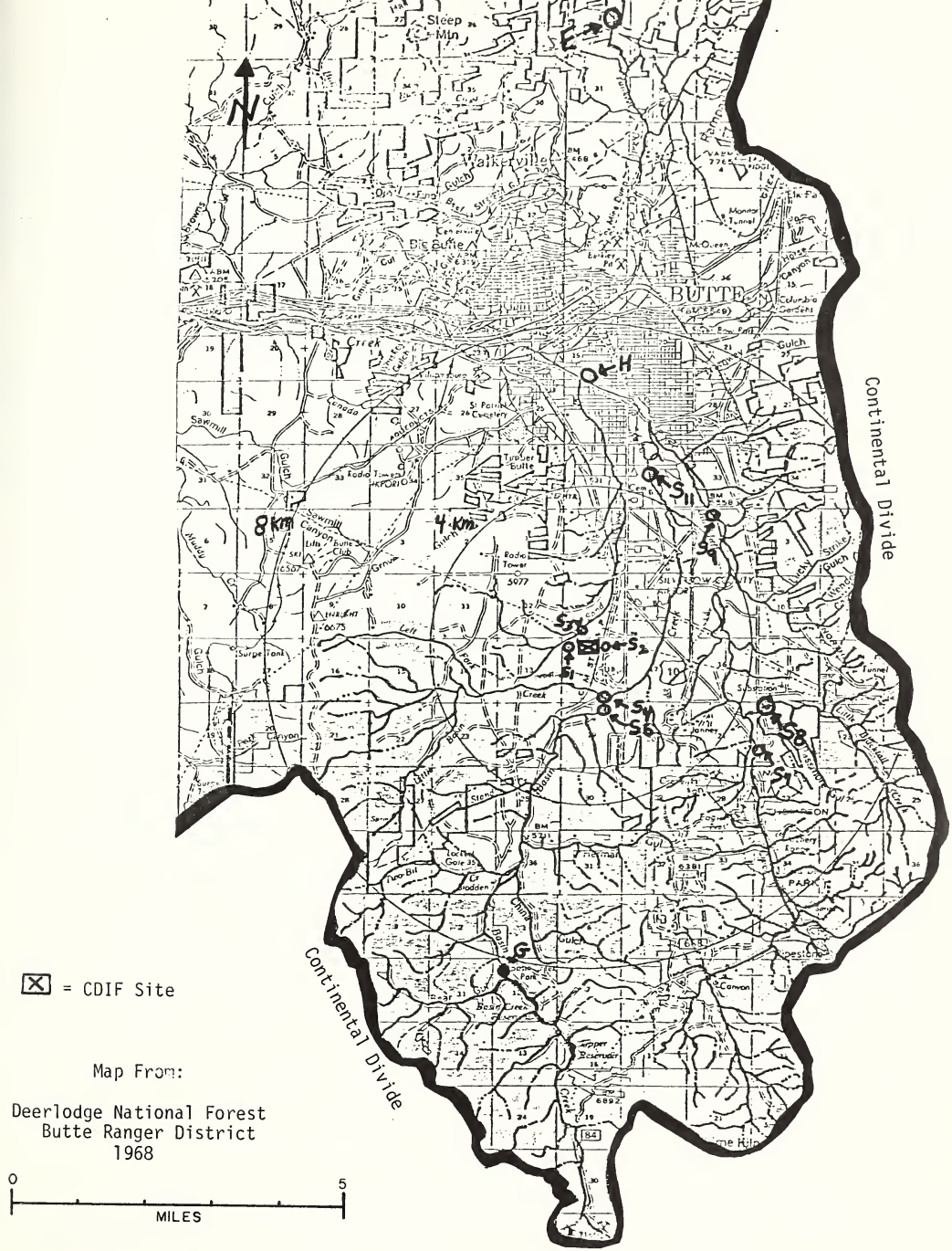

Figure 2.--Location of Aquatic Sampling Sites

Figure 3.--Site locations of the Groundwater Sampling Wells.

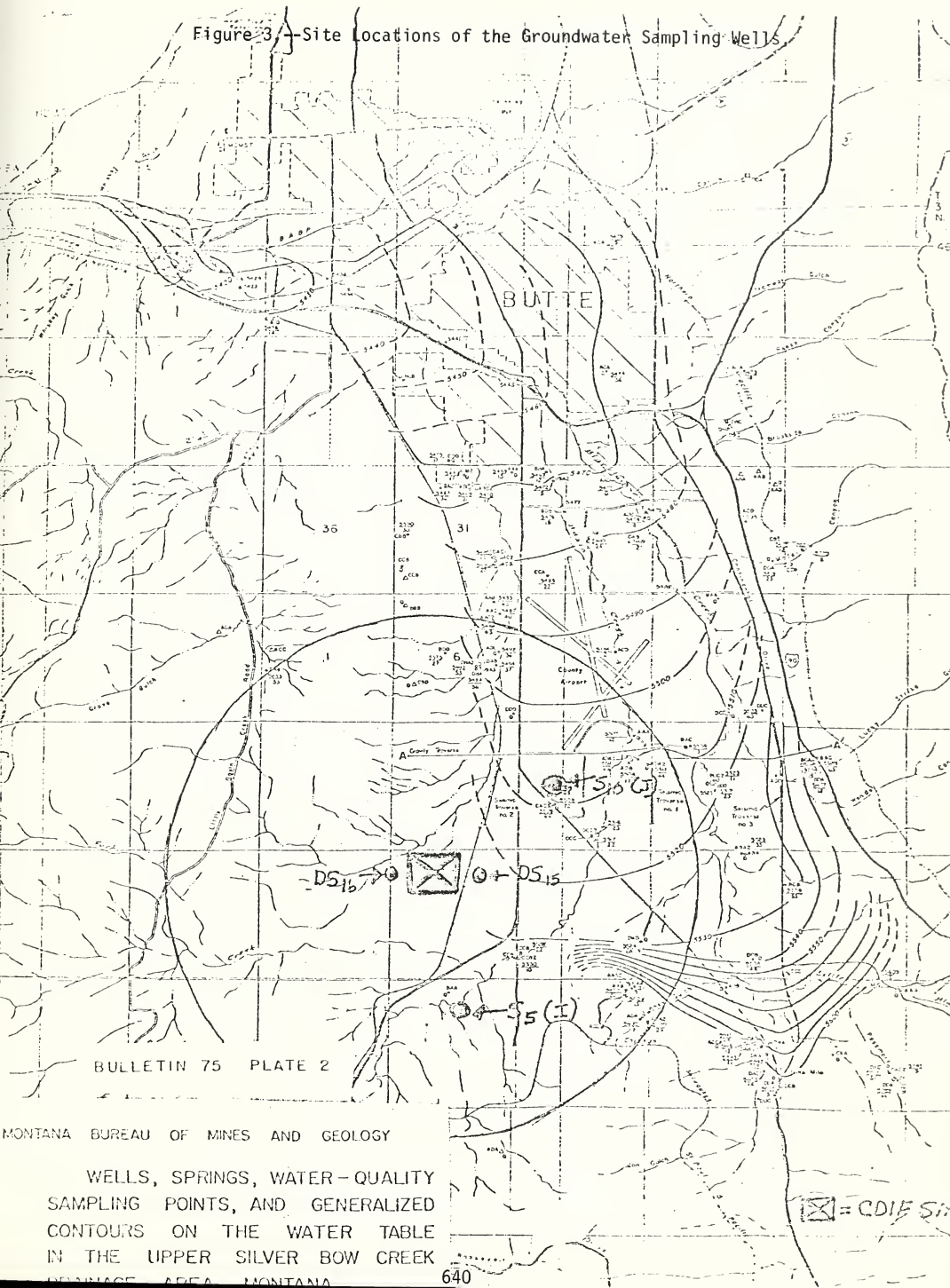

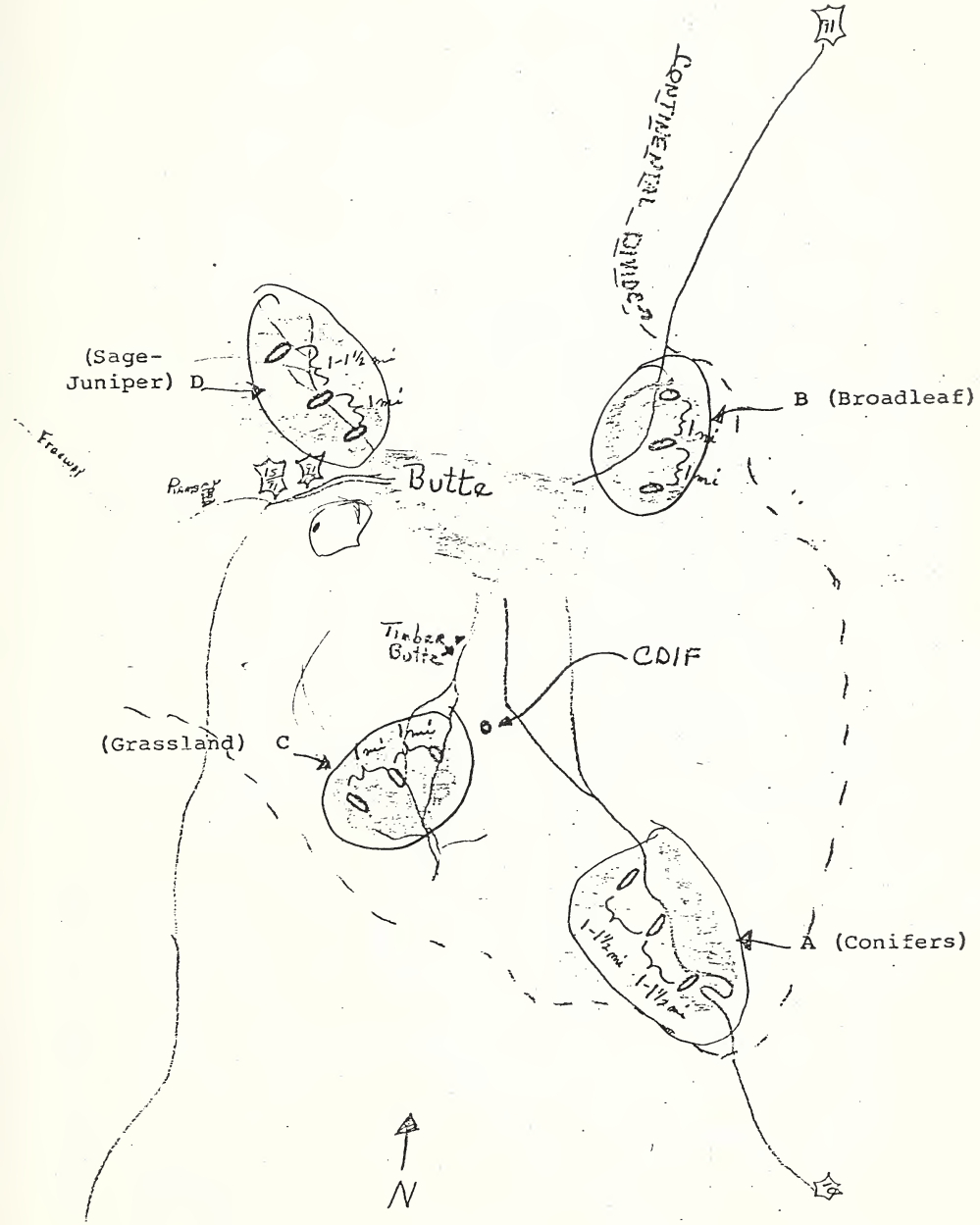

Figure 4.--Terrestrial Sampling Biotypes in the Study Area as Determined by W. T. Barry[13]

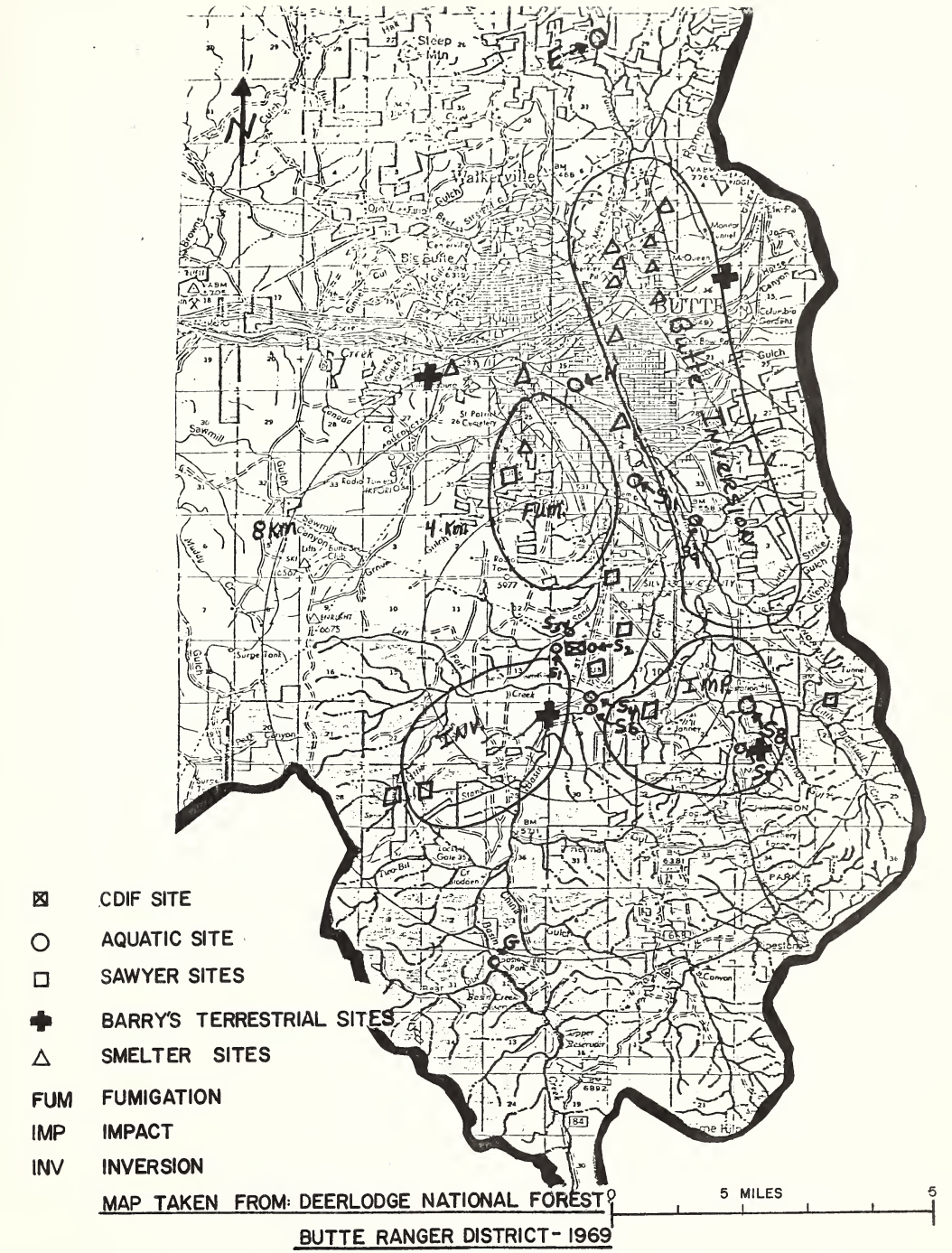
N
Steep Mtn
Walkerville
Big Butte
BUTTE
Creek
Sawmill
Gulch
8 Km
4 Km
FUM.
IMP.
INV.
S1
S2
S3
S4
S5
S6
S7
S8
S9
S10
S11
S12
S13
S14
S15
S16
S17
S18
S19
S20
S21
S22
S23
S24
S25
S26
S27
S28
S29
S30
S31
S32
S33
S34
S35
S36
S37
S38
S39
S40

FIGURE 6. GRAPHICAL PRESENTATION OF THE SITE S-6 DATA
BACTERIAL COUNTS
UPPER BASIN CREEK' SITE S-6

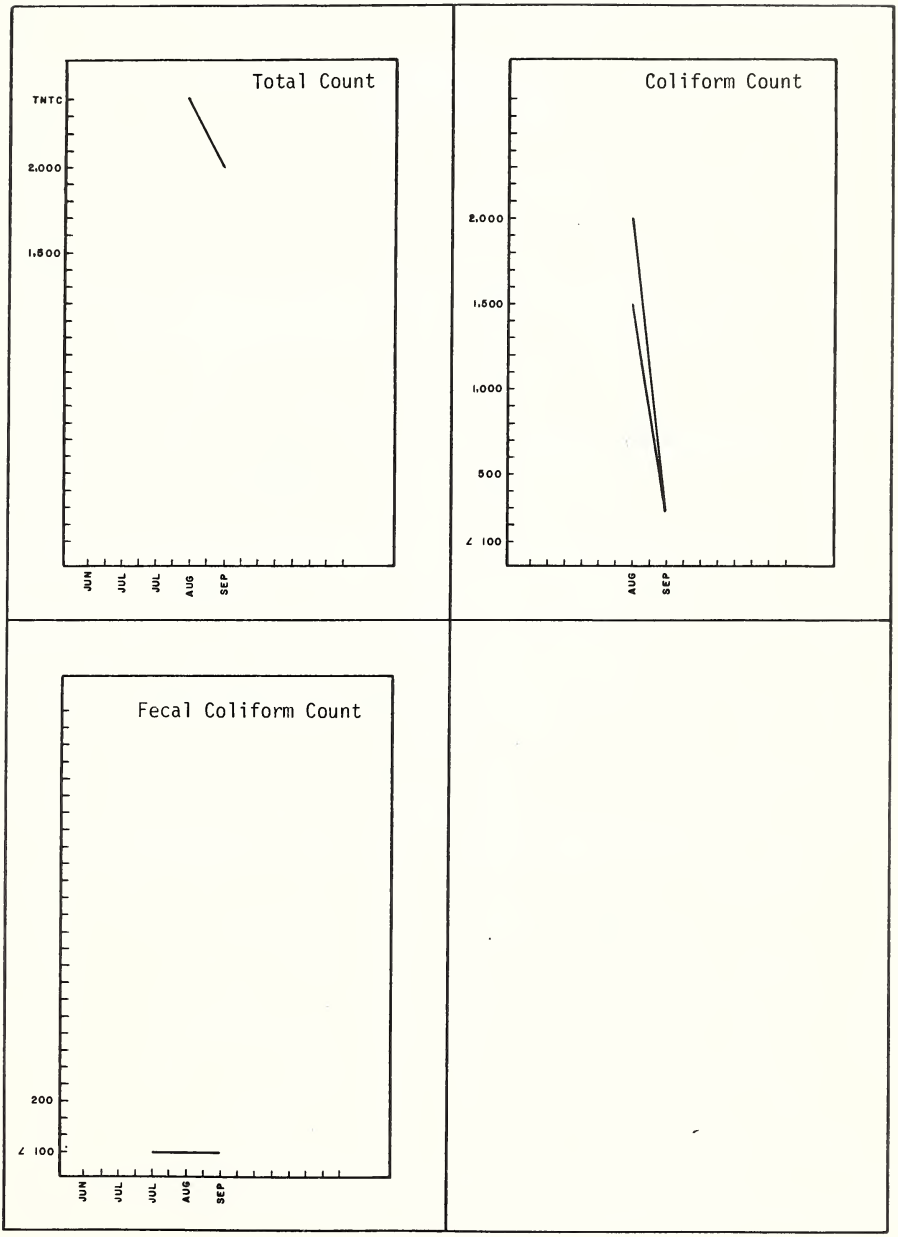

CHEMICAL DATA
STATION S-6
UPPER BASIN CREEK

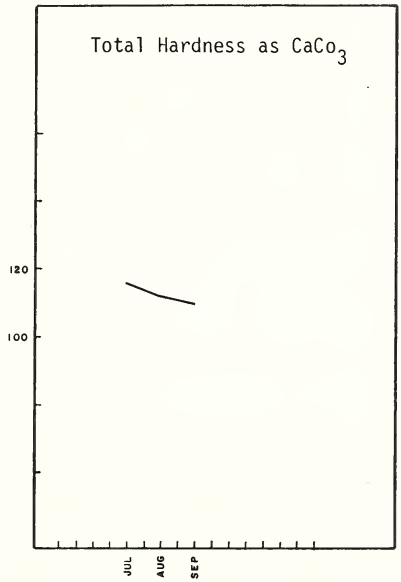

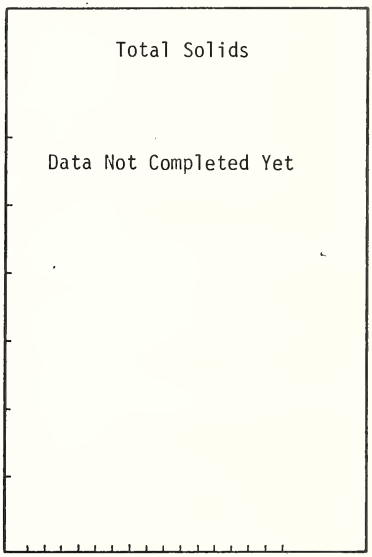

Concentration in PPM

Sampling Dates

CHEMICAL DATA
STATION S-6
UPPER BASIN CREEK

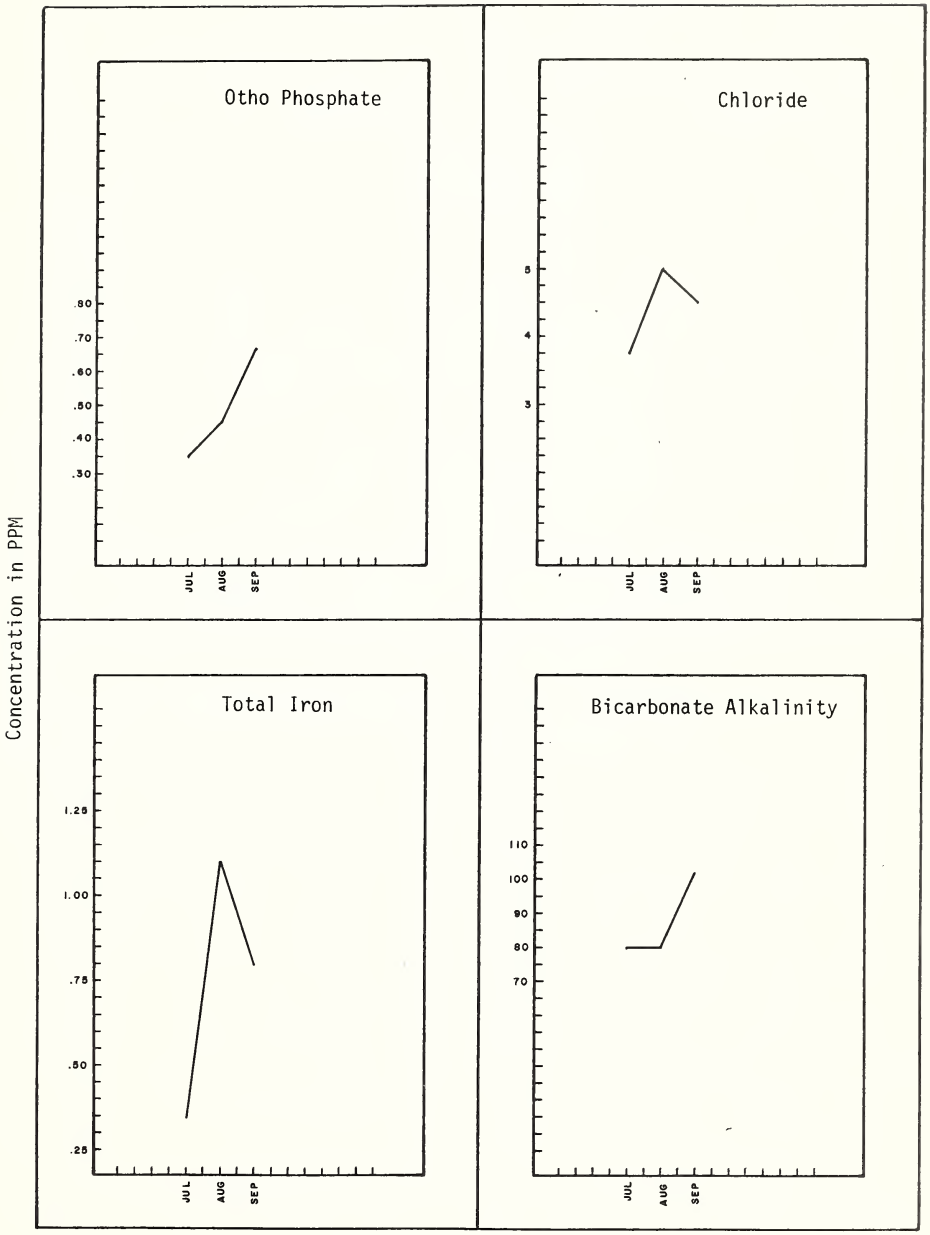

Concentration in PPM

Sampling Dates

FIGURE 7. GRAPHICAL PRESENTATION OF THE SITE S-11 DATA
BACTERIAL COUNTS
LOWER BASIN CREEK SITE S-11

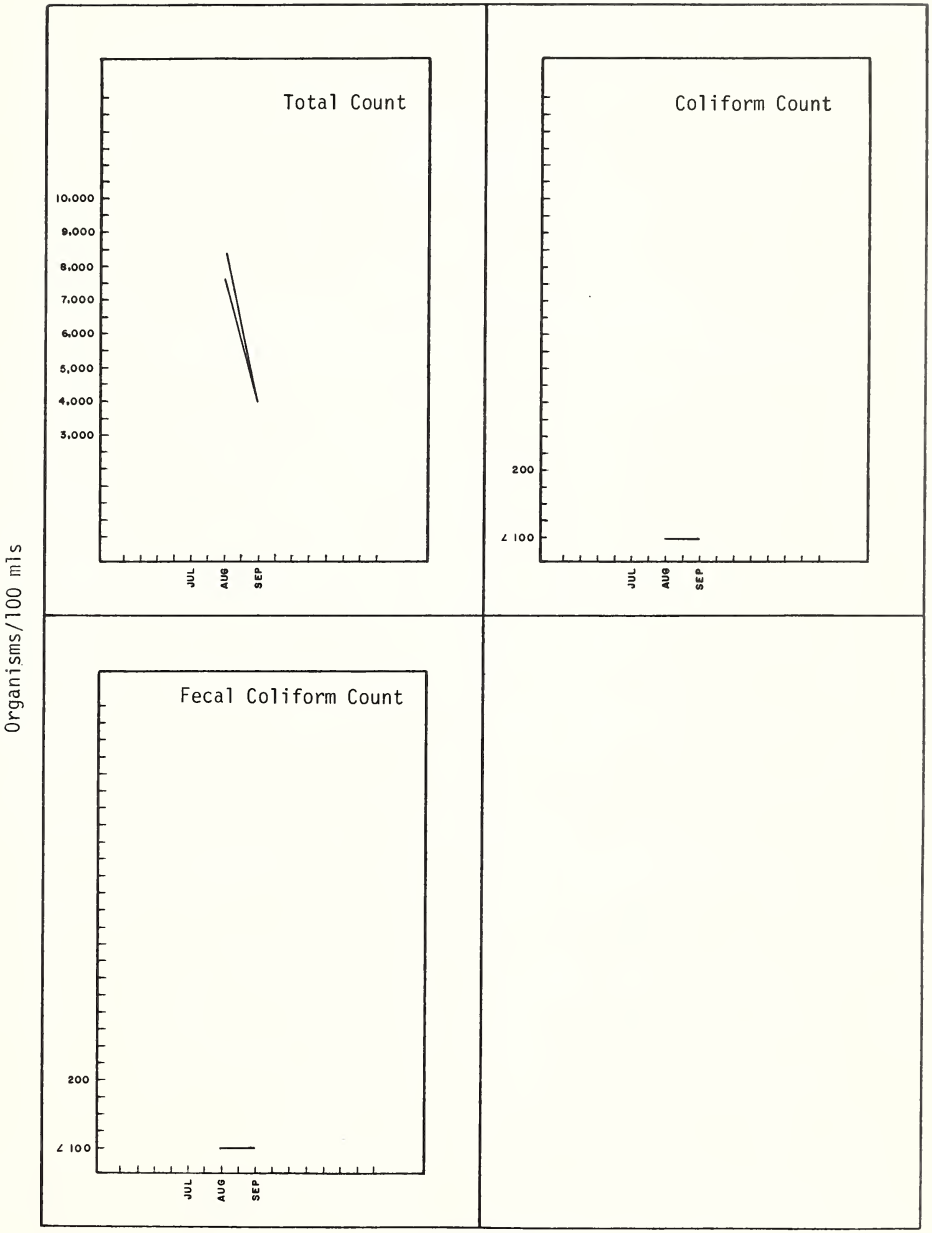

CHEMICAL DATA
STATION S-11
LOWER BASIN CREEK

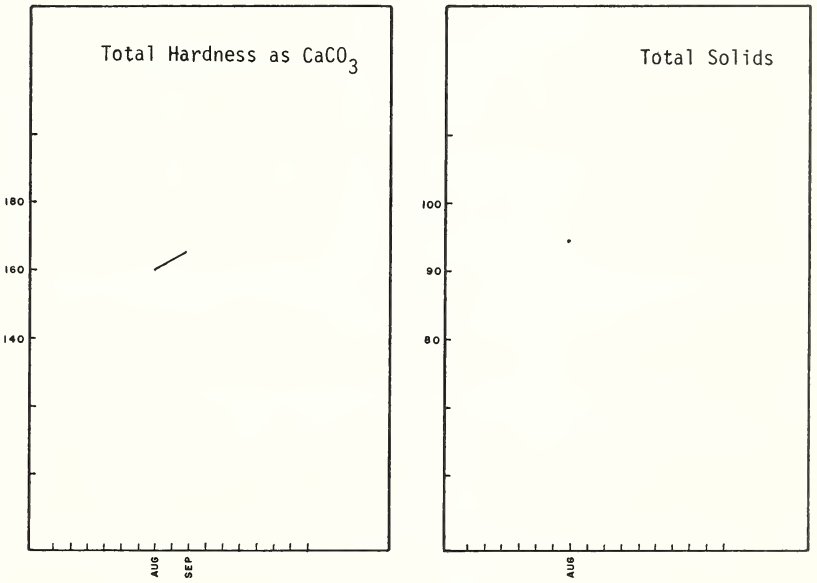

Concentration in ppm

Sampling Dates

CHEMICAL DATA
STATION S-11
LOWER BASIN CREEK

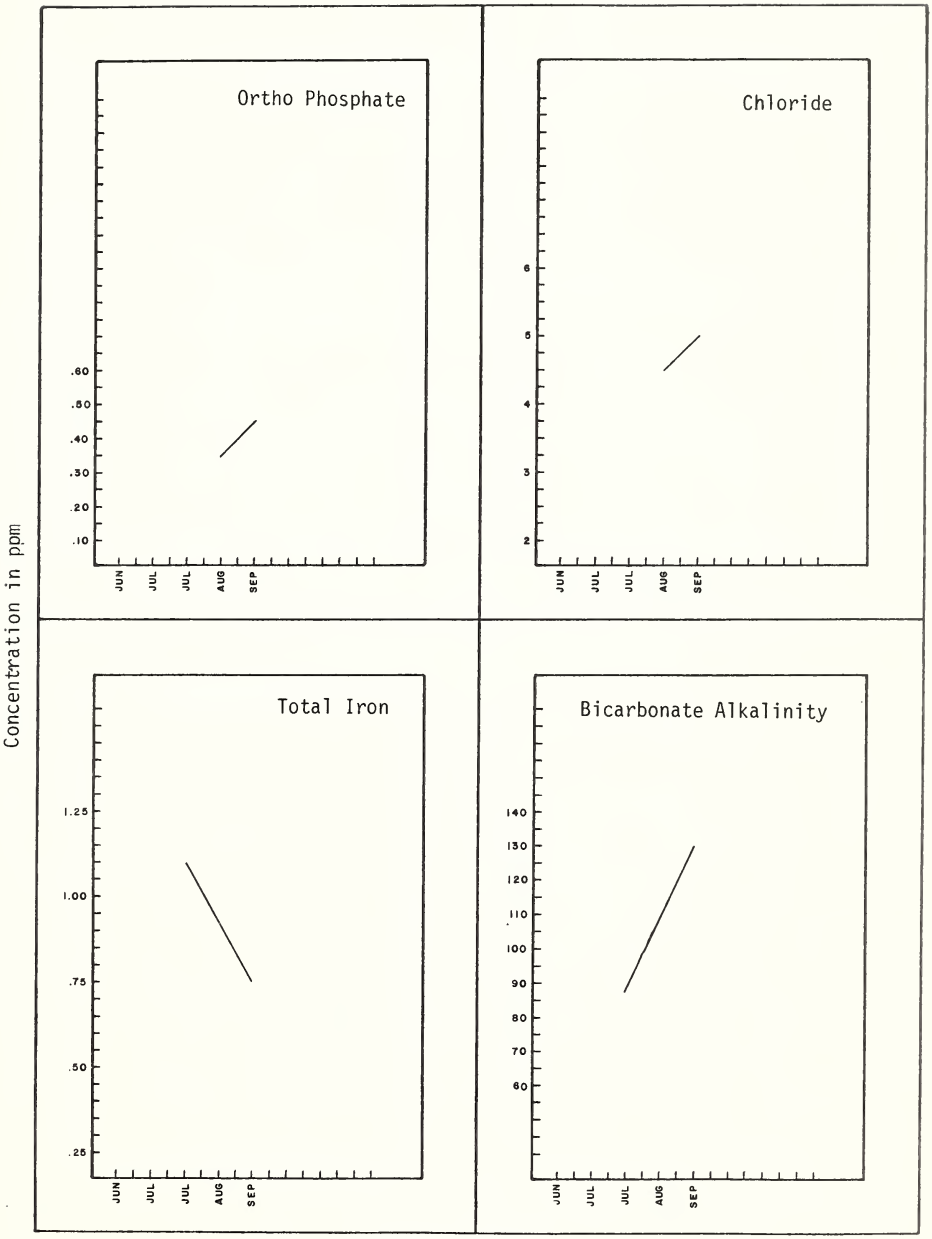

FIGURE 8. GRAPHICAL PRESENTATION OF THE SITE S-7 DATA

BACTERIAL COUNTS

UPPER BLACKTAIL CREEK SITE S-7

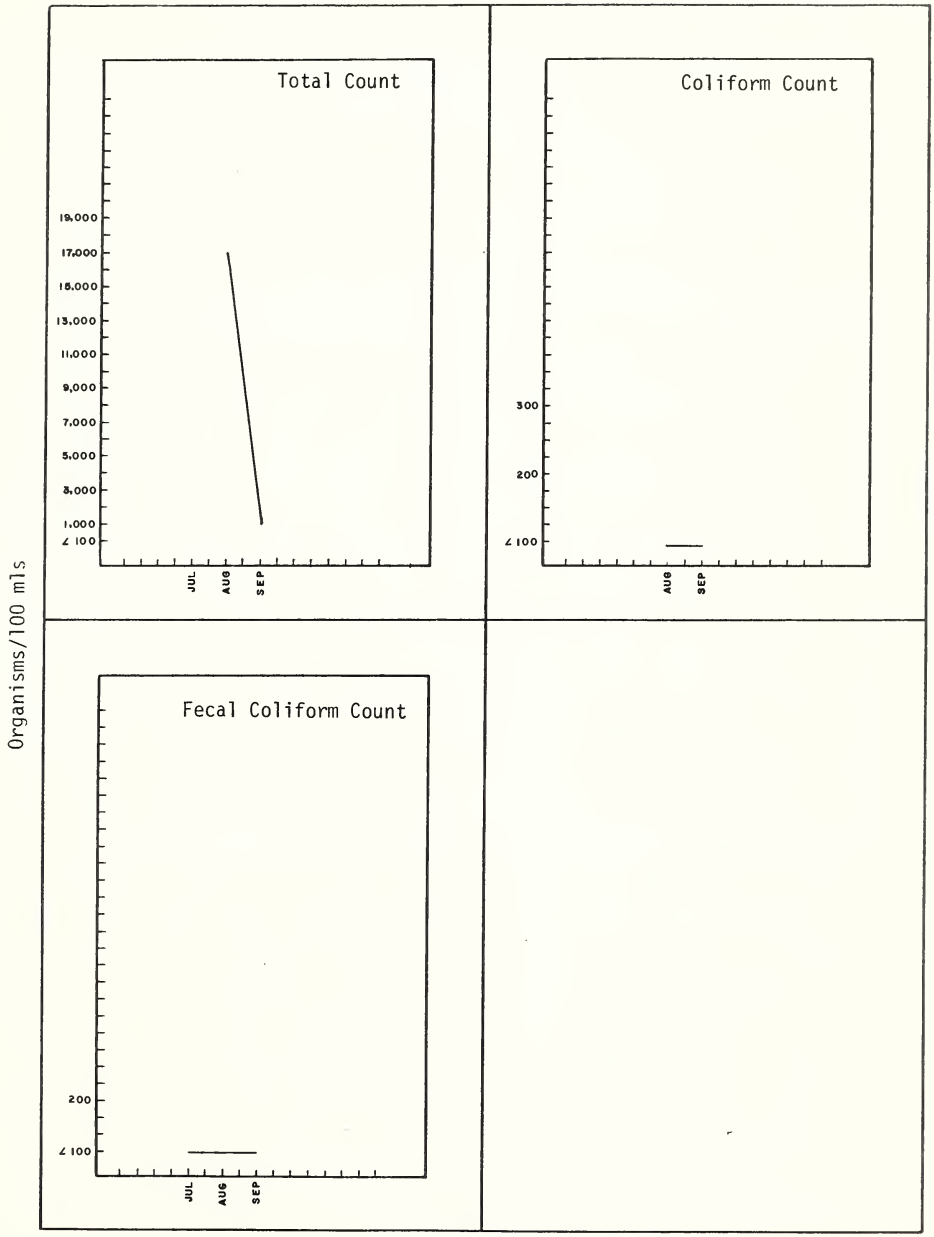

CHEMICAL DATA
STATION S-7
UPPER BLACKTAIL CREEK

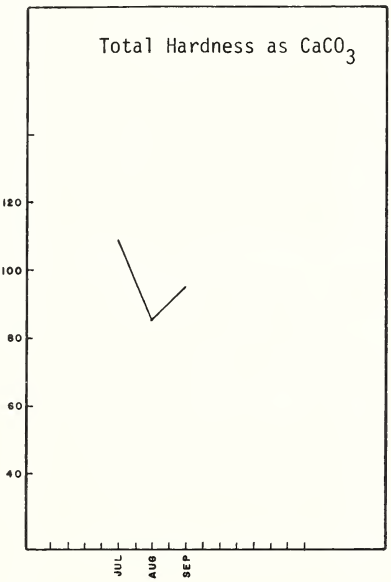

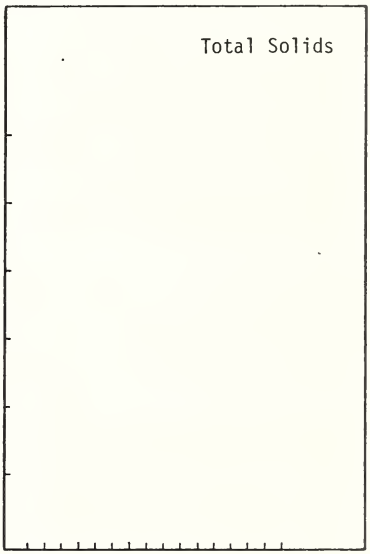

Concentration in ppm

Sampling Dates

CHEMICAL DATA
STATION S-7
UPPER BLACKTAIL CREEK

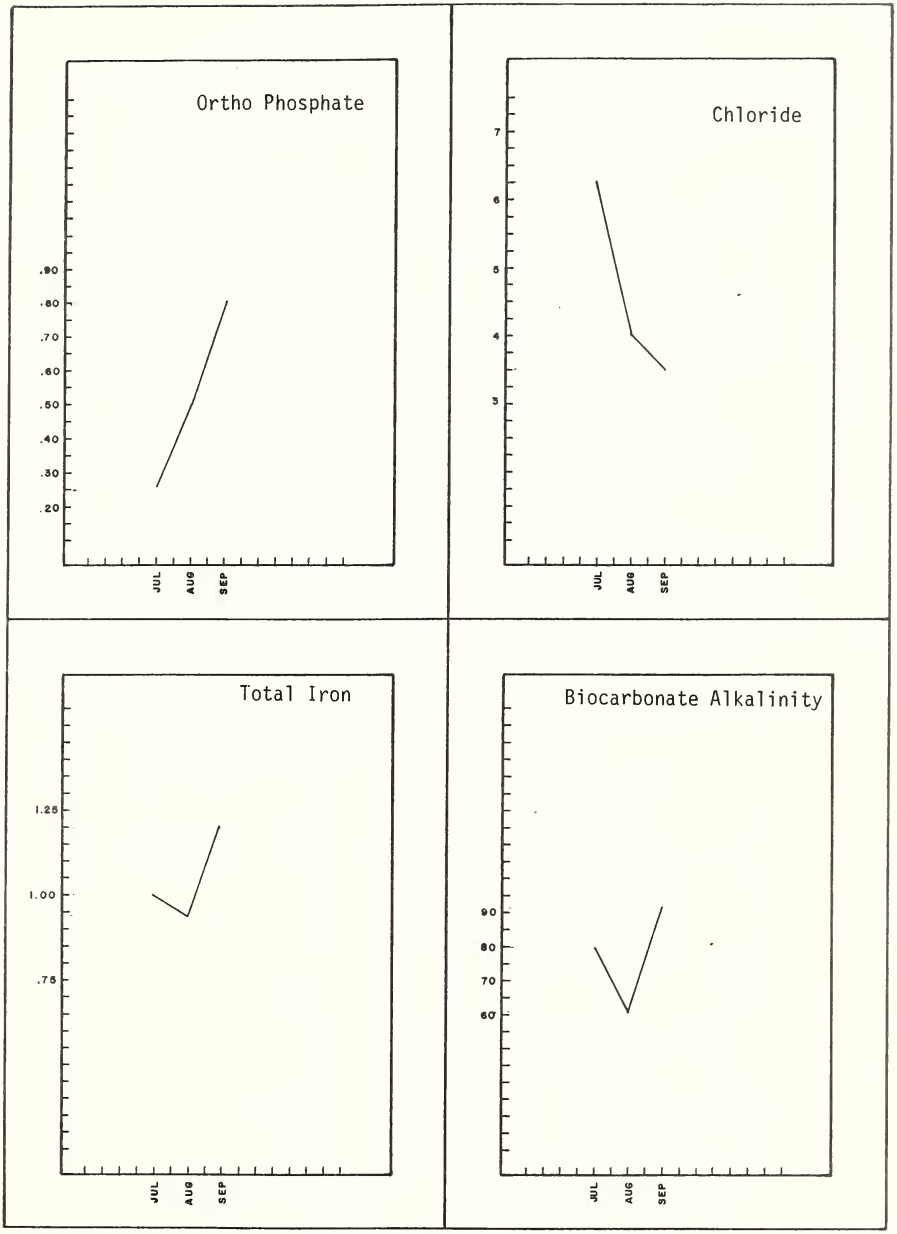

FIGURE 9. GRAPHICAL PRESENTATION OF THE SITE S-8(F) DATA
BACTERIAL COUNTS
LITTLE BLACKTAIL CREEK SITE S-8(F)

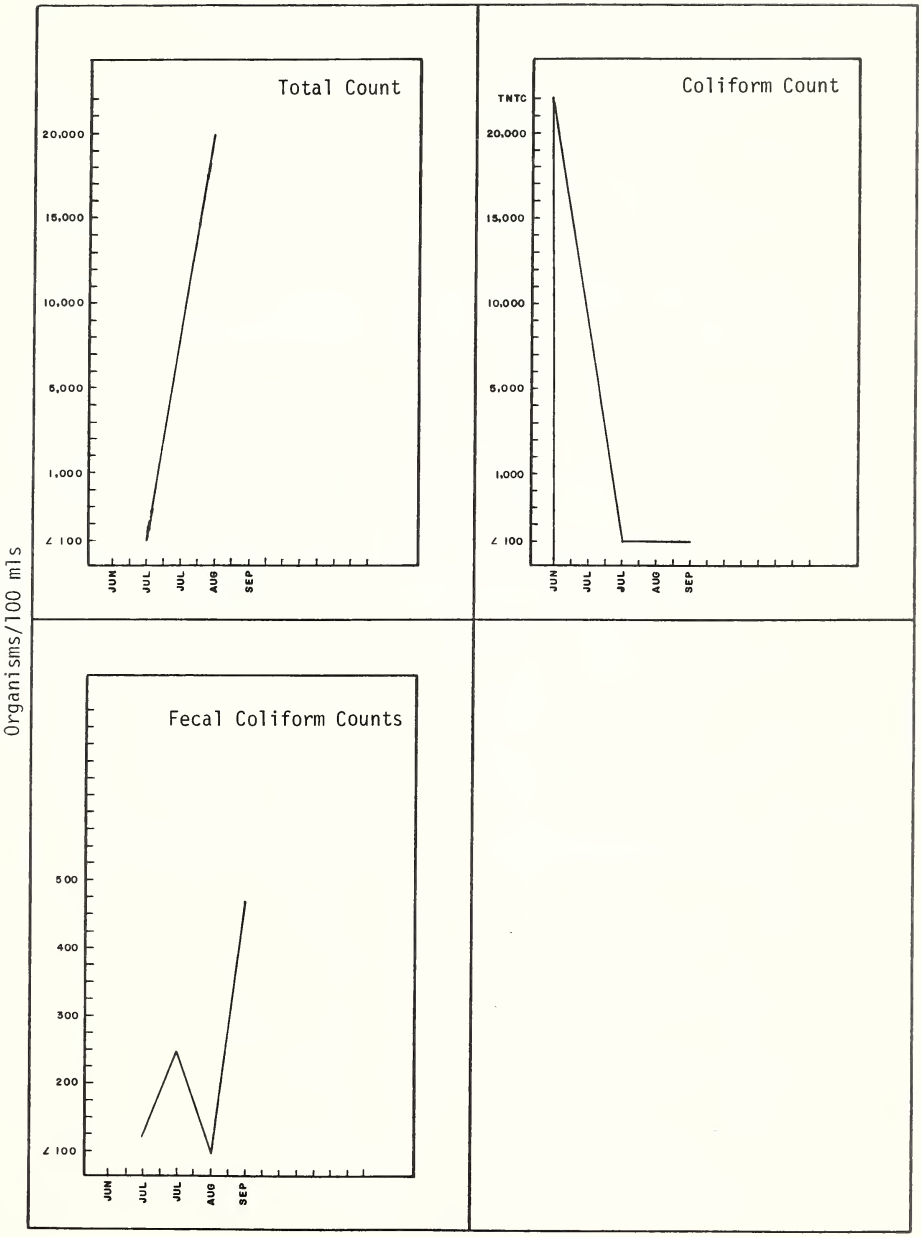

CHEMICAL DATA
"BEAVER DAM" STATION F
LITTLE BLACKTAIL CREEK

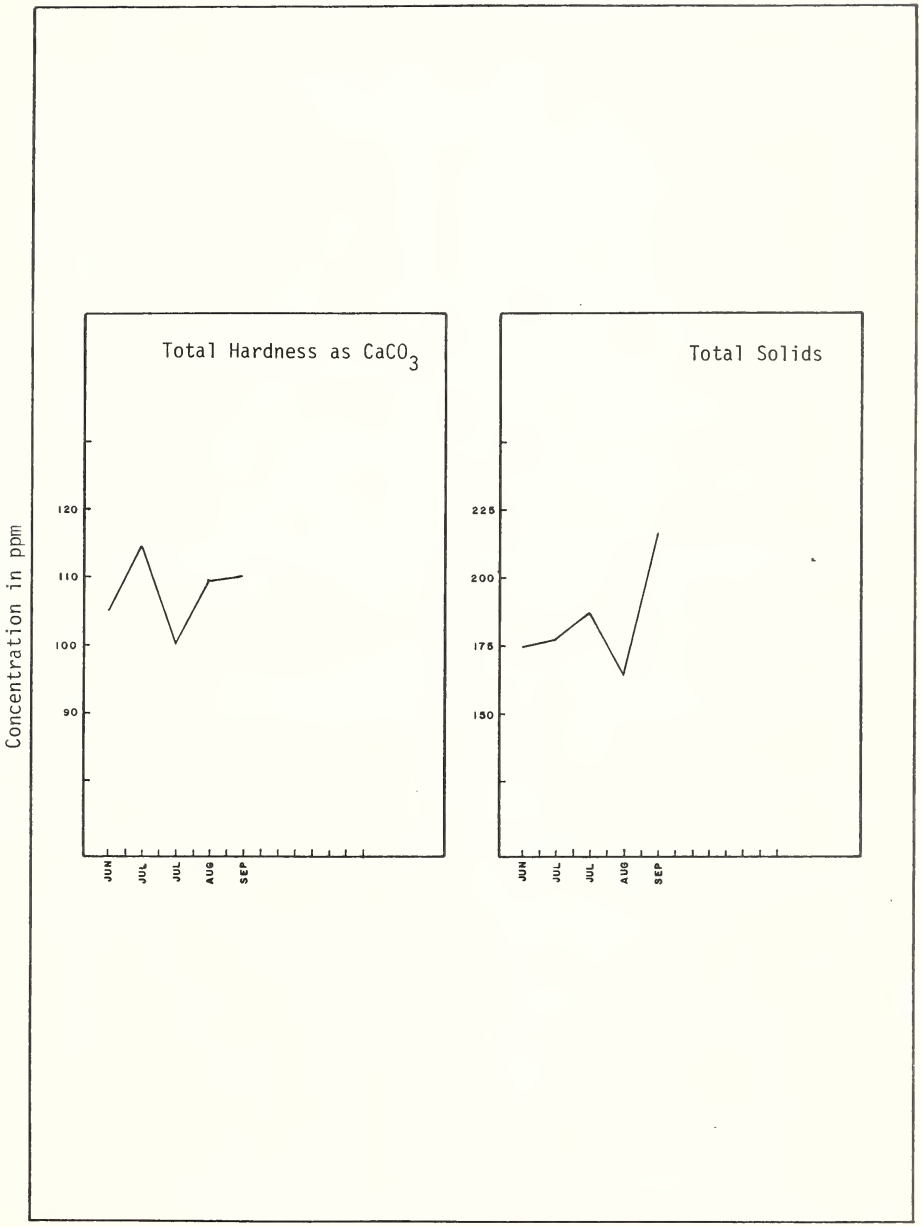

CHEMICAL DATA
"BEAVER DAM" STATION F
LITTLE BLACKTAIL CREEK

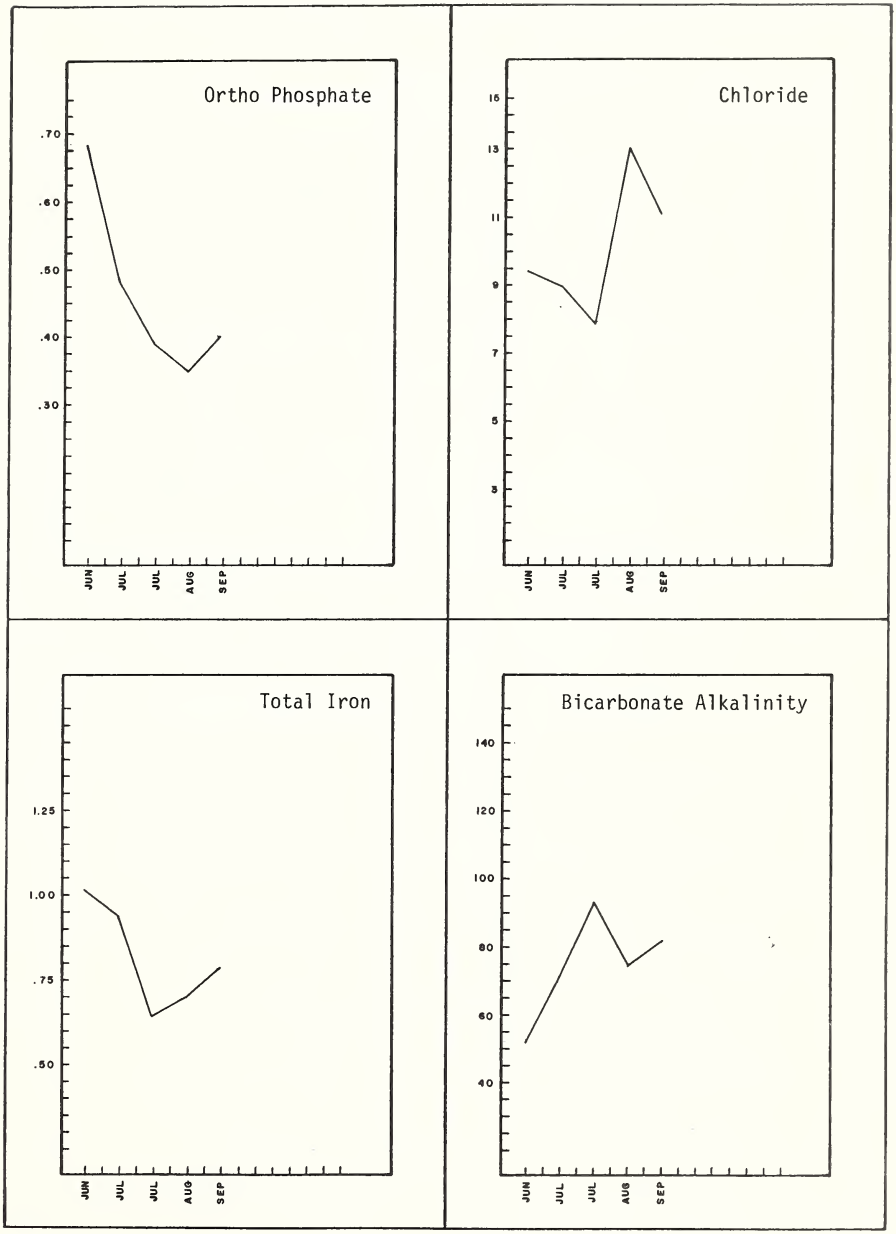

Concentration in PPM

Sampling Dates

FIGURE 10. GRAPHICAL PRESENTATION OF THE SITE S-9 DATA
BACTERIAL COUNTS
LOWER BLACKTAIL CREEK SITE S-9

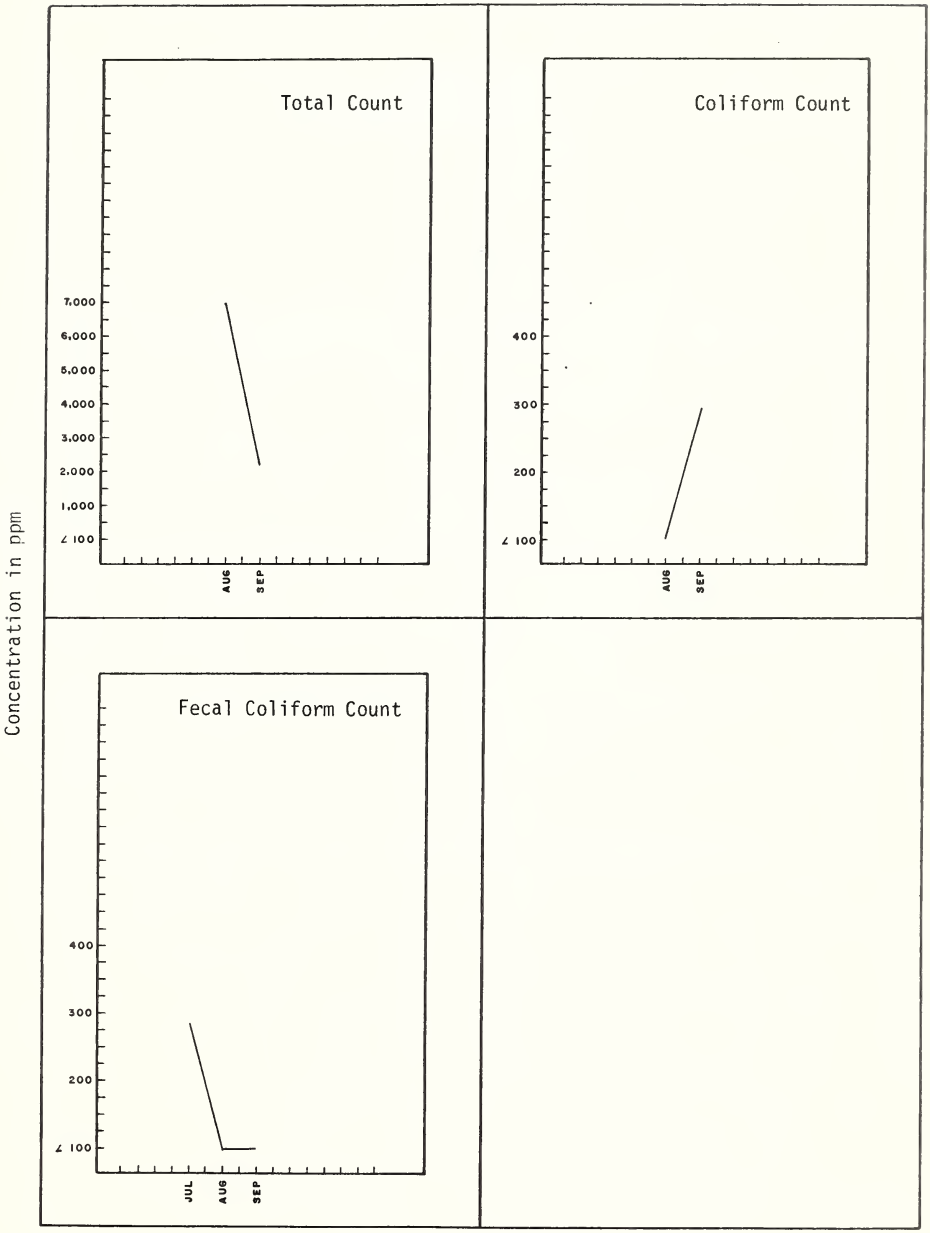

CHEMICAL DATA
STATION S-9
LOWER BLACKTAIL CREEK

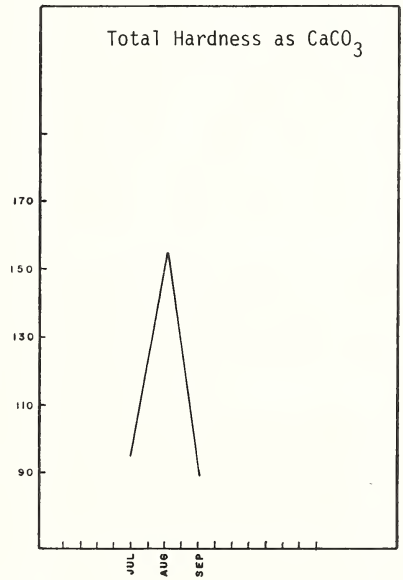

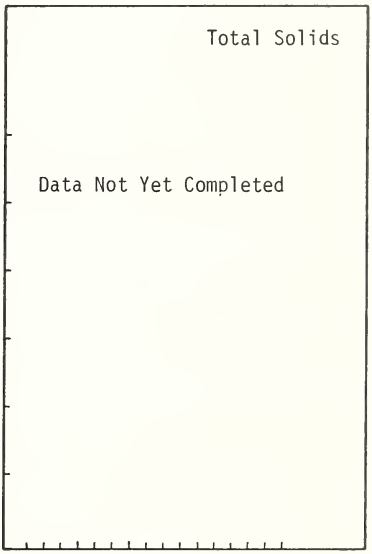

Concentration in ppm

Sampling Dates

CHEMICAL DATA
STATION S-9
LOWER BLACKTAIL CREEK

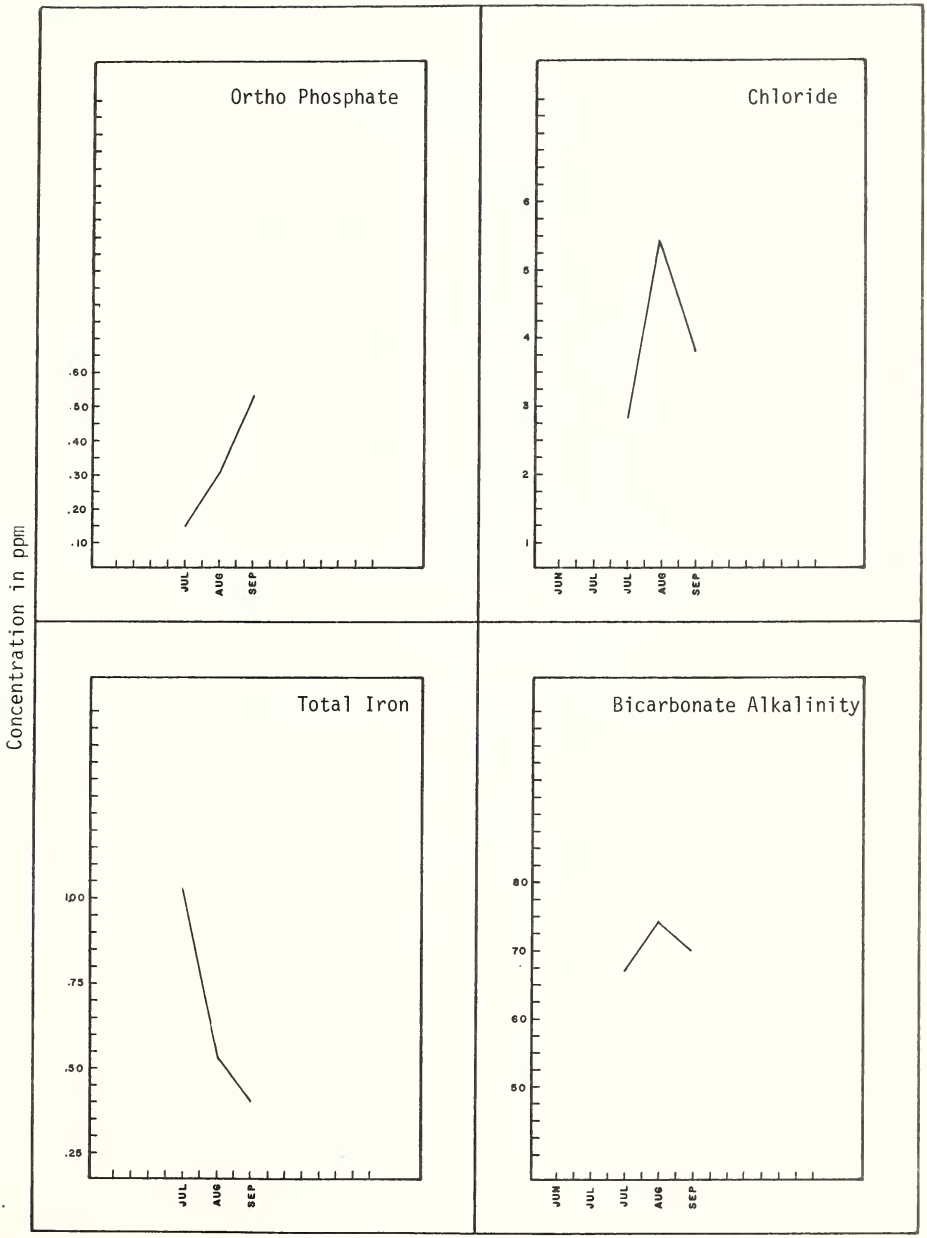

FIGURE 11. GRAPHICAL PRESENTATION OF THE SITE E DATA
BACTERIAL COUNTS
YANKEE DOODLE CREEK SITE E

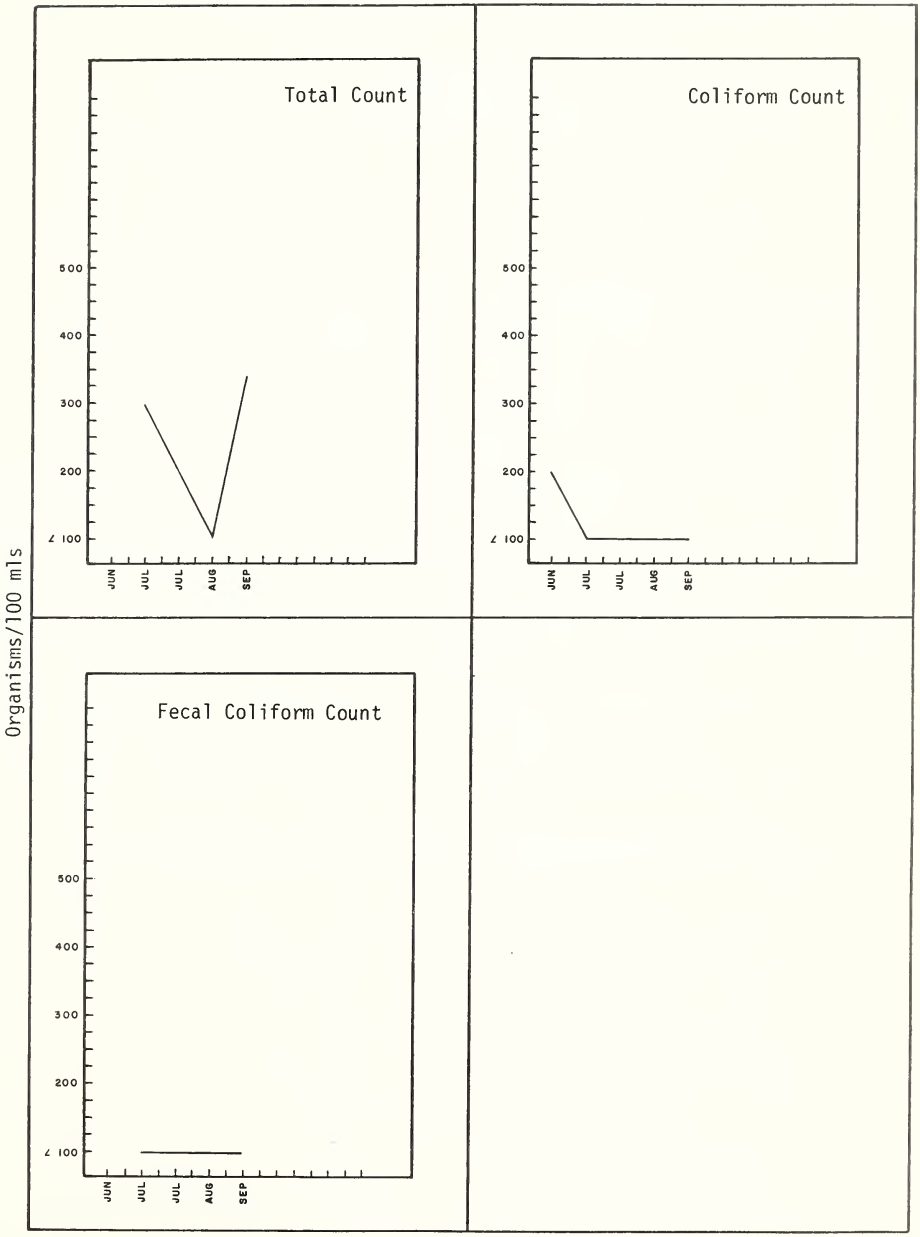

CHEMICAL DATA
STATION E
YANKEE DOODLE CREEK

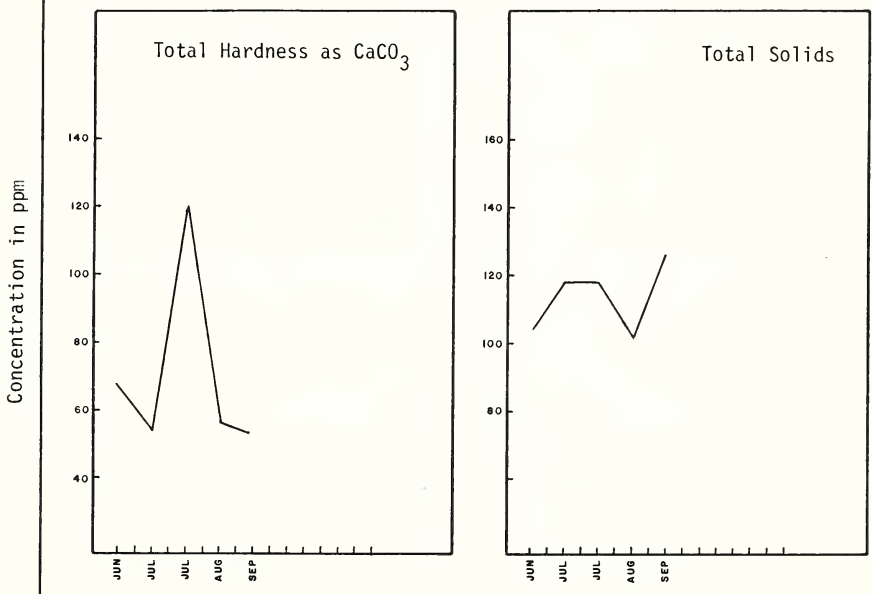

Concentration in ppm

Sampling Dates

CHEMICAL DATA
STATION E
YANKEE DOODLE CREEK

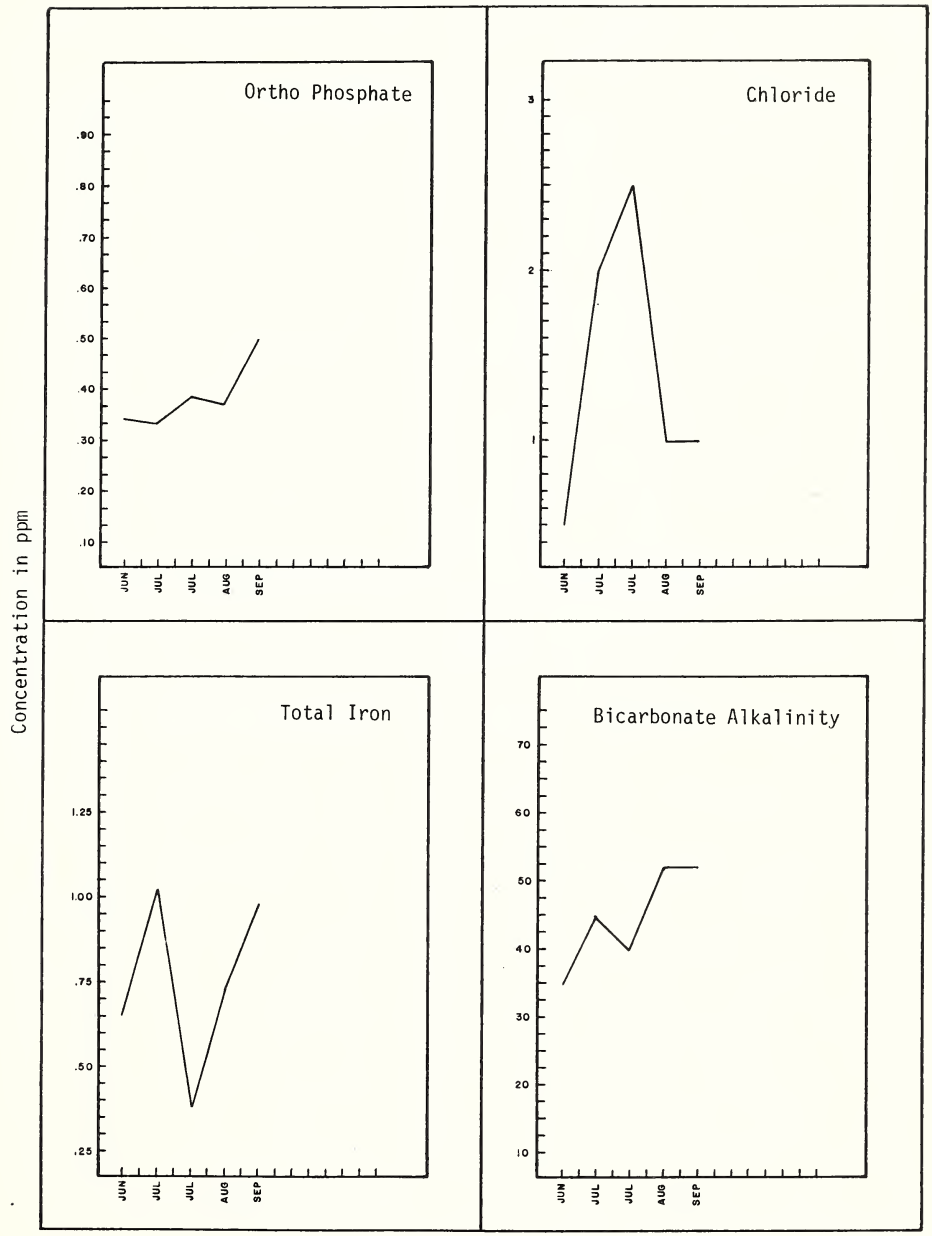

FIGURE 12. GRAPHICAL PRESENTATION OF THE SITE G DATA
BACTERIAL COUNTS
BASIN CREEK SITE G

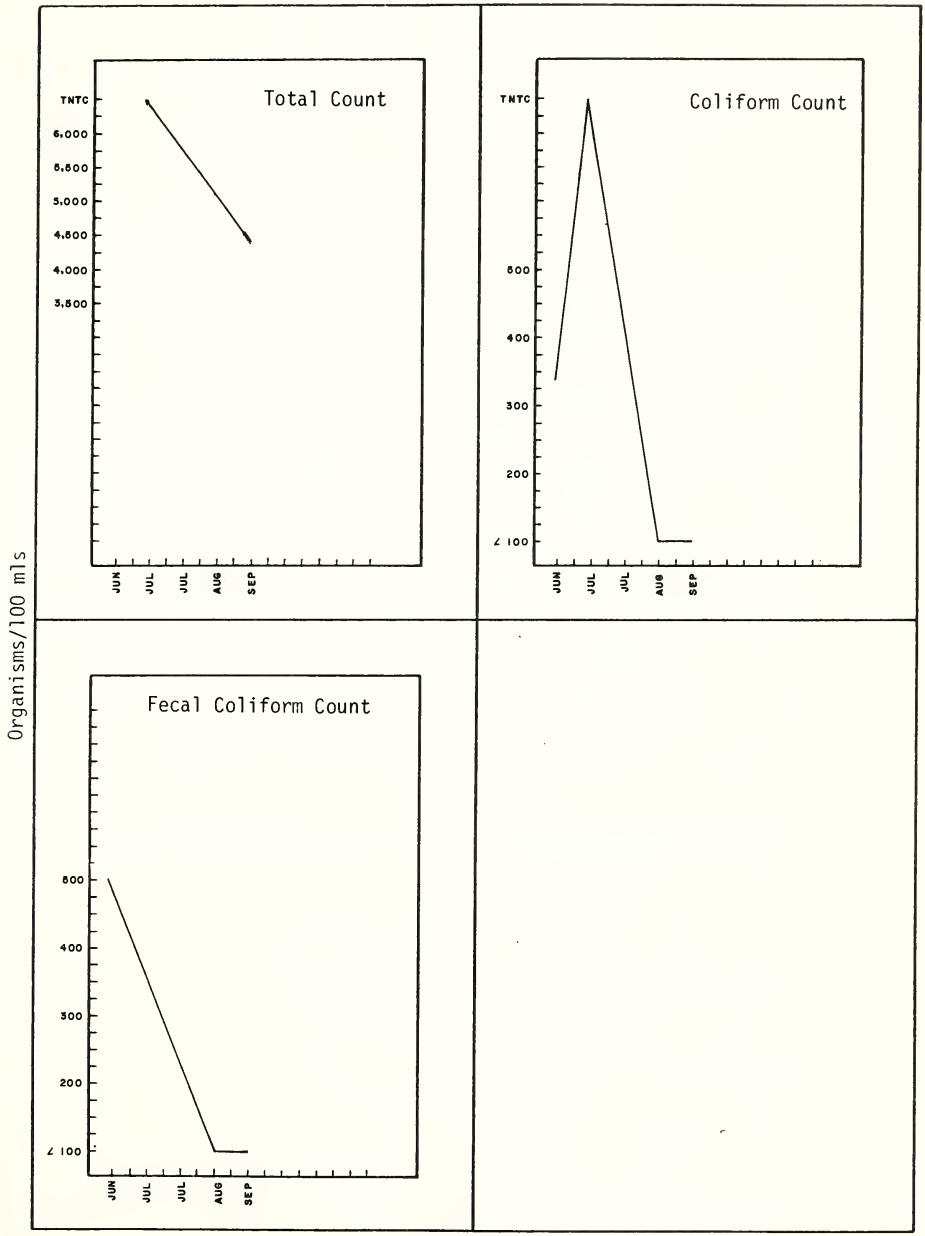

CHEMICAL DATA
STATION G
BASIN CREEK RESERVOIR

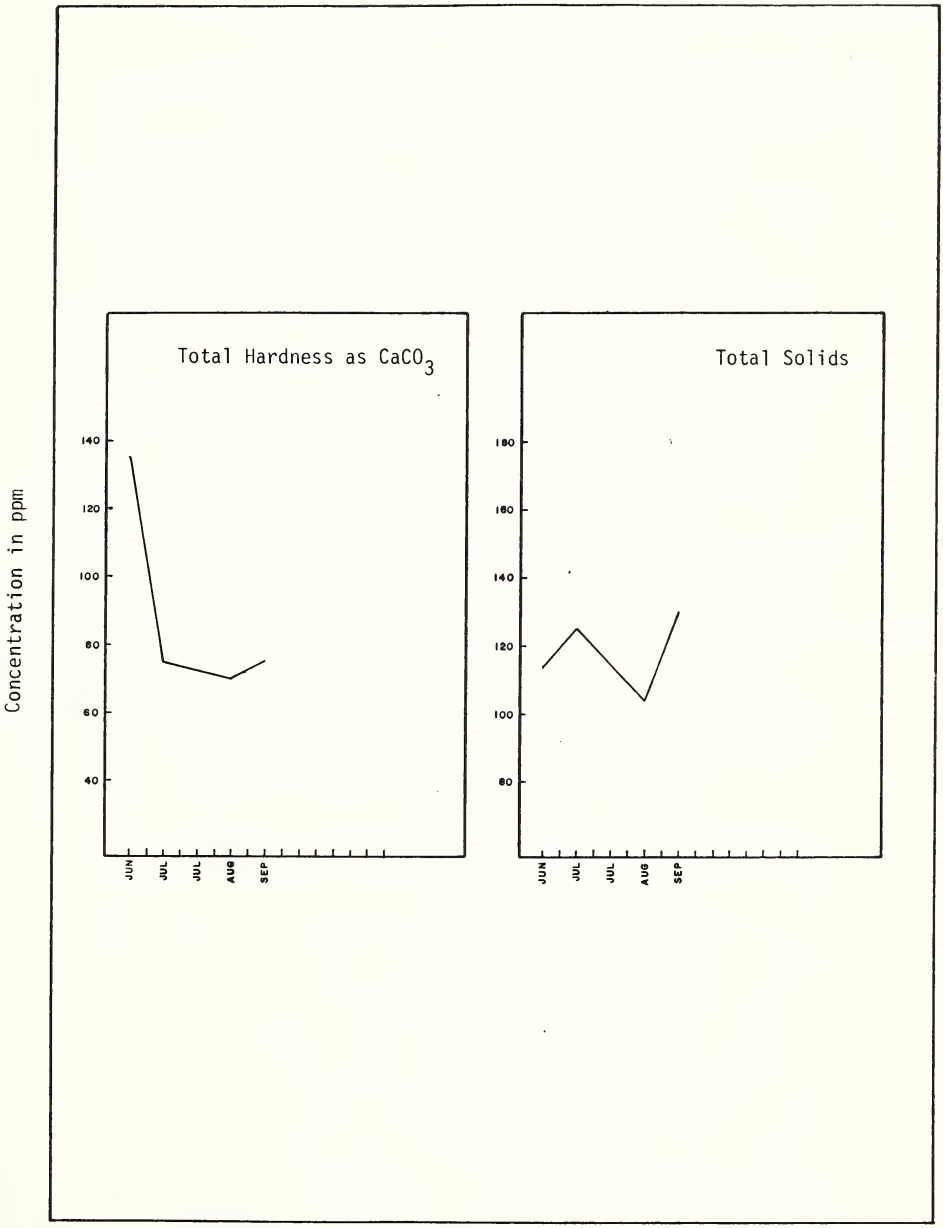

CHEMICAL DATA
STATION G
BASIN CREEK RESERVOIR

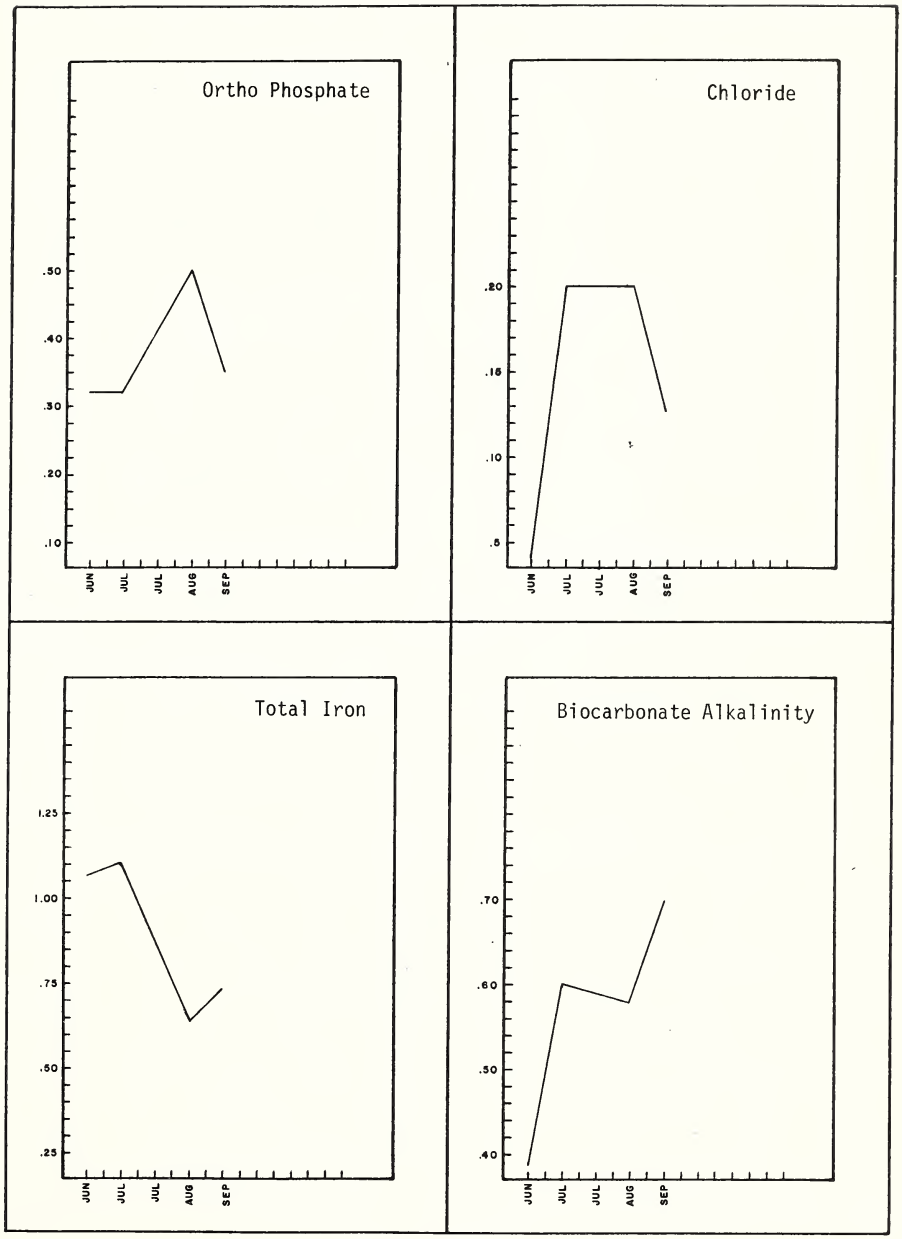

FIGURE 13. GRAPHICAL PRESENTATION OF THE SITE H DATA
BACTERIAL COUNTS
WILDLIFE BIRD SANCTUARY
"SWAMP" SITE H

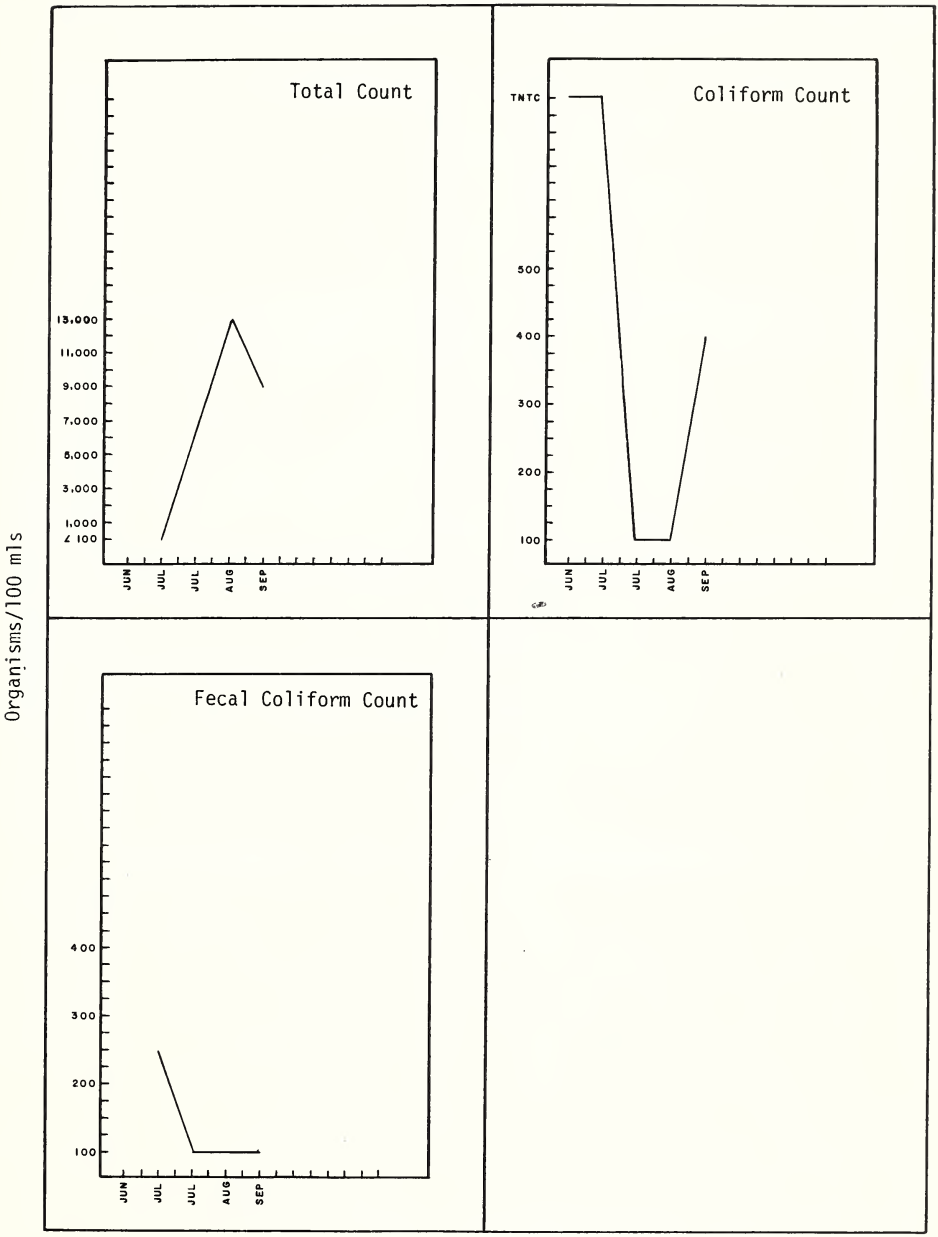

CHEMICAL DATA
STATION H
WILDLIFE BIRD SANCTUARY
"SWAMP"

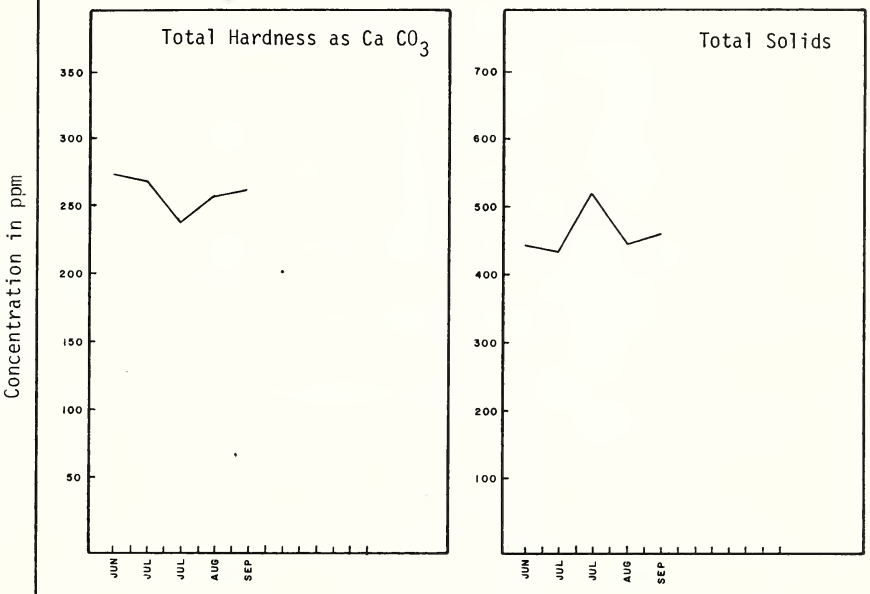

Concentration in ppm

Sampling Dates

CHEMICAL DATA
STATION H
WILDLIFE BIRD SANCTUARY
"SWAMP"

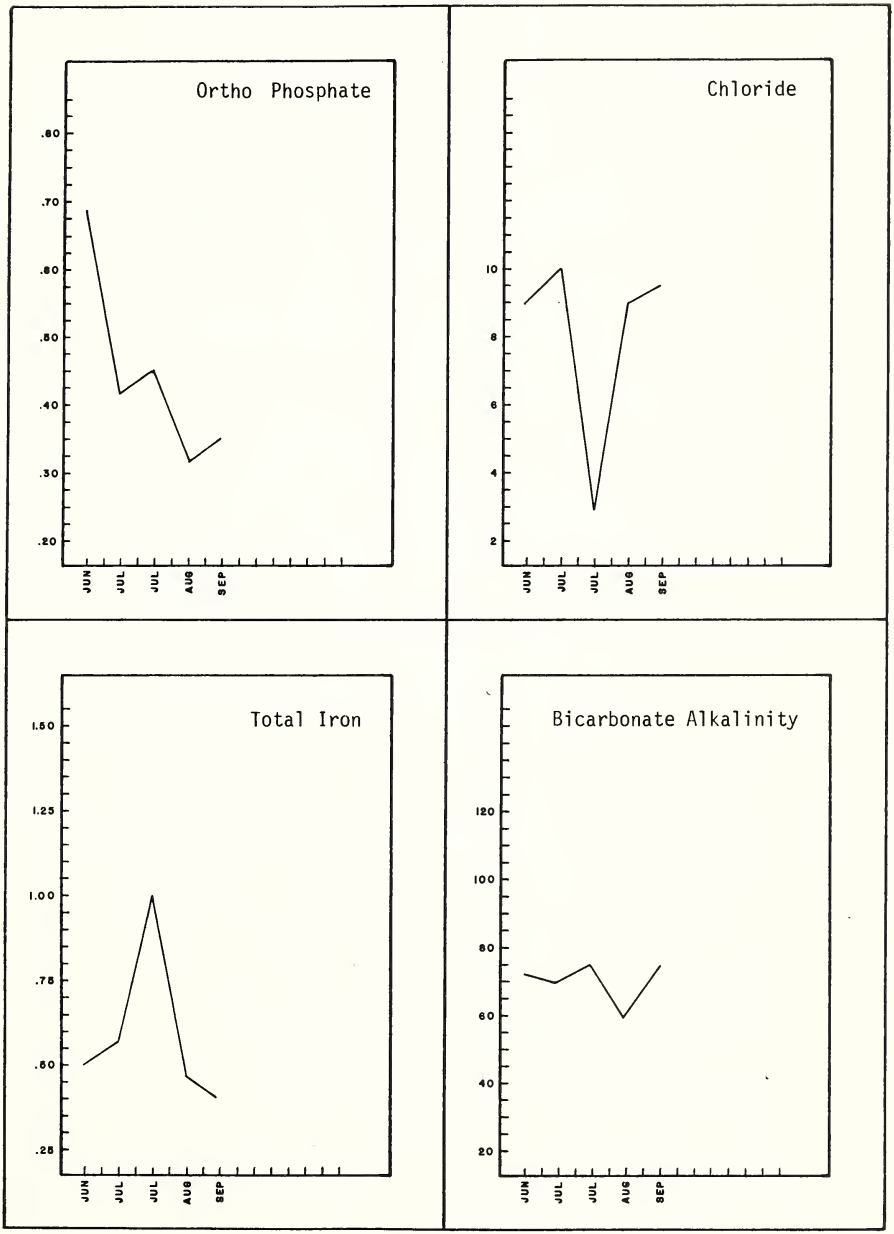

FIGURE 14. GRAPHICAL PRESENTATION OF THE SITE S-10(J) DATA
BACTERIAL COUNTS
WEBSTER'S WELL SITE S-10(J)

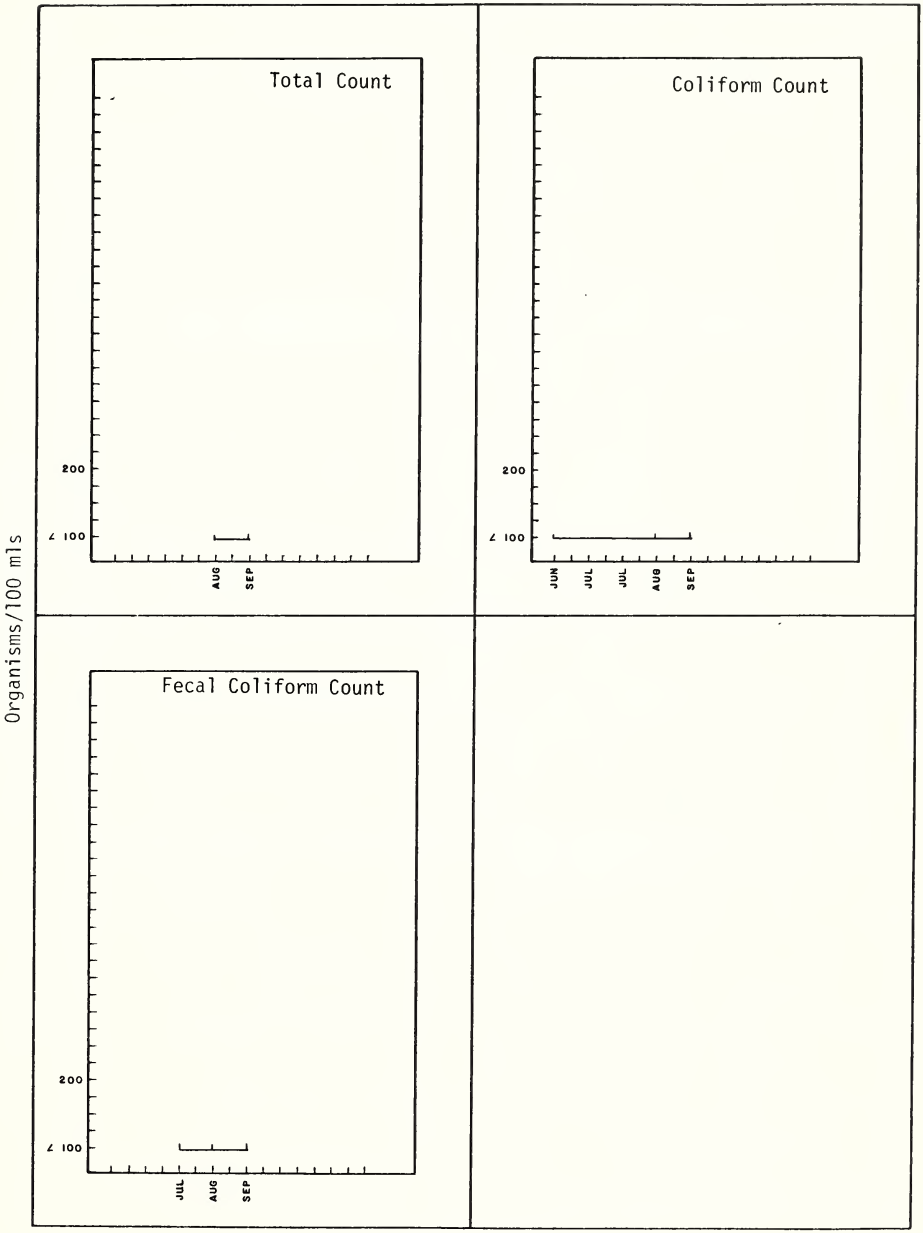

CHEMICAL DATA
STATION J
WEBSTER'S WELL

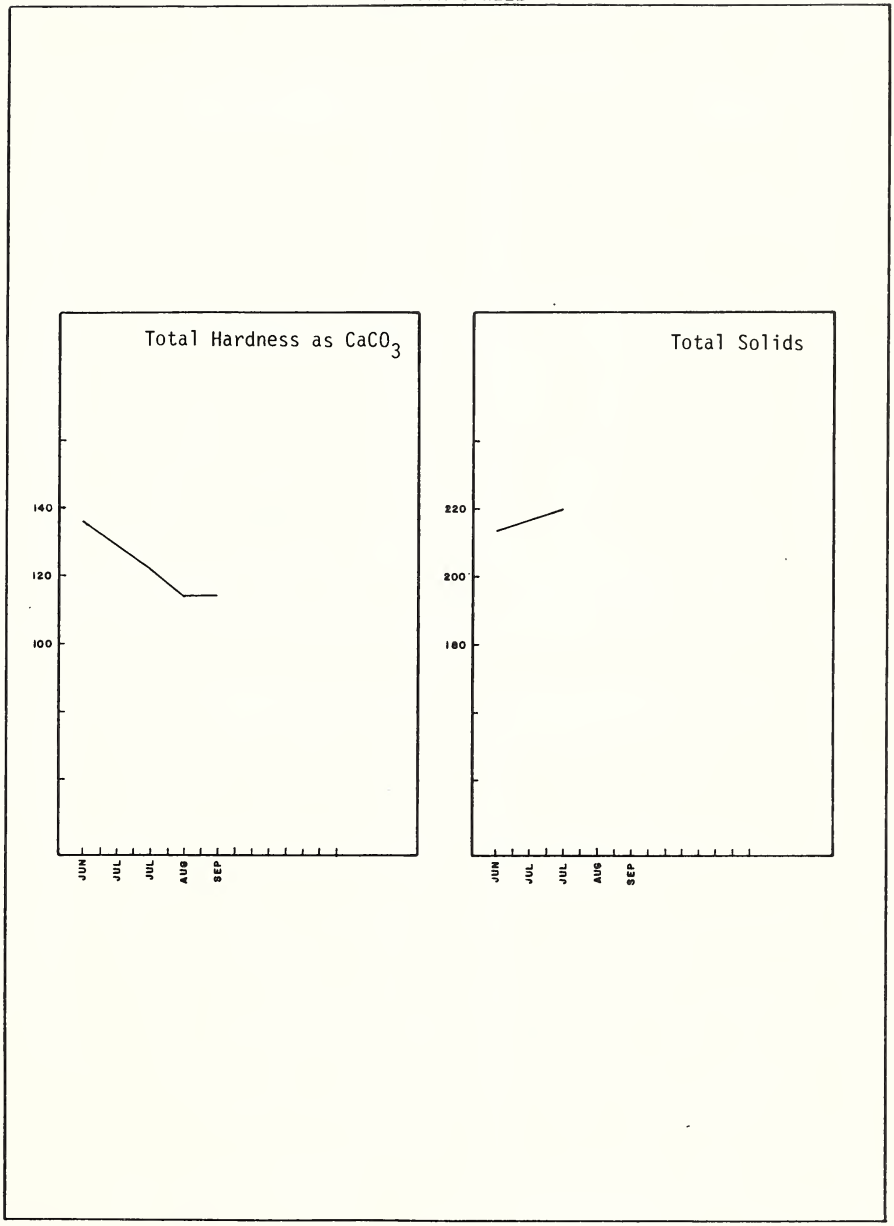

CHEMICAL DATA
STATION J
WEBSTER'S WELL

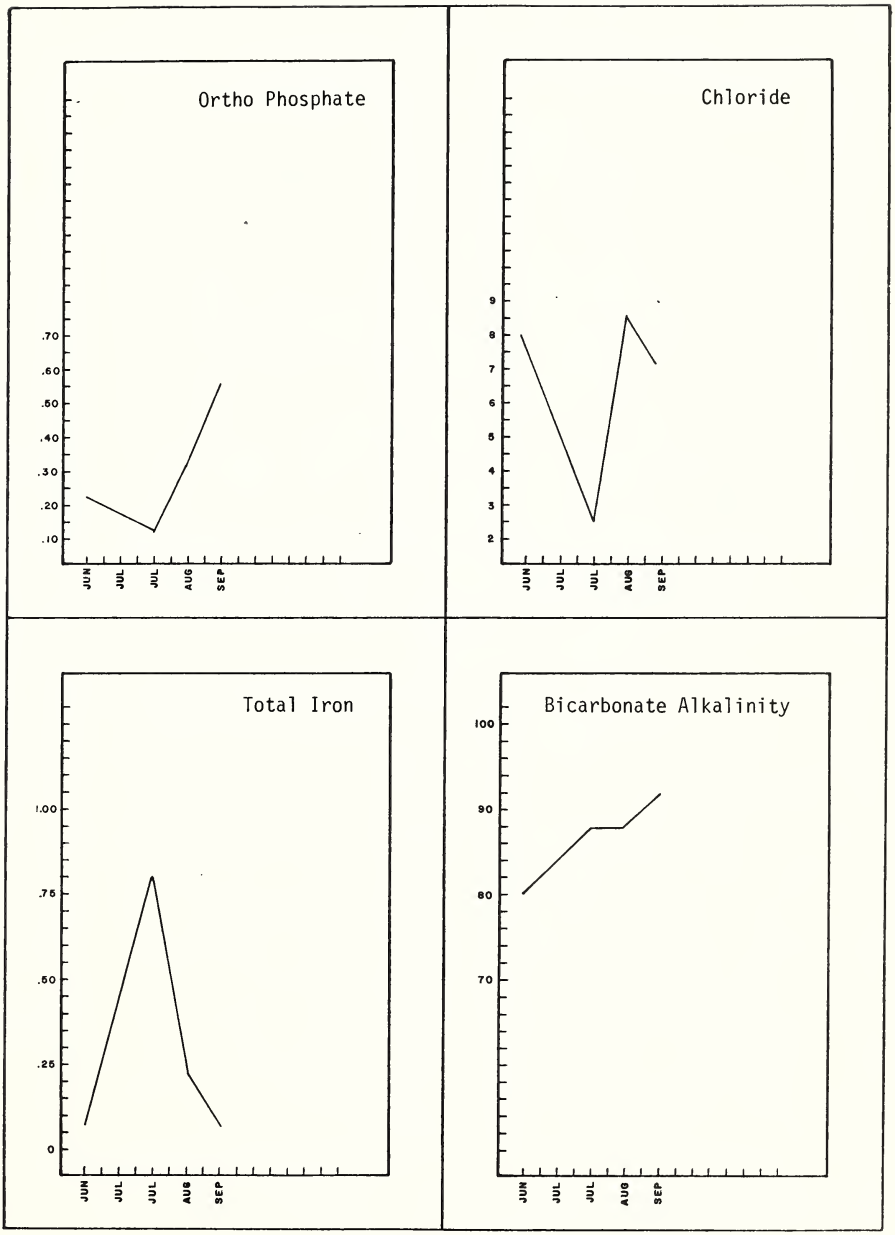

FIGURE 15. GRAPHICAL PRESENTATION OF THE SITE S-5(I) DATA
BACTERIAL COUNTS
KRAUSE'S WELL SITE S-5(I)

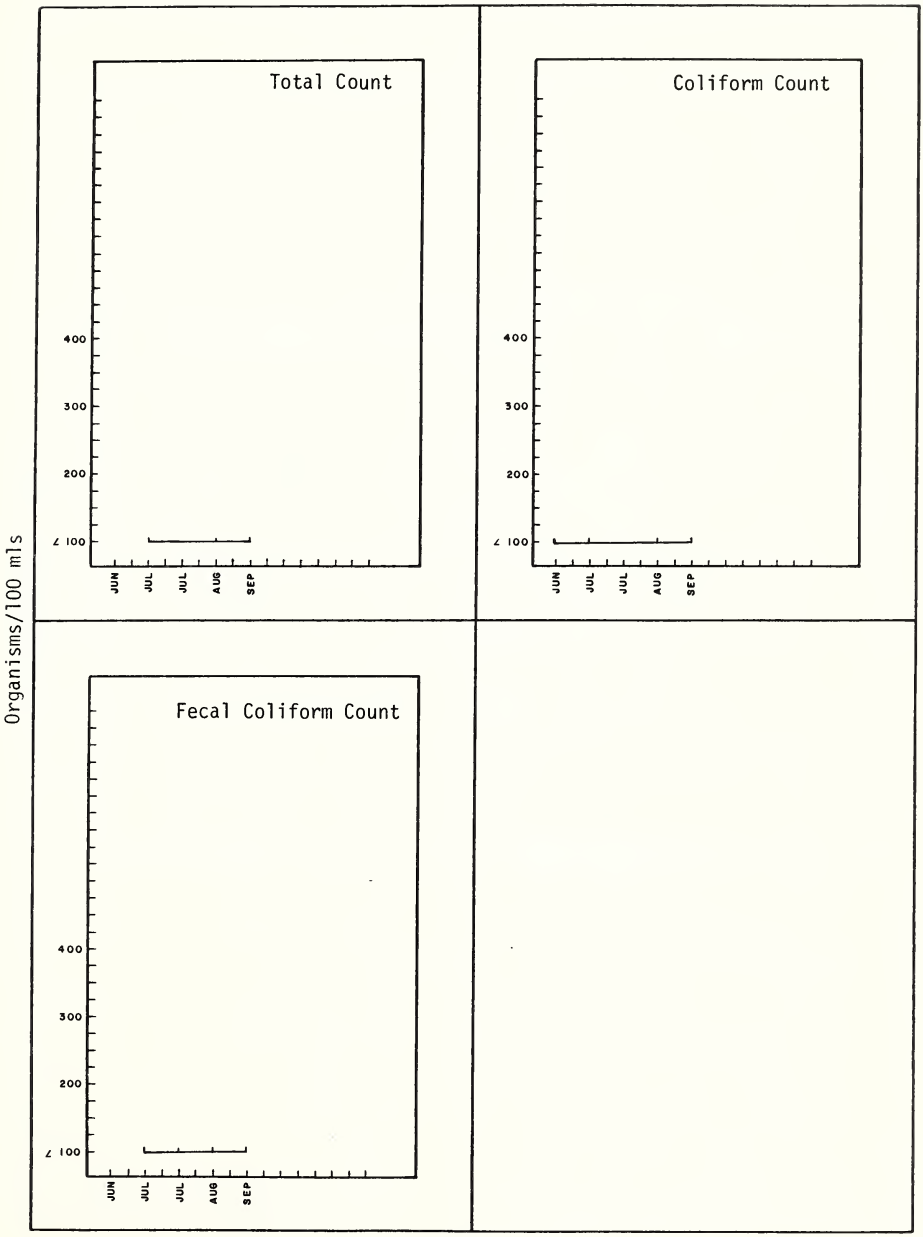

CHEMICAL DATA
STATION I
KRAUSE'S WELL

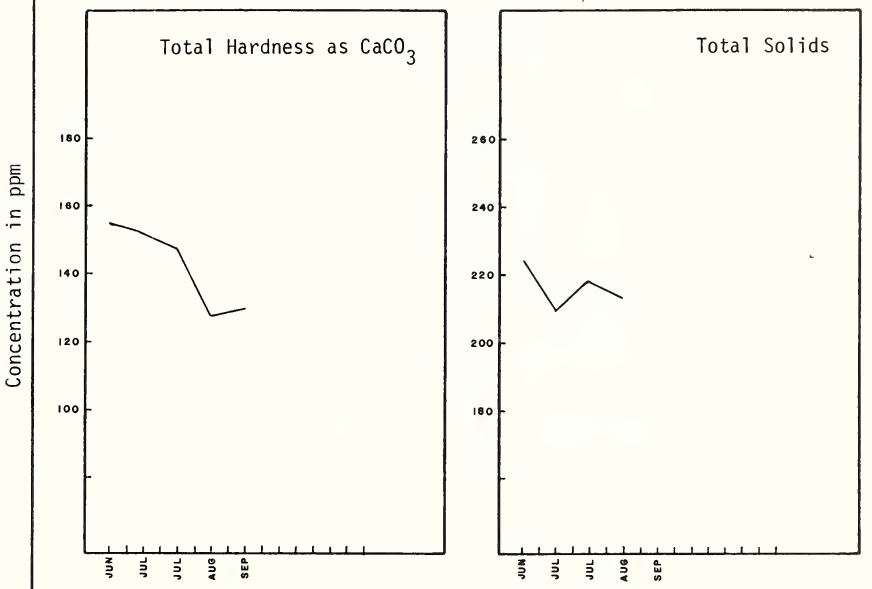

Concentration in ppm

Sampling Dates

CHEMICAL DATA
STATION I
KRAUSE'S WELL

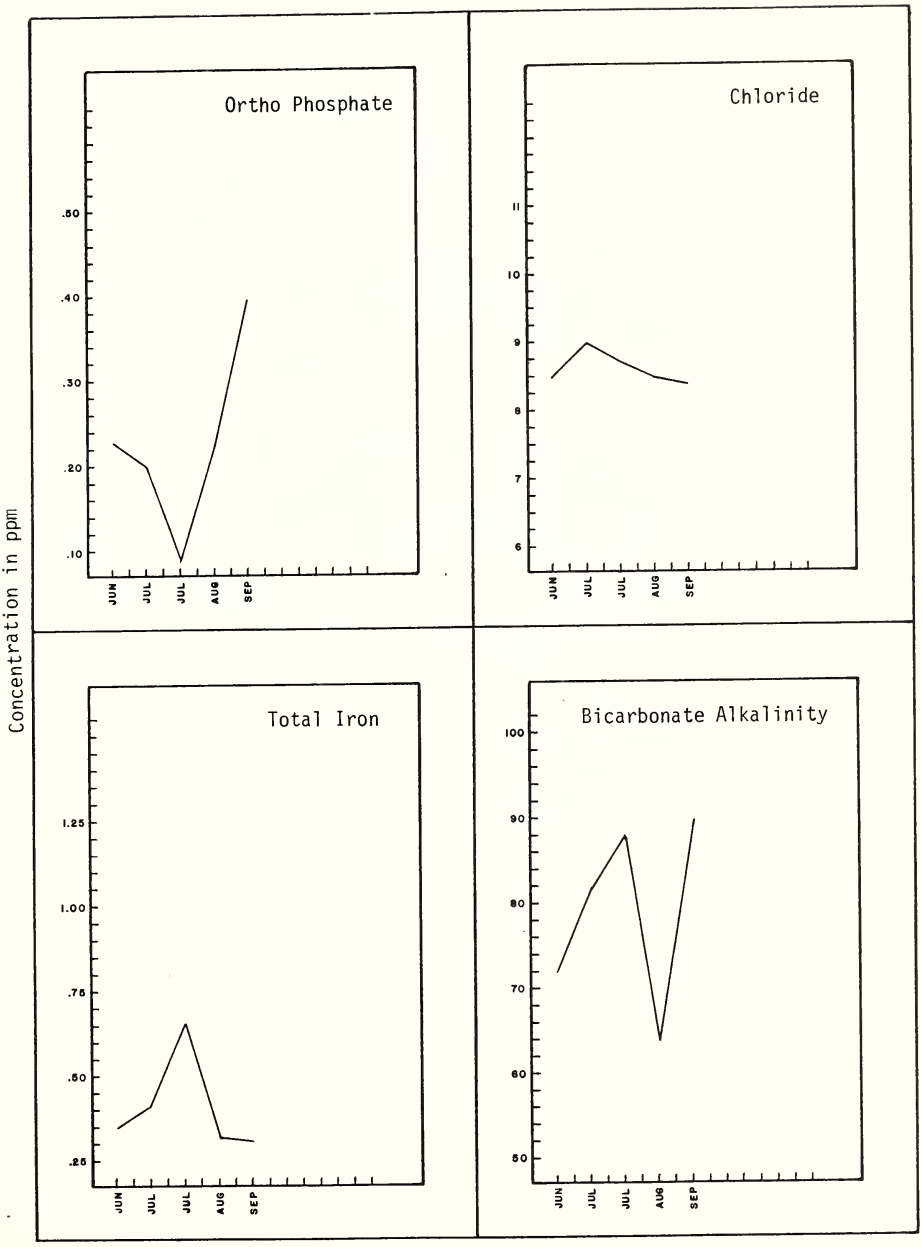

EXHIBIT 1

The Montana Energy and MHD Research and Development Institute, Inc.
Post Office Box 3809
Butte, Montana 59701
(406) 494-4569
FTS 585-2421

Date: September 26, 1977

To: Rod Portch ✓

Copies: D. Brelsford, R. Kramarsic

From: M. W. Penttila M.W. Penttila

Subject: Status Report - Biological, Physical and Chemical Data Handling System (BPCDHS)

Some time has been spent in becoming familiar with the work being done on the CDIF-Baseline Biological Surveillance Program in order to better develop the preliminary design specifications of the Biological, Chemical, and Physical Data Handling System (BCPDHS). Examples of data sheets, procedures for taking the data and for filling in the data sheets, and actual filled in data sheets were looked at to see just what type of input BCPDHS will need to handle.

Some of the data such as descriptive and commentary data do not readily lend themselves to input and storage on MERDI's computor system. Numerical data, such as water quality results, trace ion analysis results, etc. will be somewhat easier to input and store in the computor system in a meaningful manner.

Future efforts will involve defining what data needs to be stored, what forms the data will be stored in, and what types of data manipulation (eg. reports, correlation, etc.) will be required. Once the input and output requirements for BCPDHS have been better defined, a preliminary design specification document will be drafted and circulated for comments.

MWP/mo

STATUS DATE

TASK S_2

Table 1.--Milestone Chart

PROGRESS

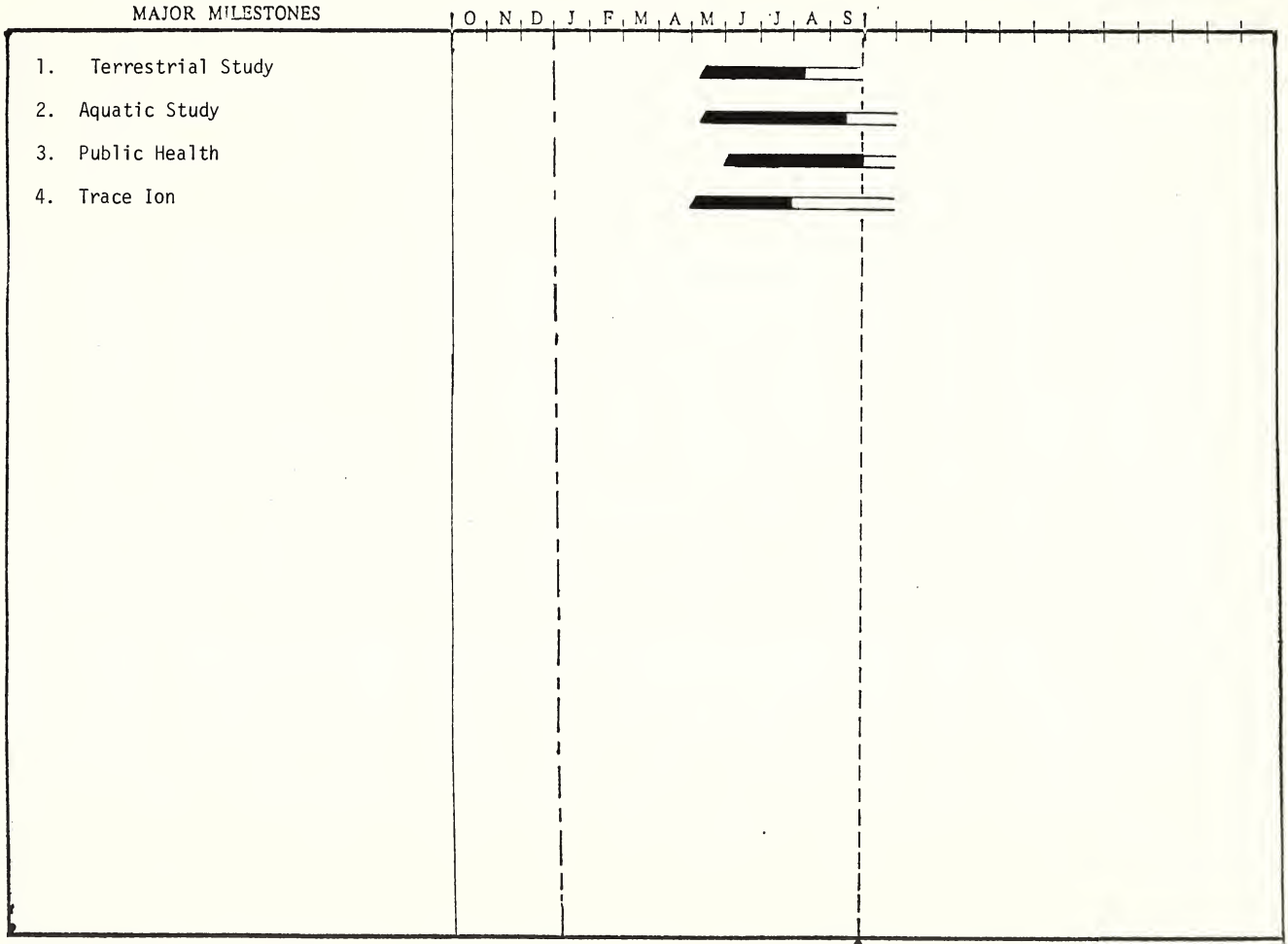

TABLE 2.--Floristic Inventory of the Existing Terrestrial Sites

Station A Plant List

FAMILY	SPECIES	COMMON NAME
CARYOPHYLLACEAE	*Stellaria jamesiana* Torr.	Chickweed or Starwort.
	Stellaria nitens Nutt.	Chickweed or Starwort
CHENOPODIACEAE	*Salola kali* L.	Russian Thistle
COMPOSITAE	*Achillea millefolium* L.	Yarrow
	Adenocaulon bicolor Hood	Pathfinder
	Antennaria sp. Gaertn.	Pussytoes
	Cirsium arvense (L.) Scop.	Canada Thistle
	Taraxacum officinale Weber.	Dandelion
GRAMINEAE	*Agropyron cristaltum* (L.) Gaertn.	Crested Wheatgrass
	Agropyron trachycaulum (LINK.) Matte.	Slender Wheatgrass
	Bromus inerm Leys.	Smooth Brome
LEGUMINOSAE	*Astragalus sp.* L.	Locoweed or Milk Vetch
	Melilotus alba Desr.	White Sweet Clover
	Melilotus officinalis (L.) Lam	Yellow Mililot
	Trifolium pratense L.	Red Clover
	Trifolium repens L.	White Clover
LILIACEAE	*Allium cernvum* Roth	Nodding Onion
	Streptopus anplexifolium (L.) DC.	Twisted Stalk
ONOGRACEAE	*Epilobium angustifolium* L.	Fire Weed

TABLE 2.--Continued (Station A Plant List)

FAMILY	SPECIES	COMMON NAME
PINACEAE	*Pinus contorta* Dougl.	Lodge-pole Pine
	Pseudotsuga menzierii (Birbel)	Douglas Fir
POLYGONACEAE	*Polygonum sp.* L.	Doorwood
RHAMNACEA	*Ceanothus sanquineus* Pursh.	Buckbrush
ROSACEAE	*Amelanchier alnifolia* Nutt.	Service Berry
	Fragaria vesca L.	Wild Strawberry
	Geum triflorum Pursh.	Old Man's Wiskers
	Potentilla glandulosa Lindl.	Cinquefoil
	Rosa sp. L.	Rose
SALICACEAE	*Populus tremulodies* Michx.	Quaking Aspen
	Populus trichocarpa T. & G.	Black Cottonwood
	Salix sp. L.	Willow
SAXIFRAGACEAE	*Heuchera parvifolia* Nutt.	Little Leaf Allum Root
	Ribes aureum Pursh.	Golden or Flowering Currant
SCROPHULARIACEAE	*Castilleja sp.* Mutis.	Indian Paintbrush
	Penstemon sp. Mitch	Penstemon
	Verbascum thapsus L.	Mullein
URTICACEAE	*Urtica gracilis* Ait.	Stinging Nettle

TABLE 2.--Continued (Station B Plant List)

FAMILY	SPECIES	COMMON NAME
CARYOPHYLLACEAE	*Silene alba* Muhl.	White Campion
CHENOPODIACEAE	*Chenopodium sp.* L.	Pigweed
COMPOSITAE	*Achillea millefolium* L.	Yarrow
	Aster sp. L.	Aster
	Chrysothamnus nauseosus (Pall.) Britt.	Rabbitbrush
	Cirsium arvense (L.) Scop.	Canada Thistle
	Cirsium sp. Mill.	Thistle
	Cirsium vulgare (Savi.) Airy-Shaw	Bull Thistle
	Erigeron sp. L.	Fleabane
	Lactuca sp. L.	
	Taraxacum officinale Weber.	Dandelion
ERICACEAE	*Cornus stolonifera* Michx.	Red-osier Dogwood
GRAMINEAE	*Alopecurus sp.* L.	Foxtail
	Hordeum jubatum L.	Foxtail Barley
LEGUMINOSAE	*Medicago sativa* L.	Alfalfa
	Melilotus alba Desr.	White Sweet Clover
	Melilotus officinalis (L.) Lam.	Yellow Melilot
ONAGRACEAE	*Epilobium angustifolium* L.	Firewood
PINACEAE	*Juniperus scopulorum* Sarg.	Rocky Mountain Juniper

TABLE 2.--Continued (Station B Plant List)

FAMILY	SPECIES	COMMON NAME
PINACEAE	*Picea engelmannii* (Parry.) Engelm.	Engelmann's Spruce
	Pseudotsuga menzierii Mirbel	Douglas Fir
ROSACEAE	*Prunus virginiana* L.	Chokecherry
	Rosa sp. L.	Rose
	Rubus idaeus L.	Red Raspberry
SALICACEAE	*Populus tremuloides* Michx.	Quaking Aspen
SAXIFAGACEAE	*Ribes aureum* Pursh.	Golden Currant
SCROPHULARIACEAE	*Linaria vulgaris* Hill.	Butter & Egg
	Penstemon sp. Mitch.	Penstemon

TABLE 2.--Continued (Station C Plant List)

FAMILY	SPECIES	COMMON NAME
CHENOPODIACEAE	*Salsola kali* L.	Russian Thistle
COMPOSITAE	*Achillea millefolium* L.	Yarrow
	Anaphalis margaritaceae (L.) Benth and Hook	Pearly Everlasting
	Anternnaria sp. Gaertn.	Pussytoes
	Chrysothamnus nauseosus (Pall.) Britt.	Rabbitbrush
	Cirsium arvense (L.) Scop.	Canada Thistle
	Erigeron sp. L.	Fleabane
	Taraxacum officinale Weber.	Dandelion
CONVOLVULACEAE	*Convolvulus arvensis* L.	Morning Glory
CRUCIFERAE	*Capsella bursa-pastoris* (L.) Medic	Shepherd's Purse
	Sisymbrium linifolium Nutt.	Plains Mustard
GERANIACEAE	*Geranium viscosissimum* Fish. and May.	Sticky Geranium
GRAMINEAE	*Agropyron spicatum* (Pursh.) Scribn. and Smith.	Bluebunch Wheatgrass
	Agropyron subsecundum Lindl.	
	Agrostis scabra Willd.	Rough Bent-grass
	Festuca idehoensis Elmer.	Idaho Fescue or Bluebunch Fescue
	Festuca scrabrella Torr.	Rough Fescue
	Stipa comata Trin. and Rupr.	Needle and Thread
	Elymus canadensis L.	Giant Wild Rye

TABLE 2.--Continued (Station C Plant List)

FAMILY	SPECIES	COMMON NAME
LEGUMINOSAE	*Astragalus sp.* L.	Locoweed or Milk Vetch
	Lupinus leucopsis Agardh.	Blue Lupine
	Lupinus sp.	Blue Lupine
	Melilotus alba Desr.	White Sweet Clover
	Melilotus officinalis (L.) Lam.	Yellow Melilot
LILIACEAE	*Allium cernuum* Roth.	Nodding Onion
ONAGRACEAE	*Epilobium angustifolium* L.	Fireweed
IRIDACEAE	*Sisyrinchium inflatum* (Suksd.) St. John	Grass Widow
POLEMONIACEAE	*Phlox hoodii* Richn.	Phlox
	Phlox sp. L.	Phlox
POLYGONACEAE	*Polygonum sp.* L.	Smartweed
ROSACEAE	*Purshia tridentata* (Pursh.) D. C.	Antelope Bitterbrush
SCROPULARIACEAE	*Linaria vulgaris* Hill	Butter & Eggs
	Verbascum thapsus L.	Mullein

TABLE 2.--Continued (Station D Plant List)

FAMILY	SPECIES	COMMON NAME
ASCLEPIADACEAE	*Asclepius sp.* L.	Milkweed
CARYOPHYLLACEAE	*Silene alba* Muhl.	White Campion
COMPOSITAE	*Achillea millefolium* L.	Yarrow
	Antennaria sp. Gaertn.	Pussytoes
	Artemisia frigida Willd.	Fringed Sagewort
	Artemisia tridentata Nutt.	Sagebrush
	Centaurea maculosa Lam.	Spotted Knapweed
	Chrysothamnus nauseosus (Pall.) Britt.	Rabbitbrush
	Cirsium sp. Mill.	Thistle
	Erigeron sp. L.	Fleabane
	Sonchus arvensis L.	Sow Thistle
	Taraxacum officinale Weber.	Dandelion
CRUCIFERAE	*Capsella bursa-pastoris* (L.) Medic.	Shepherd's Purse
	Sisymbrium linifolium Nutt.	Plains Mustard
	Thlaspi arvense L.	Pennycress or Fanweed
GRAMINEAE	*Agropyron spicatum* (Pursh.) Scriben. and Smith	Bluebrush Wheatgrass
	Elymus cinereus Seribn. and Meri.	Giant Wild Rye
	Festuca idahoensis Elmer.	Idaho Fescue
	Festuca scrabella Torr.	Rough Fescue
	Poa compressa L.	Canada Bluegrass

TABLE 2.--Continued (Station D Plant List)

FAMILY	SPECIES	COMMON NAME
LEGUMINOSAE	*Melilotus alba* Desr.	White Sweet Clover
	Melilotus officinalis (L.) Lam.	Yellow Melilot
	Trifolium repens L.	White Clover
LINACEAE	*Linum lewisii* Pursh.	Blue Flax
MALVACEAE	*Sphaeralcea coccinea* (Pursh.) Rydb.	Scarlet Globemallow
PINACEAE	*Juniperus scopulorum* Sarg.	Rocky Mountain Juniper
	Pseudotsuga menziesii Mirkel	Douglas Fir
POLEMONIACEAE	*Polemonium sp.* L.	Polemonium
ROSACEAE	*Purshia tridentata* (Pursh.) D. C.	Antelope Bitterbrush
SCROPHULARIACEAE	*Linaria vulgaris* Hill	Butter and Eggs

TABLE 2.--Continued (Station E Plant List)

FAMILY	SPECIES	COMMON NAME
BERBERIDACEAE	*Berberis repens* Lindl.	Oregon Grape
BORAGINACEAE	*Mertensia oblongifolia* (Nutt.) G. Don.	Bluebell
CAMPANULACEAE	*Campanula sp.* L.	Bellflower
CAPRIFLOIACEAE	*Linnaea borealis* L.	Twin-flower
CARYOPHYLLACEAE	*Cerastium arvense* L.	Chickweed
CHENOPODIACEAE	*Chenopodium sp.* L.	Pigweed
COMPOSITAE	*Achillea millefolium* L.	Yarrow
	Anaphalis margaritaceae (L.) Benth. and Hook	Pearly Everlasting
	Anternnaria sp. Gaertn.	Pussytoes
	Artemisia tridentata Nutt.	Sagebrush
	Cirsium arvense (L.) Scop.	Canada Thistle
	Cirsium sp. Mill	Thistle
	Cirsium vulgare (Savi.) Tenore.	Bull Thistle
	Solidago missouriensis Nutt.	Goldenrod
	Taraxacum officinale Weber.	Dandelion
CRUCIFERAE	*Capsella bursa-pastoris* (L.) Medic.	Shepherd's Purse
	Thlaspi arvense L.	Pennycress or Fanweed
EQUISETACEAE	*Equisetum sp.* L.	Horsetail

TABLE 2.--Continued (Station E Plant List)

FAMILY	SPECIES	COMMON NAME
ERICACEAE	*Arctostaphylos uva-ursi* (L.) Spreng.	Kinnikinnick
GERANIACEAE	*Geranium viscosissimum* Fish. and May	Sticky Geranium
GRAMINEAE	*Agropyron smithii*	Western Wheatgrass
	Agropyron spicatum (Pursh.) Scriben. and Smith	Bluebunch Wheatgrass
	Hordeum pusillum Nutt.	Little Barley
	Lolium perenne L.	Perennial Ryegrass
	Sitanion hystrix (Nutt.) J. G. Smith	Squirreltail
	Stipa sp.	Needlegrass
IRIDACEAE	*Iris missouriensis* Nutt.	Wild Iris or Western Blue-flag
JUNCACEAE	*Juncus sp.* L.	Juncus
LEGUMINOSAE	*Lupinus sp.* L.	Blue-Lupine
	Melilotus alba Desr.	White Sweet Clover
	Melilotus officinalis (L.) Lam.	Yellow Melilot
	Trifolium pratensis L.	Red Clover
	Trifolium repens L.	White Clover
LILIACEAE	*Streptopus amplexifolius* (L.) D. C.	Twisted Stalk
ONAGRACEAE	*Epilobium angustifolium* L.	Fireweed

TABLE 2.--Continued (Station E Plant List)

FAMILY	SPECIES	COMMON NAME
PINACEAE	*Juniperus horizontalis* Moench.	Creeping Juniper
	Pinus contorta Dougl.	Lodge-pole Pine
RANUNCULACEAE	*Ranunculus sp.* (Tourn.) L.	Buttercup
RHAMNACEAE	*Ceanothus sanguineus* Pursh.	Buckbrush
ROSACEAE	*Amelanchier alnifolia* Nutt.	Service Berry
	Fragaria vesca L.	Strawberry
	Geum triflorum Pursh.	Old Man's Wiskers
	Potentilla fruticosa L.	Shrubby Cinquefoil
	Potentilla glandulosa Lindl.	Five-finger
	Prunus virginiana L.	Chokecherry
	Purshia tridentata (Pursh.) D. C.	Antelope Bitter-brush
	Rosa sp. L.	Rose
SALICACEAE	*Populus tremulodies* Michx.	Aspen
	Salix sp. L.	Willow
SAXIFRAGACEAE	*Ribes sp.* L.	Gooseberry
	Rubus idaeus L.	Red Raspberry
	Rubus sp. L.	Raspberry
SCROPHULARIACEAE	*Mimulus guttatus* D. C.	Monkey-flower
	Penstemon sp. Mitch.	Penstimon
TAXACEAE	*Taxus brevifolia* Nutt.	Western Yew

TABLE 2.--Continued (Station E Plant List)

FAMILY	SPECIES	COMMON NAME
UMBELLIFERAE	*Daucus sp.* L.	Wild Carrot
URTICACEAE	*Urtica gracilis* Ait.	Stinging Nettles

TABLE 2.--Continued (Station F Plant List)

FAMILY	SPECIES	COMMON NAME
CHENOPODIACEAE	*Chenopodium sp.* L.	Pigweed
COMPOSITAE	*Achillea millefolium* L.	Yarrow
	Artemisia tridentata Nutt.	Sagebrush
	Aster sp. L.	Aster
	Bidens cernua	Beggerticks
	Chrysothamnus nauseosus (Pall.) Britt.	Rabbitbrush
	Cirsium arvense (L.) Scop.	Canada Thistle
	Erigeron sp. L.	Fleabane
	Grindelia squarrosa (Pursh.) Dougl.	Gumweed
	Solidago canadensis (L.) Conq.	Goldenrod
	Solidago missouriensis Nutt.	Godenrod
	Sonchus arvensis L.	Sow Thistle
	Taraxacum officinale Weber.	Dandelion
CRUCIFERAE	*Sisymbrium linifolium* Nutt.	Plains Mustard
CYPERACEAE	*Carex sp.* (Rupp) L.	Sedge
GERANIACEAE	*Geranium viscosissimum* Fish. and Mey.	Sticky Geranium
GRAMINEAE	*Agropyron desertorum* (Fisch.) C. Richt	Crested Wheatgrass
	Agropyron smithii Rydb.	Bluestem
	Agropyron spicatum (Pursh.) Scribn. and Smith	Bluebunch Wheatgrass

TABLE 2.--Continued (Station F Plant List)

FAMILY	SPECIES	COMMON NAME
	Agrostis tenuis Sibth.	Colonial Bentgrass
	Alopecarus aequalis Sobol.	Short-awn Foxtail
	Alopecarus sp. L.	Foxtail
	Bromus tectorum L.	Downy Brome
	Festuca idahoensis Elmer.	Idaho Fescue
	Festuca scrabrella Torr.	Rough Fescue
	Hordeum jubatum L.	Foxtail Barley
IDIDACEAE	*Iris missouriensis* Nutt.	Wild Iris or Western Blue-flag
JUNCACEAE	*Juncus balticus* Willd. var. *montanus* Engelm.	Rush or Juncus
LABIATAE	*Mentha arvensis* L.	Field Mint
LEGUMINOSAE	*Melilotus alba* Desr.	White Sweet Clover Clover
	Melilotus officinalis (L.) Lam.	Yellow Melilot
LEMNACEAE	*Lemna minor* L.	Common Duckweed
ONAGRACEAE	*Epilobium angustifolium* L.	Fireweed
	Epilobium paniculatum Nutt.	Panicled Willow-herb
	Epilobium suffruticosum Nutt.	
PINACEAE	*Juniperus scopulorum* Sarg.	Rocky Mountain Juniper
POLYGONACEAE	*Erigonum sp.* Michx.	
	Polygonum sp. L.	Smartweed

TABLE 2.--Continued (Station F Plant List)

FAMILY	SPECIES	COMMON NAME
RANUNCULACEAE	*Ranunculus sp.* (Tourn.) L.	Buttercup
RHAMNACEAE	*Ceanothus sanquineus* Pursh.	Buckbrush
ROSACEAE	*Fragaria vesca* L.	Strawberry
	Geum trifolorum Pursh.	Old Man's Wiskers
	Potentilla glandulosa Lindl.	Five-finger or Cinquefoil
	Rosa sp. L.	Rose
SALICACEAE	*Populus trichocarpa* T. & G.	Black Cottonwood
	Salix sp. L.	Willow
SAXIFRAGACEAE	*Ribes sp.* L.	Gooseberry
SCROPHULARIACEAE	*Mimulus guttatus* D. C.	Monkey-flower
	Penstemon sp. Mitch	Penstemon
	Verbascum thapsus L.	Mullein
SOLANACEAE	*Hyoscyamus niger* L.	Henbane

TABLE 2.--Continued (Station G Plant List)

FAMILY	SPECIES	COMMON NAME
BETULACEAE	*Alnus tenuifolia* Nutt.	Alder
BORAGINACEAE	*Mertensia oblongifolia* (Nutt.) G. Don	Bluebell
CAMPANULACEAE	*Campanula sp.* L.	Harebell
	Campanula rotundifolia L.	Roundleaf Harebell
CAPRIFLOIACEAE	*Linnaea borealis* L.	Twin-flower
COMPOSITAE	*Achillea millefolium* L.	Yarrow
	Anternnaria sp. Gaertn.	Pussytoes
	Artemisia tridentata Nutt.	Sagebrush
	Chrysothamnus nauseosus (Pall.) Britt.	Rabbitbrush
	Cirsium arvense (L.) Scop.	Canada Thistle
	Cirsium sp. Mill	Thistle
	Cirsium vulgare (Savi.) Airy-Shaw	Bull Thistle
	Erigeron sp. L.	Fleabane
	Solidago canadensis L.	Goldenrod
	Sonchus arvensis L.	Sow Thistle
	Taraxacum officinale Weber.	Dandelion
CRUCIFERAE	*Capsella bursa-pastoris* (L.) Medic	Shepherd's Purse
	Thlaspi arvense L.	Pennycress or Fanweed

TABLE 2.--Continued (Station G Plant List)

FAMILY	SPECIES	COMMON NAME
CYPERACEAE	*Carex festivella* Mack.	Ovalhead Sedge
ERICACEAE	*Cornus stolonifera* Michx.	Red-osier Dogwood
EQUISETACEAE	*Equisetum sp.* L.	Horsetail
GERANIACEAE	*Geranium viscosissimum* Fish. and May.	Sticky Geranium
GRAMINEAE	*Agropyron repens* (L.) Beauv.	Quackgrass
	Agropyron smithii Rydb.	Western Wheatgrass
	Alopecurus sp. L.	Foxtail
	Bromus inermis	Smooth Brome
	Phleum pratense L.	Thimothy
	Poa palustris L.	Fowl Bluegrass
IRIDACEAE	*Iris missouriensis* Nutt.	Wild Iris or Western Blue-flag
	Sisyrinchium inflatum (Suksd.) St. John	Grass Widow
JUNCACEAE	*Junus sp.* L.	Juncus
LABIATAE	*Mentha arvensis* L.	Field Mint
LEGUMINOSAE	*Lupinus sp.* L.	Blue-Lupin
	Medicago sativa L.	Alfalfa
	Melilotus alba Desr.	White Sweet Clover
	Melilotus officinalis (L.) Lam.	Yellow Melilot

TABLE 2.--Continued (Station G Plant List)

FAMILY	SPECIES	COMMON NAME
	Trifolium pratensis L.	Red Clover
	Trifolium repens L.	White Clover
LILIACEAE	*Allium cernuum* Roth.	Nodding Onion
	Streptopus amplexifolius (L.) D. C.	Twisted Stalk
ONAGRACEAE	*Epilobium angustifolium* L.	Fireweed
	Epilobium paniculatum Nutt.	Willow-herb
	Epilobium sp. L.	
PINACEAE	*Juniperus horizontalis* Moench.	Creeping Juniper
	Pinus contorta Dougl.	Lodge-pole Pine
	Pseudotsuga menzierii Mirkel	Douglas Fir
PLATAGINACEAE	*Plantago major* L.	Broadleaf Plantain
POLYGONACEAE	*Rheum rhaponticum* L.	Rhubarb
RANUNCULACEAE	*Ranuculus sp.* (Tourn.) L.	Buttercup
RHANMACEAE	*Ceanothus sanquineus* Pursh.	Buckbrush
ROSACEAE	*Amelanchier alnifolia* Nutt.	Service Berry
	Cercocarpus ledifolius Nutt.	Mountain Mahogany
	Fragaria vesca L.	Strawberry
	Geum triflorum Pursh.	Geum
	Potentilla fruticosa L.	Shrubby Cinquefoil
	Potentilla glandulosa Lindl.	Five-finger

TABLE 2.--Continued (Station G Plant List)

FAMILY	SPECIES	COMMON NAME
	Potentilla palustris (L.) Scop.	Marsh Cinquefoil
	Prunus virginana L.	Rose
	Rosa sp. L.	Aspen
SALICACEAE	*Populus tremuloides* Michx.	Aspen
	Salix sp. L.	Willow
SAXIFRAGACEAE	*Ribes aureum* Pursh.	Golden or Flowering Currant
	Ribes sp. L.	Gooseberry
	Rubus idaeus L.	Red Raspberry
SCROPHULARIACEAE	*Linaria vulgaris* Hill.	Butter and Egges
	Penstemon sp. Mitch.	Penstemon
TAXACEAE	*Taxus brevifolia* Nutt.	Western Yew
UMBELLIFERAE	*Ci cuta douglasii* (D. C.) C. and R.	Water Hemlock
	Heracleum lanatum Michx.	Cow Parsnip
URTICACEA	*Urtica gracilis* Ait.	Stinging Nettles

TABLE 2.--Continued (Station H Plant List)

FAMILY	SPECIES	COMMON NAME
BORAGINACEAE	*Myosotis stricta* Link.	Forget-me-not
CARYOPHYLLACEAE	*Silene alba* Muhl.	White Campion
COMPOSITAE	*Achillea millefolium* L.	Yarrow
	Cirsium arvense (L.) Scop.	Canada Thistle
	Erigeron sp. L.	Fleabane
	Taraxacum officinale Weber.	Dandelion
CRUCIFERAE	*Armoracia rusticana* (Lam.) Gaertn.	Horseradish
	Capsella bursa-pastoris (L.) Medic.	Shepherd's Purse
	Nasturtium officinale R. Br.	Water Cress
	Sisymbrium linifolium Nutt.	Plains Mustard Plains Mustard
CYPERACEAE	*Carex nebraskensis* Dewey	Nebraska Sedge
	Carex rostrata Stokes.	Beaked Sedge
EQUISETACEAE	*Equisetum sp.* L.	Horsetail
GRAMINEAE	*Alopecurus sp.* L.	Foxtail
	Agropyron subcundum	
	Agrostis alba L.	Red Top
	Arrheratherum sp. (L.) Presl.	Tall Oatgrass
	Elymus cinercus Scribn. & Merrill	Basin Wild Rye
	Herdeum jubatum L.	Foxtail
LABIATAE	*Mentha arvensis* L.	Mint

TABLE 2.--Continued (Station H Plant List)

FAMILY	SPECIES	COMMON NAME
LEGUMINOSAE	*Melilotus alba* Desr.	White Sweet Clover
	Melilotus officinalis (L.) Lam.	Yellow Melilot
LEMNACEAE	*Lemna minor* L.	Common Duckweed
ONAGRACEAE	*Epilobium palustre* L.	Marsh Willow-herb
	Epilobium sp. L.	
PLANTAGINACEAE	*Plantago lancelata* L.	Plantain
POLYGONACEAE	*Polygonum sp.* L.	Smartweed
	Rheum rhaponticum L.	Rhubarb
RANUNCULACEAE	*Ranunculus sp.* (Thourn.) L.	Buttercup
ROSACEAE	*Geum triflorum* Pursh.	Old Man's Wiskers
	Rosa sp. L.	Rose
SALICACEAE	*Populus trichocarpa* T. & G.	Black Cottonwood
	Salix sp. L.	Willow
SCROPHULARIACEAE	*Castilleja sp.* Mutis.	Indian Paintbrush
TYPHACEAE	*Typha latifolia* L.	Common Cattail
VIOLACEAE	*Viola sp.* L.	Violet

TABLE 3.--Analytical Results of the Aquatic Sampling Program to Date

SURVEILLANCE PROGRAM
Biological, Chemical, and Physical

TRACE ION ANALYSIS
P.O. 1393

PROJECT MHD-CDIF

Mineral Research Center
(Laboratory or Contractor)

Date Received 6/29/77

Date Analyzed July and August

Circle One: (Water,) Terrestrial Vegetation, Aquatic Vegetation, Macroinvertebrates, Filter Paper, Algae, ___

Sample #	Cd	Pb	Zn	As	Se	Hg	F	B	Ni	Be
770622-G-1	1.9	3	13	1			21		<1	
(Basin Creek)										
770622-I-1	9.0	6	17	<1			50		1	
(Krause Weld)										
770622-J-1	2.5	4	21	<1			28		1	
(Webster Well)										
770623-E-1	5.4	7	16	6			14		2	
(Multon Res)										
770623-F-1	9.2	4	9	10			37		1	
(Beaver Dam)										
770623-H-1	2.6	<1	21	3			110		3	
(Swamp)										

REMARKS: Ion's reported in ppb or ug's/ml
Se, Hg, B, Be will be reported at a later date

6/10/77

(initials)

TASK S1

Table 4.--Status of the PBBSP

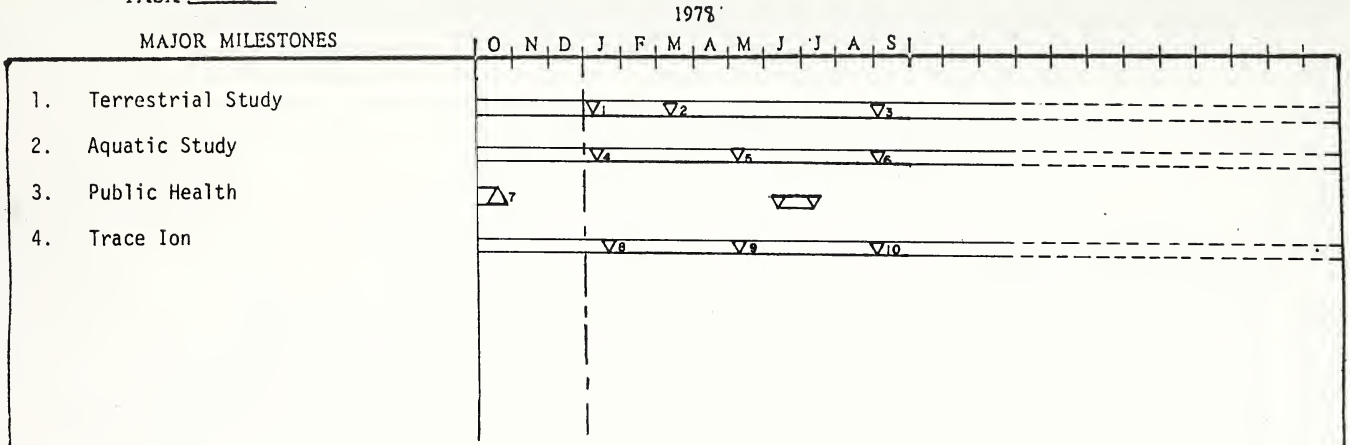

▽ 1 Review of terrestrial sitings and areas completed' procedure manual, etc. printed.

▽ 2 Major field work on soil and vegatation (spring).

▽ 3 Major field work on soil and vegatation (fall).

▽ 4 Review of 1977 aquatic data: procedure manual, etc. printed.

▽ 5 Major field work on periphyton.

▽ 6 Major review of field work.

▽ 7 Final report on Public Health.

▽ 8 Review of existing trace ion data and establishment of MERDI-PBBSP capabilities.

▽ 9 Major review of laboratory work; procedure manual, etc. printed.

▽ 10 Major review of laboratory work.